THE DESIGN OF NOVEL TRANSPARENT HEAT MIRRORS FOR ENHANCED SOLAR THERMAL APPLICATIONS

Mohsen Rostami

A THESIS SUBMITTED TO

THE FACULTY OF GRADUATE STUDIES

IN PARTIAL FULFILLMENT OF THE REQUIREMENTS

FOR THE DEGREE OF

MASTER OF APPLIED SCIENCE

Graduate Program in

MECHANICAL ENGINEERING

York University

Toronto, Ontario

May 2019

Abstract

Herein the design of transparent heat mirrors for enhanced solar thermal applications is presented. Dielectric mirrors are considered to function as infrared mirrors that reduce heat losses in the receiver of solar concentrators. The alternating layers have been designed to selectively reflect light strongly over the infra-red spectral region while being highly transmissive towards solar irradiance. This is achieved by designing the interfaces between the high- and low- index films within the dielectric mirror to have a graded refractive index profile. Three different graded index profiles are considered including: 1. a linear index variation, 2. a cubic index variation and 3. a quintic index variation. The effects of altering the dielectric mirror parameters on its performance are investigated. Accordingly, the sensitivity of the transmittance and reflectance spectra of the dielectric mirror towards its number of layers, resolution of the refractive index profiles, refractive index, number of stacked dielectric mirrors, absorption, and incident angle of the incoming light is analyzed. Results show that a single stack infrared dielectric mirror coated on top of the receiver of a solar concentrator system operating at 500 K can increase its power electric generation by more than 60 % and using a triple stack design can increase the power by more than 100 %. Furthermore, considering a typical Dish-Sterling system operating at a temperature of T=1000 K, the electricity generated can be increased by ~ 30 % by coating the receiver within the system with the transparent heat mirrors designed in this work.

Acknowledgement

I would like to express my very great appreciation to Prof. Paul G. O'Brien, my research supervisor, for his kind interest, patience, motivation, and immense knowledge while supporting my graduate study and research. His professional guidance and valuable support helped me in all period of research and writing of this thesis. Also, I would like to thank Dr. Kempers and Dr. Lam for their supports and valuable comments which enhanced the quality of this thesis.

I would also wish to express my deep gratitude to my parents and my friends for providing me with unfailing support and continuous encouragement throughout my years of study and through the process of researching and writing this thesis.

This thesis has been written during my stay at the Mechanical Engineering Department of York University. I also would like to thank the Bergeron Centre for Engineering Excellence and Lassonde School of Engineering for providing excellent working conditions and financial support.

Toronto, May 29th , 2019

Mohsen Rostami

Table of Contents

List of Tables

List of Figures

List of Symbols

A	Projected surface area
A_{ap}	Collector aperture area
A_{rec}	Area of the receiver
a	Absorbance of the surface
B	Normalized tangential electric
B_v	Quantity of energy emitted by a blackbody at different radiation frequencies
C	Light speed
d_H	Thicknesses of the H layers within the dielectric mirror
d_L	Thicknesses of the L layers within the dielectric mirror
d_{L+H}	Thicknesses of the H and L layers within the dielectric mirror
f1	Reflectance peak position of the first stack of the dielectric mirror
f2	Reflectance peak position of the second stack of the dielectric mirror
f3	Reflectance peak position of the third stack of the dielectric mirror
G	Solar radiant power

H	Materials with a high index of refraction
H_L	Higher index film with linear graded-index profile
H_C	Higher index film with cubic graded-index profile
H_Q	Higher index film with quintic graded-index profile
h	Local convective heat transfer coefficient between the receiver and the surrounding environment
I	Direct solar flux intensity
K	Absorption coefficient
k_B	Boltzmann constant
L	Materials with a low index of refraction
L_L	Lower index film with linear graded-index profile
L_C	Lower index film with cubic graded-index profile
L_Q	Lower index film with quintic graded-index profile
L_R	Radiative losses
L_H	Convective and conductive heat losses
n	Refractive index
n_p	Refractive index of the porous material
n_H	Refractive index of the H layers within the dielectric mirror
n_L	Refractive index of the L layers within the dielectric mirror

p	Percent porosity
P_{rad}	Radiated power from the blackbody surface
P_{net}	Net radiated power
P_{in}	Entering power
P_{out}	Exiting power
q	Number of layers
r	Reflectance
T	Absolute temperature
T_s	Average receiver temperature
T∞	Ambient temperature
t	Transmittance
v	Frequency
W_{grin}	The width of the region with a graded index of refraction
W*	Resolution of the graded index of refraction profiles
ΔW	The distance over which the index of refraction is constant
x	Density of non-porous material
x_p	Density of porous material
Y	Admittance of the medium the light is incident on

λ	Wavelength
ε	Emissivity
σ	Stefan-Boltzmann's constant
ρ	Amplitude of the reflection coefficient
η_0	Admittance of the incident medium
η_s	Admittance of the s-polarized light
η_p	Admittance of the p-polarized light
Θ	Incidence angle
δ_j	Phase thickness of layer j

List of Abbreviations

ARC	Antireflective coating
ASTM	American Society for Testing and Materials
CSP	Concentrated solar thermal power
FWHM	Full width half maximum
GHG	Greenhouse gas
GRIN	Graded refractive index
HTF	Heat transfer fluid
IEA	International Energy Agency
ITO	Indium tin oxide
LFR	Linear Fresnel reflectors
Low-E	Low-Emissivity
PDC	Parabolic dish collectors
PhC	Photonic crystal
PTC	Parabolic trough collectors
PV	Photovoltaic cells
SEM	Scanning electron microscopy
STE	Solar thermal electricity

SPT	Solar power towers
SWH	Solar water heating
SWS	Sub-wavelength structures
TCE	Transparent conductive electrode
TCO	Transparent conductive oxide
TES	Thermal energy storage
TPES	Total primary energy supply
1-D	One-dimensional

1. Introduction

1-1. Global warming

Accelerated global warming due to green house gas (GHG) emissions is an important modern-day challenge. There are several factors that contribute to GHG emissions in Canada and around the world. Approximately 80% of GHG emissions from human activities are related to energy consuming activities including transportation, electricity production, building heating and cooling, goods production and operations [1].

1-2. Global energy usage

In general, two different kinds of energy usage statistics can be considered for comparison: primary energy use and secondary energy use. Primary energy use represents the total energy required for all energy users, and secondary energy use is the energy consumed by the end user in the economy. The global total primary energy supply (TPES) in 2015 was reported as follows:

- Fossil Fuels: 81% (oil 32%, coal 28%, natural gas 22%)
- Renewables: 14%
- Nuclear: 5%

Comparatively, Canada's TPES in 2015 is shown in the pie chart in Figure 1-1. As can be seen the total primary energy supply in 2015 was 11,493 PJ. Fossil fuels (natural gas, crude oil, natural gas liquids and coal) made up 73% of Canada's TPES in 2015. Renewable energies accounted for more than 17% and nuclear power contributed to almost 10% of this energy supply.

As for the secondary energy use, which is the energy used by the final consumer, Canada's secondary energy use in 2015 was estimated to be around 9,013 PJ. This amount shows about an 11% increase from 2000 to 2015.

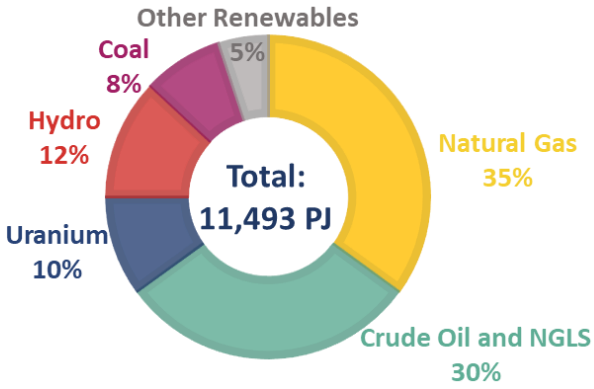

Figure 1-1. Canada's total primary energy supply by source, 2015 [1]

Generally, due to extreme climate changes, large land mass, and discrete population, Canadians consume more energy than citizens of other countries. The pie chart in Figure 1-2 shows that out of a total of 9,013 PJ of secondary energy usage in 2015 in Canada, 71% was provided from fossil fuel combustion, while electricity accounted for 20%, followed by biomass which accounted for 6%, and other fuel types such as coal and natural gas liquids accounted for 3%.

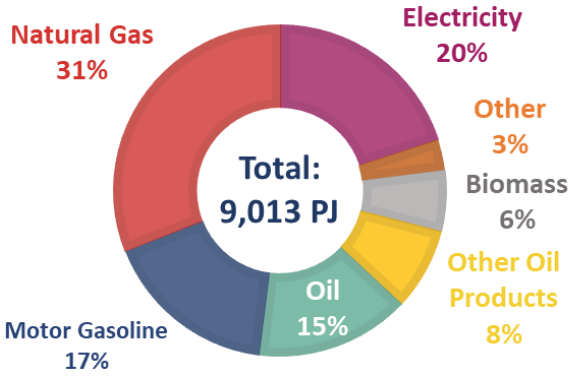

Figure 1-2. Canada's secondary energy use by fuel type, 2015 [1]

Another important element in this statistical comparison is to consider the energy usage in the different sectors. In 2015, 71% of all primary energy was transformed into secondary energy, where the energy consumption within each sector is as follows:

- Industrial: 39.4%
- Transportation: 29.6%

- Residential and Commercial: 28.2%
- Agriculture: 2.8%

Looking forward to future demands, Figure 1-3 shows the trend of energy use in the industrial sector from 2010 to 2040 [2,3]. For the reason that fossil fuel usage can result in damage to human life, particularly ecological issues concerning with these fuels, modern industries are not attracted to consume conventional fuels anymore. In contrast, using renewable energy-based technologies in productions can result in a significant reduction in the greenhouse emissions. Figure 1-4 represents GHG emission from renewable and conventional electricity generation technologies. The data used here are based on the maximum emissions for renewable energy sources and mean values for conventional electricity generation technologies. As can be seen, the life cycle GHG emissions in conventional electricity generation sources are reasonably higher than those for renewable technologies [4].

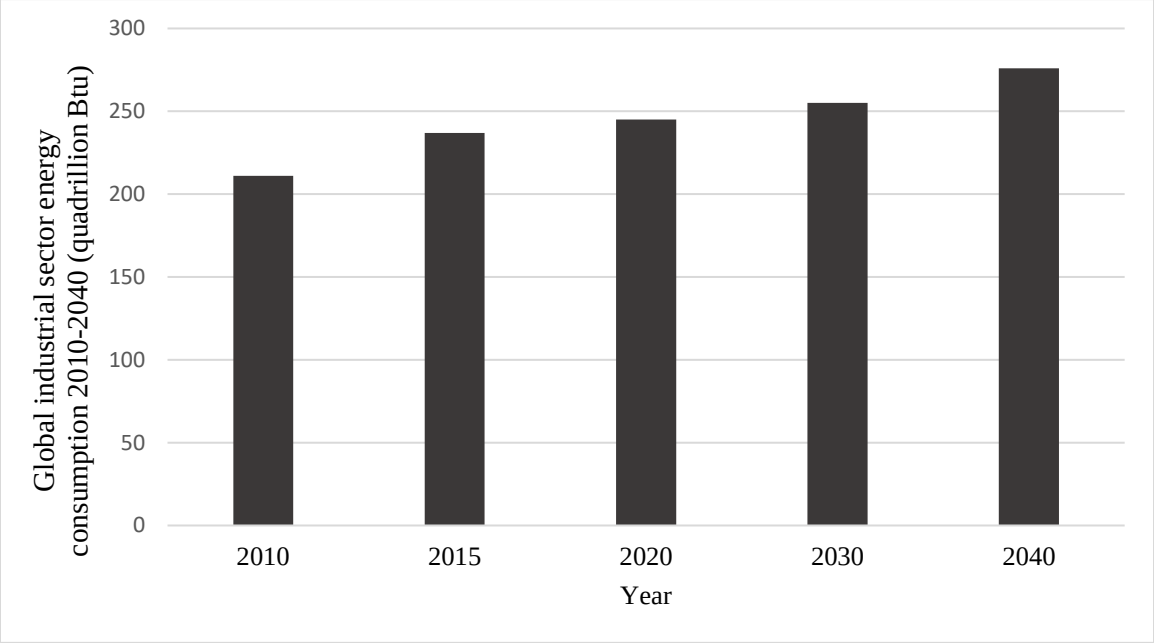

Figure 1-3. Global industrial sector energy consumption during 2010–2040 [3]

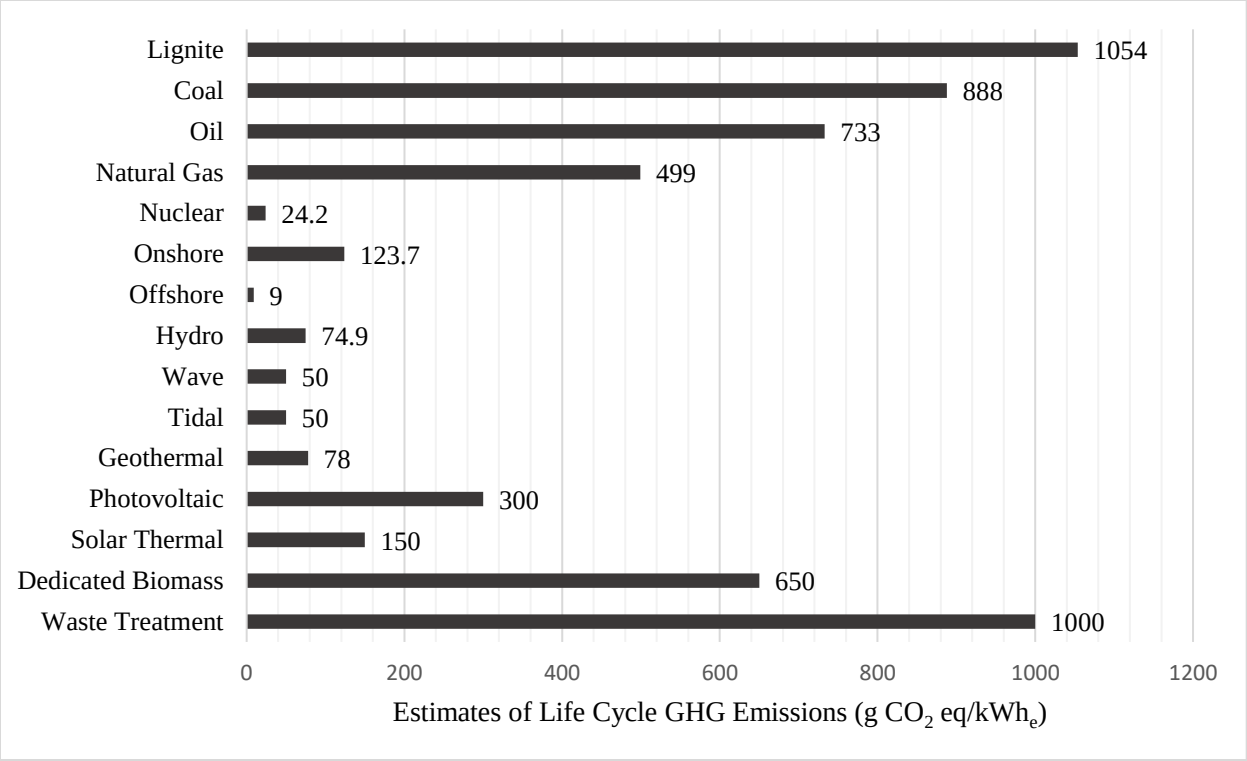

Figure 1-4. GHG emission levels produced by different methods for generation of electric power [4]

While Canada's dependency on fossil fuels is small in comparison to the global fossil fuel consumption, it is still huge and according to Figure 1-5, which is illustrating Canada's national GHG emissions in megatons of carbon dioxide equivalent (CO_2eq) from 1990 to 2016, Canada emits ~ 700 megatons (Mt) of CO_2eq every year [5]. Consequently, conventional energy supplies should be replaced with renewable energies and new systems have to be industrialized and used in companies. Furthermore, residential and commercial sectors contribute to almost 30% percent of energy usage in Canada, as building heating and cooling loads contribute largely to energy consumption and GHG emissions [1]. Therefore, more energy efficient systems using renewable energy resources are also required in the residential and commercial sectors in order to reduce our daily energy usage.

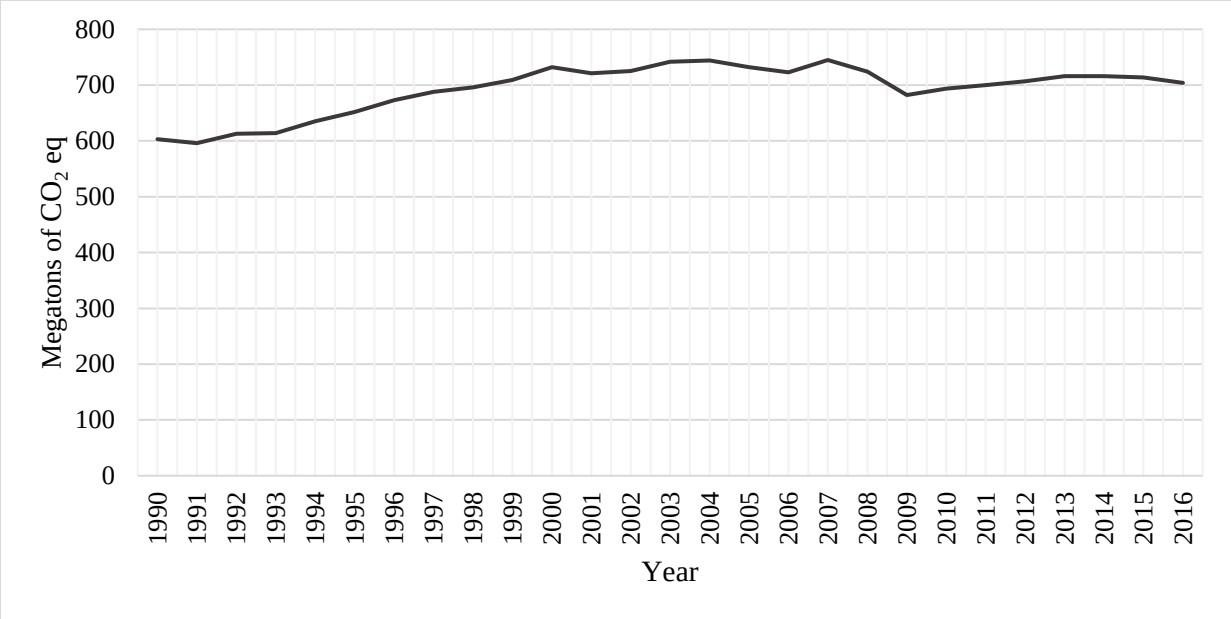

Figure 1-5. Canada's GHG emissions in megatons of CO_2 eq from 1990 to 2016 [5]

1-3. Renewable energy resources

Global energy resources can be divided into three types: fossil fuels, renewable energy resources and nuclear power. Usually fossil fuels are coal, petroleum and natural gas [6]. Renewable energy sources, also referred to as alternative energy sources, can be used to produce energy without depleting the energy source such as solar, wind, and biomass energy [7].

Although there are challenges involved with using renewable energy resources, including intermittency, cost and domestic and environmental restrictions, they can potentially provide energy services with negligible emissions of GHGs and air pollutants. Advances in renewable energy based technologies will open a new area to better resolve the recent significant challenges such as improving energy supply reliability and organic fuel economy, solving problems regarding water purification, improving the standards of living and civilisation in remote zones, ensuring sustainable growth in the remote areas like deserts and mountains, and encouraging countries to be responsible to the international agreements concerning the ecological and environmental

preservation [8]. Interestingly, using renewable energy systems in rural areas can provide more job opportunities and diminish immigration towards cities in the long term [9]. For instance, renewable energy harvesting can be a great solution for small-scale energy needs in a reliable, reasonable and naturally sustainable manner [10].

1-4. Solar energy

Among all the renewable energy resources, solar energy is undoubtedly the largest useable resource, providing one of the cleanest energy resources. Interestingly, the sun emits more energy in one second than people have used since beginning of time. And the energy provided by the sun in an hour to the earth is much higher than all of the energy used by people in a complete year [11,12]. The amount of energy received from the sun has been estimated to be in the range of 1,575 to 49,837 EJ/year, which is approximately 3 to 100 times larger than the world's TPES in 2008 [13]. Despite its abundance and environmentally benign qualities, solar power contribution to the global energy supply is still trivial [14].

Solar energy is the most abundant, free and the cleanest renewable energy resource available which does not contribute to global warming and does not make any noise or any kind of pollution to the atmosphere. Solar energy is also called “alternative energy” to fossil fuels such as petroleum, and coal. Due to considerations of a long-term world-wide energy shortage, and the destructive ecological effects of fossil fuel energy sources, solar energy has been considered much in researches and experiments done by engineering scientists. Therefore, in the next steps, more investigations should be considered for operative and commercial methods to capture and convert solar energy into useful energy and store it in on large scales to be used later in other systems [15]. The growing lack of fossil fuel resources has raised prevalent attention towards solar energy [16-

18]. Currently, around 46 nations are enthusiastically promoting solar energy-based technologies [13].

Another important aspect of solar energy is related to present efforts to diminish global carbon emissions, which has been a major ecological, social, and economic issue throughout the world in recent years. Besides, global agreements, such as the Conference of Parties 21, can deter environmental change and will enable advances in sustainable energy-based systems to ensure a sustainable future for the planet [19,20]. For instance, reports showed that in California, USA, CO_2 emissions have been reduced through the implementation of 113,533 solar systems mostly in small scales [14]. One strategy that California benefits from is to accept electricity generation in small scale cases using a feed-in tariff (FIT). Accordingly, for a specific duration, electricity generators such as homeowners are paid based on the size and efficiency of their system [21].

Solar energy has been widely implemented under sunny conditions in warm desert zones such as Africa, the Middle East, China, the USA and Australia. Other advances can be found in more humid environments such as Sub- Saharan Africa, South America, southern Asia and Europe as well.

Considering locations with cold weather and less solar irradiance, solar energy resources can also be used in these situations, but it is always challenging in terms of share and impact. If the feasibility is reasonable, then quite a lot of factors need to be considered prior to optimizing such systems. For instance, a typical house designed in a way to use solar energy in Canada can lead to an improvement in energy consumption by 21–32% [19].

1-5. Different types of solar energy technologies

In general, solar energy technologies can be divided into two different groups: active and passive. Furthermore, active solar energy systems which are mainly used for energy harvesting, can be categorized into two areas: 1. solar photovoltaic cells (PV) and 2. solar thermal technology or concentrated solar thermal power (CSP) [22].

Generally, CSP technologies use a dish Stirling system, a parabolic trough, a solar power tower or linear Fresnel reflectors to concentrate the suns rays and harvest heat within a heat transfer fluid (HTF) to be converted to electricity in a turbine [23]. Alternatively, solar PV systems use solar cells to directly convert solar energy into electricity. The installed cost of PV electricity is significantly decreasing due to recent upgrading of PV technologies, however, in comparison with CSP systems the energy conversion efficiency of commercial PV panels is challenging yet. For comparison, the CSP facility located in Gela and the PV plant in Luxor are considered. For the same nominal energy output, the CSP system illustrates a higher electric power generation compared to the PV plant, with output of 40.7 GWh and 10.6 GWh, respectively. Although, the overall efficiency of the CSP is higher than the PV modules, due to the smaller occupied area the PV installation represents higher land use efficiency. Accordingly, considering the same area for both methods can result in a higher electricity production by PV modules, reaching to 70.5 GWh. The main drawback of PV systems is the failure of power dispatch due to the energy storage challenge as it will cost a fortune to consider the energy storage system in PV systems [23, 24]. A CSP-based system has more potential to dispatch energy compared to a PV-based system as it can provide electricity during night using thermal energy storage (TES) system over daytime at a lower cost. On account of the huge capacity of TES systems for electric energy supply, a CSP system is

now the primary choice to offer flexibility for power generation and service at a large scale (>100 MW) [25,26].

1-5-1. PV technology

There are numerous isolated areas in the world where electric power is rarely available, but solar irradiation is abundant, thus the use of solar energy to produce electricity in these areas is quite advantageous [27]. Capture and conversion of solar energy may be accomplished by PVs [28]. PV conversion can be defined as the direct conversion of sunlight into electrical energy [29].

PV systems are quite simple in design and their main advantage over other energy sources is their structure as stand-alone systems which can provide from microwatts to megawatts of electric energy. PV devices have long service times and low maintenance costs. Consequently, the technology can be used as a power generator for various operations ranging from small scale systems to large plants, in remote buildings, in solar home systems, for satellites and spacecrafts, for reverse osmosis in plants, and even for megawatt-scale power plants [30]. The main challenge here is to significantly reduce the cost per Watt of energy delivered by solar energy system [10].

PV is presently a theoretically and practically recognised technology able to produce and supply electricity in short/mid-term by means of solar energy. However, the present PV installations are still trivial [31]. The International Energy Agency (IEA) estimated that the solar power contribution to world's electricity generation by 2050 will be 11% and that solar electricity will account for approximately 20% of the global energy supply by 2050 and 60% by 2100. [32].

Due to advancing PV technology and high levels of financial support, the PV market is now being rapidly developed and distributed around the world, especially in Europe, China and in the United

States and even in Canada [33-37]. Figure 1-6 shows a typical solar PV system provided by Enviro-Energy Technologies located in Cambridge, Ontario, with 98,000 kWh electricity generation.

Figure 1-6. A typical solar PV system provided by Enviro-Energy Technologies located in Cambridge, Ontario, with 98,000 kWh electricity generation (Reprinted with permission from Ref. [34]).

1-5-2. Solar thermal technology

The earth intercepts approximately 1.8×10^{14} kW of the energy emitted by the sun at a rate of 3.8×10^{23} kW [38]. Concentrating solar power or solar thermal electricity (STE) is unique among all renewable energy resources as it can simply be coupled with TES and conventional fuels, making it extremely flexible [39]. Since 1985 CSP has been used commercially and it produces electric power with a thermal power cycle like the one used in typical fuel-operated power plants [40]. Generally, a CSP uses solar collectors and concentrators to gather sun radiation, store it and use it for heating fluids such as air or water [6]. Passive solar energy can be presented based on the concepts for heating under cold climates. Although, buildings in such areas are generally well-designed to overcome the cold, a simple method for using passive solar energy is by optimizing buildings including the color of the walls and roof for a better absorptivity, addition of infrastructures to the existing buildings and modifying the shape of the buildings. Even integrating

a limited number of these changes can have a significant effect towards reducing energy consumption.

1-5-2-1. Main CSP technologies

CSP technologies utilize four main types of solar concentrators: parabolic trough collectors (PTC), solar power towers (SPT), linear Fresnel reflectors (LFR), and parabolic dish collectors (PDC) (Figure 1-7). Also, they can be classified based on the receiver's position and the way they concentrate solar radiation [40]:

1. Systems wherein the solar irradiance is tracked along one axis and focused along one axis, referred to as the line of focus, including parabolic trough and linear Fresnel systems.

2. Systems wherein the solar irradiance is tracked along two axes and focused onto a point, such as tower and dish systems.

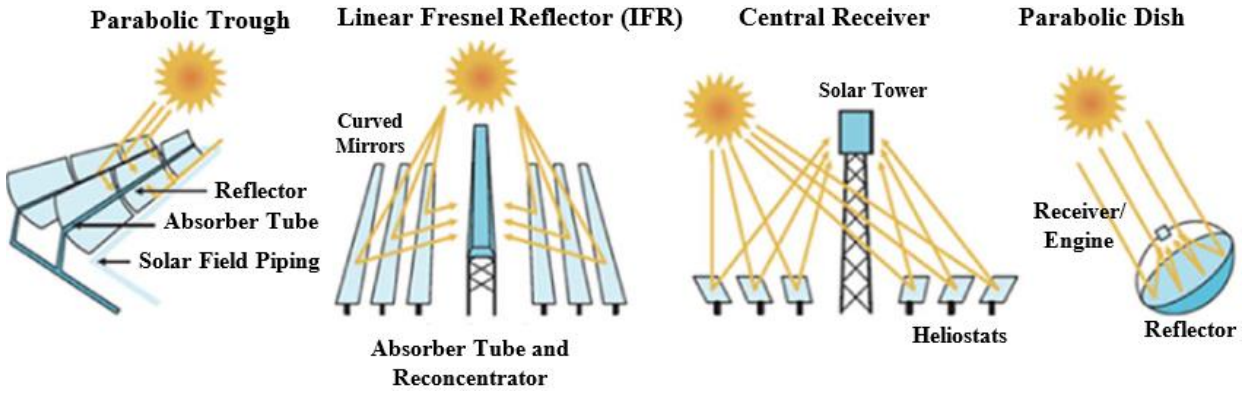

Figure 1-7. The main STE technologies (Reprinted with permission from Elsevier, Fig. 1, [40])

In tower and linear Fresnel systems the receiver is fixed, while in dish and parabolic trough systems it is moveable. The direct solar radiation in a parabolic trough system is focused by a reflector onto a receiver tube that runs along the line of focus. The reflector in this system has a parabolically curved trough shape. The heat transfer fluid (HTF) in a parabolic trough system, which is usually synthetic oil, is heated by the solar irradiance that is concentrated onto the receiver tube. The

system uses the heated HTF to generate electric power with an existing steam generator and turbine system. Parabolic trough systems can also be coupled with conventional coal-fired plants [41].

Solar power towers generate electric power from the insolation by means of many sun-tracking mirrors, commonly called heliostats. Each heliostat reflects the direct portion of the solar irradiance onto a receiver located at the top of the tower [40]. In a typical solar power tower, the HTF is usually molten salts or water/steam. Therefore, as the HTF flows through the receiver it is heated by the concentrated solar irradiance incident onto the receiver. Finally, the HTF is used in a steam generator-turbine system to generate electric power.

In a linear Fresnel system, plane (or to some extent rounded) mirrors are located on trackers to reflect the direct portion of the solar irradiance onto a receiver tube located along the focal line directly above the mirrors. Further concentration of the reflected sunrays can be achieved using a small secondary parabolic mirror mounted at the top of the receiver.

Parabolic dish technology utilizes a concentrator in the form of a parabolic-shaped dish with a focal point. Using this dish, the system reflects the direct portion of the incident solar radiation onto a receiver located at the focal point. In a parabolic dish system, a two-axis tracking system is used, and a heat engine mounted on the receiver directly uses the collected heat. Currently, for power conversion process one can use Stirling or Brayton cycle engines.

Parabolic trough technology is the most abundant CSP technology in the market and are presently the most established STE system, being used in approximately 81% of the active STE plants in the world, about 48% of which are currently under construction. As for the solar tower technology, presently among all active global STE plants, almost 14% are of this type, while this proportion increases to 28% for the plants which are under construction [40].

The growth in the solar tower projects in the current years demonstrates that this technology has reached a decent level of maturity to be used in large scales even up to hundreds of MW. However, parabolic dishes are at their initial demonstration phase. This is while, linear Fresnel system is now in the phase of transition to becoming a commercially proven technology [40].

1-5-2-2. Thermal energy storage

Time and weather dependency are the main problems associated with solar energy source. To overcome this disadvantage, one can integrate solar thermal-based technologies with a backup system that works with fossil fuel or biomass. Another solution is to use a TES system to store heat during times when there is excess solar radiation and to release it during the times with insufficient or no sunshine (Figure 1-8).

Advances in TES technologies and development of well-organized and cost-effective TES system is very important for the future of CSP systems [42, 43]. Using TES will increase the availability of the electricity produced from the system. Furthermore, integrating a TES system with CSP configurations guarantee electric power resale and the CSP production in large scales [44]. Therefore, CSP systems integrated with TES technologies will be economically viable if they can provide electricity at peak-demand hours, when tariffs are the greatest [45-46].

The simplicity of operation and flexibility of TES to be integrated with various systems, makes CSP unique among other available renewable energy resources. Recently there has been substantial growth in solar thermal energy production in industrial scale and its TES technologies. Compared to mechanical or chemical storage technologies, TES has several advantages. Many comparisons have been done between different energy storage technologies [47, 48]. For instance, capital costs of TES technologies in comparison with other storage technologies are lower. Moreover, they operate very efficiently compared to mechanical or chemical storage systems [49–

53]. A typical TES system is comprised of plentiful materials with a lot less harmful ingredients compared to the existing storage technologies [54].

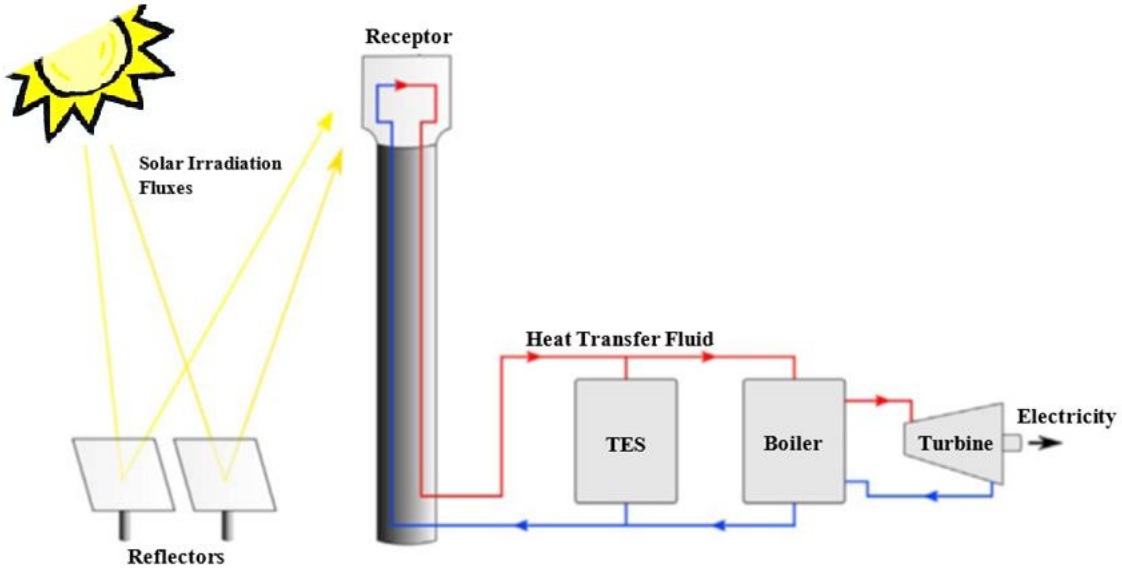

Figure 1-8. CSP plant with a TES system (Reprinted with permission from Elsevier, Fig. 1, [54])

1-5-2-3. Solar thermal energy for industrial processes

Generating thermal power by use of solar power for industrial processes not only can result in a lower reliance on fossil fuel energies but also reduced GHG emissions such as CO_2, SO_2, and NO_x emissions [2]. Presently, space and water heating require a large share of the energy consumed in residential zones: around 80% in Canada and 82% in Europe [55]. Hence, there is huge motivation to convert solar energy into heat [56]. However, there are some difficulties to transfer solar heat to industries due to the natural behaviour of solar energy including its intermittency, diluteness and variability [57]. Currently, solar energy used in industrial sectors for thermal applications can be classified as follows:

- Hot water or steam demand processes
- Drying and dehydration processes
- Preheating

- Concentration
- Pasteurization, sterilization
- Washing, cleaning
- Chemical reactions
- Industrial space heating
- Textile
- Food
- Buildings
- Chemistry
- Plastic
- Business establishments

Also, solar energy is a great choice capable of being one of the principal sources for cooking [58-60]. Currently several types of solar ovens are existing, among them a box type solar cooker (Figure 1-9) that is commonly used all over the world.

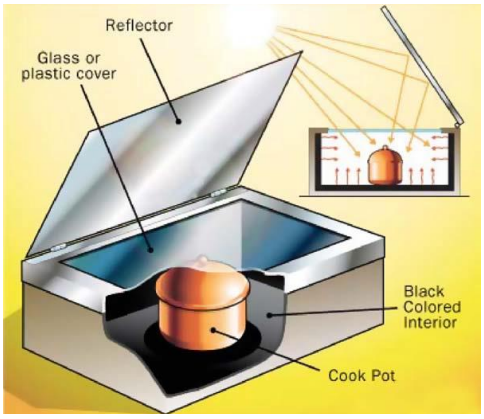

Figure 1-9. Box type solar cooker (Reprinted with permission from Elsevier, Fig. 2, [61])

Currently the solar water heating (SWH) industry is a popular application of solar thermal energy in both domestic and industrial sectors. It is considered as a great cost-effective alternative among other available solar thermal systems. SWH technology has been commercialized and is well

known in many countries all around the world. Interestingly SWH usage has been increased with an annual growth rate of 30% since 1980 [62].

SWH systems usually consist of collectors and a storage box. The system operates on the basis of the difference between the density of hot and cold water. Integrated collector/storage systems are more acceptable in colder countries due to simple and compact structure. Batch solar collectors are more suitable for compensating sun radiation limitations over the time sun is not available like during evening time or cloudy weather condition [63].

A schematic diagram for a typical solar water heating system commonly used in industrial applications is shown in Figure 1-10. In this system the water never returns to the storage space. A typical SWH system is composed of solar collectors, circulating and load pumps, storage tank, a differential thermostat and a thermal relief-valve. To control the temperature of the system, a controller block is also needed. Therefore, once the temperature goes beyond the fixed value, the valves will mix the hot water and main water to provide energy from supply system and reach the desired temperature. In situations with insufficient temperature, an auxiliary heater will compensate the weakness and the desired temperature of the tank will be available.

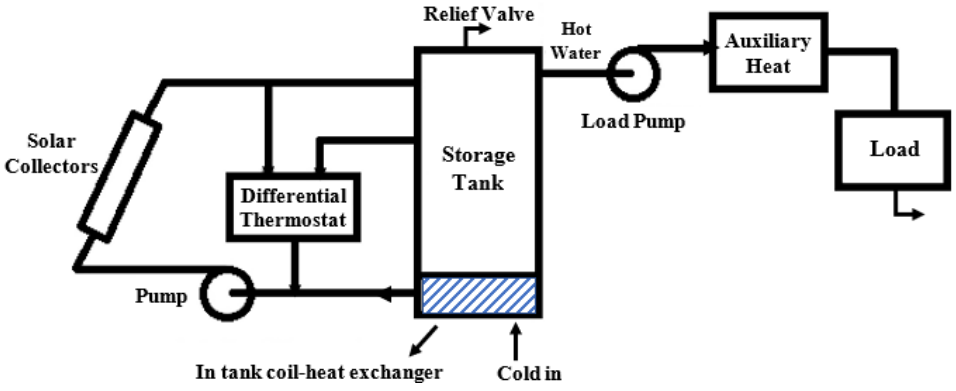

Figure 1-10. Block diagram of a SWH system (Reprinted with permission from Elsevier, Fig. 2, [2])

1-6. Thesis outline

Common to all CSP systems is the desire to absorb solar radiation without losing energy through thermal radiation. An efficient method to avoid radiative thermal losses and to achieve high temperatures on the receiver within CSP systems is to implement low-Emissivity (low-E) coatings on top of the surface of the receiver, which absorbs incident solar radiation. Low-E materials can significantly reduce energy usage by reducing radiative heat losses [64-66]. Furthermore, transparent solar selective coatings exhibit high transmittance for solar radiation and high reflectance in the near infrared and infrared spectral regions [67-72]. Consequently, by applying a transparent solar selective surface, herein also referred to as a transparent heat mirror, on the surface of a receiver (which transmits solar radiation and functions as a low-E coating in the infrared region) subjected to concentrated solar radiation will result in a considerable reduction in thermal losses [64,73]. For example, more electric power can be produced by parabolic dish systems when its receiver is coated with a highly efficient solar selective coating.

This thesis presents the design of novel transparent heat mirrors that can be used to enhance solar energy harvesting technologies such as CSP technologies and TES systems. In the following, in Chapter 2, the important background topics for designing transparent heat mirrors for solar thermal applications is presented. In Chapter 3, the thesis will be continued with the design of a transparent selective coating in the form of a dielectric mirror (often referred to as one-dimensional photonic crystal or a Bragg-reflector) comprised of alternating layers with different indices of refraction. Then, the alternating layers of films will be designed to selectively reflect light strongly over the infra-red spectral region while being highly transmissive towards solar irradiance. In order to accomplish this, thin graded index layers will be designed as anti-reflection coatings at the interfaces between the alternating layers within the dielectric mirror. Three different index of

refraction profiles will be considered including: 1. a linear index variation, 2. a cubic index variation and 3. a quintic index variation [139]. Chapter 4 will provide sensitivity analysis of the transmittance and reflectance spectra of the dielectric heat mirror towards its number of layers, resolution of the refractive index profiles, refractive index, number of stacked dielectric mirrors, absorption, and incident angle of the incoming light. In Chapter 5, the transparent heat mirrors will be used in the design of a solar concentrators operating at different temperatures to evaluate its ability to improve the performance of high-temperature solar thermal energy applications. Finally, conclusions and recommendations for future work will be provided in Chapter 6.

2. Background

In this chapter, the background information for important topics related to the design of transparent heat mirrors for solar thermal applications is presented. Accordingly, different subjects including air mass coefficient, blackbody radiation, solar radiation spectrum, emissivity, low emissivity coatings, transparent conductive oxides, solar selective surfaces and antireflective coatings are studied in depth. Finally, a brief overview is provided to outline the methods and applications of the work presented in this thesis.

2-1. Air mass coefficient

The air mass coefficient is defined as the relative optical path length through the atmosphere that is traversed by incident solar radiation. This path length is measured based on the location of the sun and when the sun is directly overhead, at the zenith, the path length is called AM 1.0 because the solar irradiance travels vertically through a path length that is 1 atmosphere thick. The air mass coefficient is an important factor in characterizing the solar spectrum incident onto Earth's surface at a specific time and location. With respect to Figure 2-1 and Figure 2-2, as the angle between the zenith and the direction towards the sun, θ, gets bigger, the air mass increases roughly by sec θ. For instance, when the direction towards the sun is about 48° and 60° from the zenith the air mass is 1.5 and 2.0 because the solar radiation incident onto the Earth's surface travels 1.5 and 2 times further through the atmosphere, respectively, as compared to the AM 1.0 case when the sun is directly overhead [74, 75].

As the air mass increases (i.e. longer path lengths), scattering and absorption of solar radiation will be increased by environmental elements such as aerosols, air molecules, and water vapor. The scattering and absorption of solar radiation depends on the environmental circumstances (e.g.,

clouds and aerosols). Both of these variables, air mass and environmental conditions, change with region, and time of day and year. Consequently, it is important to consider the environmental circumstances and air mass at the location of interest when designing a system or technology whose performance depends on the solar irradiance [75].

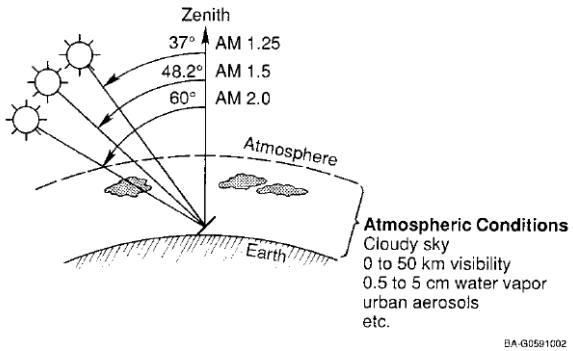

Figure 2-1. Examples of other realistic atmospheric and air mass conditions compared to AM 1.5 (Reprinted with permission from Ref. [75], IEEE).

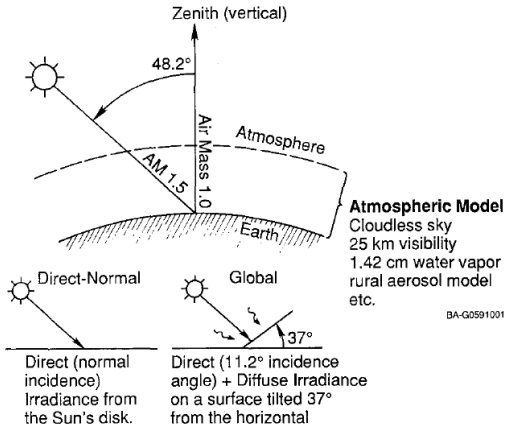

Figure 2-2. Schematic of AM 1.5 reference spectral conditions (Reprinted with permission from Ref. [75], IEEE).

The commonly used AM 1.5 spectra is defined based on a radiative simulation referred to as BRITE developed by Radiation Research Associates [76, 77]. The global AM 1.5 spectrum was simulated for a collector body tilted 37° from the horizon looking directly at the sun with respect to the "U.S. Standard Atmosphere" in a vertical column up to 100 km above sea level [75].

2-2. Blackbody radiation

A blackbody can be defined as an ideal surface that emits the maximum possible amount of radiation. A blackbody is also a perfect absorber of radiant energy. Thus, it can absorb the energy from all incident light regardless of its direction and wavelength. Finally, a blackbody acts as a diffuse emitter. That is, the radiant energy emitted from a blackbody only depends on its temperature and wavelength and is independent of direction [78].

The name blackbody comes from the fact that ideal absorbers of visible light seem black to the eye. However, except for the visible spectral region, the eye is not a good tool to evaluate the absorbing capability of an absorber. For instance, a surface coated with white oil-base paint can be a perfect absorber of infrared radiation, while for shorter wavelengths in the visible spectral region it reflects most of the light incident onto its surface.

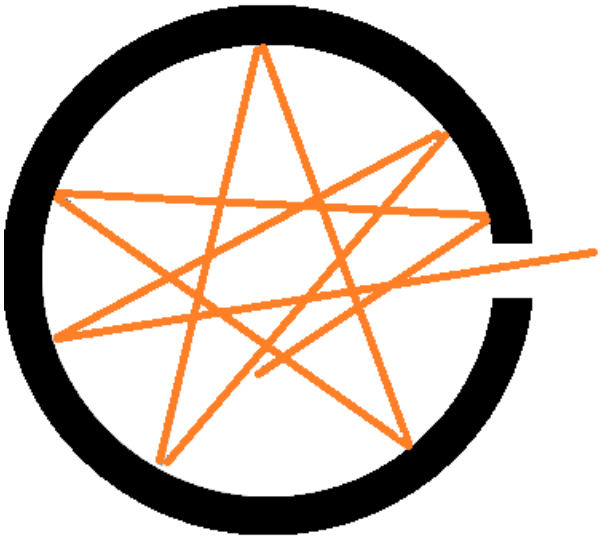

Figure 2-3. Schematic model of a blackbody

Figure 2-3 shows a schematic model of a blackbody surface as a tiny hole in a cavity with walls which are opaque to radiation. Once incident radiation reaches the hole it will enter the cavity, and if the cavity is big it is unlikely to be re-emitted.

Only a handful of materials can act as a blackbody to absorb radiant energy. Among those one can refer to carbon black, carborundum, platinum black, and gold black. The radiative properties of the blackbody have been recognized using quantum mechanics and experiments [79].

Using Planck's law, one can illustrate the spectral density of radiation emitted by a blackbody in thermal equilibrium at a selected temperature. The law was proposed by Max Planck in 1900 and is an innovative result of modern physics and quantum theory.

The spectral radiation, B_v, represents the quantity of energy emitted by a blackbody at different radiation frequencies. Based on Planck's investigations, the spectral radiance of a blackbody can be defined per unit frequency as follows

$$B_v(v,T) = \frac{2hv^3}{c^2}\frac{1}{e^{\frac{hv}{k_BT}}-1} \quad \text{2-1}$$

Where h stands for the Planck constant, v is the frequency, c is the light speed, k_B is the Boltzmann constant, and T is the absolute temperature. It can also be defined per unit wavelength, λ as follows

$$B_\lambda(\lambda,T) = \frac{2hc^2}{\lambda}\frac{1}{e^{\frac{hc}{\lambda k_BT}}-1} \quad \text{2-2}$$

Plank's law can also be represented based on the quantity of photons emitted at a selected wavelength, or the energy density in a volume of radiation.

2-3. Solar radiation spectrum

The solar spectrum is well-approximated by the spectral radiance emitted from a black body with a temperature of ~ 5,700 K [80]. Figure 2-4 shows the solar spectral irradiance for direct light where the maximum irradiance with 2.142 $W/m^2 \cdot nm$ intensity occurs at around 450 nm. As sunrays pass through the atmosphere their energy decreases because of scattering and absorption. Gases with specific absorption bands absorb some portions of light. Sunrays are also redirected by Rayleigh scattering, which is the main reason for the blue color of the sky. In a sense, the observer receives more blue light from the sky because higher-frequency light is scattered into an indirect path to a greater extent. Conversely, when looking directly at the sun, the observer sees less blue light and relatively more light with longer wavelengths and the sun appears yellow. The curve shown in Figure 2-4 is based on the American Society for Testing and Materials Terrestrial Reference Spectra (ASTM). These spectra are standards accepted by industries to guarantee reliable test environments [74].

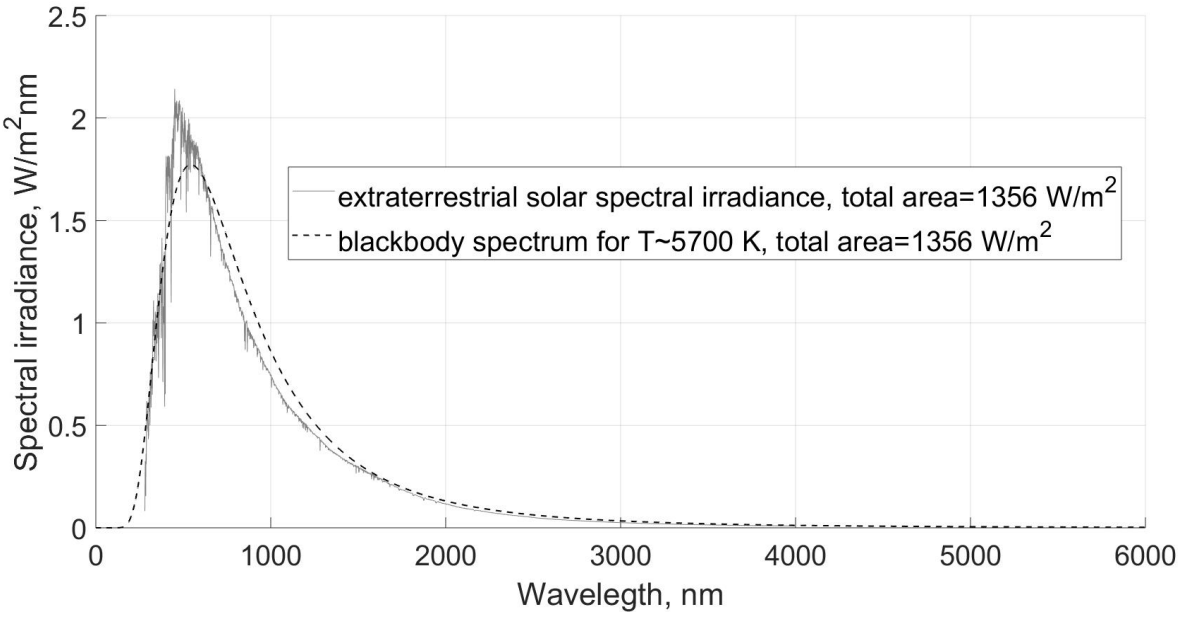

Figure 2-4. Solar irradiance spectrum and the spectral distribution of radiation emitted from that of a blackbody with temperature of ~ 5700 K

2-4. Emissivity

Emissivity is a property of the surface of a material which describes the level of infrared energy radiation it emits [81]. The emissivity of an object is the ratio between the amount of radiation it emits to the amount of radiation emitted by a blackbody at the same temperature. This ratio varies between 0 and 1 depending on the properties of the selected material. For example, the surface of an ideal blackbody at room temperature emits thermal radiation at an intensity of approximately 448 W/m^2 at room temperature (298 K). All real objects in the world can be categorized by their emissivity ratios which range between 0 and 1. It should be noted that the emissivity of real objects are all lower than a perfect blackbody which, by definition, has an emissivity equal to 1. An object with an emissivity of 0 is unable to emit infrared energy [82]. Also, another important thing about emissivity is that it is spectrally dependent and generally a function of surface temperature and direction. However, there is still limited data available for the spectral emissivity of most materials and most often the emissivity is reported solely for the normal direction. Accordingly, usually average values are being considered for emissivity over direction, wavelength, or both. The temperature and emissivity of an object are properties which can define how much infrared energy can be emitted by an object. An example of the spectral radiant emittance of an ideal blackbody and the common mineral quartz at 600 K is shown in Figure 2-5 . As can be seen, quartz as a real object in the world emits less thermal radiation than a perfect blackbody as expected [81].

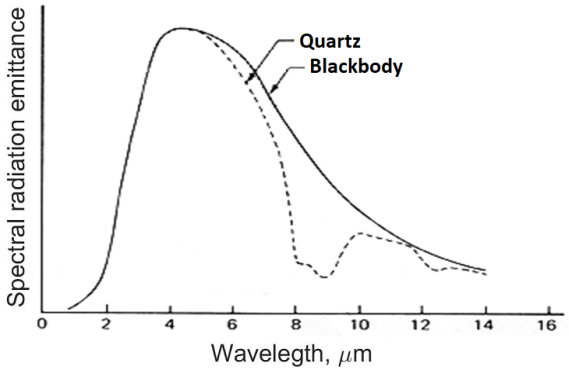

Figure 2-5. Comparing the spectral radiant emittance of an ideal blackbody and quartz (Reprinted with permission from Ref. [81]).

2-5. Low emissivity coatings

An efficient method to save energy is to apply low-Emissivity (low-E) coatings on top of surfaces, such as windows. Low-E materials can significantly reduce energy usage by reducing radiative heat losses [83-85].

In general, transparent low-E coatings can be divided into two categories: hard coatings based on metal oxides and soft coatings based on thin-film metallic materials. Metal-oxide based low-E coatings, which typically comprise transparent conductive oxides (TCOs) such as tin oxide (SnO), indium oxide (In_2O_3) or zinc oxide (ZnO), generally exhibit lower infrared reflectance and higher solar transmittance in comparison to thin-film metallic low-E coatings, which are mainly comprised of metals such as silver (Ag), copper (Cu) and gold (Au) [86-89]. Depending on the optical properties of coatings and their environmental stability, mechanical specifications and combined effects, they can be used for different applications [90].

In order to increase the performance of solar thermal collectors, the proper combination of properties with regard to solar gains, thermal losses and resistance to temperature, humidity, mechanical stress as well as their combined effects should be considered. For example, soft coatings like silver are not a good choice for humid and wet areas because of their high sensitivity to corrosion [84]. As a result, several works have been cited to demonstrate TCOs application for solar thermal collectors [90-95]. For example, Ehrmann et al. [96] reported a solar transmittance of about 85% for a double glazing with selective layers of ZnO and Al_2O_3 to be used in solar-thermal flat-plate collectors. Furthermore, nanoparticles can be used for filtering and optical purposes [97,98]. For example, Dejanette et al. [98] provided a spectrally selective filter to maximize absorption and transmission in desired wavelength ranges by means of a nanoparticle

fluid (transmitting more than 82 % insolation above a desired bandgap and absorbing 86% of insolation below the bandgap).

2-6. Transparent conductive oxides

First investigation of transparent conductive oxides (TCOs), which are a specific class of transparent conductive electrodes (TCEs), was reported by Bädeker in 1907 with CdO, Cu_2O and PbO. Although TCOs have been identified for more than a century, industrial outcomes only appeared almost 5 decades later after Bädeker's investigations in the 1950s. Furthermore, the most notable innovation introduced in the 1970s was the application of low-E TCO/metal/TCO multilayers in architectural and window glasses as well as ITO coatings in flat-panel displays with liquid crystals. By 2005, TCO layers became very convenient in solar cell applications, particularly with photovoltaics for electrical power generation. Among all kinds of TCOs nowadays, ITOs are still the most dominant material for flat-panel displays. This is while, ZnO and SnO_2 are used in the production of solar cells with thin films. The main reason for using these materials instead of ITO for solar cells is the high price of ITO compared to those materials [99-103].

2-6-1. Sandwich dielectrics

Recently sandwich dielectrics have also been widely studied to improve the spectrally selective coating of the receiver for a more efficient solar collector. Taylor et al. [104] reported that indium tin oxide (ITO) and ZnS-Ag-ZnS provided the highest efficiency factor for selectivity (a nondimensional metric term for materials and configuration to serve as a transparent selective solar coating) among other existing materials. Bellas and Lidorikis [105] studied the performance of nano-composite metal-dielectric absorbers with selective coatings in parabolic trough collectors.

They simulated various coatings with selective filters for a temperature range from 400-1000 ℃ with maximum efficiency at approximately 850 ℃ (~30% better performance).

A significant weakness of low-E coatings is the lower transmittance in the visible wavelength range compared to that of a bare glass pane. Although this area is still open for research, one method to overcome this drawback is to add an antireflective coating (ARCs) to increase transparency in the visible region [86, 87, 106]. ARCs will be illustrated more in depth in Section 2-8.

2-6-2. Nanoparticle films

Nanoparticles refer to particles with dimensions up to 100 nm. These particles may exhibit extraordinary features that are different from those of the larger scale substance. Due to their flexibility in various aspects, they have been used in various industries with different applications including catalysts, electronics, drug carriers, magnetic and optical materials, pigments, and sensors. It is imperative to investigate novel procedures for the synthesis of nanoparticles to control properties such as composition, crystallinity, morphology and size distribution. So far, various methods have been introduced by scientists for nanoparticle synthesis such as gas-phase-, liquid phase- and solid-phase-processes [97].

Preparation of nanoparticles can be done using aerosol spray methods including spray pyrolysis, spray drying, and the flame spray methods. Aerosol spray methods are simple and rapid for processing. They can be use to prepare phosphor nanoparticles, transparent conductive nanoparticles, composite particles, and porous particles. Nanoparticle fabrication using organized pores with spray drying is of interest. Generally, porous particles can be prepared with oxide materials, if colloidal oxide nanoparticles are existing. When the particles and pores are small enough, they do not scatter light and can be used as thin optical films. In this case, the precursor

is a combination of two colloids: 1. silica nanoparticles with different sizes and 2. polymer (polystyrene latex (PSL)). The size of the resulting nanoparticles is on the order of ~ 10 to 100 nm [107].

In order to reduce the index of refraction of a material, porosity can be introduced because the index of refraction is related to the density [108-109]. However, the pore size needs to be significantly smaller than the light wavelength. Also, in order to avoid scattering, the pore distribution has to be homogenous. The relation between the density and index of refraction can be defined as follows

$$\frac{n_p^2-1}{n^2-1} = \frac{x_p}{x} \qquad 2\text{-}3$$

where n is the refractive index of non-porous material, x is the density of non-porous material, n_p is the index of the porous material and x_p is the density of porous material.

Equation 2-3 can also be written in terms of porosity as follows

$$\frac{n_p^2-1}{n^2-1} = 1 - \frac{p}{100} \qquad 2\text{-}4$$

where P is percent porosity. As an example, Figure 2-6 shows the refractive index variation with porosity for TiO_2, A1203, and SiO_2 [108].

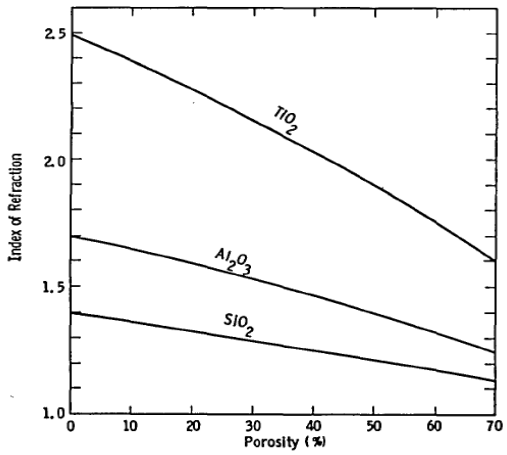

Figure 2-6. Porosity effect on refractive indices of different oxides (Reprinted with permission from Ref. [108], The Optical Society)

2-7. Solar selective surfaces

In the context of a building, by applying low-E coatings on glass windows a large portion of the radiant heat that would otherwise be exchanged between the structure and surrounding environment can be prevented. As a result, to keep the building at a desired temperature (e.g. warm enough in the winter and cool in the summer) less power is required. Low-E coatings can also be used for solar thermal applications [110-115]. A solar selective surface is similar, but the solar light that is transmitted is absorbed for the case of the solar selective surface. Consequently, by applying low-Emissivity coatings to the surface of a solar concentrator it will result in a considerable reduction in thermal losses [83,116]. For example, more electric power can be produced by Dish-Stirling systems using these types of solar concentrators.

In order to improve the conversion of solar energy into useful heat, with respect to Figure 2-7.a, an object should be able to provide two properties. Both of these properties can be presented based on the reflectance phenomenon. The first is that it should have low reflectance (i.e. high absorptance) in visible and near IR wavelength and high reflectance (i.e. low emittance) in the IR and far IR wavelength ranges for thermal radiation [117]. The ideal case can be stated quantitatively with the following expressions:

$$R(\lambda) = 0 \text{ for } 300 < \lambda < 4000 \text{ nm} \quad (2\text{-}5)$$

and

$$R(\lambda) = 1 \text{ for } 4000 < \lambda < 50\,000 \text{ nm} \quad (2\text{-}6)$$

a.

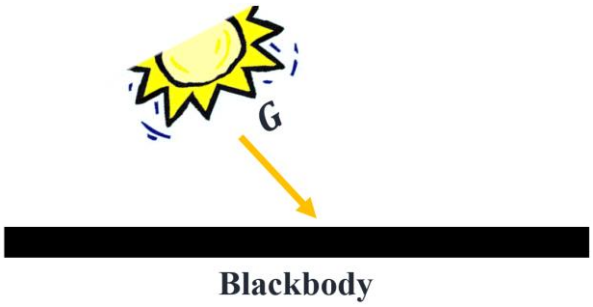

b.

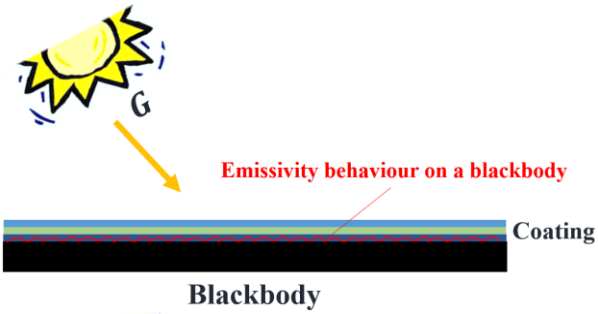

c.

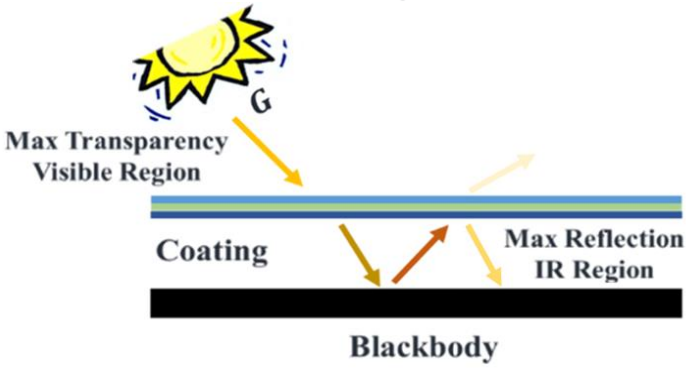

Figure 2-7. a. Schematic diagram of a black surface with high solar absorbance b. Solar selective coating behaviour on the surface of a blackbody c. Solar selective coating behaviour far from the blackbody surface (G represents the solar radiant power)

How can the temperature of a blackbody under solar radiant energy be maximized? As shown in Figure 2-7.b, a transparent low-E coating deposited onto a black body functions as a solar selective surface that absorbs solar radiation (with wavelengths between 0.3 to 4 μm) while preventing infrared radiant energy from exiting the blackbody (with wavelengths on the order of ~10 μm depending on the temperature of the blackbody) . Figure 2-7.c shows a transparent heat mirror film with a gap, and yet the combination of the transparent low-E coating on glass and the black body together still function as a solar selective surface with capability to maximize transparency in

visible wavelengths to allow solar radiation pass through the coating and provide highest reflection in infrared wavelengths to reflect IR thermal radiation [118].

Figure 2-8 shows the solar spectrum and four different blackbodies with temperatures of 500, 1000, 1500 and 2000 K. It can be seen that these spectra are bell-shaped and have different maximum intensities for different temperatures, which decrease towards smaller wavelengths as the temperature increases. Thus, the temperature of a blackbody like the one shown in Figure 2-8 under solar radiation can be maximized by coating it with a selective surface that maximizes the transmittance of solar radiation while reflecting thermal radiation. The ability to maximize the temperature of a blackbody subjected to incident solar radiation using transparent low emissivity films is described quantitatively in the next section.

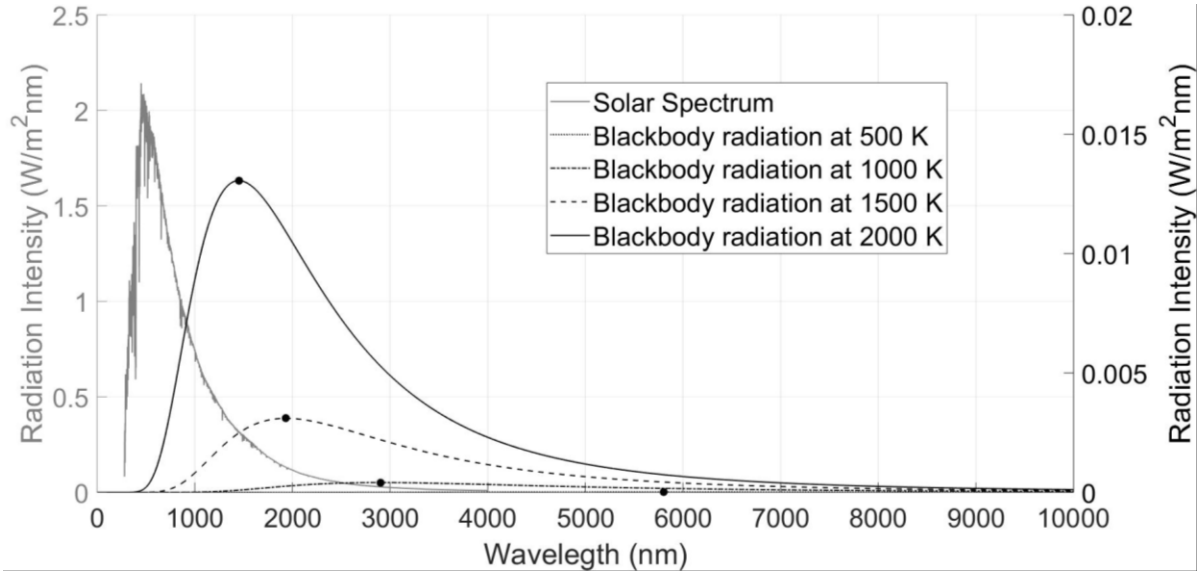

Figure 2-8. Solar irradiance (left scale) and radiant blackbody spectra (right scale) for blackbodies at different temperatures (500, 1000, 1500 and 2000 K)

2-7-1. Maximizing the temperature of a blackbody subjected to incident solar radiation

Considering a transparent cover with a low-E coating over top of a black body (e.g. the diagram shown in Figure 2-7.c), the power radiated from the blackbody surface can be determined by the Stefan-Boltzmann law for absolute temperature T and body surface area of A with emissivity ε as follows: [119-120]

$$P_{rad} = \varepsilon\sigma T^4 A \tag{2-7}$$

Furthermore, the net power radiated between an emitting object with temperature T and surroundings with temperature T_0 is the difference between the power emitted and the power absorbed:

$$P_{net} = P_{emit} - P_{absorb} = \varepsilon\sigma(T^4 - T_0^4)A \tag{2-8}$$

where Stefan-Boltzmann's constant is:

$$\sigma = \frac{2\pi^5 k_B^4}{15h^3c^2} = \frac{\pi^2 k^4}{60\hbar^3 c^2} \approx 5.67 \times 10^{-8} \ \ W/(m^2K^4) \tag{2-9}$$

where $k_B \approx 1.38 \times 10^{-23}$ is Boltzmann's constant, $h \approx 6.63 \times 10^{-34}$ Js is Plank's constant, $\hbar = \frac{h}{2\pi} \approx 1.05 \times 10^{-34}$ Js is the reduced Plank's constant and $c \approx 3.00 \times 10^8$ m/s is the velocity of light.

Moreover, the absorbed solar power [121] can be denoted as follows:

$$P = G.t.a.A \tag{2-10}$$

where G is the solar radiant power, a is absorbance of the surface, t is the transmittance for solar irradiation.

For the case of a blackbody coated with a solar selective surface subjected to incident solar radiation, in equilibrium, the entering (Equation 4) and exiting (Equation 2) power should be equal (e.g. $P_{in} = P_{out}$), and this condition can be used to derive Equation 5:

$$\varepsilon\sigma T^4 = G.t.a$$

$$T^4 = \frac{G.t.a}{\varepsilon\sigma} = \frac{t}{\varepsilon}\frac{G}{\sigma}a$$

$$T = Const.\left(\frac{t}{\varepsilon}\right)^{1/4} \quad (2\text{-}11)$$

Thus, to maximize the temperature of a blackbody, the transmittance for solar irradiation and the emissivity of a spectral selective coating should be maximized and minimized, respectively. In order to satisfy the conservation condition for the total energy in the solar radiation beam, the relationship between transmittance (t), absorbance (a) and reflectance (r) can be defined as follows [96]:

$$t(\lambda) + a(\lambda) + r(\lambda) = 1 \ \ (100\%) \quad (2\text{-}12)$$

Where all these parameters are functions of wavelength, incident angle and the material's optical properties such as index of refraction and extinction coefficient.

Kirchhoff's law of thermal radiation states that for a given wavelength the emissivity and absorptivity of an object are equal:

$$\varepsilon(\lambda) = a(\lambda) \quad (2\text{-}13)$$

Where ε stands for the emittance.

Considering an opaque material ($T(\lambda) = 0$) for the case of a transparent cover with a low-E coating over top of the black body the emittance can be represented as follows [83, 122-123]:

$$\varepsilon(\lambda) = 1 - r(\lambda) \quad (2\text{-}14)$$

This leads to an important conclusion that in the design of a transparent heat mirror a low-E coating can be achieved by maximizing the reflectance over the infra-red region. More theoretical background and details are given by Jelle [83, 124].

2-7-2. Solar selective surfaces

A spectrally selective, or solar selective, surface can be realized using different materials structured in different forms. Among these, six different kinds of solar selective surfaces reported by Kanu and Binions [117] are shown through Figure 2-9 to Figure 2-14.

Figure 2-9 shows a material which is comprised of solar selective materials with intrinsic optical properties. It is also called a "mass absorber" in which selective absorption and emissivity are intrinsic characteristics of the materials and examples include MoO_3-doped Mo, Silicon doped with Boron (Si doped with B), Calcium fluoride (CaF_2), Hafnium Carbide (HfC), Zirconium Diboride (ZrB_2, SnO_2), Indium(III) Oxide (In_2O_3), Europium(III) Oxide (Eu_2O_3), Rhenium Trioxide (ReO_3), Vanadium(V) oxide (V_2O_5) and Lanthanum hexaboride (LaB_6) [125, 126]. However, there are limited materials which ideally exhibit this property and further work needs to be done in order to develop these materials further.

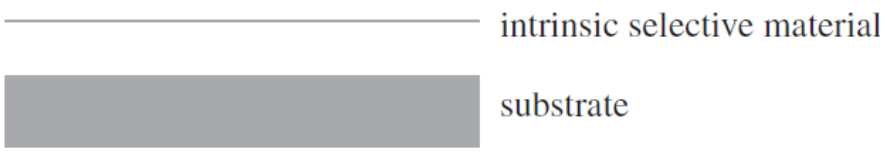

Figure 2-9. Solar selective materials with intrinsic optical properties (Reprinted with permission from Ref. [117], The Royal Society).

Figure 2-10 illustrates a semi-conductor-metal tandem design with spectrally selective properties. Semiconductors with band gaps of approximately 0.5 eV to 1.26 eV absorb incident solar radiation while exhibiting low emissivity in the IR spectral range on account of their band-gap. As mentioned, the drawback of this surface is that working with semiconductors leads to larger refractive index materials, which means higher reflection losses and demands for an additional anti-reflection layer [117]. As an example, one can refer to Si (1.1 eV) and Ge (0.7 eV) [126].

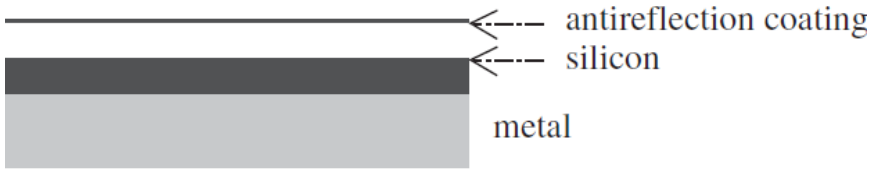

Figure 2-10. A semi-conductor metal design with spectral selectivity property (Reprinted with permission from Ref. [117], The Royal Society).

Figure 2-11 shows a multi-layer coating design comprised of alternate layers of dielectric/metal/dielectric (D/M/D). D/M/D absorbers or multilayer interface stacks can be designed so that they become efficient selective absorbers. The selectivity is achieved by tuning the thickness of the bottom dielectric layer such that interference effects occur for selective wavelengths, and is not dependent on the selectivity of the dielectric material within the structure. Various multilayer absorbers comprised of different metals (e.g., Mo, Ag, Cu, Ni) and dielectric layers (e.g., Al_2O_3, SiO_2, CeO_2, ZnS) have been used for high-temperature applications [126]. This type of solar selective surface, with Mo and Al_2O_3 as the metal and dielectric layers, respectively, has been produced at large-scales via vacuum coating technology [117].

Figure 2-11. Multi-layer coatings design consisting of dielectric/metal/dielectric layers (Reprinted with permission from Ref. [117], The Royal Society).

A metal/dielectric-composite-metal tandem, or absorber-reflector tandem design, is shown in Figure 2-12, wherein a dielectric medium hosts metallic nanoparticles. In order to optimize the spectral selectivity, one can choose different materials, layer thicknesses, concentration of particles, shape and orientation of the particles and grading. Another version of this type is a powder semiconductor-reflector design in which the solar selective characteristics of inorganic metal oxides, organic black pigments, metal-dust-pigmented selective paints and semiconductors are of interest.

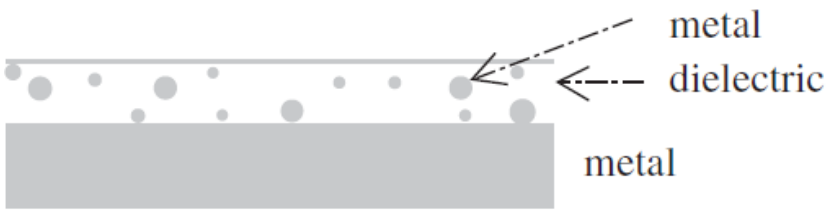

Figure 2-12. A metal/dielectric-composite-metal tandem design (Reprinted with permission from Ref. [117], The Royal Society).

Figure 2-13 shows the high solar absorptance in textured metal surfaces which can be produced by frequent internal reflections against metal dendrites with 2μm separation. As here the corresponding wavelengths are much larger than the dendrite deviation, the low-E term is unaltered by this design [117]. An ideal textured surface provides low emissivity at long wavelengths while at the same time gives high absorptivity at shorter wavelengths. Surface texturing can be created by several methods including: 1. ion-exchange reactions between metals, 2. oxidation of metals at high temperature, 3. unidirectional solidification of eutectic alloys, 4. vapor deposition, 5. vapor–liquid–solid mechanism, and 6. x-ray, e-beam, or nanoimprint lithography. [125].

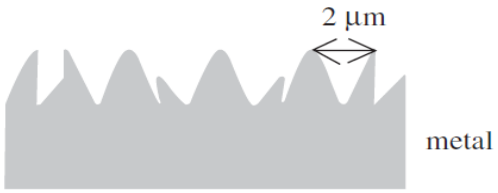

Figure 2-13. Solar absorptance in textured metal surfaces (Reprinted with permission from Ref. [117], The Royal Society).

Finally, Figure 2-14 illustrates a spectrally selective solar-transmitting coating on an absorbing surface with properties very close to a black-body [127]. In this case, the coating may be a highly doped semiconductor such as SnO_2:F, SnO_2:Sb, In_2SO_3:Sn, and ZnO:Al, and black enamel can be used as the absorber material [126].

Figure 2-14. A spectrally selective solar-transmitting coating on a blackbody-like absorber (Reprinted with permission from Ref. [117], The Royal Society).

Among all the existing materials, Nickel pigmented anodic alumina [128] is the most well-known coating in the market and is provided by AC anodization of an aluminium sheet in dilute phosphoric acid followed by AC electrolysis in a $NiSO_4$ bath [127].

2-8. Photonic crystals

The thermal radiation spectra of emitter surfaces depend on their photon density of states. The photon density of states can be controlled by structuring the emitter in the form of a photonic crystal (PhC) such that it behaves as a selective solar absorber. PhCs are comprised of a pattern of materials arranged in a periodic form with different dielectric constants. PhCs can provide a

complete photonic band gap over particular wavelength ranges wherein all light is reflected, regardless of its incident angle or polarization. Moreover, by using 2D and 3D arrangements, the angle-dependant photonic density of states can be tuned. Accordingly, higher values for emission is achieved, which result in better thermal transfer efficiencies.

Figure 2-15 shows some examples of photonic crystals with one-, two-, and three-dimensional structures. The distinct colors represent materials with distinct dielectric constants. The distinguishing property of a PhC is its periodic dielectric constant in at least one direction [129].

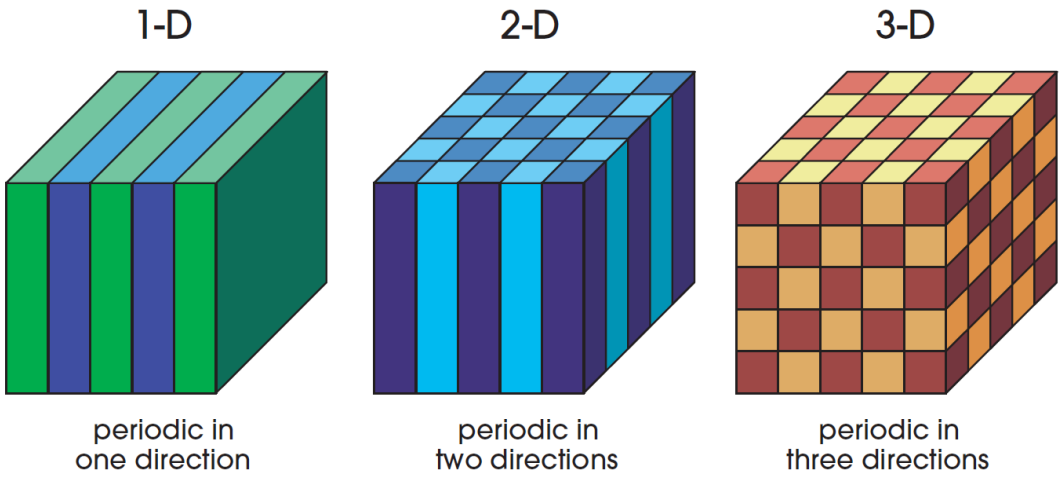

Figure 2-15. Samples for one-, two-, and three-dimensional photonic crystals with regard to their periodicity along one, two and three directions, respectively (Reprinted with permission from Ref. [129], The Princeton University Press).

2-8-1. One-dimensional photonic crystals

Applying a one-dimensional (1-D) periodic structure on the surface of a material strongly changes the effective optical absorption and emission of that material. The main parameters that can be altered in this design are the periodicity and depth which have been studied in the literature [125].

For the case of a 1-D PhC deposited on a surface, wherein the layers within the PhC are parallel to the surface, the surface may exhibit a photonic stop-gap, wherein normally incident light is very

strongly reflected over a spectral region. Any 1-D PhC at the surface will provide distinct reflecting zones where the reflectance is a function of the number of repeat units of the structure and wavelength of the incident light. The high reflectance wavelength regions are known as the photonic band gaps, or stop-gaps for the case of a 1-D PhC [130]. Furthermore, by fabricating the 1-D PhC with transparent materials, the 1-D PhC may still be transmissive to light that is outside the stop-gap. Herein, 1-D PhCs are being used to function as coatings for solar concentrators that transmit solar radiation while reflecting infrared radiation to reduce radiative heat losses. In comparison to 2-D and 3-D PhCs, 1-D PhCs have the broadest and most intense reflection spectra for normally incident light (or near-normal). Moreover, it is generally easier to fabricate 1-D PhCs than 2-D and 3-D PhCs.

2-9. Antireflective coatings

Antireflective coatings (ARCs) provide minimal reflection and are used in the design of numerous optical devices. Recently, researches in biological and optical fields focused on the reflectance minimization and importance of nanotechnology to enhance ARCs design [131-132].

The term reflection in optical literatures is originated from a transition in the medium (glass, water, air, etc.) where light is moving forward. The medium here is defined by refractive index (n) which represents the light speed in the medium with regard to that in vacuum. Consequently, as light shines on an object, eyes will be able to discover an optical disturbance if there is a variation in refractive index (RI). The basic model of reflection and refraction is defined by the Fresnel equation. With respect to the model provided by Augustin-Jean Fresnel, the reflected portion of incident light at the interface is calculated by reflectance, R and the rest which is transmitted is calculated by transmittance, T.

With respect to Figure 2-16.a and Figure 2-16.b, the Fresnel model for the anti-reflection condition considers a thin film (RI = n) on a glass substrate (RI = n_s) and the reflectance for normal incidence is illustrated as follows

$$r = \left[\frac{n_{air}n_s - n^2}{n_{air}n_s + n^2}\right]^2 \quad (2\text{-}14)$$

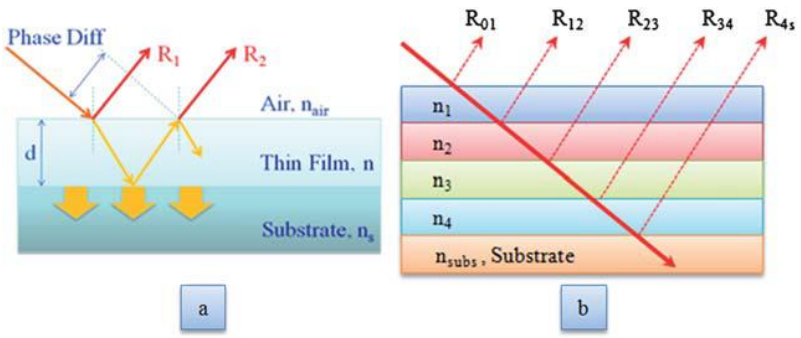

Figure 2-16. Light propagation through (a) a 1-layer film on substrate (n_s > n) (b) multilayer film on substrate absorber (Reprinted with permission from Ref. [132], The Royal Society of Chemistry).

As the goal here is to reach zero reflectance, setting r to zero in Equation 2-14, one can find the refractive index of the film (n) as follows

$$n = \sqrt{n_{air} n_s} \tag{2-15}$$

As the term reflectance (r) in Fresnel model is related to the s-polarization and p-polarization of the light, the antireflective phenomenon is also analyzed on the basis of these two. The analysis provided so far is with respect to a single layer on the substrate. For multi layered ARCs, the main idea remains the same and just the mathematical model changes based on the vector analysis of the individual rays. Overall, by adjusting the RI and thickness of the film, antireflective coatings are attainable.

2-9-1. Strategies to achieving anti-reflection

Antireflective coatings can be realized at a surface using two methods. First, one can use porous/patterned surfaces and the second method involves grading the refractive index at a surface, and both methods will be discussed here. The basic design has been introduced based on existing natural species like moth eyes and it has been enhanced by computational discoveries and techniques to advance innovative procedures.

2-9-1-1. Porous/patterned anti-reflection coatings

Zero reflectance can be achieved at a surface by applying an anti-reflective coating with an index of refraction equal to $\sqrt{n_{air} n_s}$, where n_{air} is the refractive index of the incident medium, which is assumed to be air, and n_s is the substrate refractive index. In order to adjust the refractive index of a film one can make it porous. For example, porous/density graded silicon (PSi) is a well-known material with a decreased index of refraction compared to that of solid Si [133]. Moreover, the

index of refraction of PSi depends on its volume fraction. Consequently, the index of refraction can be decreased by decreasing the fraction, *f*, of Si and increasing the pore volume (1-*f*).

In the natural world, the "moth's eye" functions as a highly effective ARC. In order to avoid detection from predators, the eye of the moth has changed into a dull surface to prevent reflection of light [132]. As shown in Figure 2-17, sub-wavelength structures (SWS) or fine nanostructure patterns captured by scanning electron microscopy (SEM) has feature sizes that are smaller than the wavelength of light. In fact, it is these microscopic nanostructured patterns that interact differently with light compared to macroscopic structures.

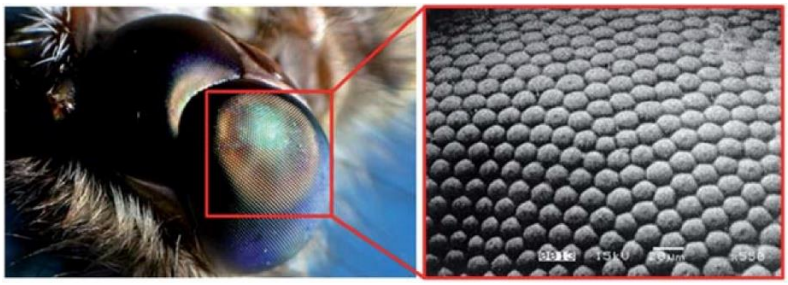

Figure 2-17. The eye of the moth and the scanning electron microscopy image illustrating the Nano bumps on the outer domain of the corneal lens (Reprinted with permission from Ref. [132] , The Royal Society of Chemistry).

In macroscopic structures the incident light would normally be reflected after being partly absorbed as shown in Figure 2-18.a. However, in microscopic structures, especially the SWSs with dimensions less than the wavelength of light by a factor of ~10 [134], it will interact in a completely different way. That is, when the wavelength of incident light is much longer than the size of the surface structures, the effective index of refraction at the surface is graded. Consequently, incident light tends to bend significantly at the surface while reflection is suppressed (Figure 2-18.b). Figure 2-18.c illustrates that in applying similar dimensional restrictions to the spacing and depth of the nanostructured pattern, light rays undergo several internal reflections and are more likely to be

absorbed before being reflected. This phenomenon causes the maximum absorption of the incident light and reflection over the visible wavelength range may be reduced to as low as 0.1%.

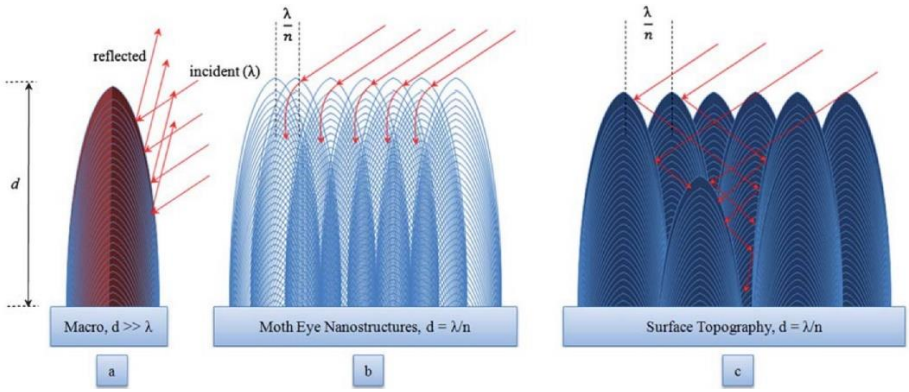

Figure 2-18. (a) reflection of light in a macrostructure pattern, (b) interaction of light with the rough domain because of similar size, (c) internal reflections of light over a nanostructure pattern (Reprinted with permission from Ref. [132] , The Royal Society of Chemistry).

2-9-1-2. Graded-index anti-reflection coatings

Another method to decrease the reflectance from a surface is to apply an ARC whose index of refraction gradually decreases from that of the substrate (n_s) at the substrate surface to that of the air (n_{air}). The reduction of the index of refraction can be defined by different profiles such as those shown in Figure 2-19. This phenomenon can also be seen in nature such as the antelope's eyes which have a broad field vision, human's eyes with aberration reduction, and the eyes of eagles with high spatial resolution.

The concept behind this work was initially provided by Lord Rayleigh [135] in 1880 once he solved the gradual transition problem using numerical solutions to show that as density varies in a variable medium design, reflection decreases and light rays twists (Figure 2-19c). This design is also referred to as graded refractive index (GRIN) and the variation in index of refraction can be done by means of different profiles (such as linear, cubic, and quintic) as will be discussed in Chapter 3 of this thesis.

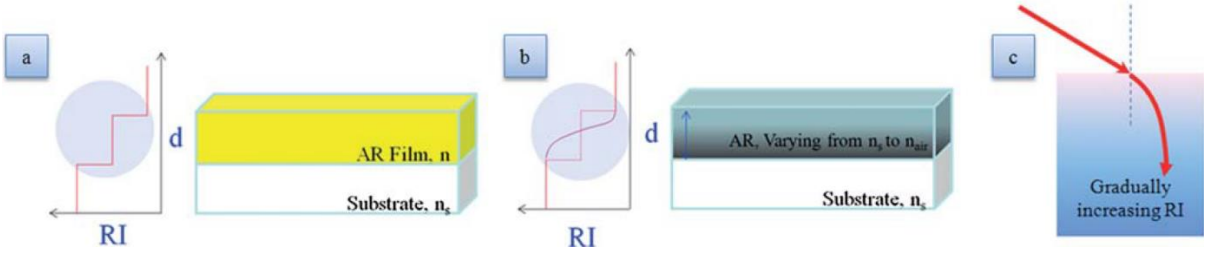

Figure 2-19. (a) Refractive index variation with a step profile in a single layer antireflective design (b) gradual decrement of the index of refraction from n_s to n_{air} (c) bending of sun rays with smooth index variation of medium (Reprinted with permission from Ref. [132], The Royal Society of Chemistry).

2-9-2. Different types of antireflective coatings

Anti-reflection coatings can be classified into two different categories including homogeneous or inhomogeneous coatings. They can be further classified into single-layer, digital, or structured, and homogenous multilayer or complex inhomogeneous coatings as shown in Figure 2-20.a through d. Due to the importance in industries, antireflective coatings for the visible and infrared wavelengths have been studied carefully over the past years.

2-9-2-1. Homogeneous anti-reflective coatings

A single homogeneous antireflective layer with index of refraction n, is optimized according to Equation 11 and reflection is minimized when its thickness is equal to $\lambda/4$ (Figure 2-20.a). However, in case of a substrate surrounded by air, n_{air} is equal to 1 and n principally depends on the refractive index of the substrate. Considering dense ARCs, a suitable material that satisfies Equation 11 can only be guaranteed when $n_s > 2.0$. This is while usually optical glasses have lower refractive indices (e.g. the index of refraction of a dense film is just ~ 1.45 for glass). To decrease the effective refractive index one can use porous or patterned layers (Figure 2-20.b). Besides, several homogeneous thin films in certain arrangements also can lead to zero reflectance at certain

wavelength(s) (Figure 2-20.c), however, it is difficult to minimize reflection over the broad solar spectrum using this technique. [132, 136-138].

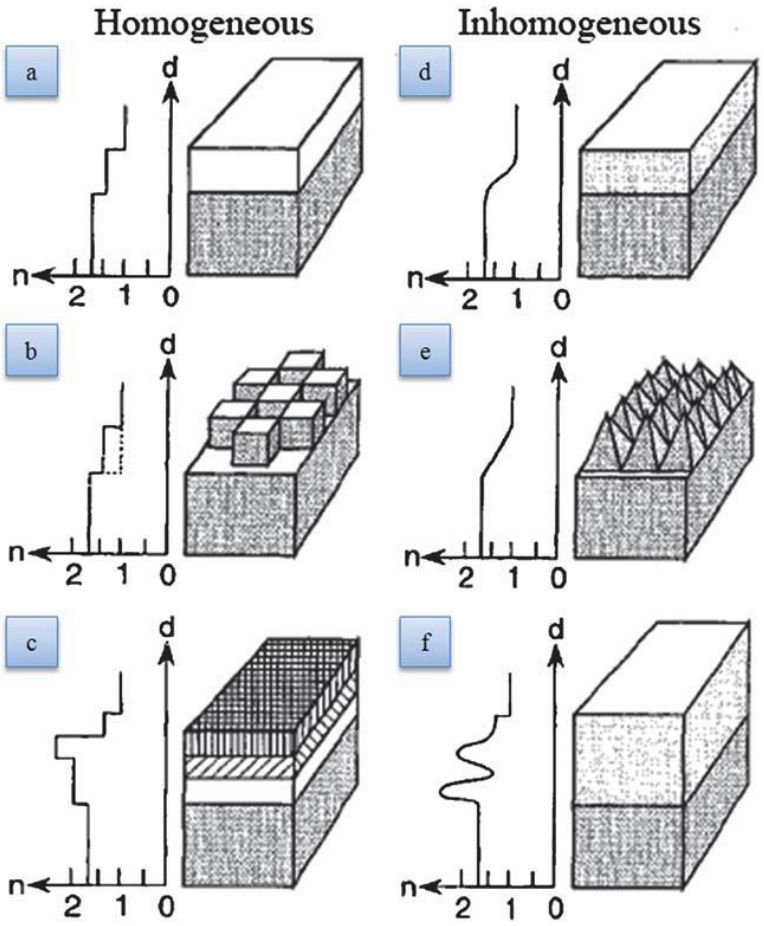

Figure 2-20. Homogeneous ARCs, single layer (a), patterned (b) and multilayer (c) and inhomogeneous ARCs, single layer (d), patterned (e) and multi-layer (f). Notice the variation in refractive index with respect to film thickness (Reprinted with permission from Ref. [132], The Royal Society of Chemistry).

2-9-2-2. Inhomogeneous anti-reflective coatings

Inhomogeneous ARCs use a GRIN structure to achieve anti-reflectivity. As shown in Figure 2-20.d, the reflection from abrupt interfaces is decreased by gradually decreasing the index of refraction with depth from n_{air} to n_s. For this design, the total thickness of the layer is not important, however, results from the literature suggest that the thickness should be more than λ_U or $2\lambda_U$,

where λ_U stands for the upper wavelength, or longest wavelength, of the incident light. The primary reason for AR behaviour of an inhomogeneous layer is that in such a design the influence of an abrupt interface on the reflection of the surface is mitigated. However, it is very difficult to deposit inhomogeneous layers with precise control.

Assuming n_{air} =1, the inhomogeneous ARC can reach almost zero reflectance if the thickness of the layer obeys the aforementioned λ_U border and that the lateral dimensions of the patterns are less than the wavelength of light (Figure 2-20.e). When these situations are guaranteed the effective medium theory can be used and the material–air structure can be represented by the layer set up be similar to SWS structure with indices of refraction vary gradually from n_{air}=1 to n_s (Figure 2-20.f) [132, 136-138].

2-10. Fabrication and characterization

In this section methods for fabrication and characterization of graded-index thin films is reported.

2-10-1. Fabrication

Although graded index profiles exhibit excellent improvement in the design of transparent heat mirrors, it would be very difficult to precisely fabricate the linear, cubic, and quintic graded index profiles throughout the dielectric mirror. The main reason is that it is difficult to control the continuous change of the refractive index profile over the large number of periods in the dielectric mirror [139, 140]. However, results recently reported in the literature show various emerging methods to fabricate graded-index films including lithography and wet etching, integrated nano-island coating arrays on nano-conical-frustum arrays, improved metal-induced chemical etching, oblique-angle deposition, electron beam coevaportion, ion beam assisted deposition, plasma-enhanced chemical vapor deposition and sol-gel process [139-144]. Most of the reports demonstrate oblique-angle decomposition technique as a successful method to fabricate graded-index films [144-147].

Oblique-angle deposition is categorized as a vapour deposition technique usually used to fabricate thin films with a nanostructure, predesigned tilt angle and controllable porosity. The precise control of the porosity can allow one to control the refractive indices ranging from n_L=1.09 to n_H=2.6. Accordingly, almost all graded index profiles can be realized by this technique [147].

Although fabrication of the graded-index profile is still challenging, a low refractive index of 1.063 was achieved by Zhang Jun-Chao et al. [144] for SiO_2 with a quintic profile grown by the glancing angle deposition technique using electron-beam evaporation. Recently, the lowest refractive index

with n= 1.05 was reported by Xi and Schubert et al. [140] using oblique-angle deposition to control the graded refractive index profile with flat substrates.

As discussed earlier, it is still problematic to fabricate graded-index profiles throughout the dielectric mirror. Consequently, the dielectric mirrors presented in this work are not presently expected to the best option from an economic standpoint when compared to commercially available solar selective films. However, results recently reported in the literature show various emerging methods. Future work will focus on using these fabrication techniques to demonstrate a decent method to simply fabricate graded index profiles and dielectric heat mirrors presented in this work such that they can be economically used in various solar thermal applications.

2-10-2. Characterization

Characterization of deposited layers with a graded-index profile can be done using ellipsometry. Although in the beginning application of ellipsometry in gradient index analysis showed some inhomogeneity in the layers because of the deposition process, several reports demonstrate characterization of the deposited layers with graded-index profiles using ellipsometry [139, 148-149].

Ellipsometry is an optical technique allowing accurate investigation of the optical properties of thin films such as refractive index of the films, film thickness and the dielectric constant. Ellipsometry uses the changes in the light polarization upon reflection or transmission [149].

As an example, Figure 2-21 shows a scanning-electron-micrograph (SEM) image of a graded-index multilayer thin films design. As shown in the Figure 2-21, the refractive indexes of each layer are characterized by ellipsometry, and their thicknesses are 69, 78, 81, 101, 113, 145, and

156 nm, from bottom to top, respectively. Two layers of TiO_2 are fabricated in the bottom with high refractive indexes of n=2.60 and 2.52, respectively. In the middle, three layers using SiO_2 and TiO_2 are co-sputtered. Finally, for the top two layers SiO_2 nanorods are fabricated [147].

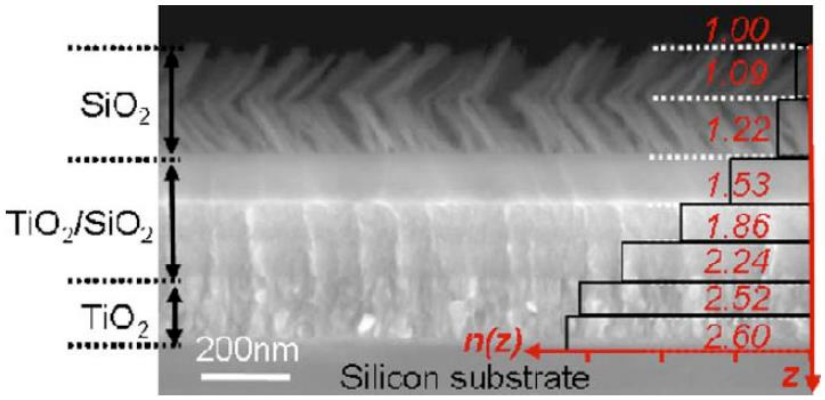

Figure 2-21. SEM image of a sample with a graded refractive index multilayer thin film design (Reprinted with permission from Ref. [147], The Optical Society)

2-11. Motivation and objectives

As discussed earlier in Section 2-5, an efficient method to save energy is to implement low-E coatings on top of the receiver of a CSP system as a solar selective surface and reduce radiative heat losses. In the design of a selective surface, a low-E coating can be achieved by maximizing the reflectance over the infra-red region. This solar selective surface can be designed as a 1-D PhC deposited on a surface to provide high reflectance wavelength regions as the photonic band gaps. However, as discussed earlier and as will be shown in Section 3-2-1, a 1-D design provides lower transmittance in the visible wavelength regions which finally requires higher incoming energy source as well. In order to compensate for this weakness, the 1-D PhC should be designed in such a way to exhibit high transmittance for solar radiation and high reflectance in the near infrared and infrared spectral regions. Using a 1-D design, higher transmittance in the visible wavelengths can be achieved by implementing graded-index anti-reflection coatings where the refractive index profile between its high and low index of refraction regions is defined with a graded-index profile rather than a step function. Considering the new selective surface, one can increase the efficiency of a CSP system without loosing the incoming energy.

With regards to the technology gap addressed by this work, in practice, commercially available selectively absorbing surfaces such as black chrome and $TiNO_x$, are used for making solar receivers. However, for receiver designs that require a transparent cover, such as porous volumetric receivers, the technology is not well developed. Thus, the work presented in this thesis focuses on the advancement of transparent solar selective covers. The approach taken towards advancing transparent solar selective covers is to use dielectric mirrors comprised of materials that are highly transparent in the visible region. In the literature it has been suggested that this approach is not technologically feasible because of the number of layers (on the order of hundreds) that

would have to be deposited in the dielectric mirror to achieve a selective coating of high quality [150]. However, the novelty of the dielectric mirrors designed in this thesis, as discussed in Chapter 3, is that the index of refraction between the high- and low- index of refraction films within the dielectric mirror is graded. This feature greatly increases the selectivity of these dielectric mirrors while drastically reducing the number of layers they are comprised of.

2-12. Thesis outline

The important background topics for designing transparent heat mirrors for solar thermal applications was presented in this chapter. In the following, in Chapter 3, the thesis will be continued with the design of a transparent selective coating in the form of a dielectric mirror (often referred to as one-dimensional photonic crystal or a Bragg-reflector) comprised of alternating layers with different indices of refraction. Then, the alternating layers of films will be designed to selectively reflect light strongly over the infra-red spectral region while being highly transmissive towards solar irradiance. In order to accomplish this, thin graded index layers will be designed as anti-reflection coatings at the interfaces between the alternating layers within the dielectric mirror. Three different index of refraction profiles will be considered including: 1. a linear index variation, 2. a cubic index variation and 3. a quintic index variation [139]. Chapter 4, will provide sensitivity analysis of the transmittance and reflectance spectra of the dielectric heat mirror towards its number of layers, resolution of the refractive index profiles, refractive index, number of stacked dielectric mirrors, absorption, and incident angle of the incoming light. In Chapter 5, the transparent heat mirrors will be used in the design of a solar concentrators operating at different temperatures to evaluate its ability to improve the performance of high-temperature solar thermal energy applications. Finally, conclusions and recommendations for future work will be provided in Chapter 6.

3. Dielectric mirrors and graded index antireflection coatings

In this chapter, dielectric mirrors as well as graded index antireflection coatings will be studied. A dielectric mirror (otherwise referred to as a Bragg-reflector or a one-dimensional photonic crystal) is comprised of several thin layers of dielectric material, usually deposited on a substrate of glass or other optical specimen. They can be used to produce high reflectivity over a certain range of wavelengths. Conversely, in order to decrease the reflectance from a surface one can apply an antireflection coating whose index of refraction gradually decreases from that of the substrate (n_s) at the substrate surface to that of the incident medium, which is typically air (n_{air}).

3-1. Dielectric mirrors

A dielectric mirror is composed of alternating thin film layers with a higher and lower index of refraction, denoted herein as H and L, respectively. For the case of optical coatings, a film is considered to be thin if reflections from its interfaces cause wave interference effects in the visible spectral region. On the other hand, films that do not cause significant wave interference effects for light with wavelengths in the visible spectral region or lower are considered to be thick. Normally, in a multilayer coating design the films are thin and the substrates are thick [151].

The reflected light at each interface within a dielectric mirror depends on the refractive indices of the materials on either side of the interface. Consequently, the intensity of the reflected light waves can be controlled by tuning the refractive indices of the films within the dielectric mirror. On the other hand, the phases of the light reflected at each interface can be controlled by the layer thickness. Accordingly, two key parameters for each layer within the multilayer coating, namely

the thickness and refractive index, are used to control its wavelength dependent reflectance and transmittance.

Using electromagnetic wave theory, and with reference to Figure 3-1, the reflectance, r, and transmittance, t, of light incident onto a surface are provided by Equations 3-1 and 3-2, respectively.

$$r = \rho\rho^* = \left[\frac{\eta_0 - Y}{\eta_0 + Y}\right]\left[\frac{\eta_0 - Y}{\eta_0 + Y}\right]^* \quad (3\text{-}1)$$

$$t = \frac{4\eta_0 \mathrm{Re}(Y)}{(\eta_0 + Y)(\eta_0 + Y)^*} \quad (3\text{-}2)$$

where ρ is the amplitude of the reflection coefficient, η_0 represents the admittance of the incident medium and Y is the admittance of the medium the light is incident on. Also, Re denotes the real part of Y in Equation 2. However, Equations 1 and 2 are valid only for normal incidence. For the case of oblique incidence, one can define p-polarized and s-polarized light, which have electric vectors parallel and perpendicular to the plane of incidence, respectively (Figure 3-2). Accordingly, the new expressions will be defined for the admittance for the case of oblique incidence for s-polarized and p-polarized light as in Equations 3 and 4:

$$\eta_s = Y\cos\theta = (n - ik)\cos\theta \qquad \text{for s-polarized light} \quad (3\text{-}3)$$

$$\eta_p = Y/\cos\theta = (n - ik)/\cos\theta \qquad \text{for p-polarized light} \quad (3\text{-}4)$$

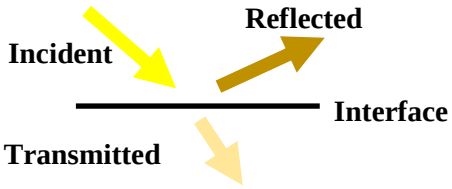

Figure 3-1. Transmitted and reflected light at an interface between two media

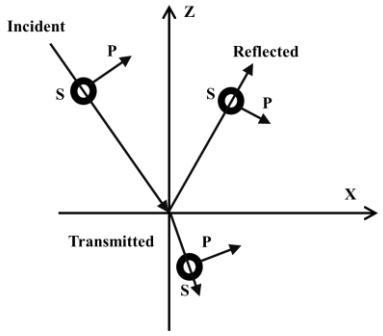

Figure 3-2. P-polarized and s-polarized light obliquely incidence onto a surface.

The surface admittance of the multilayer thin films can be calculated as follows

$$Y = \frac{C}{B}$$

$$\begin{bmatrix} B \\ C \end{bmatrix} = \left\{ \prod_j^q \begin{bmatrix} \cos\delta_j & \frac{i\sin\delta_j}{y_j} \\ iy_j \sin\delta_j & \cos\delta_j \end{bmatrix} \right\} \begin{bmatrix} 1 \\ y_{sub} \end{bmatrix} \quad (3\text{-}5)$$

Where, B and C are normalized tangential electric and magnetic fields, respectively, δ_j is the phase thickness of layer j, y_j is the characteristic admittance of layer j, q is the number of layers and y_{sub} is the characteristic admittance of the substrate [151].

3-1-1. Designing dielectric heat mirrors

One-dimensional dielectric mirrors can be designed to function as coatings for solar concentrators that reflect infrared radiation to reduce radiative heat losses. The term "one-dimensional" here refers to the fact that there is no variation in the dielectric function, ε, along directions other than z, which is the direction that is normal to the surface of the coating [152]. It should be noted that the dielectric function is proportional to the square root of the refractive index ($\varepsilon = \sqrt{n}$) [153, 154].

The quarter-wave stack, which is a type of distributed Bragg reflector or one-dimensional photonic crystal, is comprised of a series of alternating films with quarter-wave thicknesses, and of different H and L refractive index values. The structure provides a strongly reflected spectrum over a region around the wavelength for which the coatings are quarter-waves, usually denoted as the reference wavelength, λ_0 [155]. The reflectance peak is usually described by its full-width at half-maximum (FWHM). Accordingly, the quarter-wave thickness can be expressed as

$$\text{quarter} - \text{wave thickness} = \lambda_0/4n \quad (3\text{-}6)$$

where n denotes the refractive index, H or L, of the high or low index materials within the structure, respectively.

In this thesis, films with an index of refraction of 2 and 1.3 are selected as the H and L layers respectively. The L layer is representative of materials with a low index of refraction such as SiO_2 nanoparticle (NP) films [156-159] and the H layer is representative of materials with a high index of refraction including TCO films such as titanium dioxide (TiO_2), colloidal yttrium oxide (Y_2O_3) and indium-doped tin oxide (ITO) films. In Chapter 4, a sensitivity analysis will be done to study the effects of altering the dielectric mirror parameters, including the H and L values of its constituent layers, on its performance to show the effects of selecting different materials on the properties of the dielectric mirror. A dielectric mirror with a stacking sequence of $[HL]^5$ where H and L represent films with an index of refraction of 2 and 1.3, respectively, and the superscript denotes that there are 5 bilayers in the dielectric mirror, is shown in Figure 3-3. Using the methods described in the following section, the thicknesses of the H and L films were chosen such that the spectral position of the reflectance peak from the dielectric mirror minimizes the radiative heat losses from a receiver (or absorber) being heated by a solar concentrator to a temperature of 500 K. Accordingly, the dielectric mirrors are designed to maximally reflect radiation from a black-body with a temperature of 500 K, and the resulting thicknesses of the H and L layers are 725 nm and 1,154 nm, respectively.

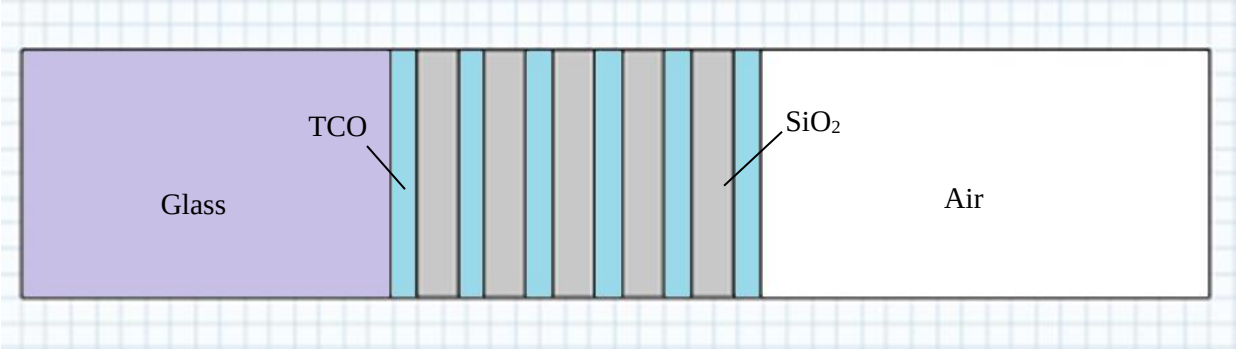

Figure 3-3. A one-dimensional dielectric mirror comprised of alternating layers of a high index film, H, (blue color) and a low index film, L, (gray color). This dielectric mirror is coated onto glass.

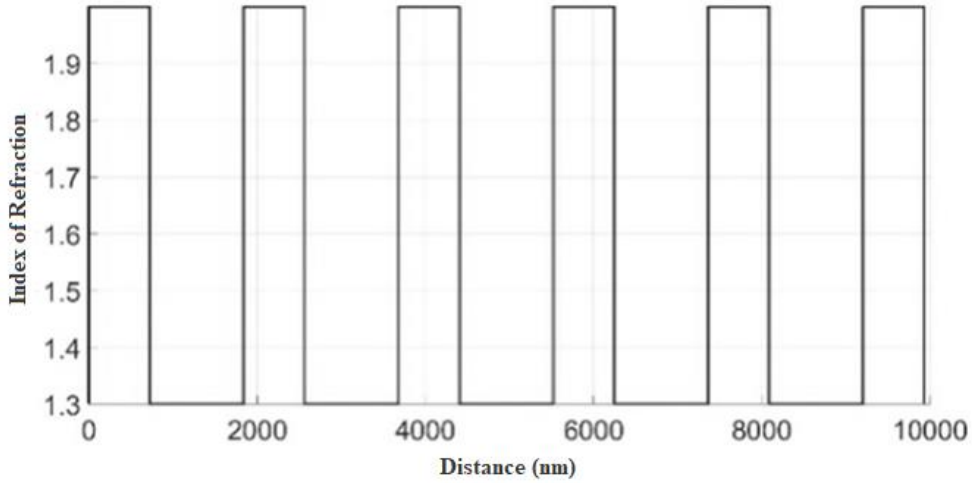

Figure 3-4. Refractive index profile for a quarter-wave dielectric mirror comprised of high index films (725 nm, n=2) and low index films (1,115.4 nm, n=1.3)

With respect to Figure 3-5, a light beam (e.g. with power flux equal to the solar irradiance, *G*, and a spectral distribution similar to that from the sun) is incident onto a dielectric film which is highly transmissive towards solar radiation, allowing sunlight to pass, and highly reflective towards thermal radiation, preventing a large portion of the infrared radiant energy from exiting the absorber which is acting like a blackbody (emitting radiation with wavelengths on the order of ~10 μm depending on the temperature of the blackbody). Accordingly, to illustrate the method of designing a dielectric mirror to function as a solar control film, the blackbody receiver is assumed to be at an equilibrium temperature of 500 K. Figure 3-6 illustrates the radiation spectrum for a

blackbody at an equilibrium temperature of 500 K. As can be seen in Figure 3-6, the highest intensity emitted from such a blackbody occurs at a wavelength of 5,810 nm, and therefor this has been chosen as the reference wavelength for the Bragg-peak position of the dielectric mirror. Accordingly, the thicknesses of the H and L films are set to be that of a quarter-wave stack with a reflectance peak wavelength of 5,810 nm. Considering the dielectric mirror with a stacking sequence of $[HL]^5$ shown in Figure 3-4, the thicknesses of the H and L layers within the mirror would be 725 nm and 1,115.4 nm, respectively.

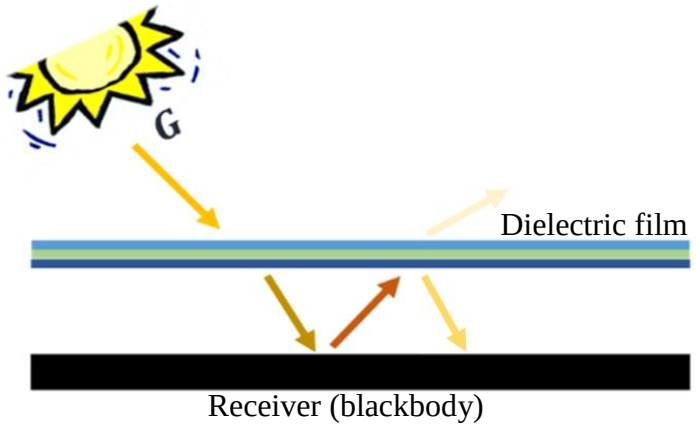

Figure 3-5. Schematic diagram of a dielectric mirror functioning as a solar selective film

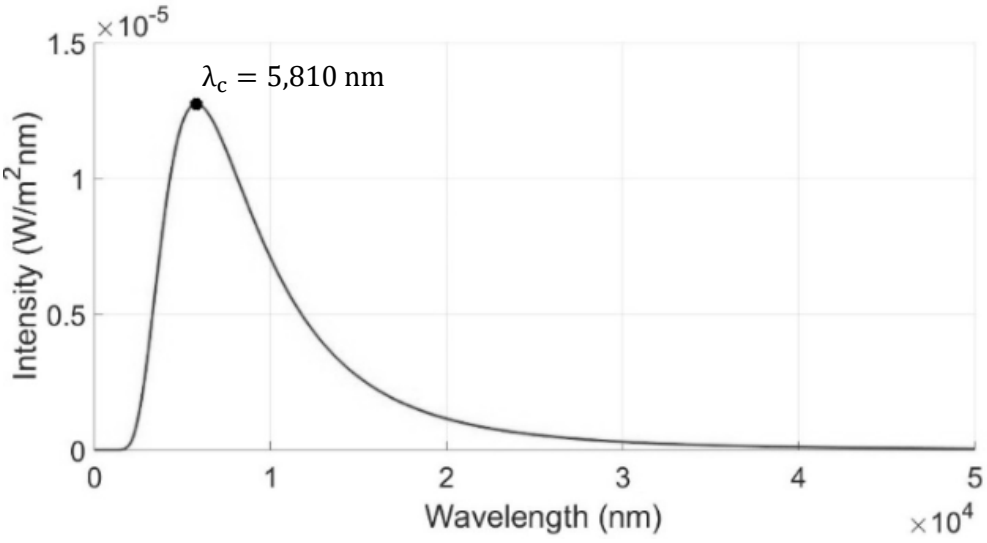

Figure 3-6. Radiation spectrum for a blackbody at a temperature of 500 K

The reflectance spectrum for the $[HL]^5$ stack is shown in Figure 3-7. This reflectance spectrum exhibits a strong reflectance peak with a FWHM of 2,150 nm, starting at 4,920 nm and ending at 7,070 nm, and a maximum reflectance value of ~98% in the spectral vicinity of 5,810 nm. Over the near infrared and infrared spectral regions, the reflectance spectrum shows fluctuations, with the reflectance value remaining below 30%. For the visible wavelength range the reflectance spectra for the $[HL]^5$ stack exhibits drastic fluctuations with reflectance peak values exceeding 90 %. These reflectance peaks in the solar spectral region cause ~ 23% of the solar irradiance to be reflected. Considering Figure 3-7, the amount of solar radiation incident onto the solar receiver would be reduced to almost 77% of its original value, and thus these reflectance peaks reduce the efficiency and performance of the dielectric mirror in functioning as a solar control film. To reduce reflection in the solar spectrum region, one can apply the graded index technique to increase transmittance in the visible wavelength range while keeping the high reflectance values in the infrared spectral regions, which will be discussed in the next section.

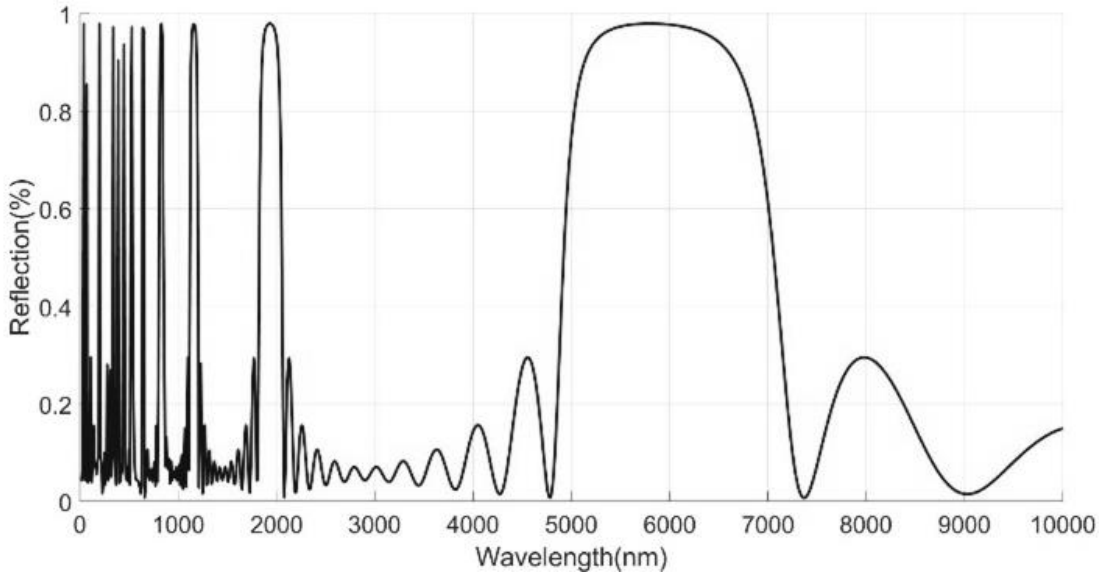

Figure 3-7. Reflectance spectrum for the quarter-wave dielectric mirror with alternating 725 nm thick H and 1,154 nm thick L layers with indices of refraction of 2 and 1.3, respectively (e.g. the dielectric mirror shown in Figure 3-3)

3-1-2. Modelling and validation of the dielectric mirror design

In this thesis, a MATLAB code was developed based on the methods described in Section 3-1-1, that calculates the reflectance and transmittance spectra of dielectric mirrors. Accordingly, Equation 3-5 provides the admittance of each layer in matrix arrays to be formulated for all layers and used as input to calculate the reflectance and transmittance presented in Equations 3-1 through 3-4. In order to calculate the blackbody radiation, Planck's equations for spectral radiance provided in Section 2-2 has been used. Also, in order to have the graded-index coating behaviour, instead of a constant value for the refractive index, the calculated refractive index based on the method which will be discussed in Section 3-2 is used. The developed code is presented in the appendix.

To validate the code, the reflectance and transmittance of dielectric mirrors are calculated and compared to those studied in the literature. For example, the reflectance from a dielectric mirror comprised of nine layers of polystyrene and tellurium is calculated and the results are compared to experimentally measured results in Figure 3-8 [160]. Also, the transmittance of dielectric mirrors comprised of alternating layers of indium-tin oxide (ITO) and SiO_2 nanoparticle films is calculated and the results are compared to experimentally measured results [161]. As shown in Figure 3-9, the reflectance and transmittance spectra calculated using the MATLAB code provides a good approximation to those reported in the literature. Discrepancies between the calculated and experimentally measured spectra shown in Figure 3-8 and 3-9 are attributed to differences between the thickness or index of refraction values used in the experiment as compared to the values assigned to parameters in the analytical method. Furthermore, the reflectance and transmittance spectra calculated using the MATLAB code are compared with the results from COMSOL Multiphysics software (version 5.3), which offers two separate modules that can be used for thin-film calculations (Ray Optics and Wave Optics). The results from the MATLAB code are

compared with those from COMSOL in Figure 3-9 and Figure 3-10. The results from both ray optics and wave optics modules agree well with those of the MATLAB code.

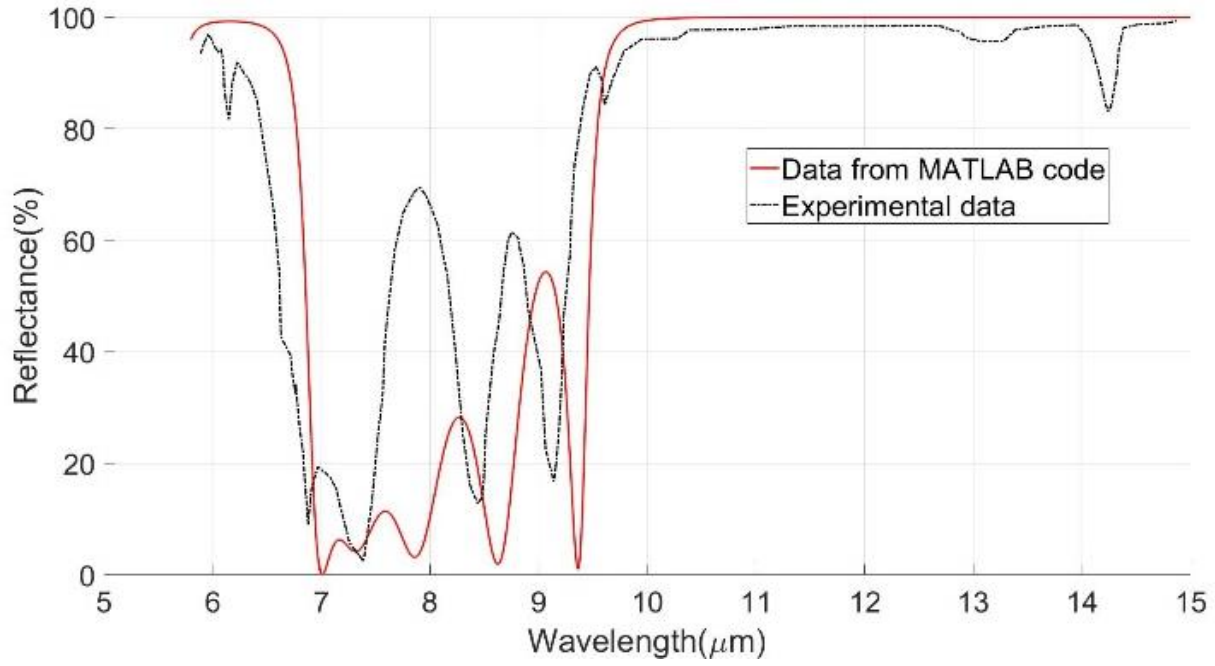

Figure 3-8- Experimentally measured and calculated (MATLAB code) reflectance spectra of a dielectric mirror comprised of nine layers of polystyrene and tellurium [160]

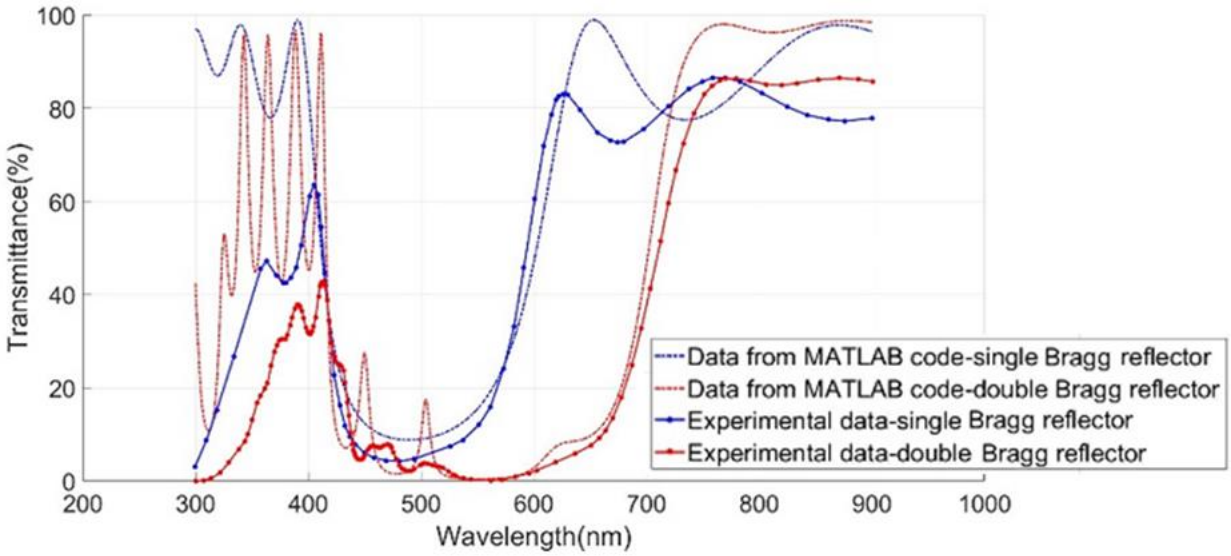

Figure 3-9. Experimentally measured and calculated (MATLAB code) transmittance spectra of dielectric mirrors comprised of alternating layers of ITO and SiO_2 nanoparticle films [161]

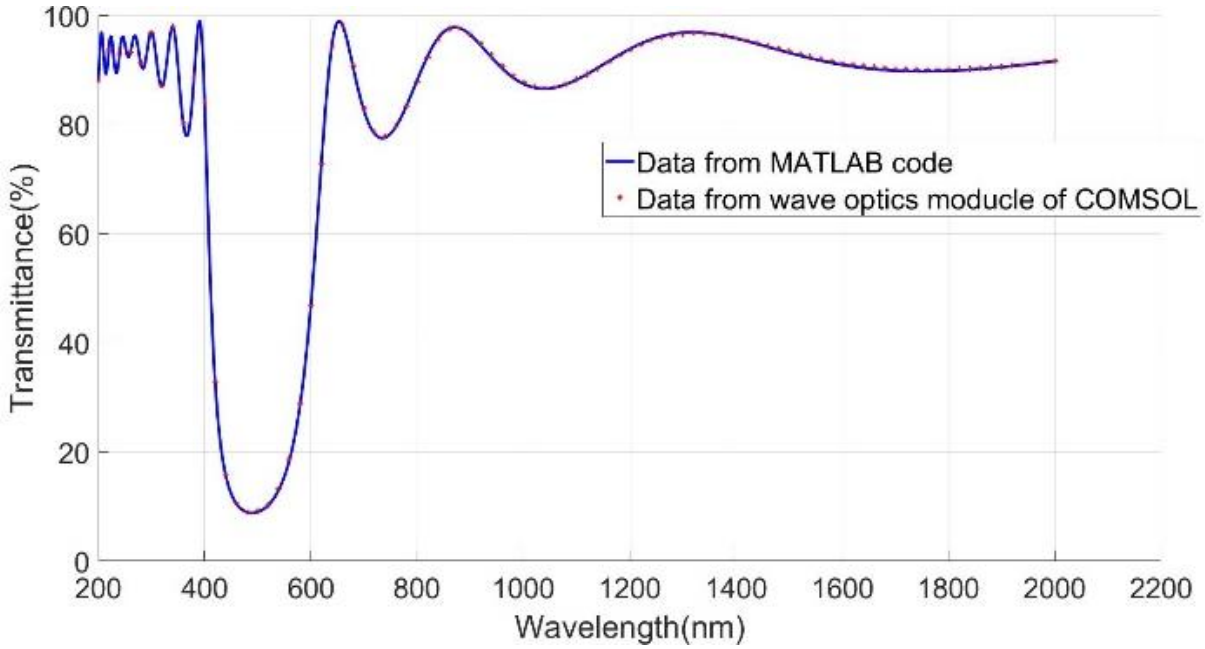

Figure 3-10. Transmittance of a dielectric mirror comprised of alternating layers of TCO and SiO_2 nanoparticle films calculated using our MATLAB code and COMSOL Multiphysics software (five layers of TCO and SiO_2 with thicknesses of 60 and 90 nm, respectively).

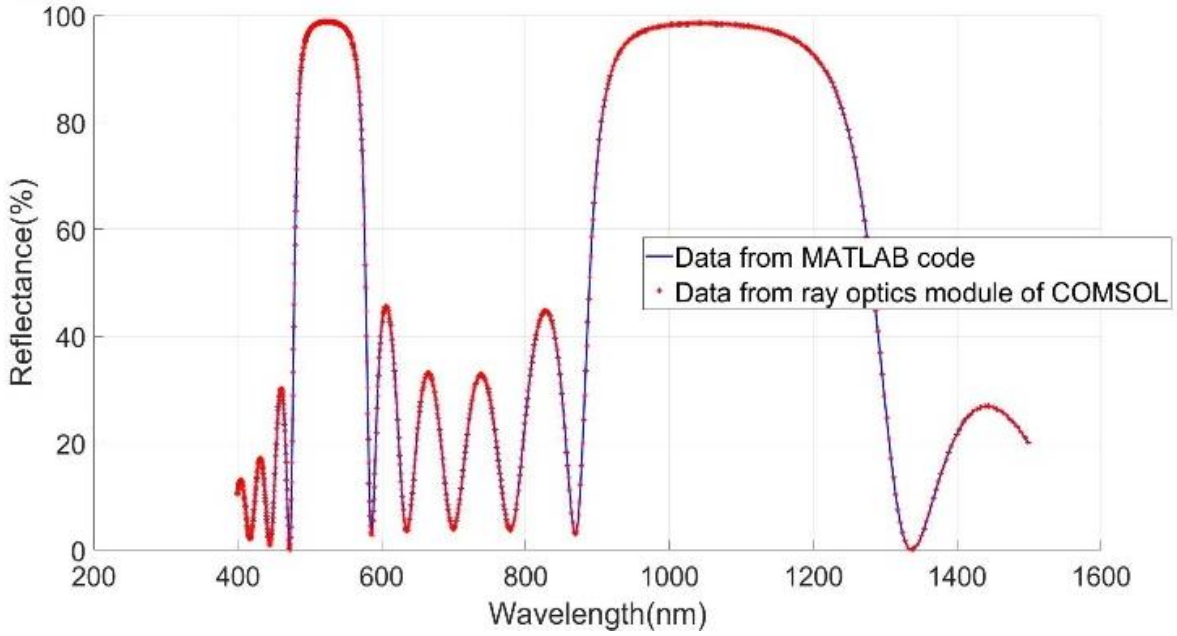

Figure 3-11. Reflectance spectra from a dielectric mirror comprised of alternating layers of TCO and SiO_2 nanoparticle films calculated using our MATLAB code and COMSOL Multiphysics software (five layers of TCO and SiO2 with thicknesses of 73 and 257 nm, respectively).

3-2. Graded-index antireflection coatings

One way to increase the transparency in the visible range is to design the dielectric mirror such that the refractive index profile between the H and L films within the mirror is a graded-index profile rather than a step function. This technique involves using a continuously varying index of refraction profile at the interfaces between the H and L layers within the dielectric mirror. Southwell [141] investigated three different index of refraction profiles (e.g. linear, cubic and quintic profiles) to study their antireflection properties at the interface between two dielectric media. Here, the dielectric media are two films with $n_H = 2$ and $n_L = 1.3$, and n_H and n_L are the refractive indices of the two films at the interface. Southwell applied these graded refractive index profiles to glass surfaces to reduce the reflection from these surfaces in the visible spectral region. In this work the graded index of refraction profiles that Southwell considered are applied to each interface in the dielectric mirrors that are designed to reflect infrared radiation. That is, Southwell's graded index of refraction profiles are applied at the interfaces between the H and L layers within a dielectric mirror to reduce reflection over spectral regions wherein the wavelength of light is considerably shorter than the Bragg-peak wavelength. Herein, this technique is referred to as the interfacial graded index technique. Accordingly, a dielectric mirror is designed to function as a transparent heat mirror that exhibits minimal reflection in the solar spectral region and a strong reflectance peak in infrared spectral regions. Furthermore, the effects of altering the dielectric mirror parameters on its performance are investigated. In this work several cases have been considered wherein the width of the graded index of refraction profile at the interface between the H and L layers is varied. The width of the region with a graded index of refraction, denoted herein as W_{grin}, is varied from $0.5\cdot(d_{L+H})$ to $0.1\cdot(d_{L+H})$, where $d_{L+H} = d_L + d_H$, and d_H and d_L are the thicknesses of the H and L layers within the dielectric mirror, respectively.

To show how graded-index of refraction profiles can reduce reflection, consider an interface with a stacking sequence of [LH], as shown in Figure 3-12. The figure illustrates the refractive index variation for the linear (Figure a.), cubic (Figure b.) and quintic (Figure c.) profiles based on the graded-index technique where W_{grin}, is varied from $0.1\cdot(d_{L+H})$ to $0.5\cdot(d_{L+H})$ and n is varied from $n_L = 1.3$ to $n_H = 2$.

a.

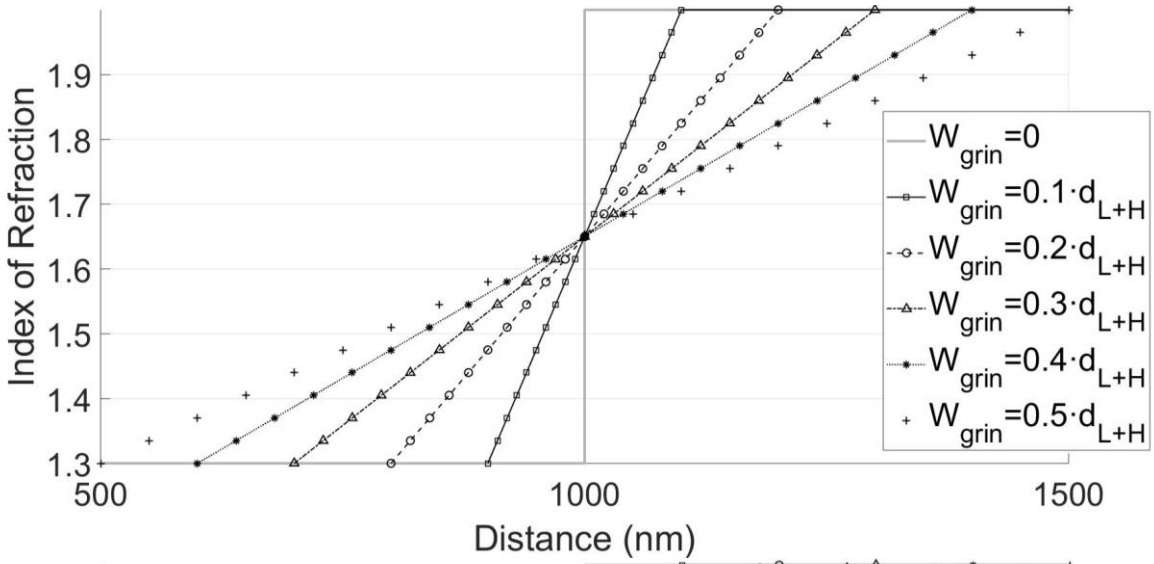

b.

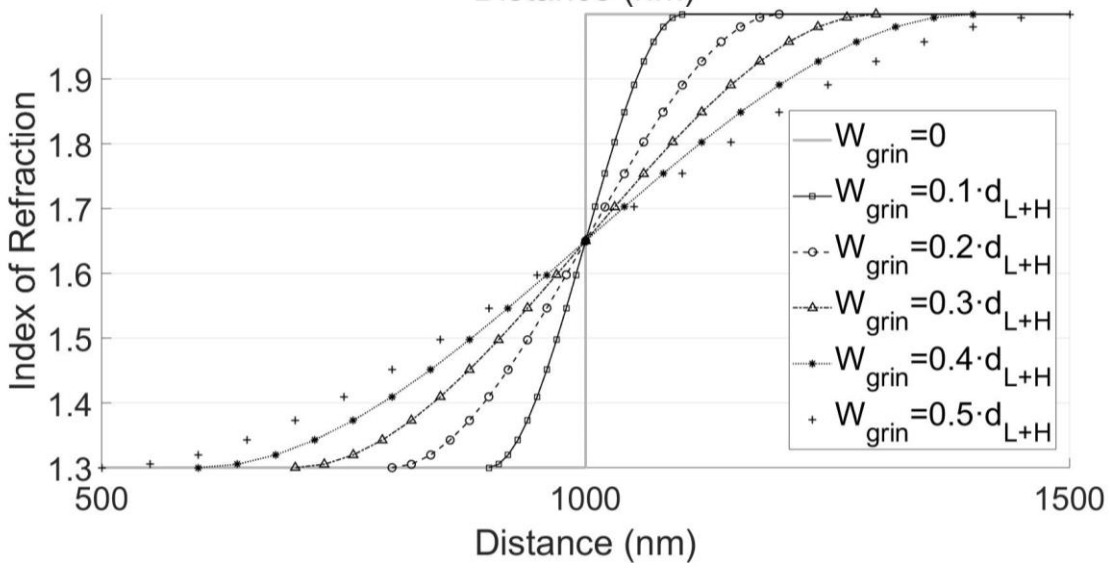

c.

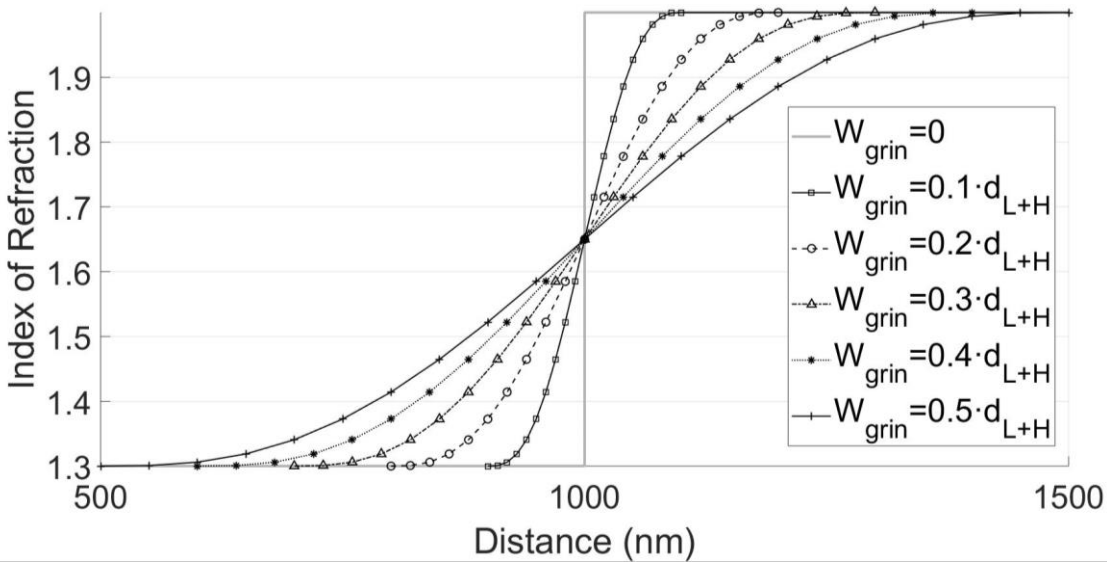

Figure 3-12. Refractive index variation for the linear (Figure a.), cubic (Figure b.) and quintic (Figure c.) profiles based on the graded-index technique for two interfaces with W_{grin} equal to 0 to $0.5\cdot(d_{L+H})$, where $n_H = 2$ and $n_L = 1.3$

To demonstrate functionality of the technique, three different cases of interfaces are considered here with stacking sequences of [HL], [LH] and [LHL]. Figure 3-13 shows the index of refraction profile at an [HL] interface for the cases of a step profile and the linear, cubic and quintic profiles. In general, the linear, cubic, and quintic index of refraction profiles are represented by Equations 3-6, 3-7, and 3-8, respectively.

$$n = n_i + (n_s - n_i)d, \qquad 0 \le d \le 1 \qquad (3\text{-}7)$$

where n_i and n_s are the indices of refraction of the incident and substrate media, respectively.

$$n = n_i + (n_s - n_i)(3d^2 - 2d^3), \qquad 0 \le d \le 1 \qquad (3\text{-}8)$$

$$n = n_i + (n_s - n_i)(10d^3 - 15d^4 + 6d^5), \qquad 0 \le d \le 1 \qquad (3\text{-}9)$$

As can be seen in Figure 3-14, the interfacial graded index technique significantly increases the transmission through the [HL] interface in the short wavelength region. On the other hand, the

reflectance from the [HL] interface in the long-wavelength spectral region, shown in Figure 3-15, remains almost the same as the case for the conventional interface wherein the index of refraction follows a simple step profile. Moreover, as shown in Figure 3-15, the reflectance from the [HL] interface with cubic or quintic interfacial graded index of refraction profiles better approximates that of the conventional quarter-wave stack interface as compared to the case when a linear interfacial profile is used. Figure 3-16 shows the index of refraction through an [LH] interface with step, linear, cubic and quintic graded index profiles. With reference to Figure 3-17, the [LH] interface exhibits the same transmittance as compared to the [HL] interface and this is obvious considering the transmittance relation provided earlier in Equation 3-2. Furthermore, as can be seen in Figure 3-19, the transmittance in the visible spectral region is the highest for a [LHL] interface with interfacial graded index of refraction profiles, which are shown in Figure 3-18.

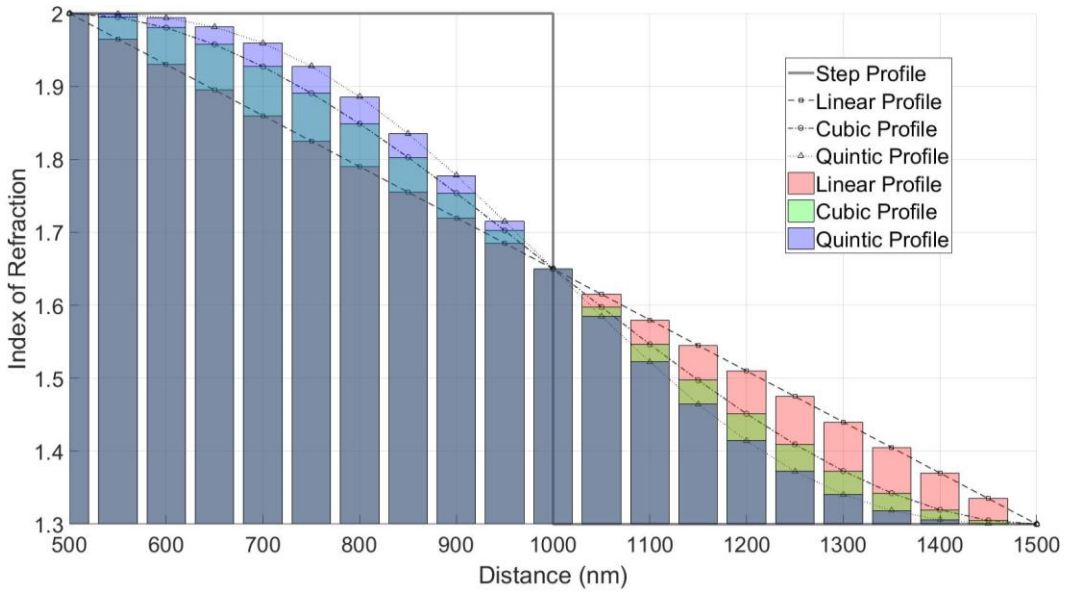

Figure 3-13. Refractive index variation for different profiles based on the interfacial graded-index technique with $W_{grin}=0.5\cdot(d_H + d_L)$ for an interface with stacking sequences of [HL], having $n_H = 2$ and $n_L = 1.3$, respectively

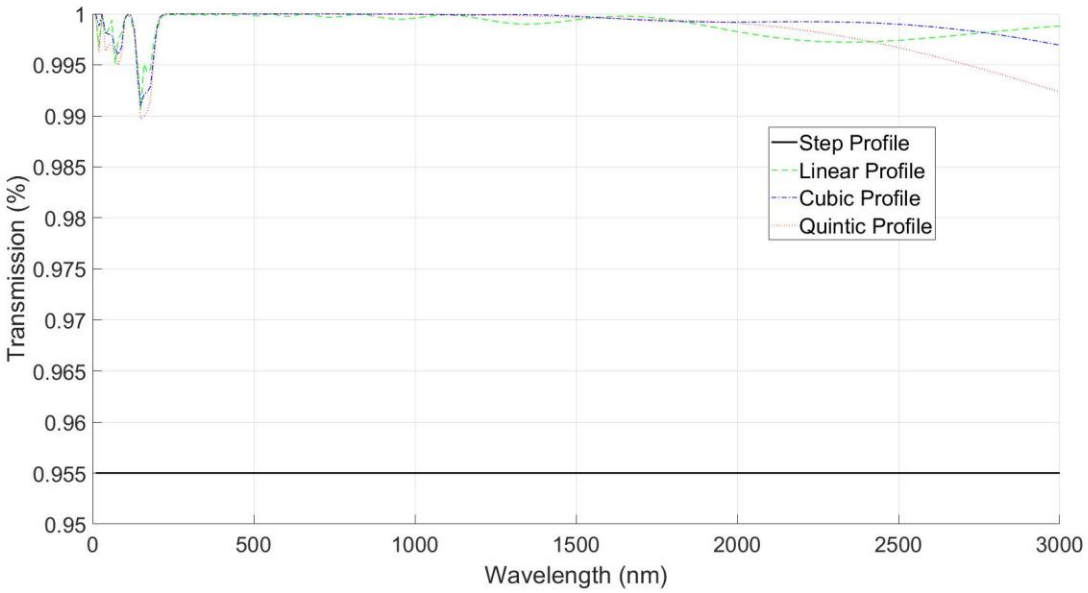

Figure 3-14. Transmission through an interface with stacking sequences of [HL] for different profiles based on the interfacial graded-index technique with $W_{grin} = 0.5 \cdot (d_{L+H})$ and comprised of two films with $n_H = 2$ and $n_L = 1.3$, respectively.

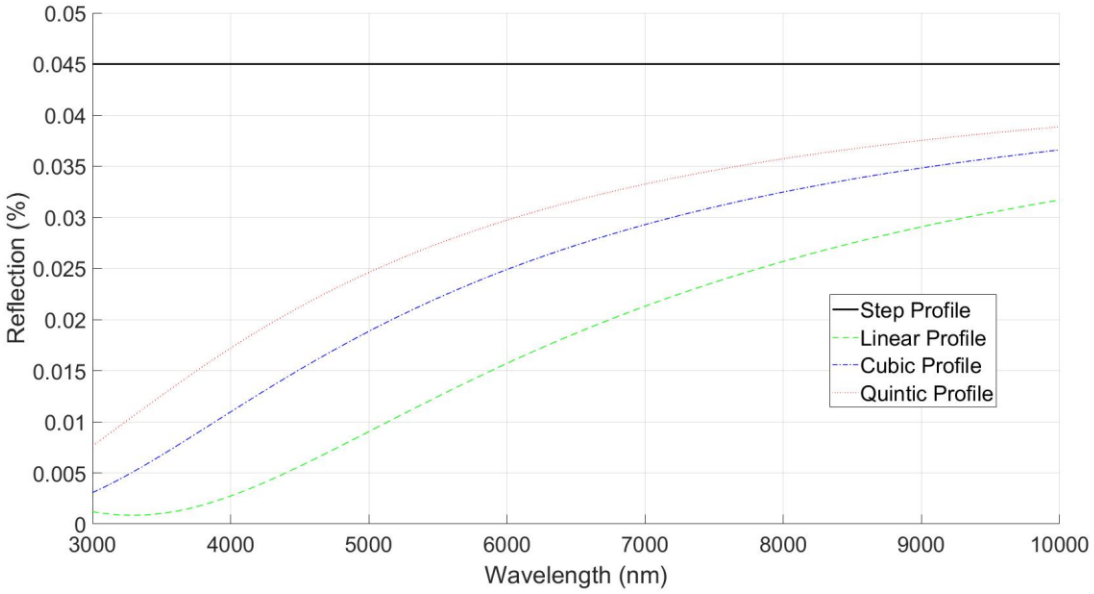

Figure 3-15. Reflectivity of an interface with stacking sequences of [HL] and different profiles based on the interfacial graded-index technique with $W_{grin} = 0.5 \cdot (d_{L+H})$ and comprised of two films with $n_H = 2$ and $n_L = 1.3$, respectively.

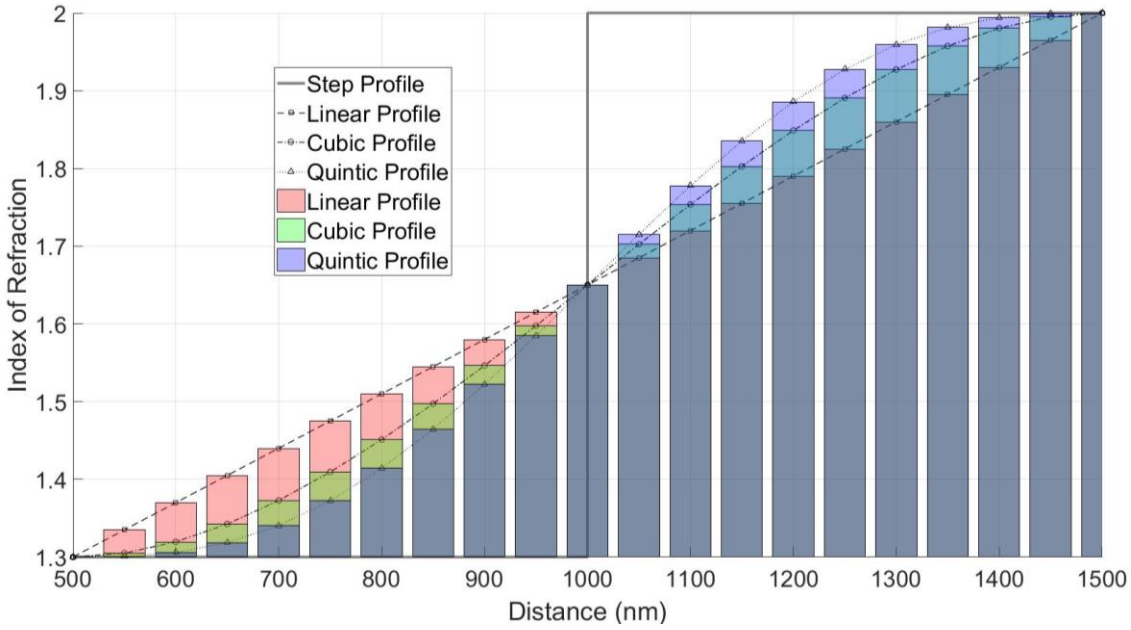

Figure 3-16. Refractive index variation for different profiles based on the interfacial graded-index technique with $W_{grin} = 0.5 \cdot (d_{L+H})$ for an interface with stacking sequences of [LH] and comprised of two films with $n_H = 2$ and $n_L = 1.3$, respectively.

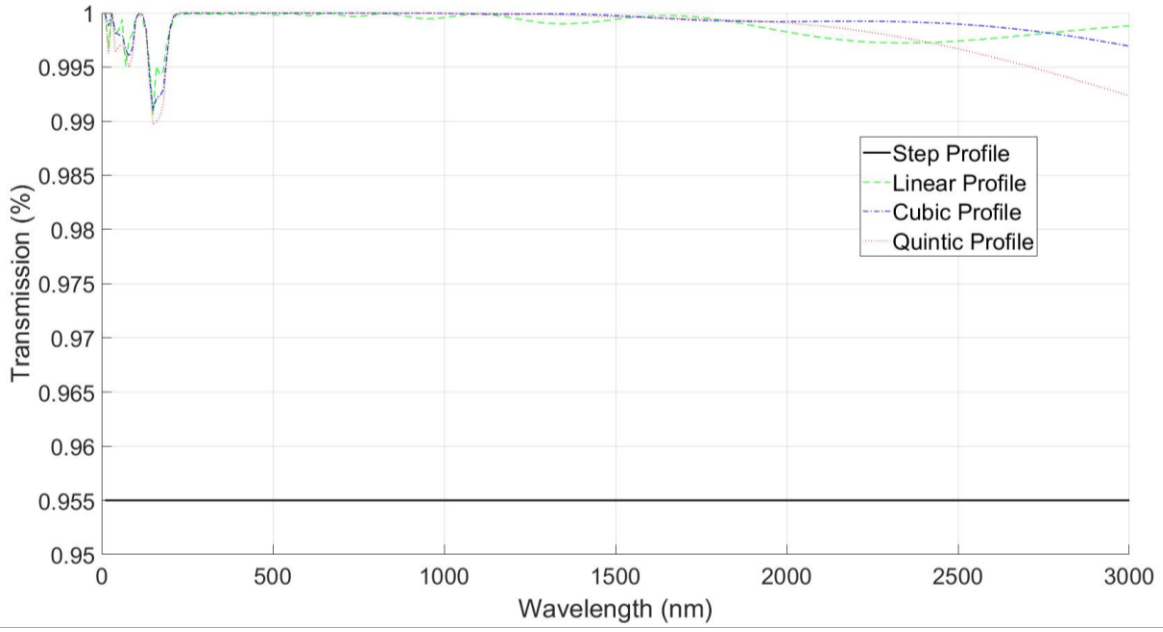

Figure 3-17. Transmission through an interface with stacking sequences of [LH] for different profiles based on the interfacial graded-index technique with $W_{grin} = 0.5 \cdot (d_{L+H})$ and comprised of two films with $n_H = 2$ and $n_L = 1.3$.

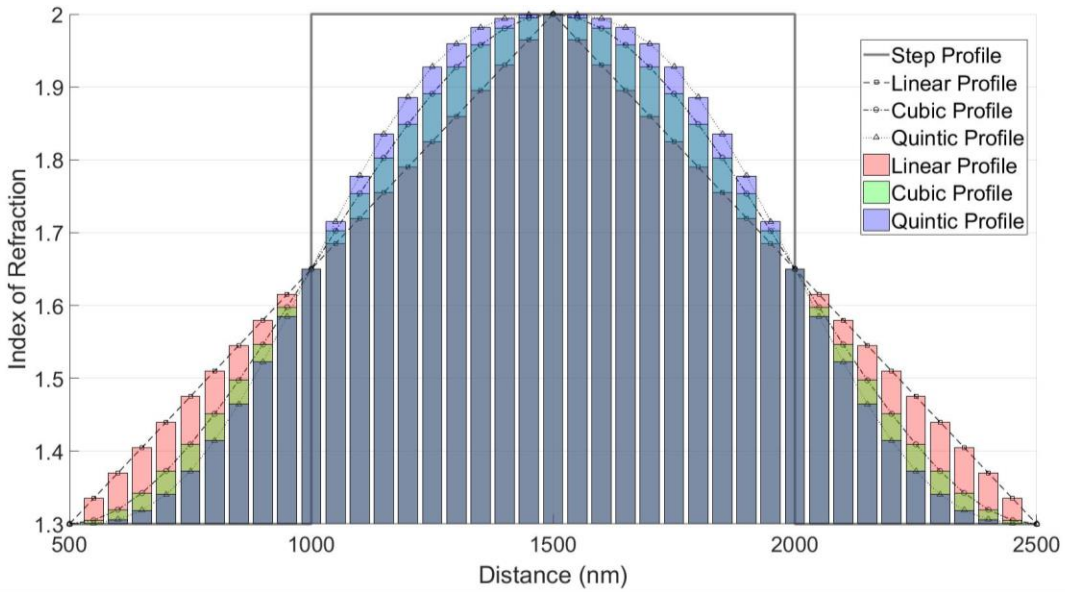

Figure 3-18. Refractive index variation for different profiles based on the interfacial graded-index technique with $W_{grin} = 0.5 \cdot (d_{L+H})$ for an interface with stacking sequences of [LHL], and comprised of films with $n_H = 2$ and $n_L = 1.3$.

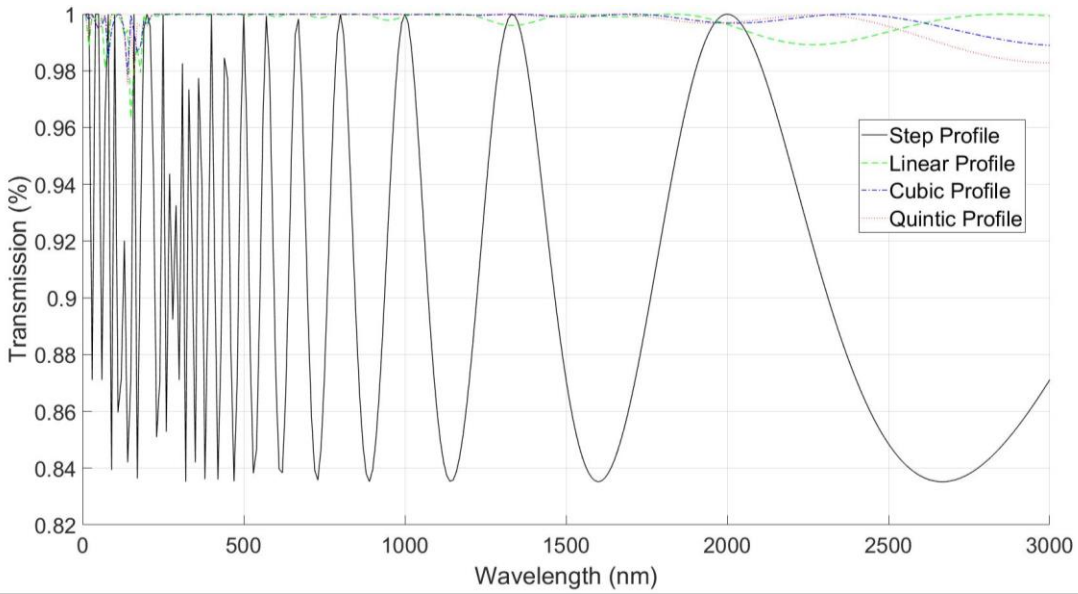

Figure 3-19. Transmission through an interface with stacking sequences of [LHL] for different profiles based on the interfacial graded-index technique with $W_{grin} = 0.5 \cdot (d_{L+H})$ and comprised of films with $n_H = 2$ and $n_L = 1.3$.

3-2-1. Design of transparent dielectric heat mirrors with different interfacial graded index profiles and their optical performance

A dielectric mirror comprised of five by-layers of films with $n_L = 2$ and $n_H = 1.3$, and with linear interfacial index of refraction profiles (denoted as $[H_LL_L]^5$), is shown in Figure 3-20 for different values of W_{grin}. As shown in Figure 3-23, $[H_LL_L]^5$ exhibits a higher transmittance in the visible spectral range without the reflectance fluctuations that are present for the case of the conventional dielectric mirror (e.g. $[HL]^5$). However, as can be seen in Figure 3-24, for $W_{grin} = 0.5\cdot(d_{L+H})$, the reflectance from $[H_LL_L]^5$ in the infrared spectral region is decreased as compared to the reflectance from the conventional dielectric mirror, $[HL]^5$. Furthermore, the FWHM for $[H_LL_L]^5$ is equal to 1,550 nm with a maximum reflectance peak of ~90%. In comparison, the FWHM for $[HL]^5$ is equal to 2,150 nm with a maximum reflectance peak of ~98%.

For a cubic interfacial index of refraction profile (denoted as $[H_CL_C]^5$), shown in Figure 3-21, the transmittance over the solar spectral region is much greater than that of $[H_LL_L]^5$. As shown in Figure 3-23Figure 3-24, the transmittance in the solar spectral region for $[H_CL_C]^5$ achieves values as high as 98 % , while the reflectance for $[H_CL_C]^5$ in the IR spectral region is greater than that of $[H_LL_L]^5$ with a FWHM equal to 1,770 nm and a peak reflectance maximum of ~95%.

When the interfaces between the films with the higher and lower refractive indices within the dielectric mirror is designed with a quintic index of refraction profile (denoted as $[H_QL_Q]^5$), as provided by Equation 7 and shown in Figure 3-22, further improvements can be achieved. As can be seen in Figure 3-24, the reflection in the infrared spectral region is significantly increased in comparison to the case for $[H_LL_L]^5$ or $[H_CL_C]^5$ and the FWHM of the reflection peak equals 1,860 nm with a maximum of ~96%. At the same time, the visible transparency is improved for $[H_QL_Q]^5$.

Figure 3-25 shows the percent transmittance of the solar irradiance by $[H_LL_L]^5$, $[H_CL_C]^5$, and $[H_QL_Q]^5$ for the cases in which W_{grin} increases from 0 to $0.5\cdot(t_{L+H})$. Accordingly, $W_{grin}=0$ is representative of the dielectric mirror that is a quarter-wave stack with an index of refraction that follows a step profile denoted by $[HL]^5$. The solar transmission through the structure has a maximum value of ~ 97 % for the case when the dielectric mirror has the form of $[H_QL_Q]^5$ with $W_{grin}=0.5\cdot(t_{L+H})$. Figure 3-26 shows the solar irradiance spectra (the solar spectrum is approximated by the radiation emitted from a blackbody at a temperature of ~ 5,700 K) and the amount of spectral power transmitted through $[HL]^5$, $[H_LL_L]^5$, $[H_CL_C]^5$ and $[H_QL_Q]^5$ with $W_{grin}=0.5\cdot(d_{L+H})$.

Figure 3-27 and Figure 3-28 show the blackbody radiation at a temperature of 500 K that is reflected by $[H_LL_L]^5$, $[H_CL_C]^5$, and $[H_QL_Q]^5$ for the cases in which W_{grin} increases from 0 to $0.5\cdot(d_{L+H})$. Results show that $[HL]^5$ provides the highest reflectance which results in the highest amount of reflected thermal radiation. However, $[HL]^5$ also has higher reflectance in the visible spectrum compared to the rest of the cases wherein W_{grin} has values ranging from $0.1\cdot(d_{L+H})$ to $0.5\cdot(d_{L+H})$, which means that $[HL]^5$ exhibits the lowest transmittance for the solar irradiance. As can be seen, considering different profiles and W_{grin}, the dielectric mirror with $[HL]^5$ exhibits the maximum thermal radiation reflectance value of ~ 42 % followed by the $[H_QL_Q]^5$ structure with $W_{grin} = 0.5\cdot(d_{L+H})$ which reflects ~ 37 % of the thermal radiation. Finally, Figure 3-28 depicts the blackbody radiation spectrum from an emitter at a temperature of 500 K and the amount of spectral power reflected by $[HL]^5$, $[H_LL_L]^5$, $[H_CL_C]^5$ and $[H_QL_Q]^5$ with $W_{grin}=0.5\cdot(d_{L+H})$.

In the following, in Chapter 4, the effects of altering the dielectric mirror parameters on its performance will be investigated. Accordingly, the sensitivity of the transmittance and reflectance spectra of the dielectric mirrors presented in this chapter on their number of layers, resolution of

their refractive index profiles, refractive index, number of stacked dielectric mirrors, absorption, and incident angle of the incoming light will be analyzed.

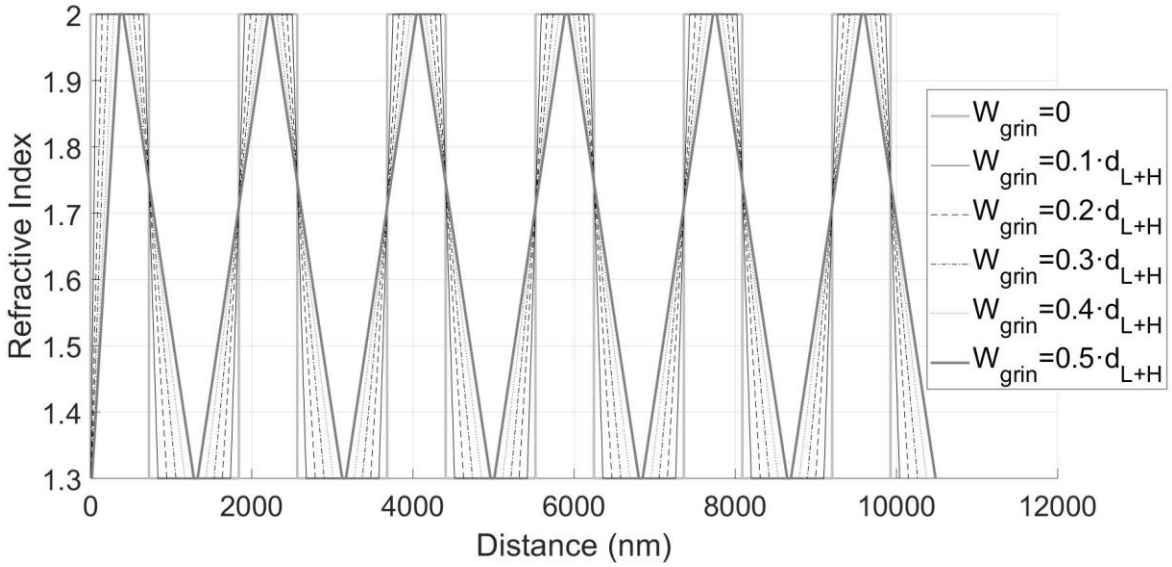

Figure 3-20. Linear refractive index variation for different W_{grin} equal to $0.1\cdot(d_{L+H})$ to $0.5\cdot(d_{L+H})$ based on the interfacial graded-index technique for two dielectric media with stacking sequences of $[H_LL_L]^5$, comprised of two alternating films with $n_H = 2$ and $n_L = 1.3$, respectively.

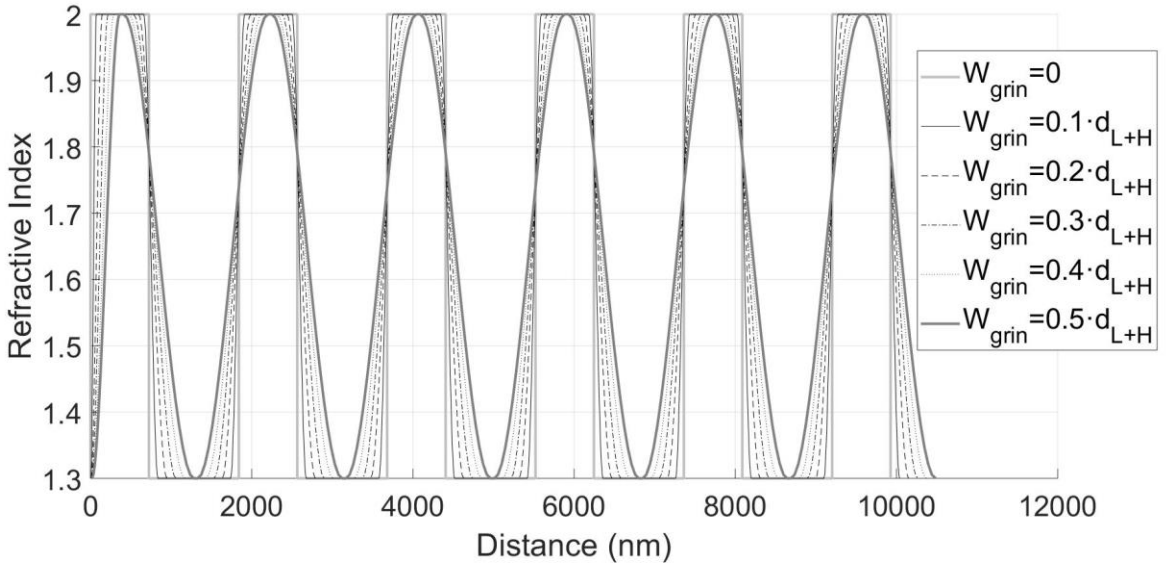

Figure 3-21. Cubic refractive index variation for different values of W_{grin} equal to $0.1\cdot(d_{L+H})$ to $0.5\cdot(d_{L+H})$ based on the interfacial graded-index technique for two dielectric media with stacking sequences of $[H_CL_C]^5$, and comprised of two alternating films with $n_H = 2$ and $n_L = 1.3$, respectively.

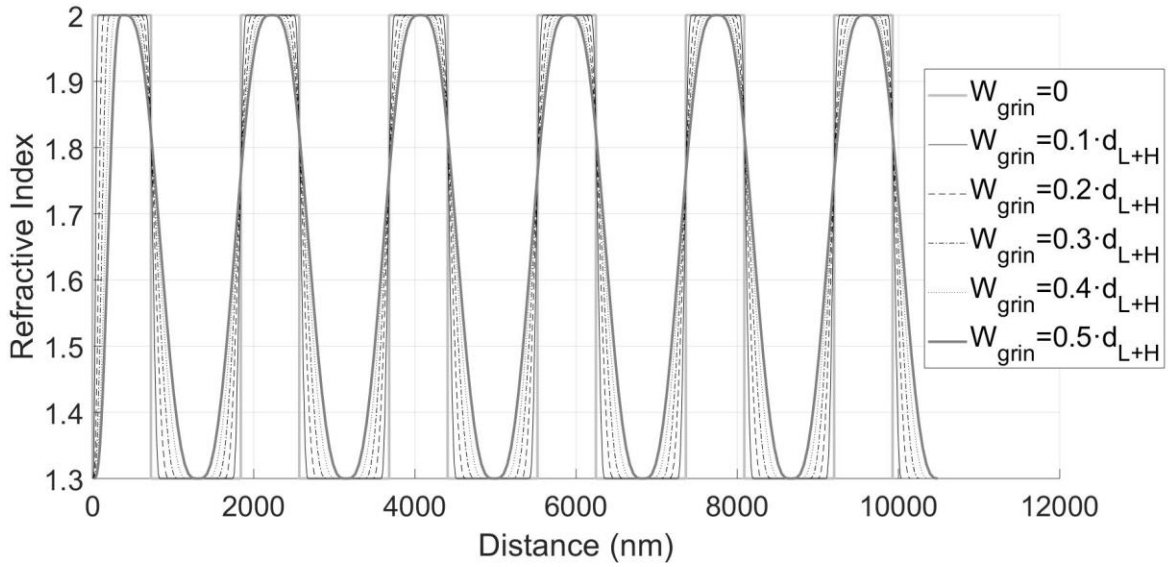

Figure 3-22. Quintic refractive index variation for different W_{grin} values equal to $0.1\cdot(d_{L+H})$ to $0.5\cdot(d_{L+H})$ based on the interfacial graded-index technique for two dielectric media with stacking sequences of $[H_QL_Q]^5$, and comprised of two alternating films with $n_H = 2$ and $n_L = 1.3$, respectively.

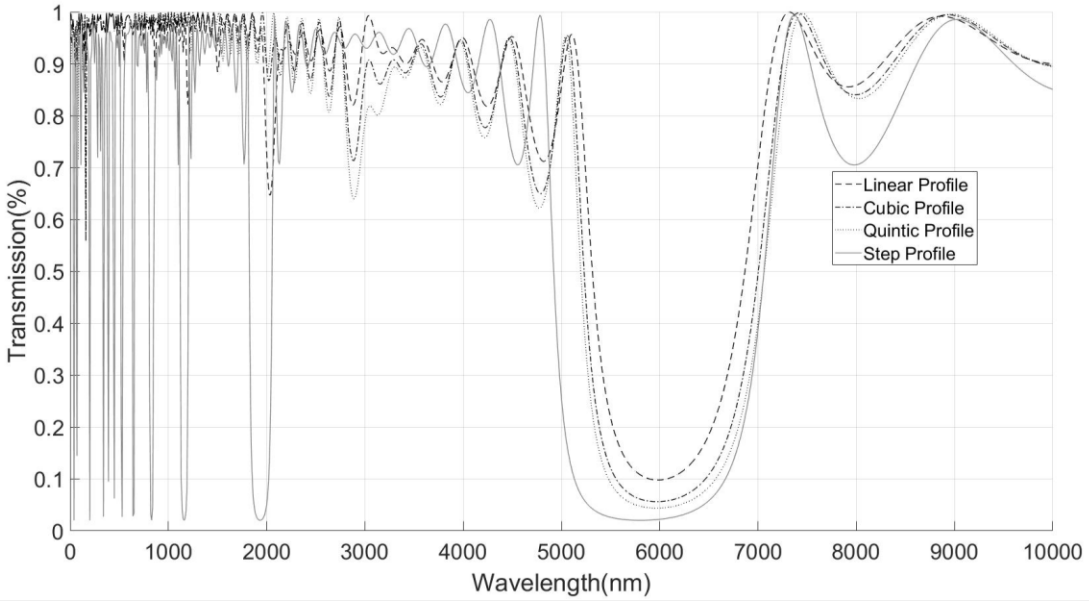

Figure 3-23. Transmission through dielectric mirrors with stacking sequences of $[HL]^5$, $[H_LL_L]^5$, $[H_CL_C]^5$, and $[H_QL_Q]^5$ with $W_{grin}=0.5\cdot(d_{L+H})$ and comprised of alternating layers with $n_H=2$ and $n_L=1.3$.

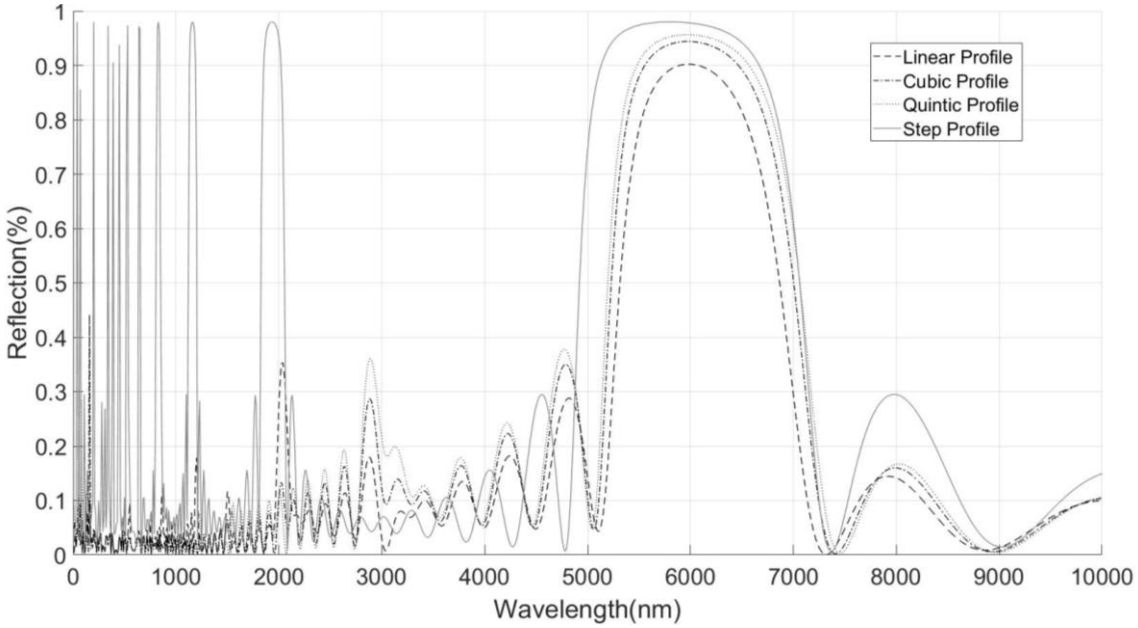

Figure 3-24. Reflection spectra for dielectric mirrors with stacking sequences of $[HL]^5$, $[H_LL_L]^5$, $[H_CL_C]^5$, and $[L_QH_Q]^5$ with $W_{grin}=0.5\cdot(d_{L+H})$ based on the interfacial graded-index technique comprised of two films with $n_H=2$ and $n_L=1.3$, respectively.

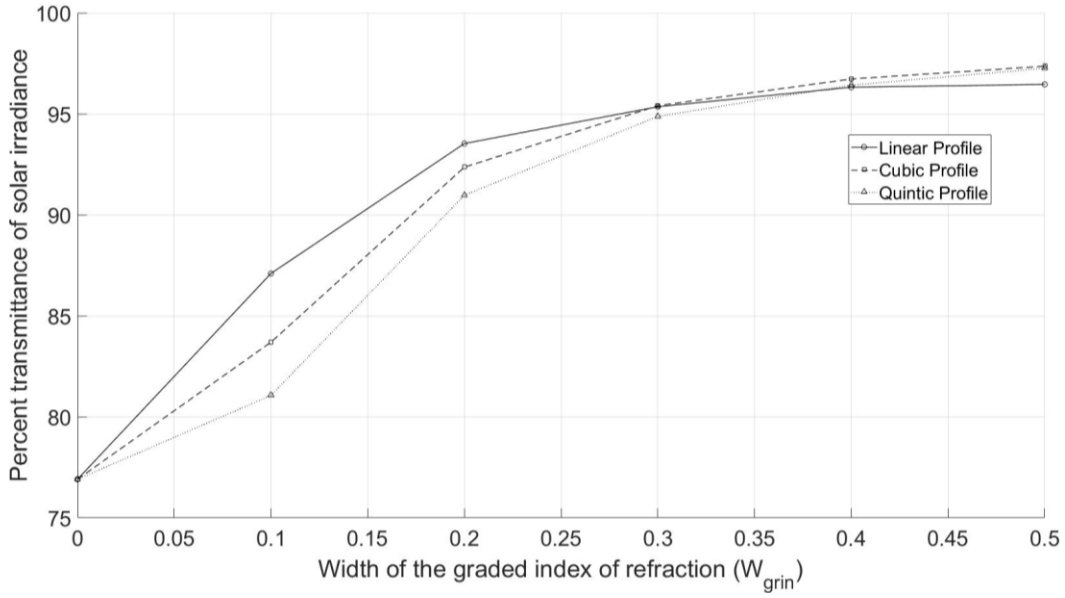

Figure 3-25. Percent transmittance of the solar irradiance as a function of W_{grin} for $[HL]^5$, $[H_LL_L]^5$, $[H_CL_C]^5$ and $[H_QL_Q]^5$ comprised of alternating films with $n_H = 2$ and $n_L = 1.3$, respectively.

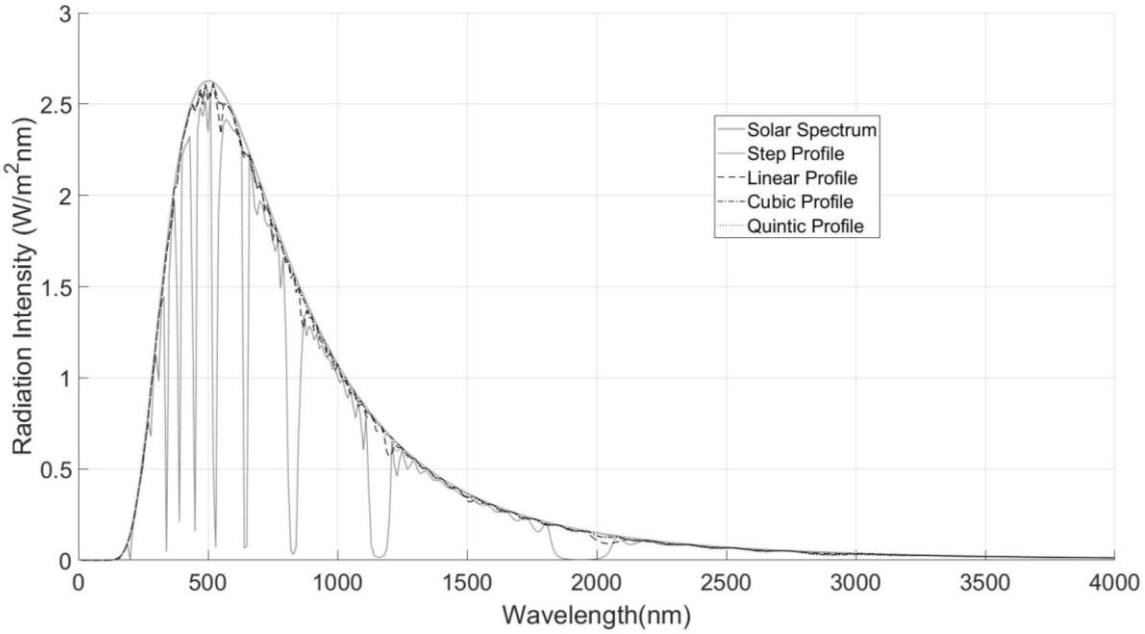

Figure 3-26. Solar irradiance spectra (the solar spectrum is approximated by the radiation emitted from a blackbody at a temperature of ~ 5,700 K) and the fraction of spectral power transmitted through $[HL]^5$, $[H_LL_L]^5$, $[H_CL_C]^5$ and $[H_QL_Q]^5$ with $W_{grin}=0.5\cdot(d_{L+H})$ and comprised of alternating films with $n_H = 2$ and $n_L = 1.3$.

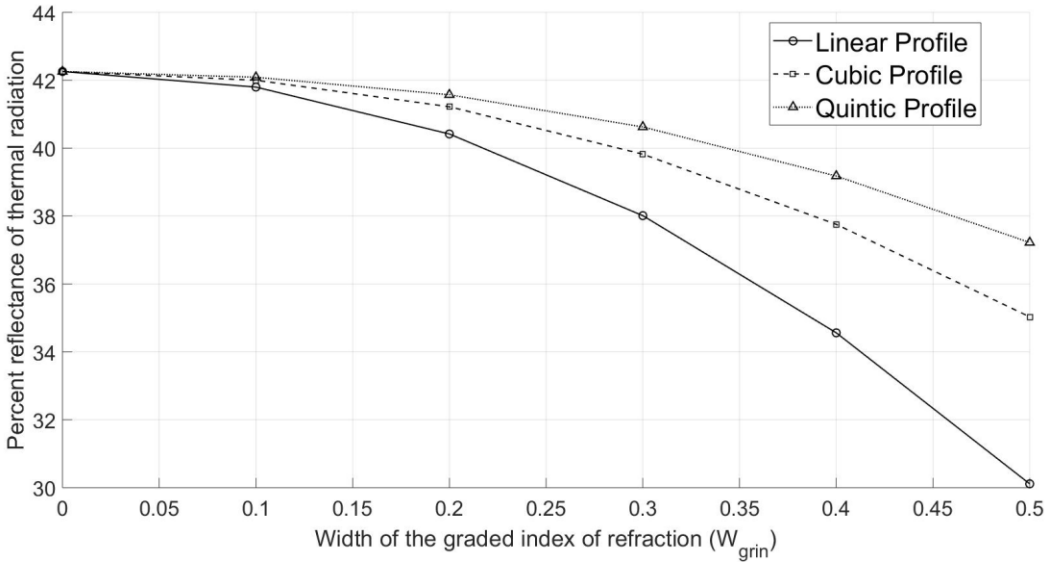

Figure 3-27. Percent reflection of the radiation spectrum emitted from a blackbody at T= 500 K with various values of W_{grin} for $[HL]^5$, $[H_LL_L]^5$, $[H_CL_C]^5$ and $[H_QL_Q]^5$ comprised of alternating films with $n_H = 2$ and $n_L = 1.3$, respectively.

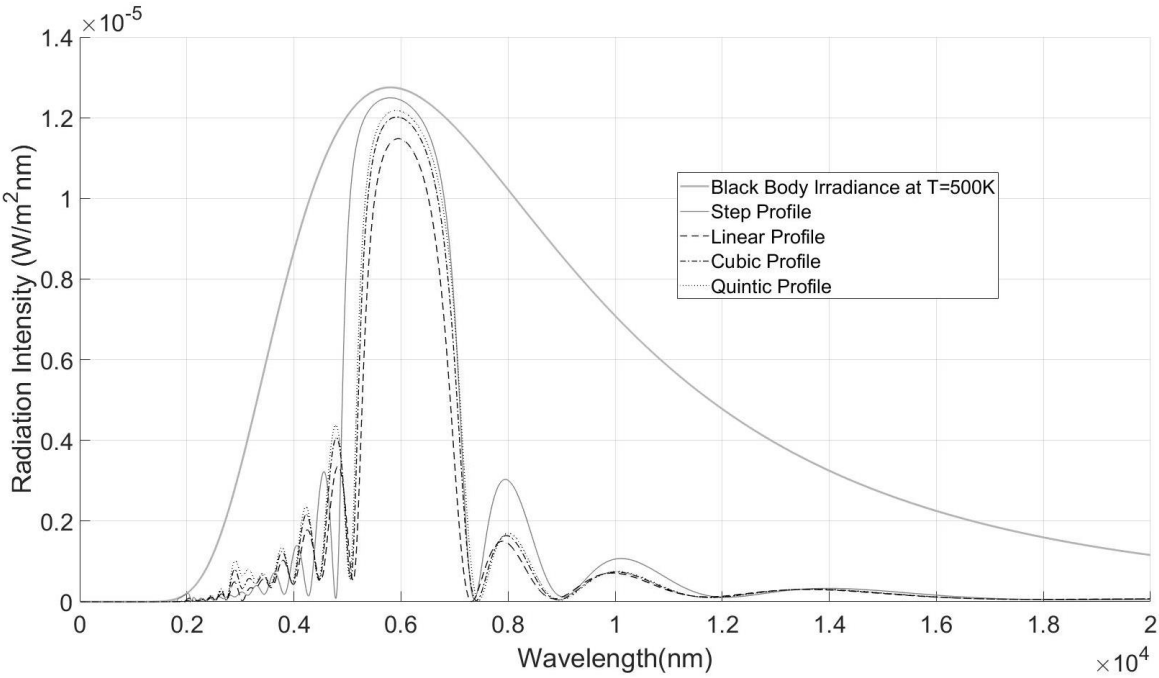

Figure 3-28. Radiation spectrum emitted from a black body at a temperature of 500 K and the amount of spectral power reflected by $[HL]^5$, $[H_LL_L]^5$, $[H_CL_C]^5$ and $[H_QL_Q]^5$ with Wgrin=$0.5\cdot(d_{L+H})$ and comprised of alternating films with nH = 2 and nL=1.3.

3-3. Summary

In this chapter, a transparent selective coating in the form of a dielectric mirror comprised of alternating layers with different indices of refraction was designed. The alternating layers of films were designed to selectively reflect light strongly over the infra-red spectral region while being highly transmissive towards solar irradiance. In order to accomplish this, thin graded index layers were designed as anti-reflection coatings at the interfaces between the alternating layers within the dielectric mirror. Three different index of refraction profiles were considered including: 1. a linear index variation, 2. a cubic index variation and 3. a quintic index variation. Results showed that the quintic profile provides better results for the reflectance and transmittance contributions compared to the cases when the graded index profile is linear or cubic. In the following, in Chapter 4, sensitivity analysis of the transmittance and reflectance spectra of the dielectric heat mirror towards different parameters will be discussed including the number of layers, resolution of the refractive index profiles, refractive index, number of stacked dielectric mirrors, absorption, and incident angle of the incoming light.

4. Sensitivity analysis

In this chapter, the effects of altering the transparent dielectric heat mirror parameters on its performance are investigated. That is, the sensitivity of the transmittance and reflectance spectra of the dielectric mirror towards its number of layers, resolution of the refractive index profiles, refractive index, number of stacked dielectric mirrors, absorption, and incident angle of the incoming light is analyzed. In this chapter all dielectric mirrors are designed, according to the methods described in Chapter 3, to maximize reflectance of the radiation spectrum emitted from a black-body solar receiver that is at a temperature of 500 K, and the corresponding thicknesses of the H and L layers with refractive indices of 2 and 1.3 within the dielectric mirrors considered in this chapter are 725 nm and 1,154 nm, respectively. Moreover, dielectric mirror designs with linear, cubic, and quintic refractive index profiles at the interfaces between their high and low index of refraction layers are considered along with the conventional case wherein the refractive index profile at the interfaces within the dielectric mirror is represented by a step-function.

4-1. Effects of altering the angle of incident light on the performance of transparent dielectric heat mirrors

To investigate the effects of altering the angle of incident light on the transmittance and reflectance spectra a dielectric heat mirror with a stacking sequence of $[HL]^5$ is considered, where H and L represent films with refractive indices equal to 2 and 1.3, respectively.

Using the methods described in Section 3-1, the dielectric mirrors are designed to optimally reflect radiation from a black-body with a temperature of 500 K, and the resulting thicknesses of the H and L layers are 725 nm and 1,154 nm, respectively. Furthermore, the dielectric mirrors investigated here are comprised of five bilayers, and the cases of linear (e.g. $[H_LL_L]^5$) , cubic (e.g. $[H_CL_C]^5$), and quintic (e.g. $[H_QL_Q]^5$) interfacial index of refraction profiles are considered along with the conventional quarter-wave stack wherein the index of refraction profile is a step-function (e.g. $[HL]^5$) at the interface between the H and L layers. Also, the width of the region with a graded index of refraction, denoted herein as W_{grin}, is equal to $0.5\cdot(d_{L+H})$ where $d_{L+H} = d_L+d_H$, and d_H and d_L are the thicknesses of the H and L layers within the dielectric stack, respectively.

Figure 4-1, Figure 4-2, Figure 4-3, Figure 4-5 and Figure 4-7 show transmittance spectra for dielectric mirrors with $[HL]^5$, $[H_LL_L]^5$, $[H_CL_C]^5$ and $[H_QL_Q]^5$ stacking sequences and $W_{grin}=0.5\cdot(d_{L+H})$ for the cases in which light is incident from angles of 0, 5, 10, 15, 20, 30, 40, and 50° with reference to the direction that is normal to the planar surfaces of the dielectric mirror. Likewise, Figure 4-2, Figure 4-4, Figure 4-6 and Figure 4-8 show the reflectance spectra for the corresponding cases. As can be seen in Figure 4-2.a, Figure 4-4.a, Figure 4-6.a and Figure 4-8.a, for the reflectance spectra of P-polarized light, increasing the angle of incidence causes the FWHM of the reflection peak for $[HL]^5$, $[H_LL_L]^5$, $[H_CL_C]^5$ and $[H_QL_Q]^5$ to decrease from 2,140 nm, 1,550

nm, 1,770 nm and 1,870 nm for an incident angle of 0° to 1,350 nm, 888 nm, 1,094 nm and 1,172 nm for an incident angle of 50°, respectively. Similarly, the corresponding maximum peak reflection values for $[HL]^5$, $[H_LL_L]^5$, $[H_CL_C]^5$ and $[H_QL_Q]^5$ decreases from 97.97%, 90.2%, 94.4% and 95.53% when light is normally incident to 88.48%, 69.85%, 78.3% and 81.22% when the light is incident from an angle of 50° with reference to the normal direction, respectively. This is while, with respect to Figure 4-2.b, Figure 4-4.b, Figure 4-6.b and Figure 4-8.b which show the reflectance spectra based on the S-polarized estimations, increasing the angle of incidence will result in the increase of the FWHM of the reflectance spectra from the dielectric mirrors with $[HL]^5$, $[H_LL_L]^5$, $[H_CL_C]^5$ and $[H_QL_Q]^5$ to 2,300 nm, 1,687 nm, 1,902 nm and 1,997 nm when light is incident from 50°, respectively. Likewise, the corresponding peak reflectance maximum values increases to ~99.63%, 96.88%, 98.48% and 98.9%, respectively. It should be noted that, although the S-Polarized estimations illustrate higher FWHM and peak reflectance maximum values which result in a higher percentage of reflected thermal radiation as shown in Figure 4-14, the reflectance values in the visible spectrum also increase which results in an undesirable reduction in the percentage of the total solar irradiance transmitted through the structure, which is shown in Figure 4-13.

Figure 4-9 and Figure 4-10 show a comparison of transmittance spectra for dielectric mirrors with $[HL]^5$, $[H_LL_L]^5$, $[H_CL_C]^5$ and $[H_QL_Q]^5$ for the cases in which light is incident from angles of 0, 10, and 20° and is P-Polarized and S-Polarized, respectively. Likewise, Figure 4-11 and Figure 4-12 show a comparison of reflectance spectra from dielectric mirrors with $[HL]^5$, $[H_LL_L]^5$, $[H_CL_C]^5$ and $[H_QL_Q]^5$ for the cases wherein the incident angles are 0, 10, and 20 ° and the light is P-polarized and S-polarized, respectively.

When the incident angle of the light is greater than 50°, the Bragg reflector behaviour is no longer seen and most of the energy from the sun is reflected by the dielectric mirror. This behaviour is noticeable in Figure 4-13 and Figure 4-14 where the percent transmittance of the solar irradiance and the percent reflection of the radiation spectrum emitted from a blackbody at T= 500 K through dielectric mirrors with different interfacial index of refraction profiles are plotted for $[HL]^5$, $[H_LL_L]^5$, $[H_CL_C]^5$ and $[H_QL_Q]^5$. As can be seen in Figure 4-13.a, the P-polarized portion of solar radiation transmitted through the dielectric mirror drops from roughly 97.25% when light is incident from the normal direction to just below 50% when the light is incident from an angle of 85°. Here, the solar radiation transmitted through a dielectric mirror with a step profile shows a drop from 76.91% when light is normally incident to 53.6% when the incoming light is incident from an angle of 85°. This is while, as shown in Figure 4-13.b, the fraction of S-polarized solar spectral power transmitted through $[HL]^5$, $[H_LL_L]^5$, $[H_CL_C]^5$ and $[H_QL_Q]^5$ decreases to ~16.81%, 30.92%, 33.54% and 34.69% at the incident angle of 85°, respectively. Moreover, Figure 4-13.c, shows the mean transmittance based on the P-Polarized and S-Polarized estimations which results in a smooth drop to approximately 42.2% for $[H_LL_L]^5$, $[H_CL_C]^5$ and $[H_QL_Q]^5$ and lower percentage of 35.21% for $[HL]^5$. On the other hand, Figure 4-14.b plots the percent reflection of the S-polarized radiation spectrum emitted from a blackbody at T = 500K by the dielectric mirror which increases from ~30.11%, 35.03%, 37.22% and 42.26% when light is normally incident to as high as 81.92%, 82.92%, 83.39% and 86.33% when light is incident from an angle of 85° for $[HL]^5$, $[H_LL_L]^5$, $[H_CL_C]^5$ and $[H_QL_Q]^5$, respectively. This is while, the percentage of P-polarized radiation emitted from a blackbody at T = 500 K that is reflected is as low as 47.45% when the incident angle is 85° as shown in Figure 3-18.a. Furthermore, Figure 4-14.c shows an increase to ~47 % in

percent reflection of the total radiation emitted from a blackbody at T= 500K for the case when the incident light is half p-polarized and half s-polarized and incident from an angle of 85°.

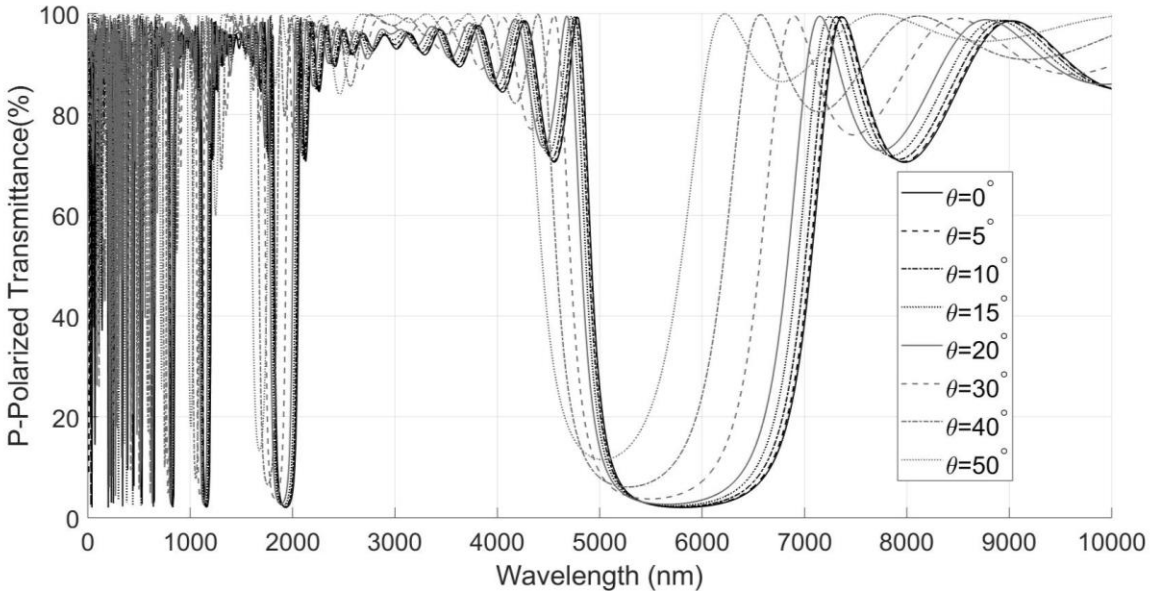

a.

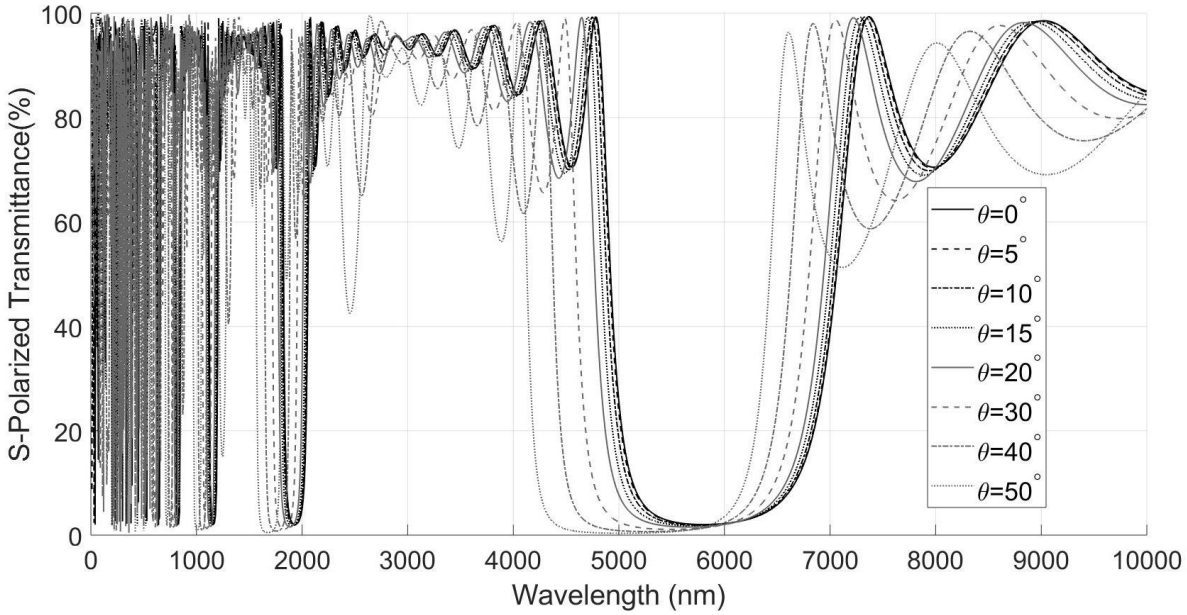

b.

Figure 4-1. Transmittance spectra for $[HL]^5$ comprised of alternating films with n_H=2 and n_L=1.3 with light incident from angles of 0, 5, 10, 15, 20, 30, 40, and 50°

a. Considering P-polarized light and $W_{grin}=0.5\cdot(d_{L+H})$

b. Considering S-polarized light and $W_{grin}=0.5\cdot(d_{L+H})$

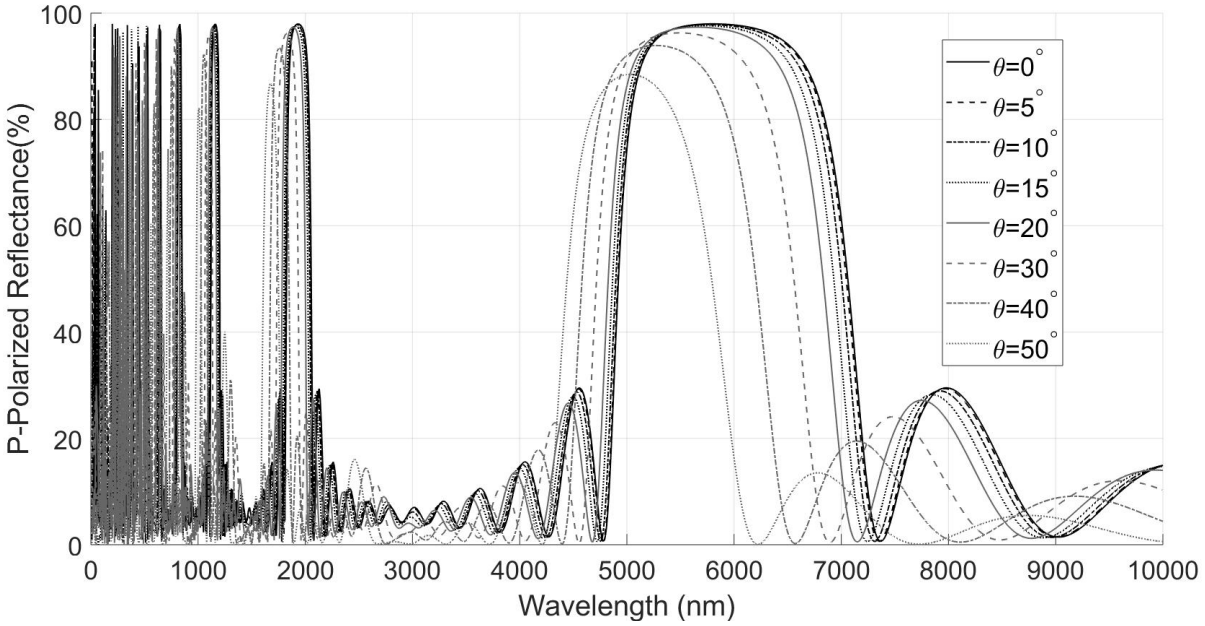

a.

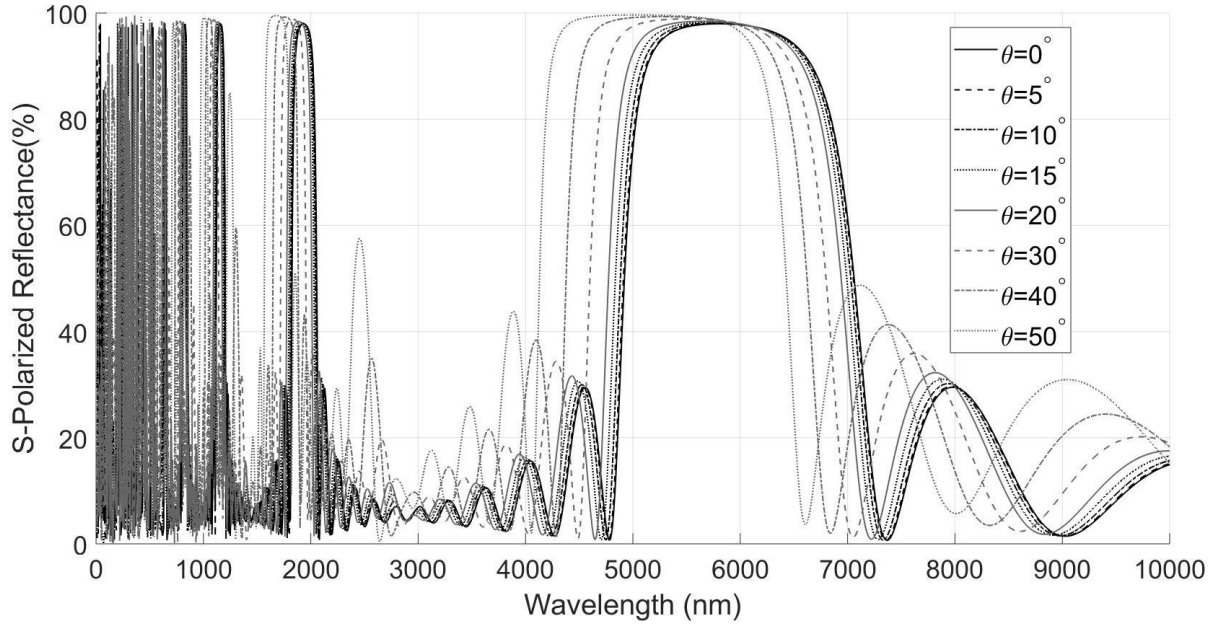

b.

Figure 4-2. Reflectance spectra for $[HL]^5$ comprised of alternating films with n_H=2 and n_L=1.3 with light incident from angles of 0, 5, 10, 15, 20, 30, 40, and 50°

a. Considering P-polarized light with $W_{grin}=0.5\cdot(d_{L+H})$

b. Considering S-polarized light with $W_{grin}=0.5\cdot(d_{L+H})$

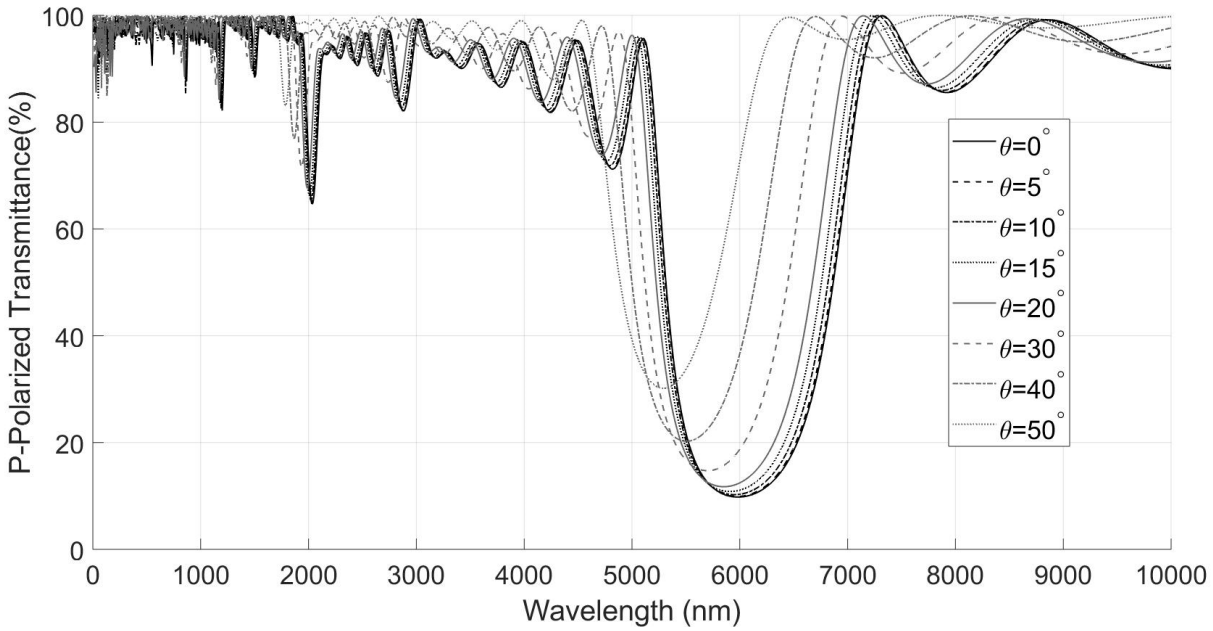

a.

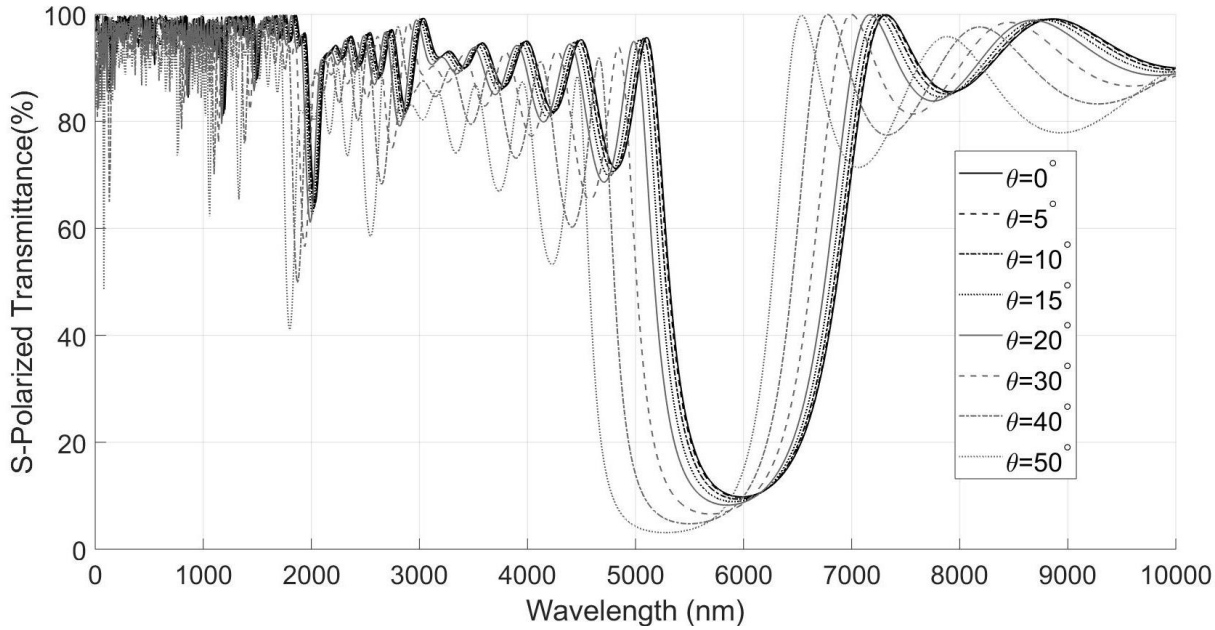

b.

Figure 4-3. Transmittance spectra for $[H_LL_L]^5$ comprised of alternating films with n_H=2 and n_L=1.3 with light incident from angles of 0, 5, 10, 15, 20, 30, 40, and 50 °

a. Considering P-polarized light and $W_{grin}=0.5\cdot(d_{L+H})$

b. Considering S-polarized light and $W_{grin}=0.5\cdot(d_{L+H})$

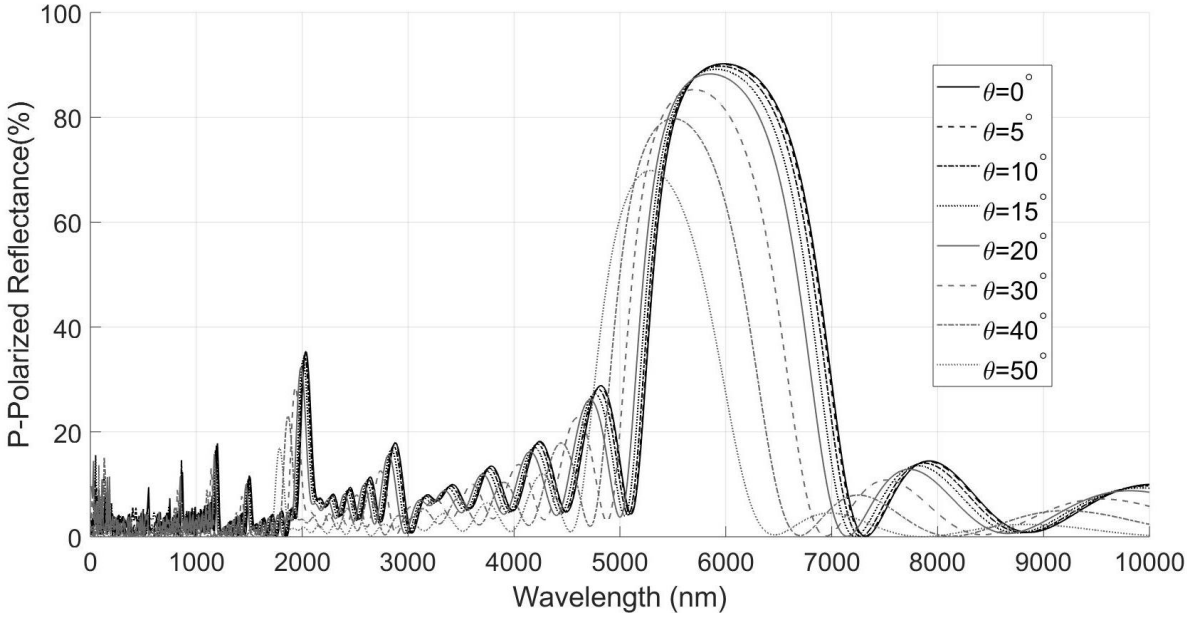

a.

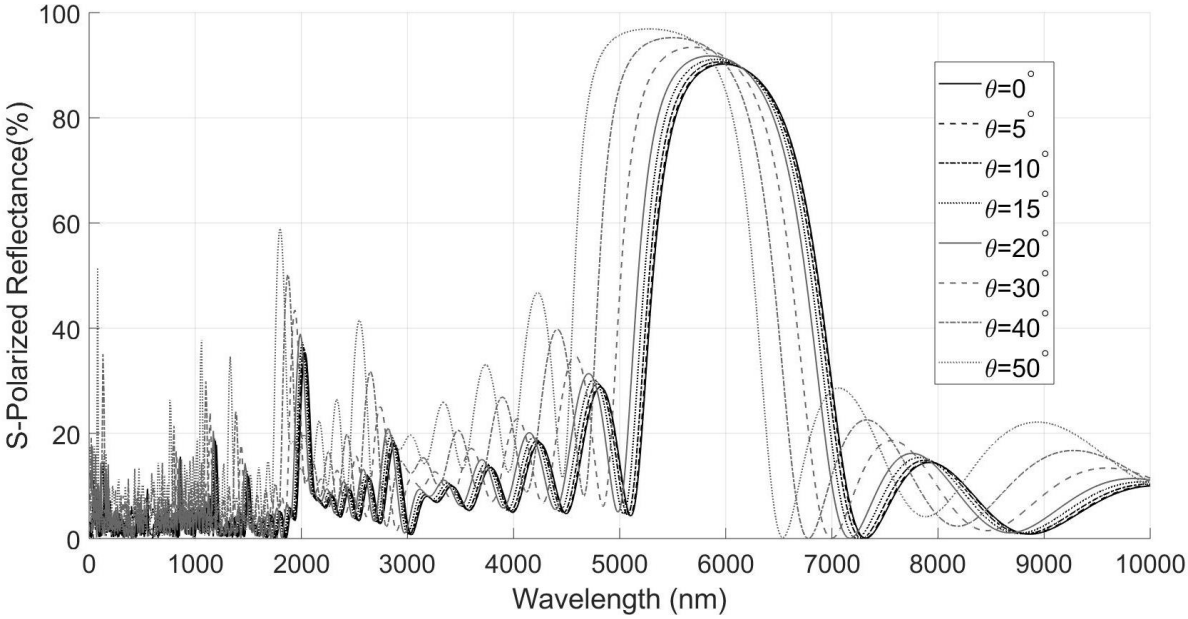

b.

Figure 4-4. Reflectance spectra for $[H_L L_L]^5$ comprised of alternating films with $n_H=2$ and $n_L=1.3$ with light incident from angles of 0, 5, 10, 15, 20, 30, 40, 50°

a. Considering P-polarized light with $W_{grin}=0.5\cdot(d_{L+H})$

b. Considering S-polarized light with $W_{grin}=0.5\cdot(d_{L+H})$

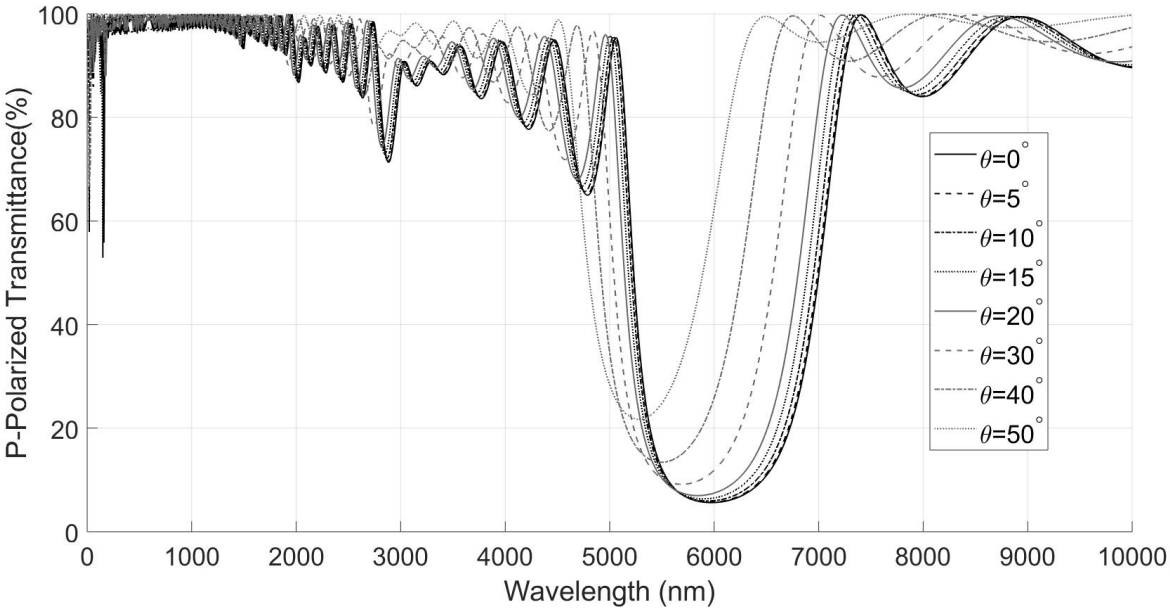

a.

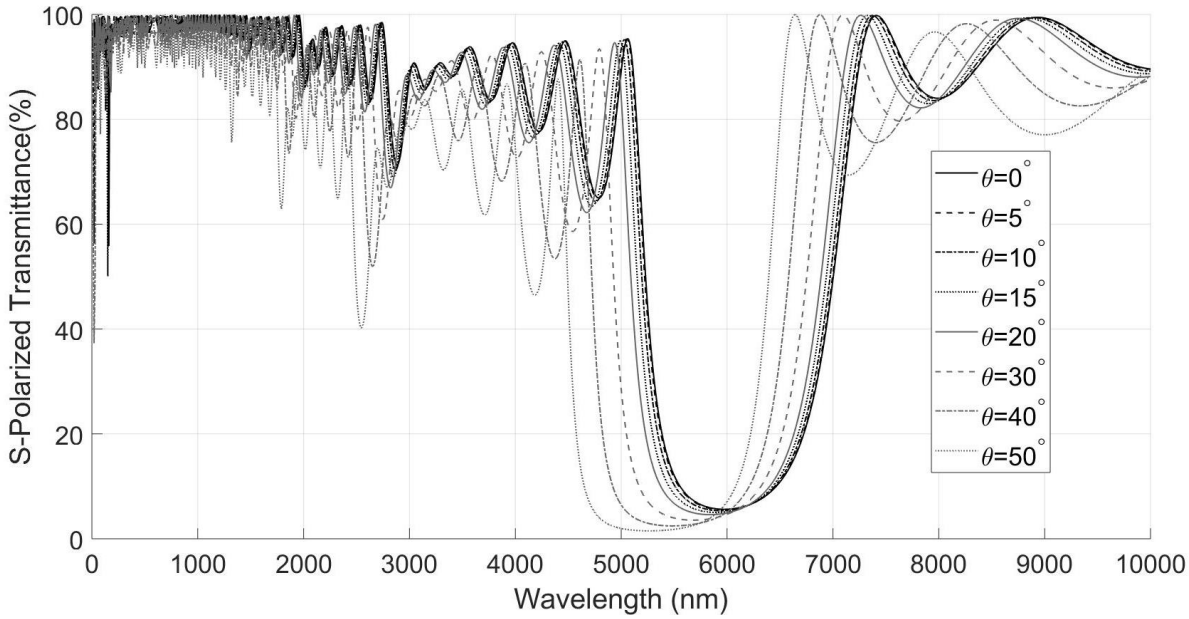

b.

Figure 4-5. Transmittance spectra for $[H_C L_C]^5$ comprised of two alternating films with n_H=2 and n_L=1.3 with light incident from angles of 0, 5, 10, 15, 20, 30, 40, and 50°

a. Considering P-polarized light with $W_{grin}=0.5\cdot(d_{L+H})$

b. Considering S-polarized light with $W_{grin}=0.5\cdot(d_{L+H})$

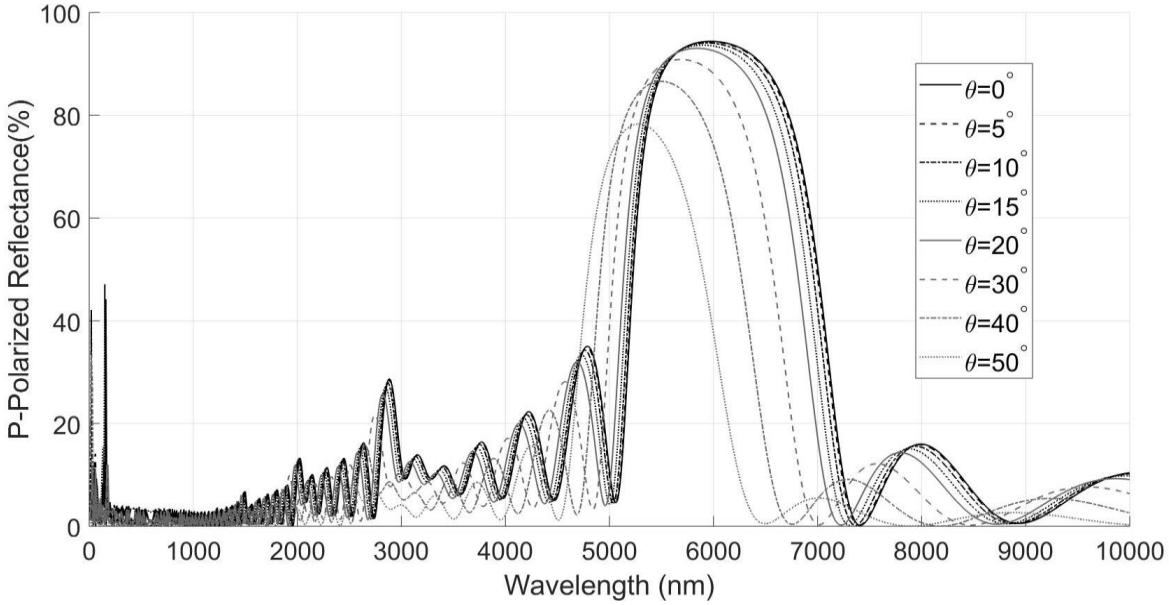

a.

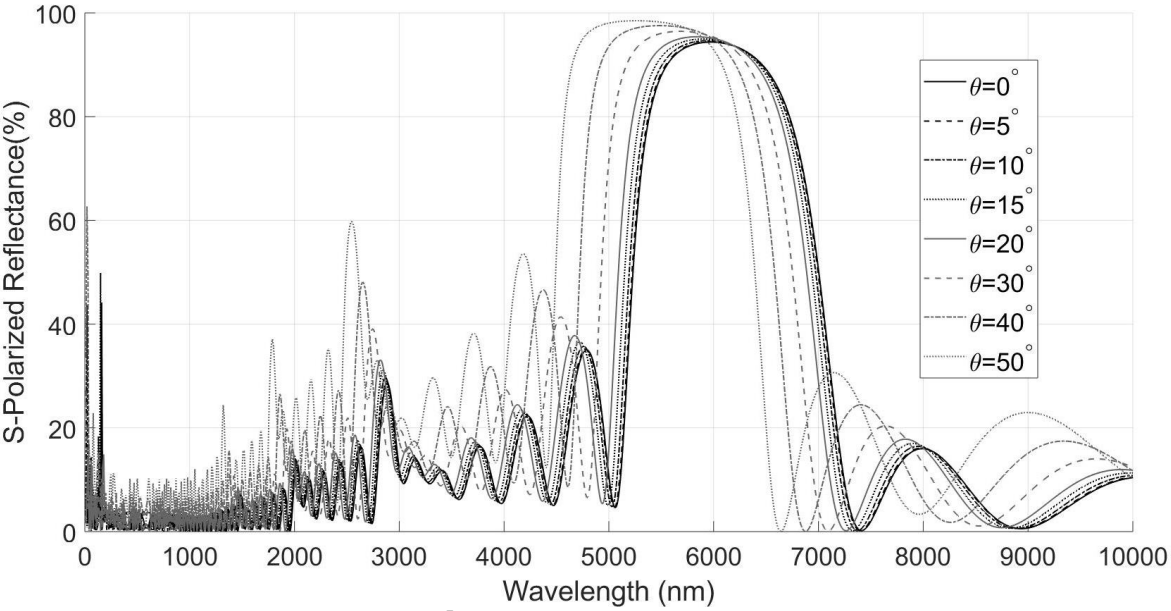

b.

Figure 4-6. Reflectance spectra for $[H_C L_C]^5$ comprised of alternating films with n_H=2 and n_L=1.3 with incident light from angles of 0, 5, 10, 15, 20, 30, 40, and 50°

a. Considering P-polarized light with $W_{grin}=0.5 \cdot (d_{L+H})$

b. Considering S-polarized light with $W_{grin}=0.5 \cdot (d_{L+H})$

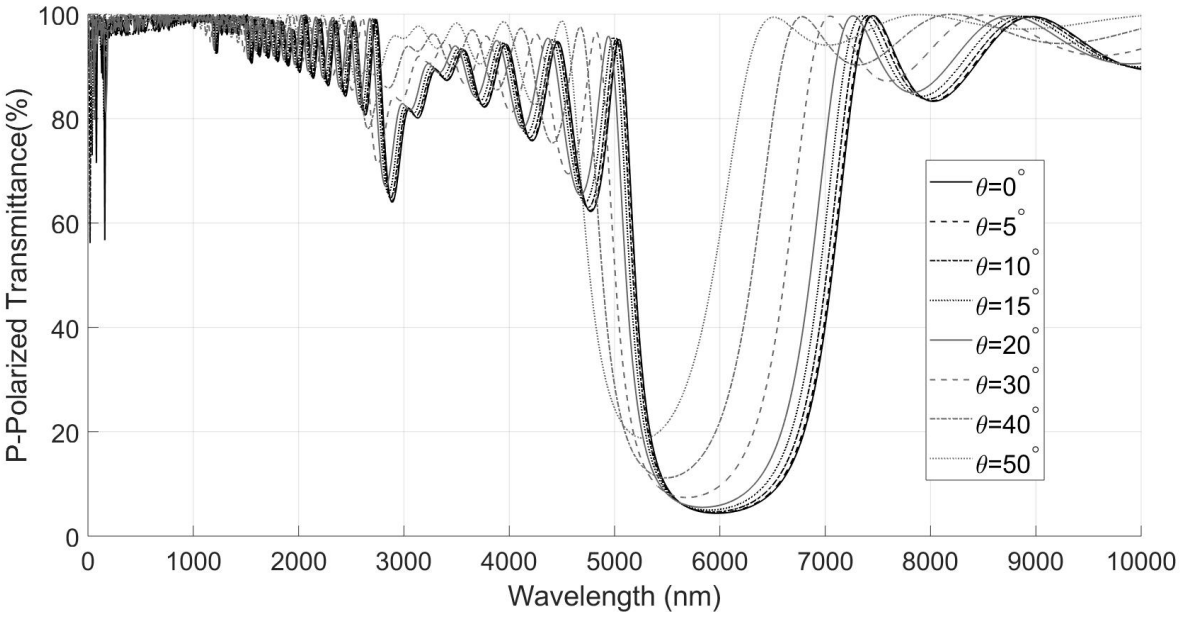

a.

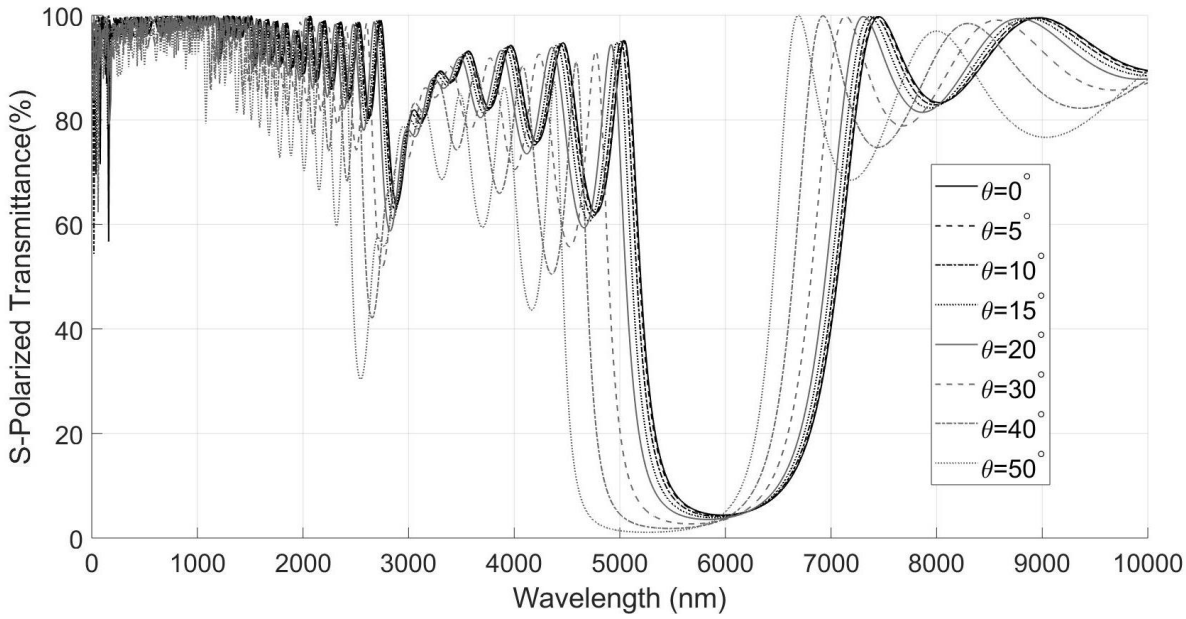

b.

Figure 4-7. Transmittance spectra for $[H_QL_Q]^5$ comprised of two alternating films with n_H=2 and n_L=1.3 with light incident from angles of 0, 5, 10, 15, 20, 30, 40, and 50°

a. Considering P-polarized light with $W_{grin}=0.5\cdot(d_{L+H})$

b. Considering S-polarized light with $W_{grin}=0.5\cdot(d_{L+H})$

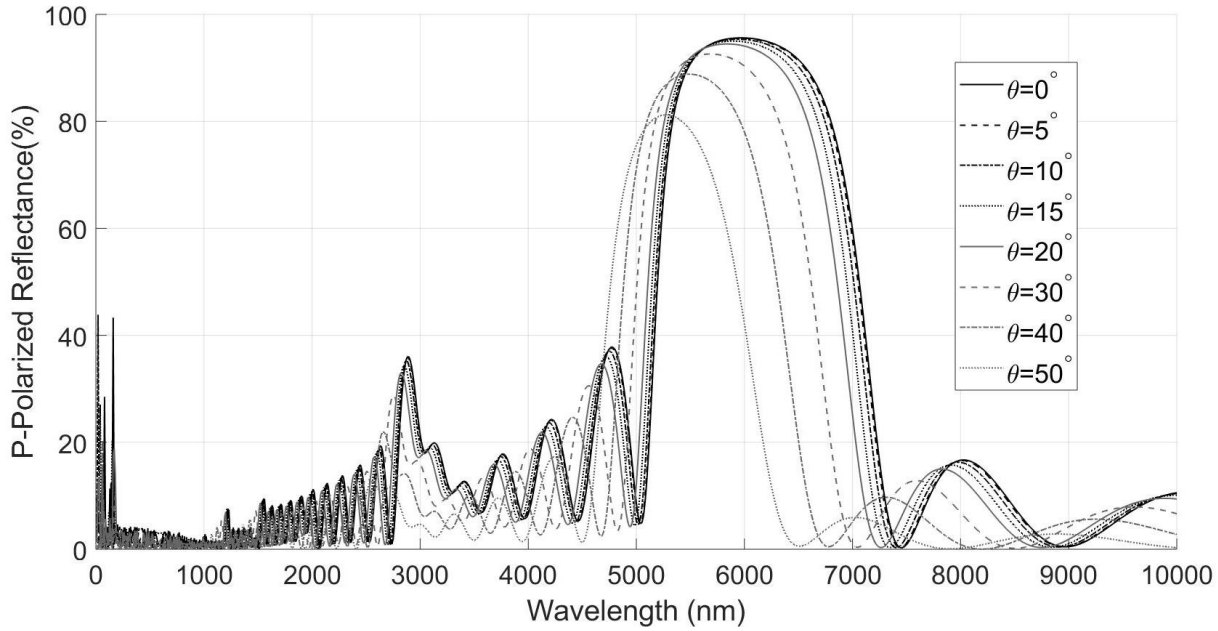

a.

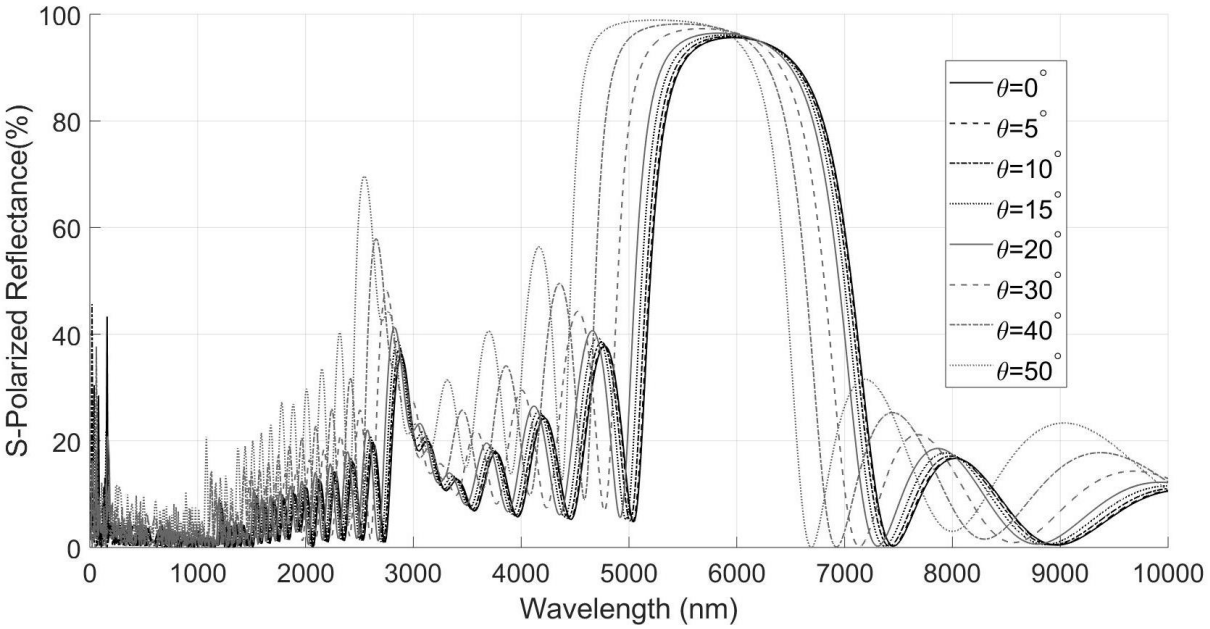

b.

Figure 4-8. Reflectance spectra for $[H_Q L_Q]^5$ comprised of two alternating films with n_H=2 and n_L=1.3 with light incident from angles of 0, 5, 10, 15, 20, 30, 40, and 50°

a. Considering P-polarized light with $W_{grin}=0.5\cdot(d_{L+H})$

b. Considering S-polarized light with $W_{grin}=0.5\cdot(d_{L+H})$

a.

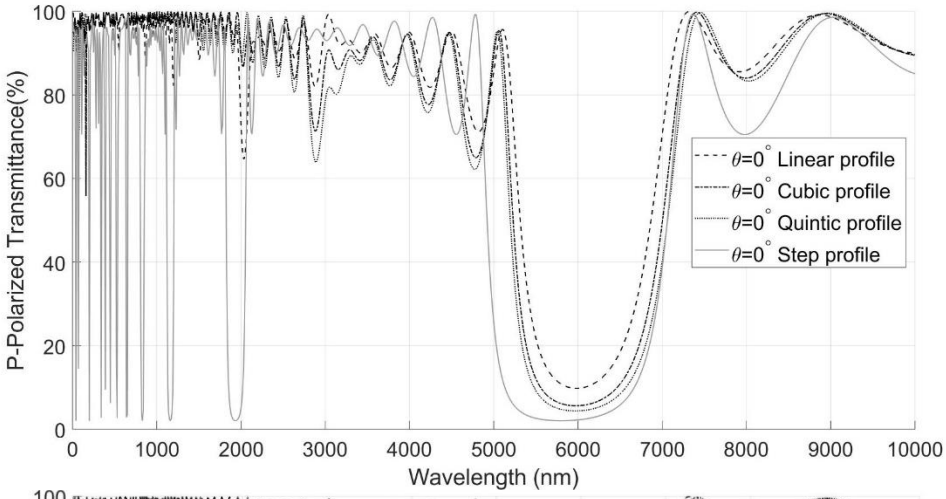

b.

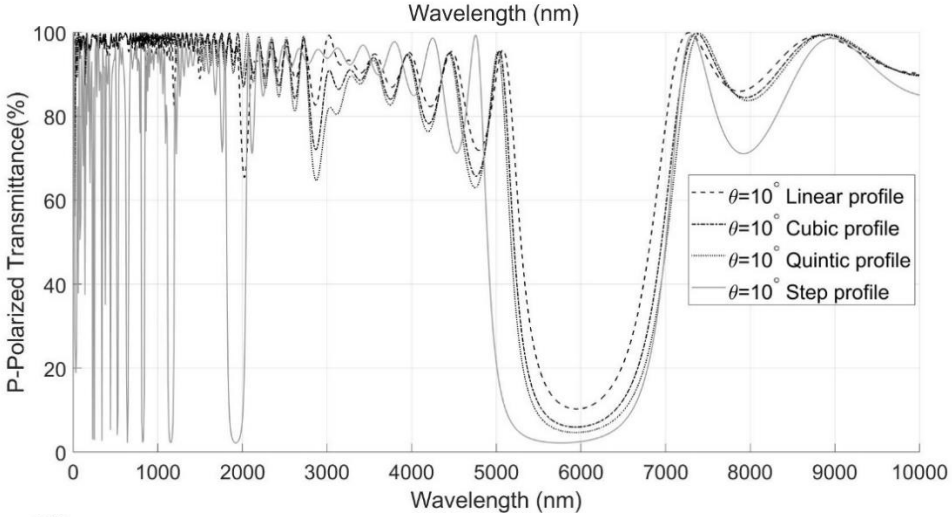

c.

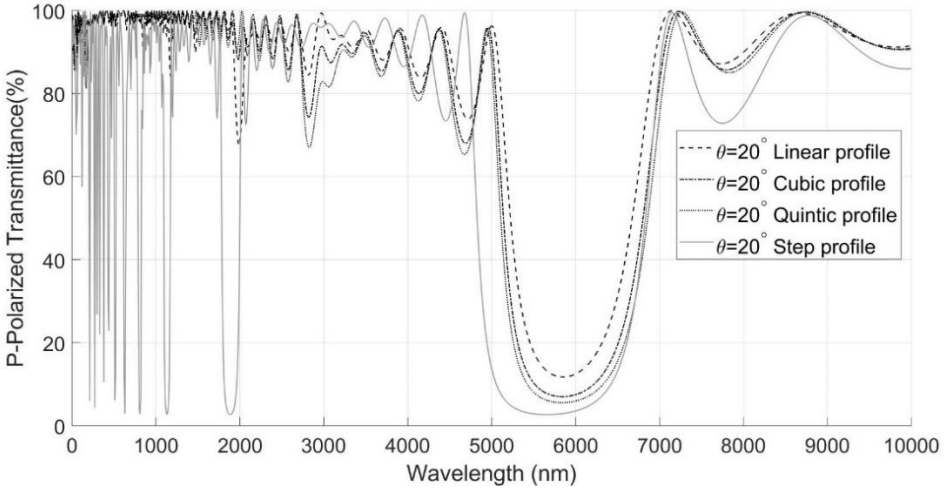

Figure 4-9. Transmittance spectra for $[HL]^5$, $[H_LL_L]^5$, $[H_CL_C]^5$ and $[H_QL_Q]^5$ comprised of alternating films with $n_H=2$ and $n_L=1.3$ with $W_{grin}=0.5\cdot(d_{L+H})$ for P-polarized light incident form angles of 0° (Figure a.), 10° (Figure b.) and 20° (Figure c.).

a.

b.

c.

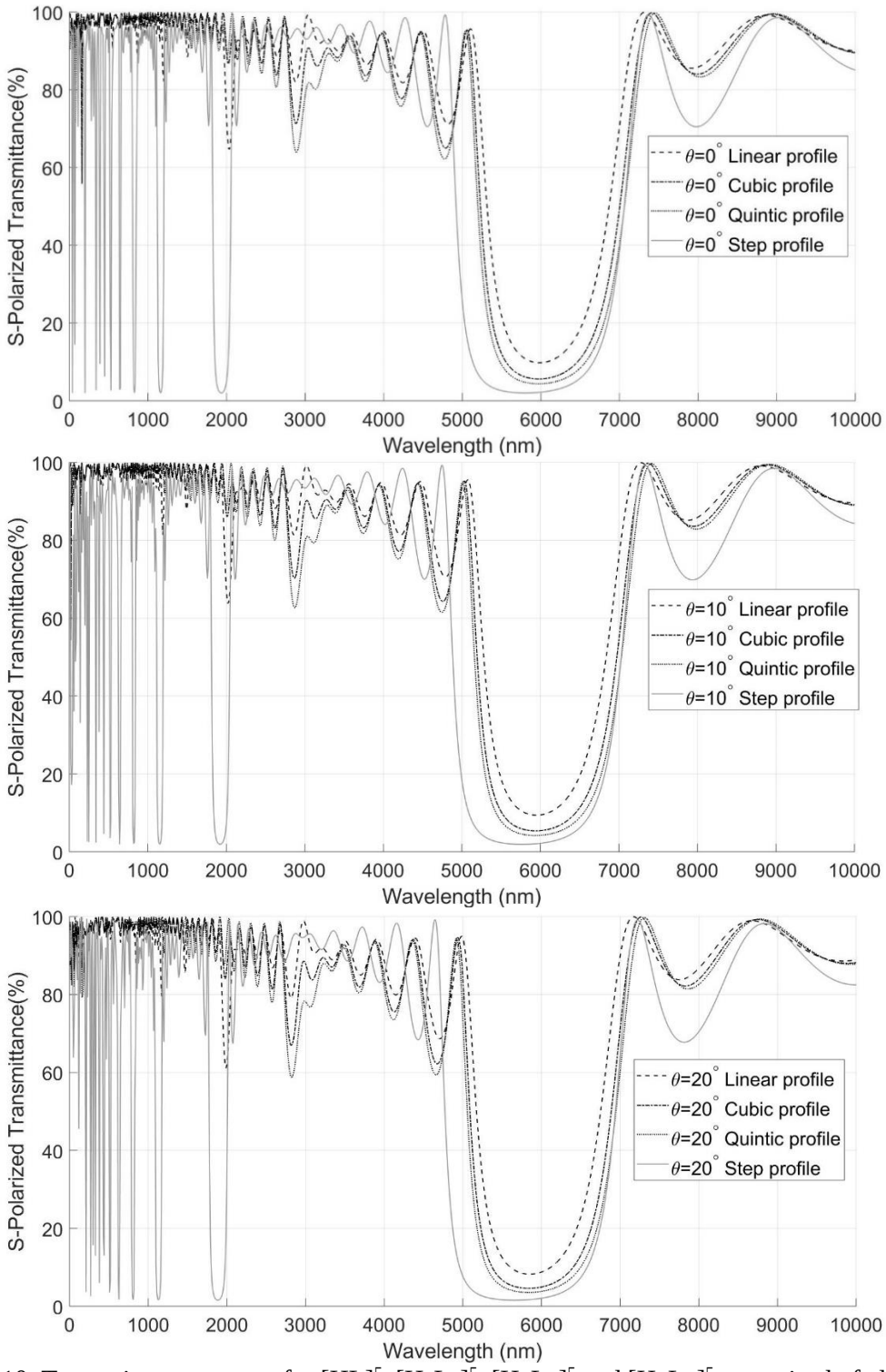

Figure 4-10. Transmittance spectra for $[HL]^5$, $[H_LL_L]^5$, $[H_CL_C]^5$ and $[H_QL_Q]^5$ comprised of alternating films with $n_H=2$ and $n_L=1.3$ with $W_{grin}=0.5\cdot(d_{L+H})$ for S-polarized light incident from angles of 0° (Figure a.), 10° (Figure b.) and 20° (Figure c.).

a.

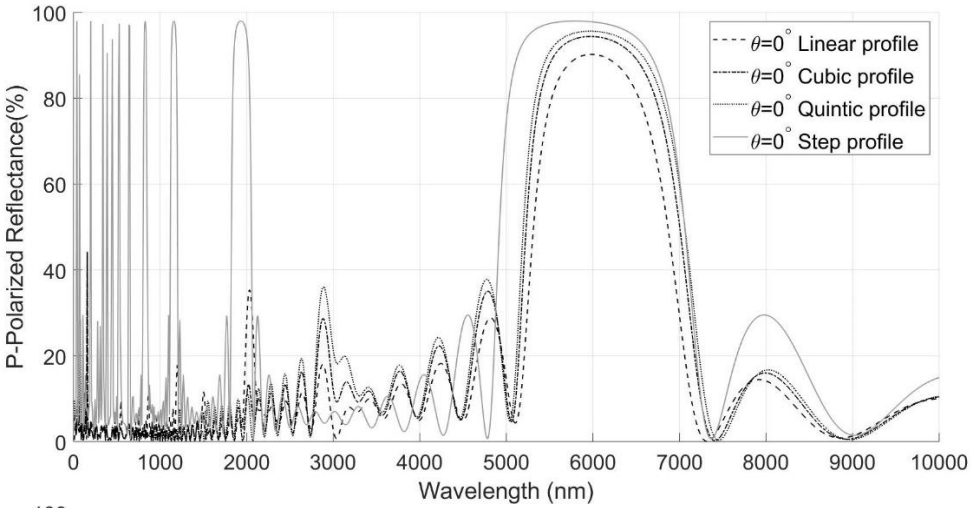

b.

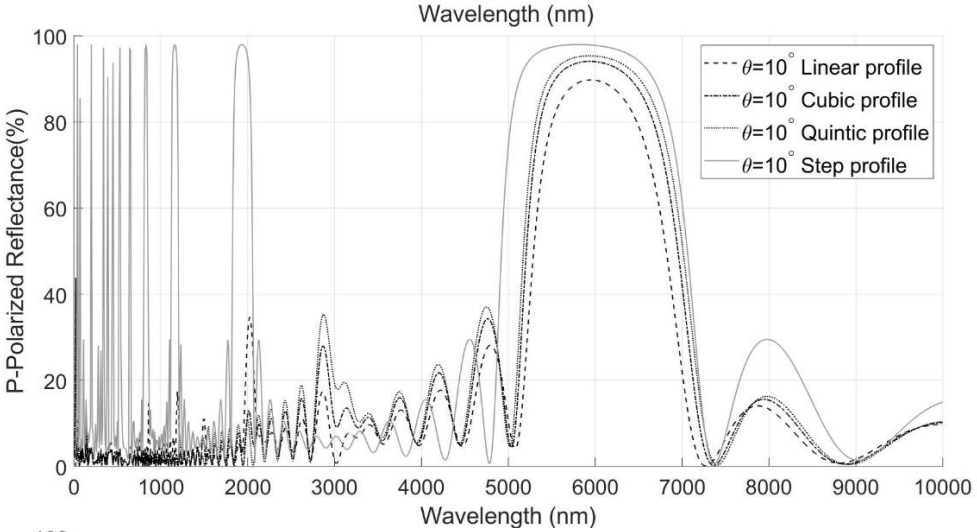

c.

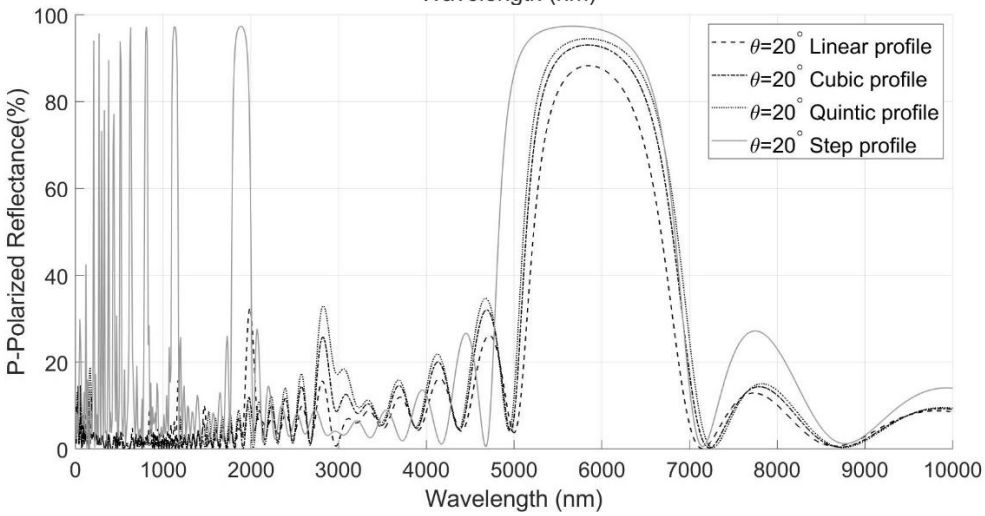

Figure 4-11. Reflectance spectra for $[HL]^5$, $[H_LL_L]^5$, $[H_CL_C]^5$ and $[H_QL_Q]^5$ comprised of alternating films with $n_H=2$ and $n_L=1.3$ with $W_{grin}=0.5\cdot(d_{L+H})$ for P-polarized light incident from angles of 0° (Figure a.), 10° (Figure b.) and 20° (Figure c.).

a.

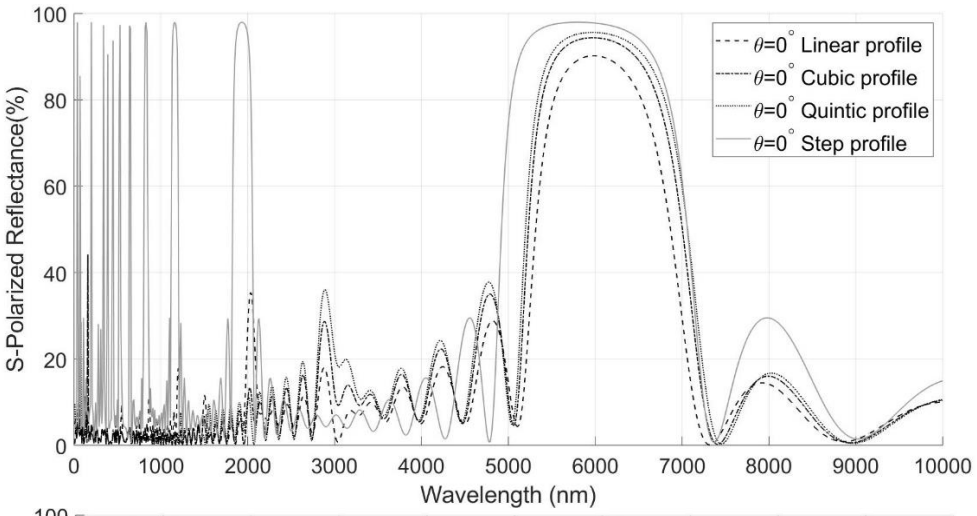

b.

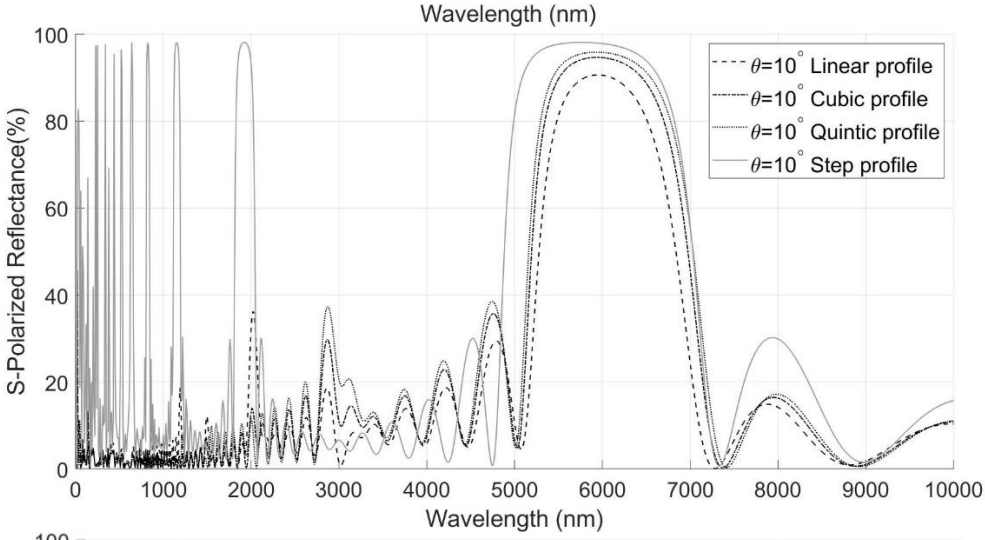

c.

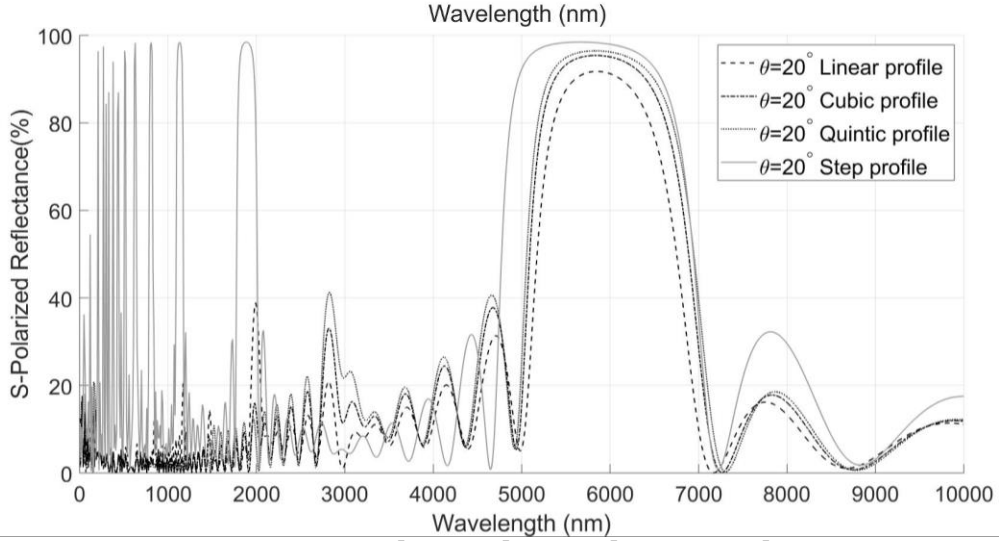

Figure 4-12. Reflectance spectra for $[HL]^5$, $[H_LL_L]^5$, $[H_CL_C]^5$ and $[H_QL_Q]^5$ comprised of alternating films with $n_H=2$ and $n_L=1.3$ with $W_{grin}=0.5\cdot(d_{L+H})$ for S-polarized light incident from angles of 0° (Figure a.), 10° (Figure b.) and 20° (Figure c.).

a.

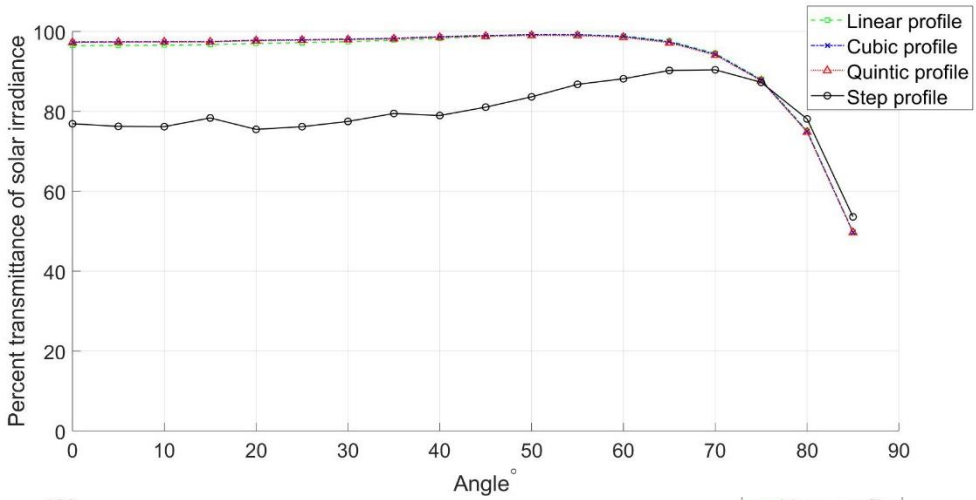

b.

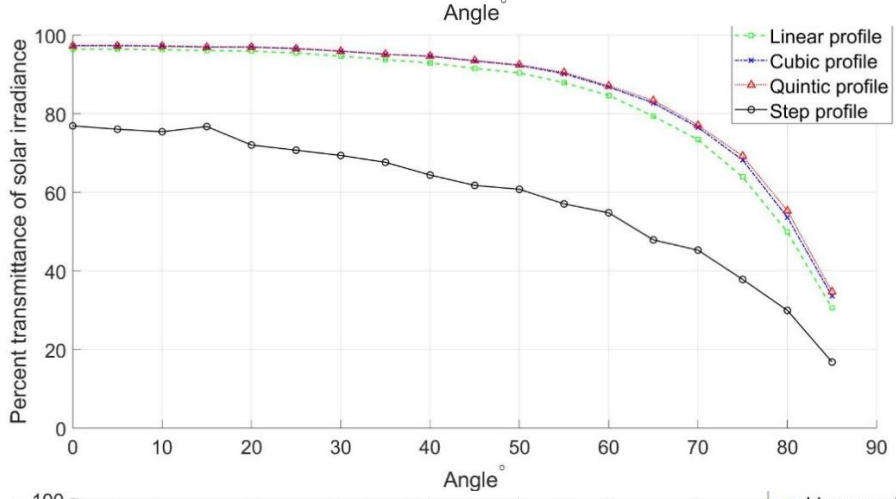

c.

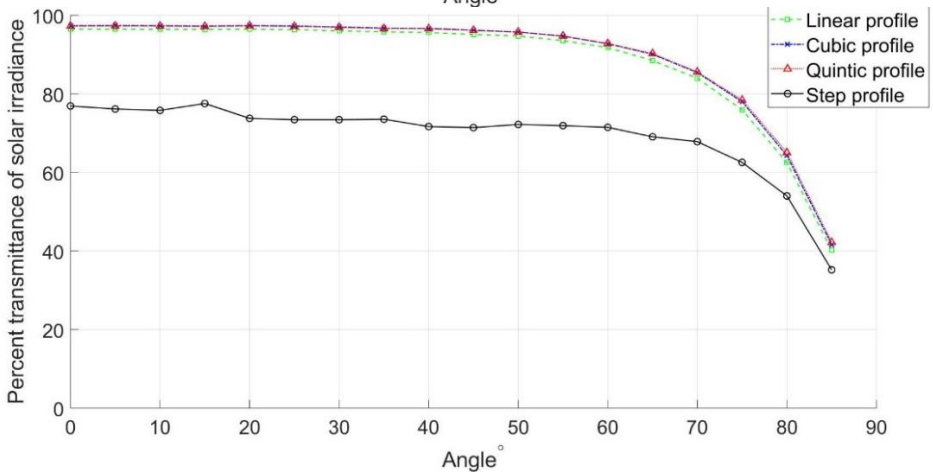

Figure 4-13. Percent transmittance of the solar irradiance through $[HL]^5$, $[H_LL_L]^5$, $[H_CL_C]^5$ and $[H_QL_Q]^5$ comprised of two alternating films with $n_H=2$ and $n_L=1.3$ with $W_{grin}=0.5\cdot(d_{L+H})$ for P-polarized light (Figure a.), S-polarized light (Figure. b) and half P-polarized and half S-polarized light (Figure c.).

a.

b.

c.

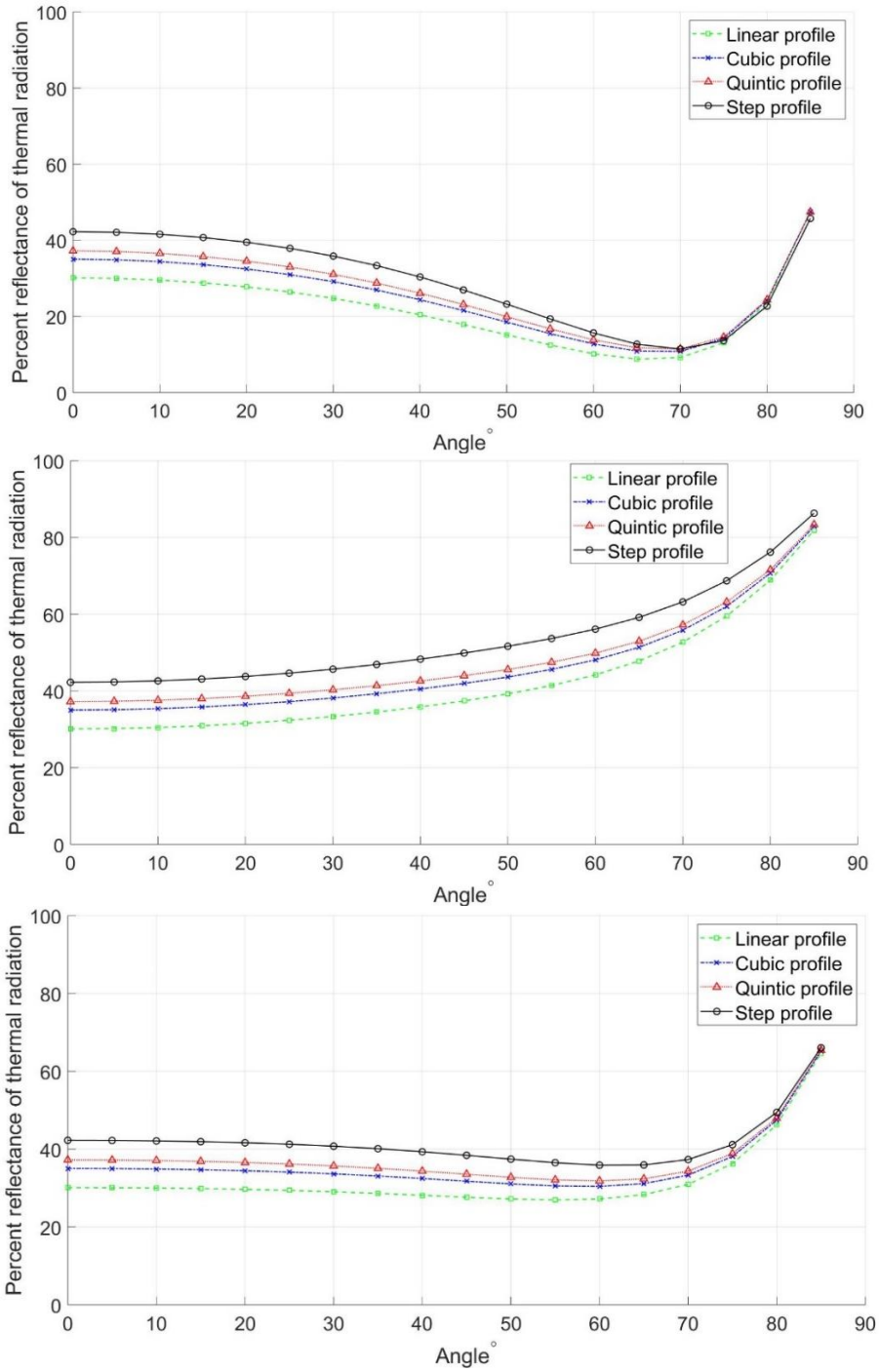

Figure 4-14. Percent reflection of the radiation spectrum emitted from a blackbody at T= 500K plotted as a function of incident angle for $[HL]^5$, $[H_LL_L]^5$, $[H_CL_C]^5$ and $[H_QL_Q]^5$ comprised of two alternating films with n_H=2 and n_L=1.3 with $W_{grin}=0.5\cdot(d_{L+H})$ for P-polarized light (Figure a.), S-polarized light (Figure. b) and half P-polarized and half S-polarized light (Figure c.).

4-2. Effects of altering the number of layers within transparent dielectric heat mirrors on their performance

In the previous section the performance of different dielectric mirrors with five bi-layers, denoted as $[HL]^5$, $[H_LL_L]^5$, $[H_CL_C]^5$ and $[H_QL_Q]^5$, with alternating films with refractive indices equal to 2 and 1.3, were considered. In this section, the transmittance and reflectance spectra of similar dielectric mirrors, but with 10, 15, and 20 bi-layers are calculated and plotted to investigate the performance of the dielectric mirrors as a function of the number of layers they are comprised of. Accordingly, the transmittance and reflectance spectra, as well as the radiation spectra emitted from a blackbody at T = 500 K that is transmitted through different dielectric mirrors with $W_{grin}=0.5\cdot(d_{L+H})$ are presented in Figure 4-15 through Figure 4-28. Also, the percent of solar radiation transmitted through the dielectric mirror and the percentage of radiation emitted from a blackbody at T = 500 K that is reflected by the dielectric mirrors are studied and compared for each case considering different values of W_{grin} of $[0, 0.1, 0.2, 0.3, 0.4, 0.5]\cdot(d_{L+H})$.

Figure 4-15 and Figure 4-16 show transmittance and reflectance spectra for $[HL]^5$, $[H_LL_L]^5$, $[H_CL_C]^5$, $[H_QL_Q]^5$, $[HL]^{20}$, $[H_LL_L]^{20}$, $[H_CL_C]^{20}$ and $[H_QL_Q]^{20}$ with $W_{grin}=0.5\cdot(d_{L+H})$. As can be seen in Figure 4-16, for the reflectance spectra, by increasing the number of layers, the FWHM of the reflection peak decreases from 1,550 nm, 1,770 nm, 1,870 nm and 2,140 nm for $[H_LL_L]^5$, $[H_CL_C]^5$, $[H_QL_Q]^5$ and $[HL]^5$ to 1,180 nm, 1,370 nm,1,460 nm and 1,680 nm for $[H_LL_L]^{20}$, $[H_CL_C]^{20}$, $[H_QL_Q]^{20}$ and $[HL]^{20}$, respectively. This is while, the corresponding maximum peak reflection values increase from 90.2%, 94.4% and 95.53% and 97.93 for $[H_LL_L]^5$, $[H_CL_C]^5$ and $[H_QL_Q]^5$, $[HL]^5$ to 100.00% for $[H_LL_L]^{20}$, $[H_CL_C]^{20}$, $[H_QL_Q]^{20}$ and $[HL]^{20}$, respectively. Accordingly, a general note here is that by increasing the number of layers the FWHM decreases and the maximum peak reflection increases.

Figure 4-17 depicts the solar spectrum and the amount of solar power transmitted through $[HL]^5$, $[H_LL_L]^5$, $[H_CL_C]^5$ and $[H_QL_Q]^5$ (Figure. a) and through $[HL]^{20}$, $[H_LL_L]^{20}$, $[H_CL_C]^{20}$ and $[H_QL_Q]^{20}$ (Figure. b) for $W_{grin}=0.5\cdot(d_{L+H})$. Figure 4-19 shows the percent transmittance of the solar irradiance with 5, 10, 15 and 20 bi-layers comprised of two films with $n_H=2$ and $n_L=1.3$ as a function of W_{grin} for step, linear, cubic and quintic profiles. With respect to Figure 4-17 and Figure 4-19, the general trend here is that by increasing the number of layers less solar radiation will be transmitted by different dielectric mirrors. As can be seen, by increasing the number of layers to 15 or greater, the results do not show a significant difference in the transmittance and reflectance spectra of the dielectric mirror.

Figure 4-18 shows the blackbody radiation spectra at T=500 K and the amount of spectral power reflected by $[HL]^5$, $[H_LL_L]^5$, $[H_CL_C]^5$ and $[H_QL_Q]^5$ (Figure. a) and $[HL]^{20}$, $[H_LL_L]^{20}$, $[H_CL_C]^{20}$ and $[H_QL_Q]^{20}$ (Figure. b) with $W_{grin}=0.5\cdot(d_{L+H})$. With respect to Figure 4-20 which illustrates the summation of the portion of blackbody irradiance reflected by $[HL]^5$, $[H_LL_L]^5$, $[H_CL_C]^5$ and $[H_QL_Q]^5$ with $W_{grin}=0$ to $W_{grin}=0.5\cdot(d_{L+H})$, increasing the number of layers increases the summation. Accordingly, for $[HL]^5$ the percent reflection of the radiation spectrum emitted from the blackbody at T= 500K is equal to ~ 42 % and for $[HL]^{10}$, $[HL]^{15}$ and $[HL]^{20}$ the percent reflection slightly increases to ~ 43 %. For $[H_LL_L]^5$ the percent reflection of the radiation spectrum emitted from the blackbody at T= 500K is equal to ~ 30 % and for $[H_LL_L]^{10}$, $[H_LL_L]^{15}$ and $[H_LL_L]^{20}$ the percent reflection slightly increases to ~ 32 %. For $[H_CL_C]^5$ the percent reflection of the radiation spectrum emitted from the blackbody at T= 500K is equal to ~ 35 % and for $[H_CL_C]^{10}$, $[H_CL_C]^{15}$ and $[H_CL_C]^{20}$ the percent reflection slightly increases to ~ 37 %. Finally, for $[H_CL_C]^5$ the percent reflection of the radiation spectrum emitted from the blackbody at T= 500K is equal to ~ 37 % and for $[H_CL_C]^{10}$, $[H_CL_C]^{15}$ and $[H_CL_C]^{20}$ the percent reflection slightly increases to ~ 39 %.

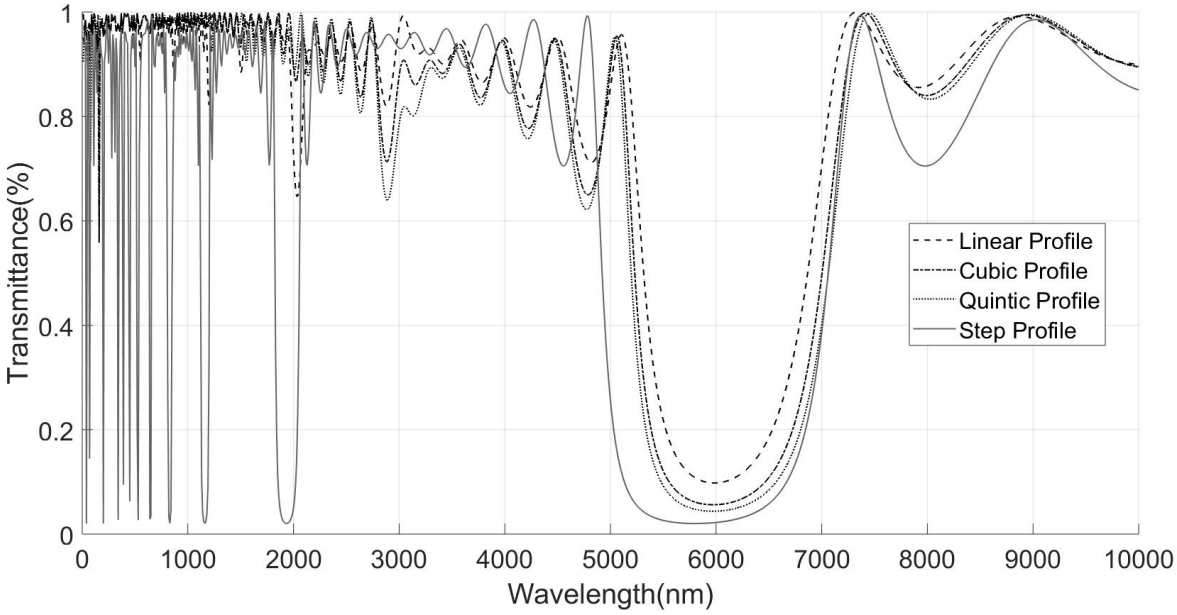

a.

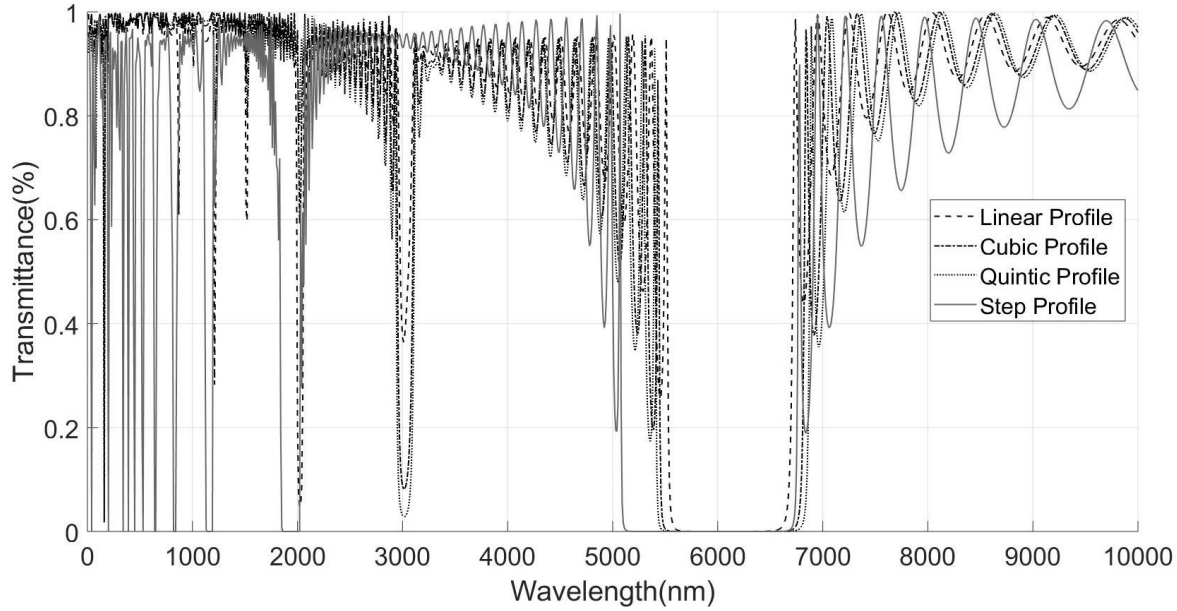

b.

Figure 4-15. Transmittance spectra for $[HL]^5$, $[H_LL_L]^5$, $[H_CL_C]^5$ and $[H_QL_Q]^5$ (Figure a.) and $[HL]^{20}$, $[H_LL_L]^{20}$, $[H_CL_C]^{20}$ and $[H_QL_Q]^{20}$ (Figure b.) with $W_{grin}=0.5\cdot(d_{L+H})$ comprised of two alternating films with $n_H=2$ and $n_L=1.3$.

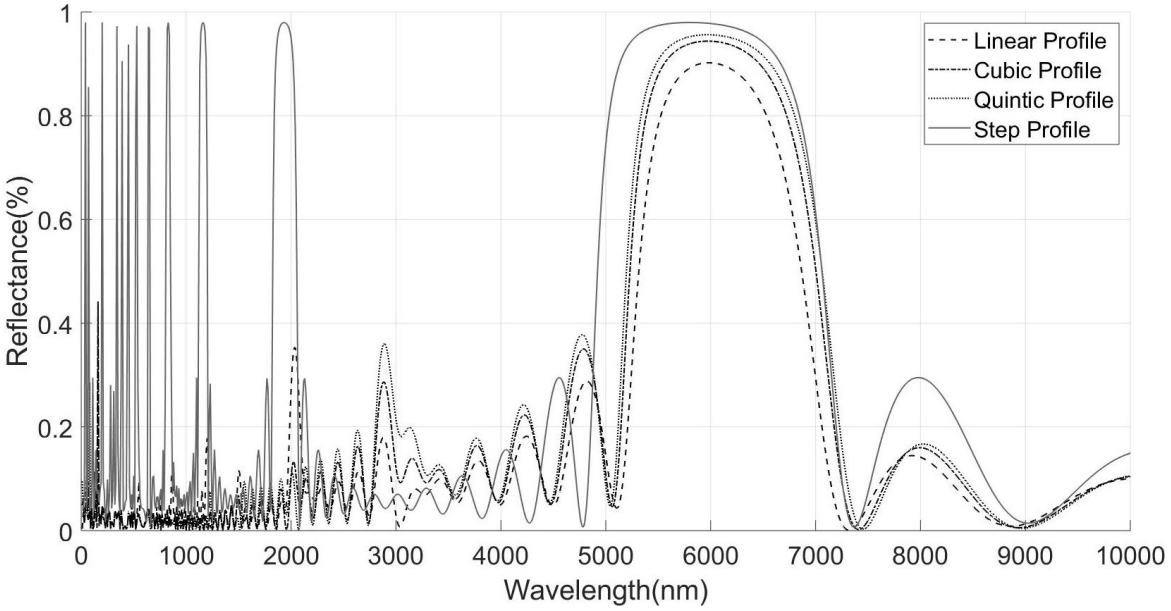

a.

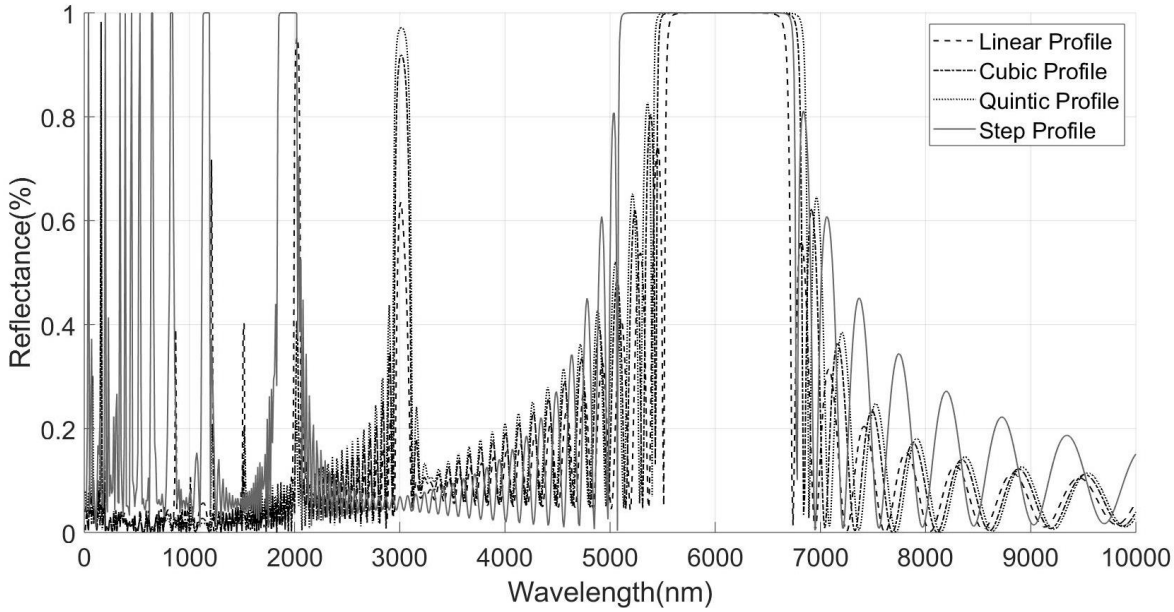

b.

Figure 4-16. Reflectance spectra for $[HL]^5$, $[H_LL_L]^5$, $[H_CL_C]^5$ and $[H_QL_Q]^5$ (Figure a.) and $[HL]^{20}$, $[H_LL_L]^{20}$, $[H_CL_C]^{20}$ and $[H_QL_Q]^{20}$ (Figure b.) with $W_{grin}=0.5\cdot(d_{L+H})$ comprised of two alternating films with $n_H=2$ and $n_L=1.3$

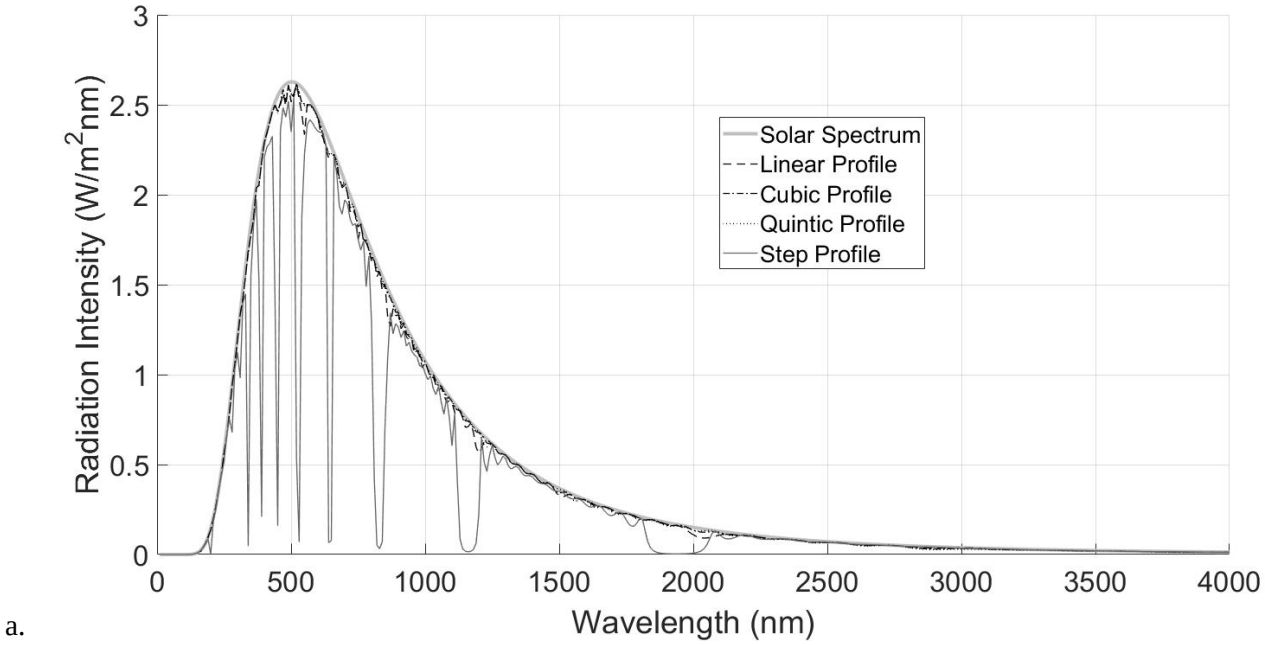

a.

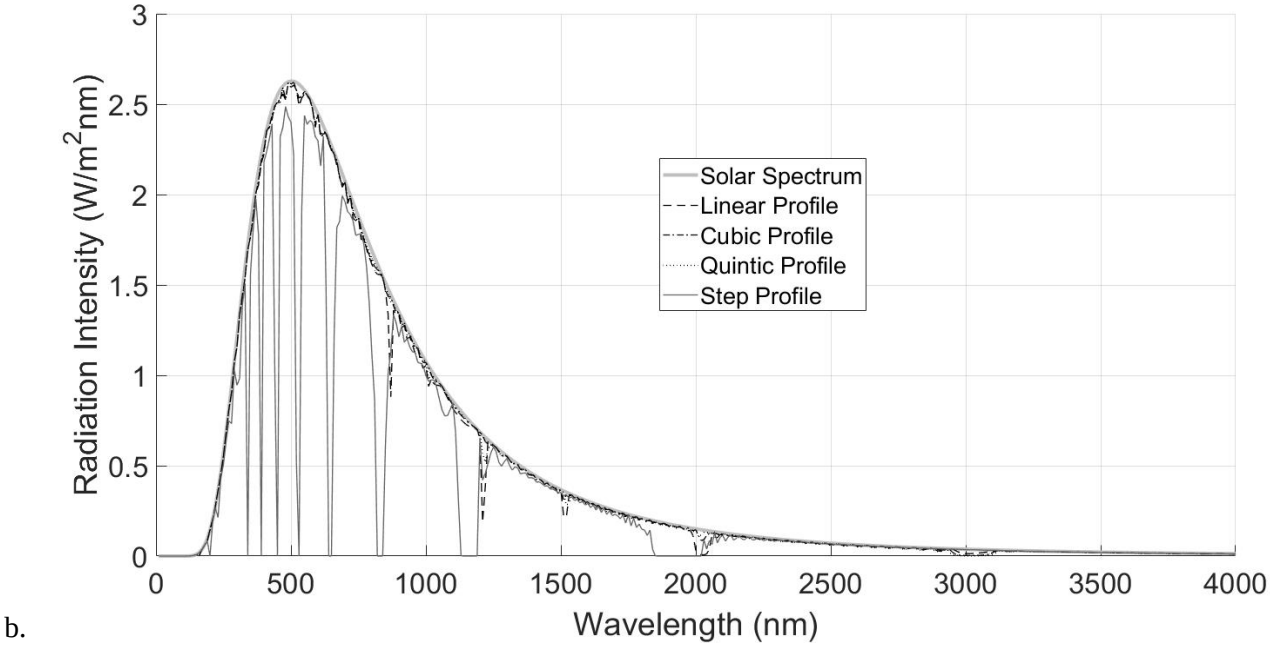

b.

Figure 4-17. Solar irradiance (the solar spectrum is approximated by the radiation emitted from a blackbody at a temperature of 5700 K) and the amount of spectral power transmitted through $[HL]^5$, $[H_LL_L]^5$, $[H_CL_C]^5$ and $[H_QL_Q]^5$ (Figure a.) and through $[HL]^{20}$, $[H_LL_L]^{20}$, $[H_CL_C]^{20}$ and $[H_QL_Q]^{20}$ (Figure b.) with $W_{grin}=0.5\cdot(d_{L+H})$ comprised of two alternating films with $n_H=2$ and $n_L=1.3$.

a.

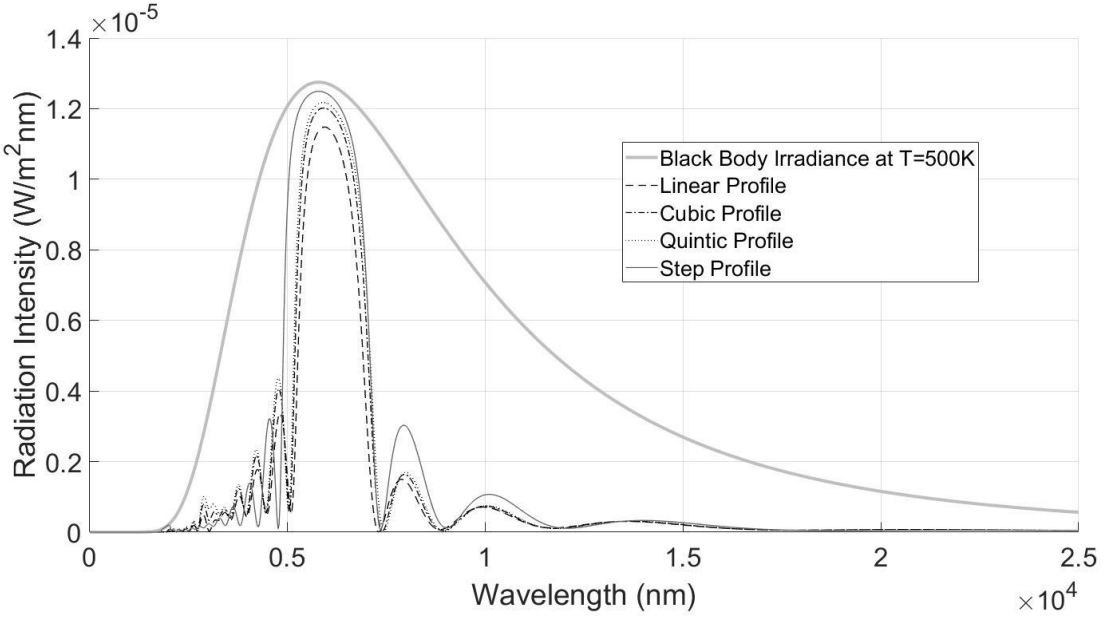

b.

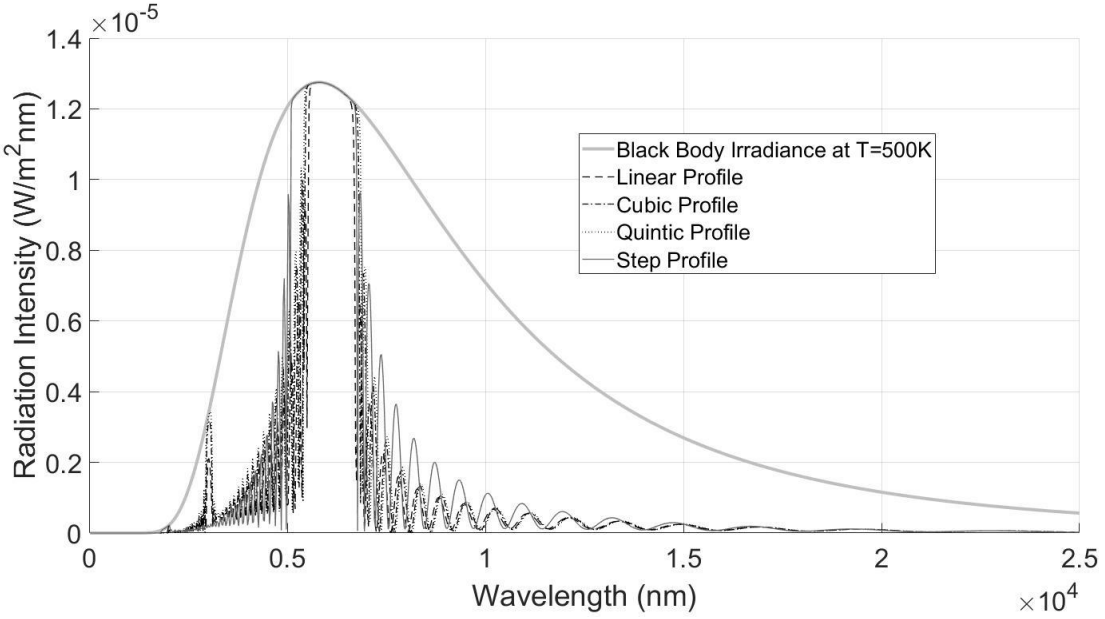

Figure 4-18. Blackbody radiation spectrum at a temperature of 500 K and the amount of spectral power reflected by $[HL]^5$, $[H_LL_L]^5$, $[H_CL_C]^5$ and $[H_QL_Q]^5$ (Figure a.) and by $[HL]^{20}$, $[H_LL_L]^{20}$, $[H_CL_C]^{20}$ and $[H_QL_Q]^{20}$ (Figure b.) with $W_{grin}=0.5\cdot(d_{L+H})$ comprised of two alternating films with $n_H=2$ and $n_L=1.3$.

a.

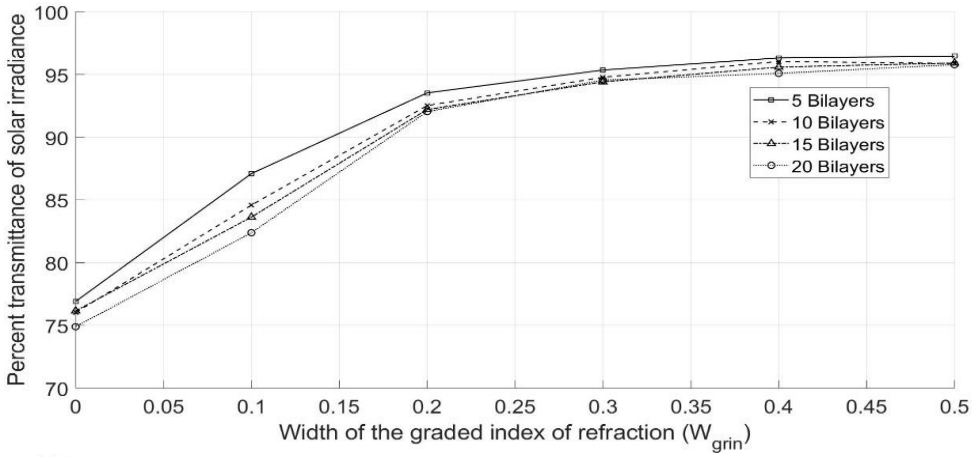

b.

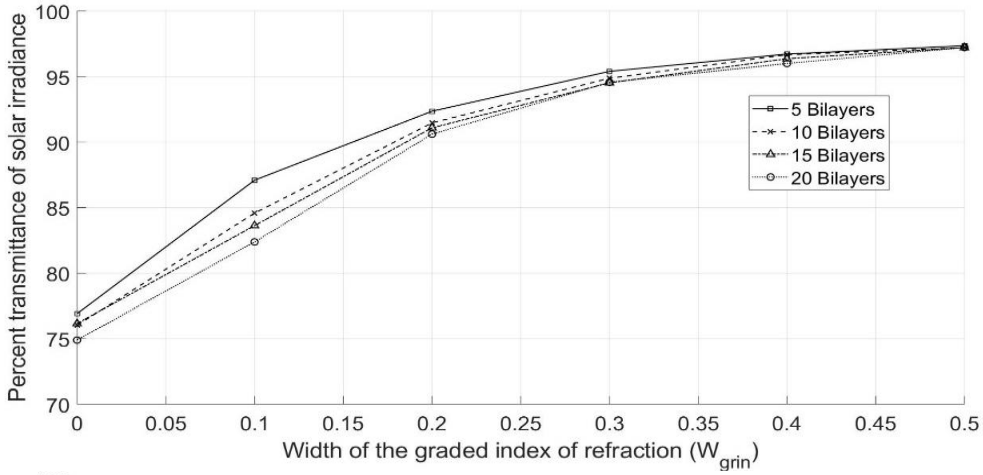

c.

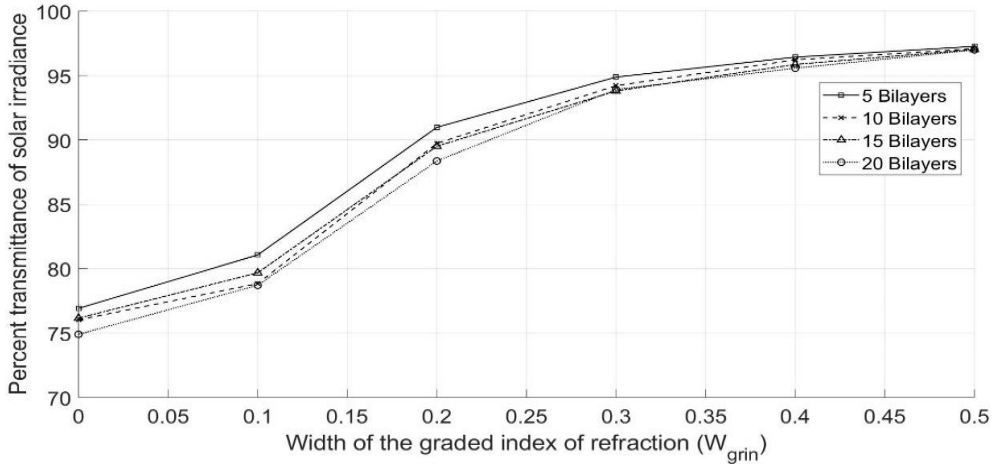

Figure 4-19. Percent transmittance of the solar irradiance with 5, 10, 15 and 20 bi-layers comprised of two films with n_H=2 and n_L=1.3 plotted as a function of W_{grin} for step, linear, cubic and quintic profiles.

a.

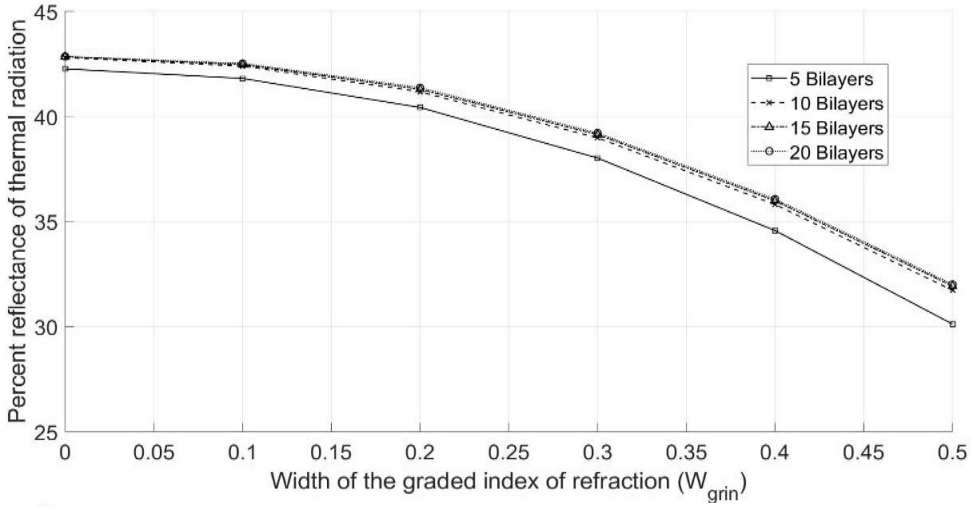

b.

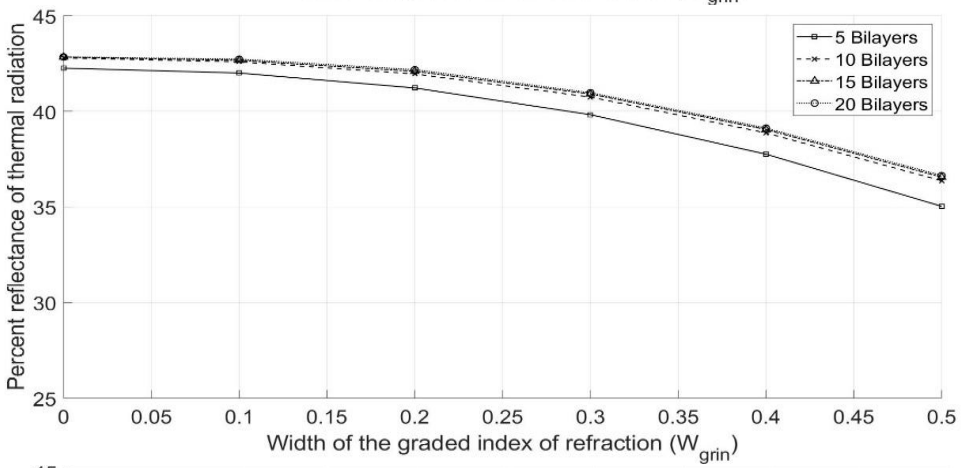

c.

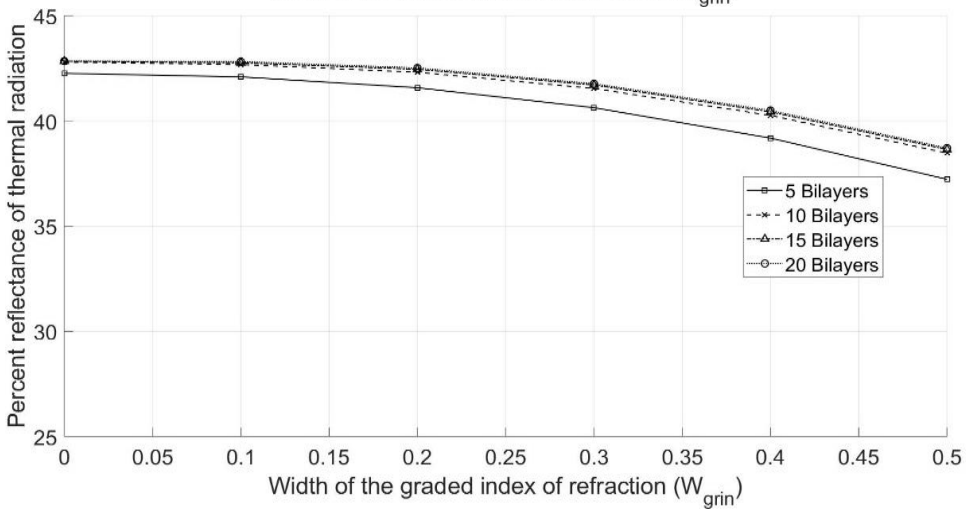

Figure 4-20. Percent reflection of the radiation spectrum emitted from a blackbody at T= 500K with 5, 10, 15 and 20 bilayers comprised of two films with n_H=2 and n_L=1.3 plotted as a function of W_{grin} for linear (Figure a), cubic (Figure b) and quintic (Figure c) profiles.

4-3. Performance dependence of the dielectric mirrors on the resolution of their refractive index profiles

In this section sensitivity analysis has been carried out for dielectric mirrors with graded refractive index profiles at their internal interfaces. However, from a practical standpoint, it would be very difficult to precisely fabricate the linear, cubic, and quintic graded index profiles throughout the dielectric mirror. The main reason is that, as described in Chapter 2, it is difficult to control the continuous change of the refractive index profile over the large number of periods in the dielectric mirror. It may be more practical to fabricate a graded refractive index profile in a layer by layer fashion. Thus, in this section the performance dependence of the dielectric heat mirrors on the resolution of their refractive index profiles is investigated.

Herein the resolution of the graded index of refraction profiles is defined as $W^* = W_{grin}/\Delta W$, where W_{grin} is set to be equal to $0.5\cdot(d_{L+H})$ and ΔW is the distance over which the index of refraction is constant. For results presented in previous sections calculations were performed using a refractive index profile resolution of $W^* = 20$. That is, as shown in Figure 4-21, $\Delta W = 0.05\cdot W_{grin}$, and the graded refractive index profile increased from the value of 1.3 at the L layer to 2 at the H layer over 20 discrete steps.

In this section the effects of changing the refractive index profile resolution on the reflectance and transmittance spectra of the dielectric mirror are investigated. The width of the H and L layers within the dielectric mirror are 725 nm and 1,154 nm, respectively, and linear, cubic and quintic interfacial refractive index profiles are considered.

The resolution of the index of refraction profile is varied and set to the values $W^* = 1$, 3, 5, 10, 20, 50, and 100. The results are provided in Figure 4-22 through Figure 4-29.

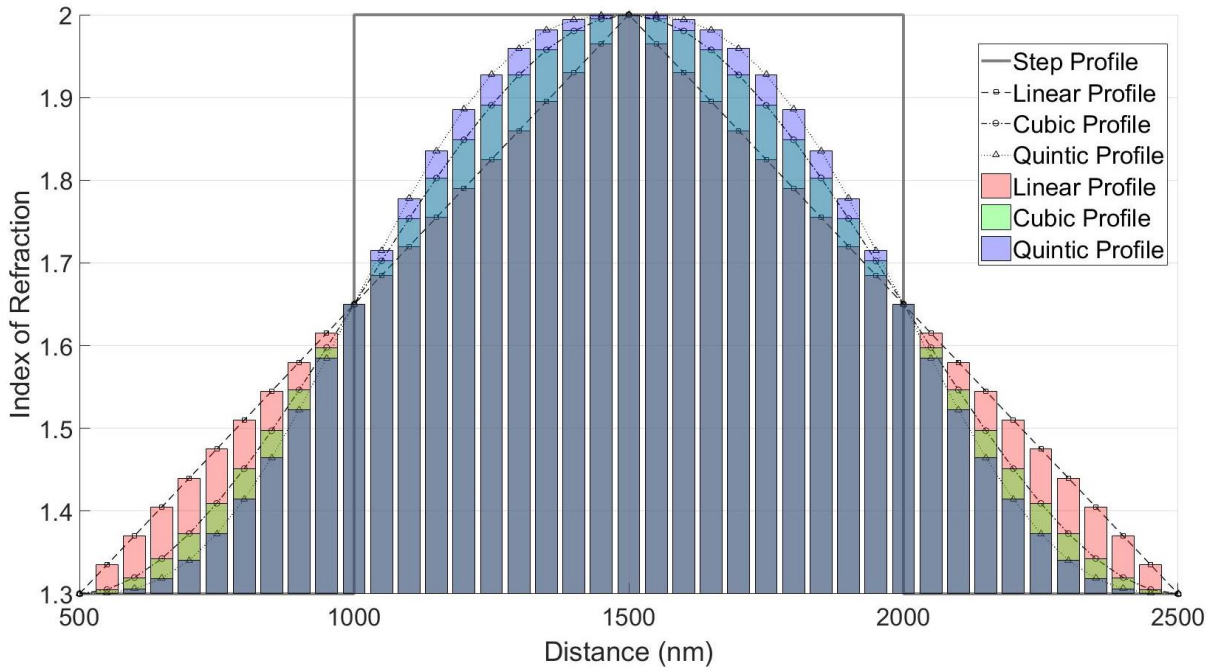

Figure 4-21. Schematic diagram for a [LHL] stack with the graded refractive index profile increased from the value of 1.3 at the L layer to 2 at the H layer over 20 discrete steps ($\Delta W = 0.05 \cdot W_{grin}$)

Figure 4-22 and Figure 4-24 show the transmittance spectra for the dielectric mirror design with W* = 3, 10 and 100 and $W_{grin}=0.5\cdot(d_{L+H})$. Figure 4-23 and Figure 4-25 show the reflectance spectra for the dielectric mirror design with W* = 3, 10 and 100 and $W_{grin}=0.5\cdot(d_{L+H})$. As can be seen, by increasing W* from 3 to 100, the FWHM of the reflection peak for the case of linear, cubic and quintic refractive index profiles decreases from 1,820 nm, 1,870 nm and 1,910 nm for W*=3 to 1,510 nm, 1,570 nm, and 1,845 nm for W*=100, respectively. Also, the corresponding maximum peak reflection values decrease from ~94.6%, 95.6% and 96.1% for W* = 3 to ~89% for the linear profile, ~94% for the cubic profile and ~95.4 for the quintic profile. Accordingly, a general note here is that increasing W* will result in a decrease of both the FWHM and the maximum peak reflection. With respect to the results from Figure 4-22 to Figure 4-25, he resolution of the index of refraction profile has the greatest effect on the linear index of refraction profile, followed by cubic and quintic profile.

Figure 4-26 illustrates the solar radiant spectra and the amount of spectral power transmitted through different designs for selected W_{grin} and W*. As can be seen, by increasing the value for W* more solar radiation will be transmitted by the different dielectric mirrors. However, with respect to Figure 4-28, for percent transmittance of the solar irradiance this trend is not valid for the dielectric mirror design with W*=1 with a drop from ~77% for W_{grin}=0 to ~71.5% for $W_{grin}=0.5\cdot(d_{L+H})$. For the design with W*=100 the ~77% transmitted solar radiation increases for all profile types including linear, cubic and quintic to ~96%, ~97% and ~97%, respectively. As can be seen from Figure 4-19, by increasing the value for W* from 20 to 50 and 100 the results do not change significantly.

Figure 4-27 shows the blackbody radiation spectra at T=500 K and the amount of spectral power reflected by different dielectric mirrors for selected values of W_{grin} and W*. Considering these results, increasing W* results in a lower maximum peak reflectance value. And with respect to Figure 4-29 which illustrates the summation of the fraction of spectral power reflected by different dielectric mirrors for various W_{grin}, generally the results illustrate a decrease for the cases with W_{grin}=0 to those with $W_{grin}=0.5\cdot(d_{L+H})$. However, for the dielectric mirror with W*=1 the summation increases from ~42.2% with W_{grin}=0 to ~43.2% with $W_{grin}=0.5\cdot(d_{L+H})$. The design with W* = 100 shows the highest drop with ~29% for linear profile, ~34.5% for cubic profile and ~37% for quintic profile.

a.

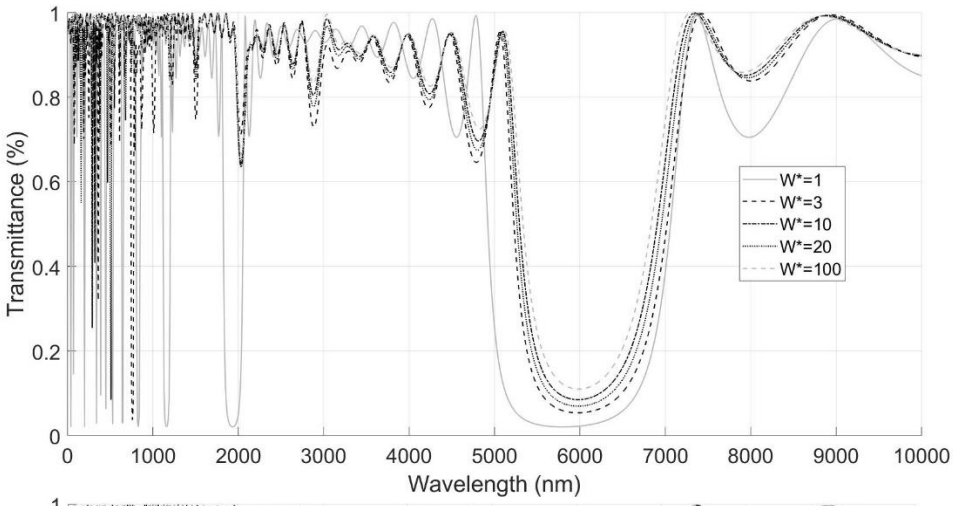

b.

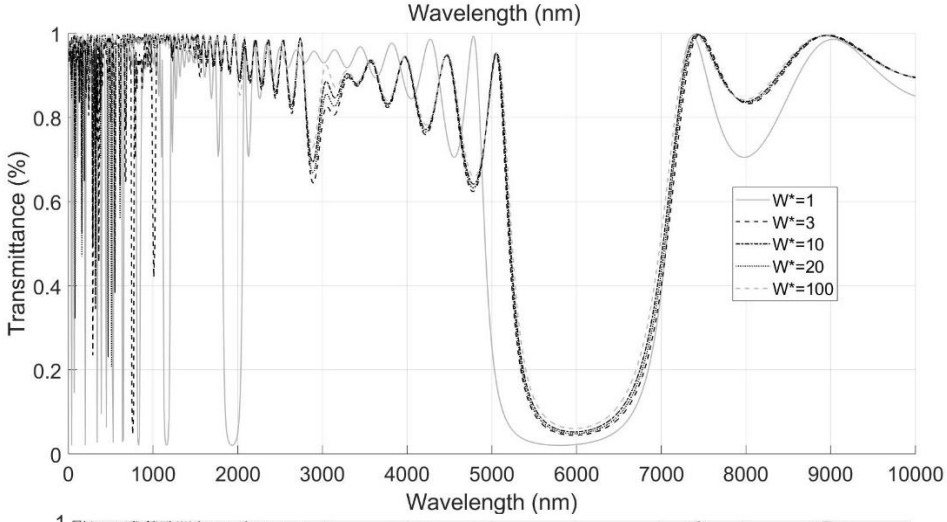

c.

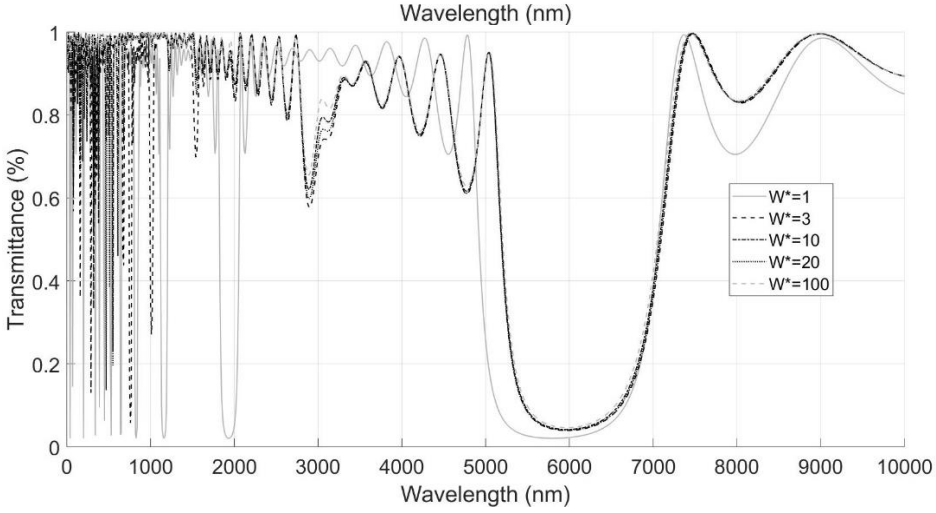

Figure 4-22. Transmittance spectra for $[H_LL_L]^5$ (Figure a.), $[H_CL_C]^5$ (Figure b.) and $[H_QL_Q]^5$ (Figure c.) with $W_{grin}=0.5\cdot(d_{L+H})$ and W* = 1, 3, 10, 20 and 100. Here, W* = 1 is representative of $[HL]^5$.

a.

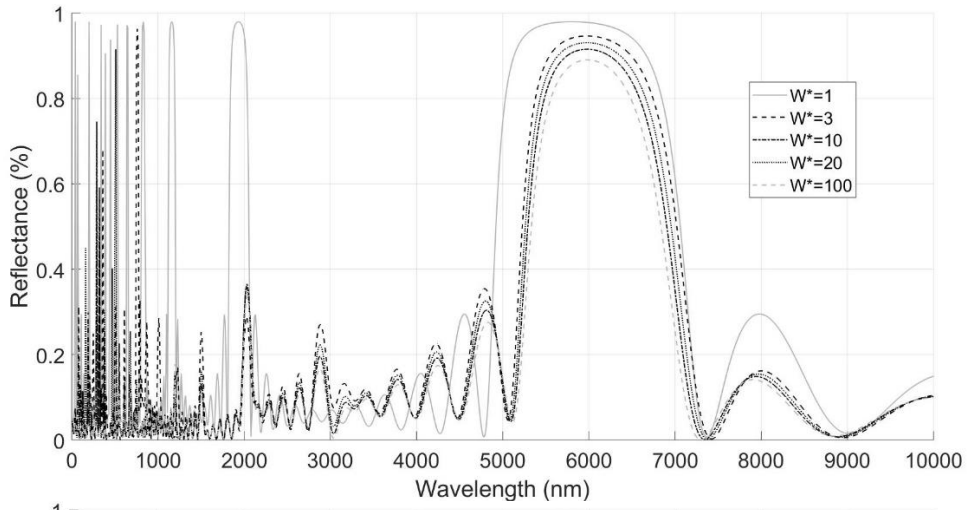

b.

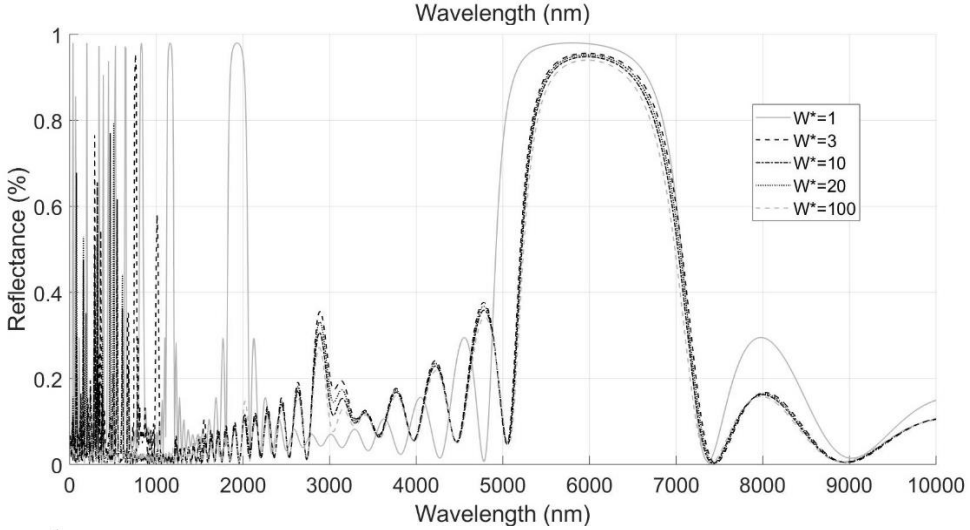

c.

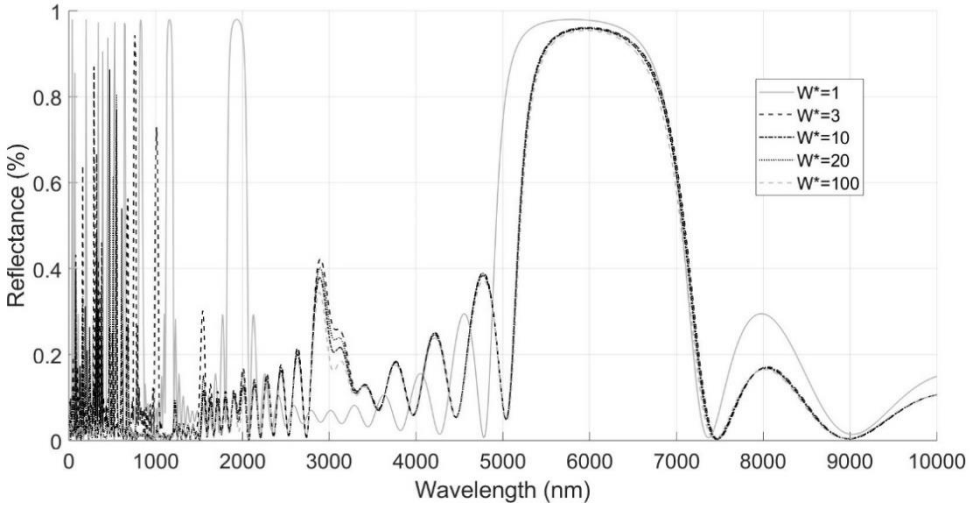

Figure 4-23. Reflectance spectra for $[H_LL_L]^5$ (Figure a.), $[H_CL_C]^5$ (Figure b.) and $[H_QL_Q]^5$ (Figure c.) with $W_{grin}=0.5\cdot(t_{L+H})$ and W* = 1, 3, 10, 20 and 100. Here, W* = 1 is representative of $[HL]^5$.

a.

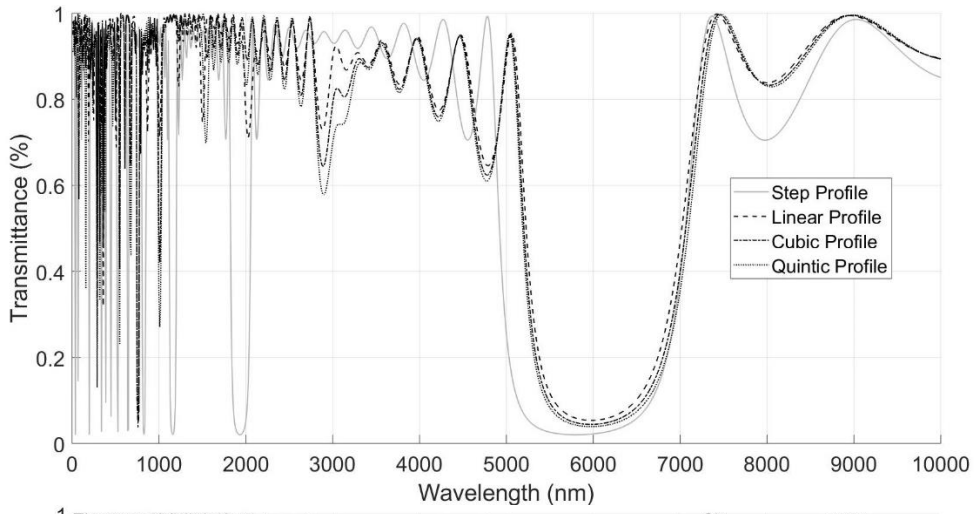

b.

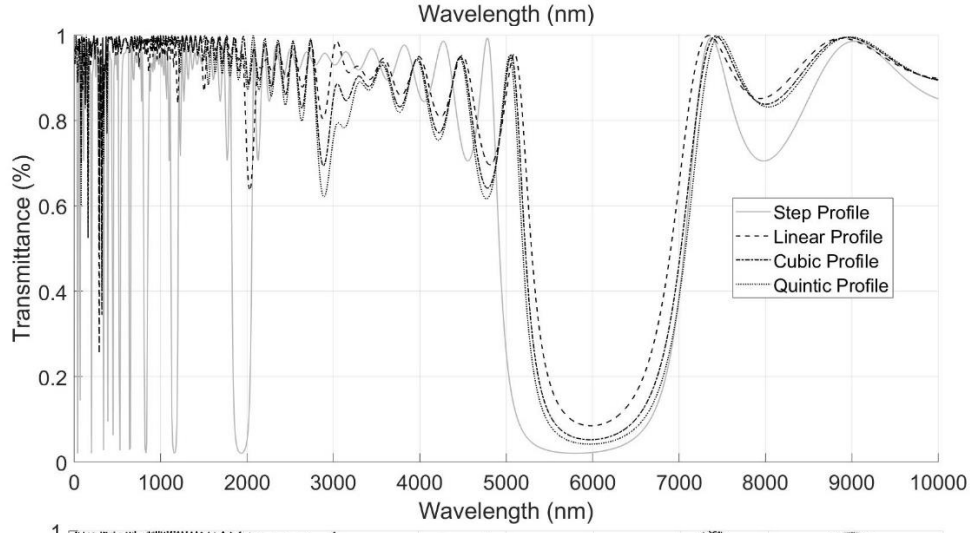

c.

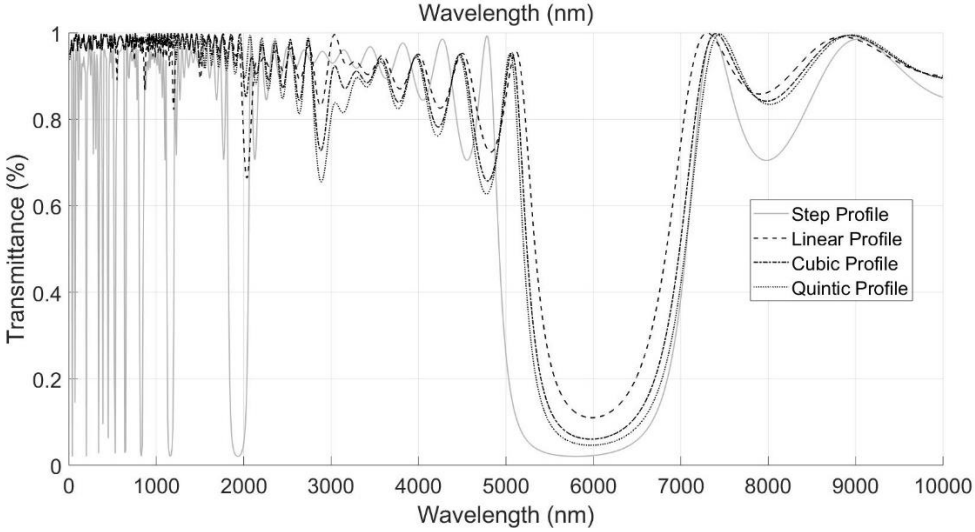

Figure 4-24. Transmittance spectra for $[HL]^5$, $[H_LL_L]^5$, $[H_CL_C]^5$ and $[H_QL_Q]^5$ with $W_{grin}=0.5\cdot(t_{L+H})$ and W* = 3 (Figure a.), W* = 10 (Figure b.) and W* = 100 (Figure c.)

a.

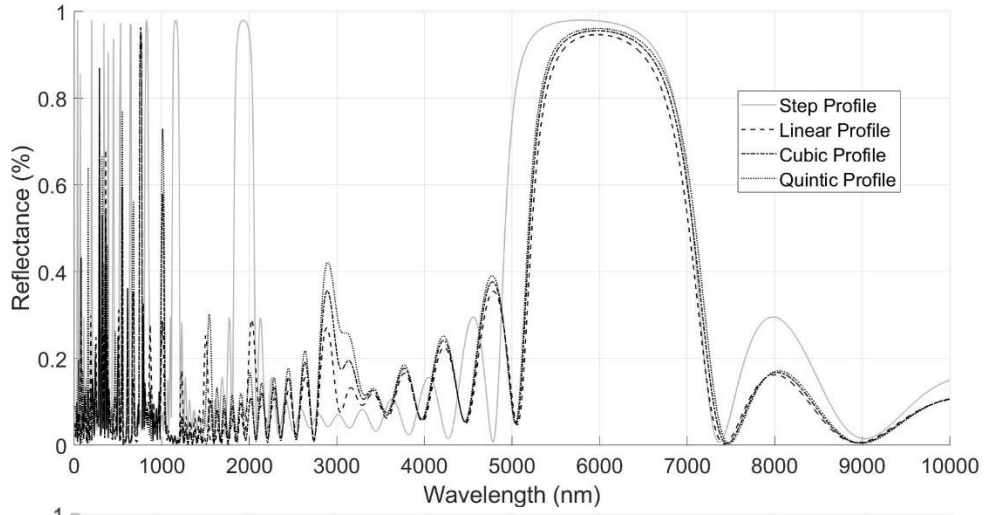

b.

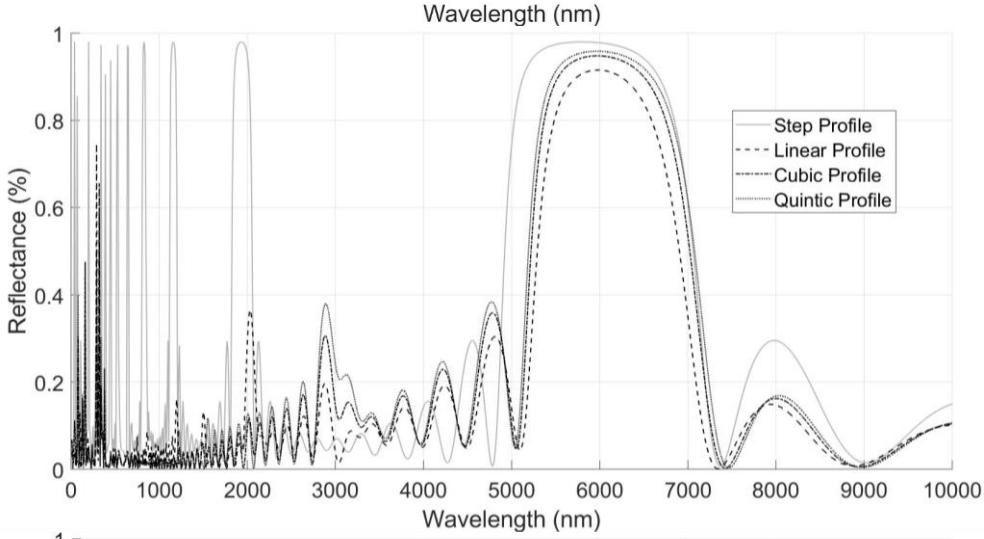

c.

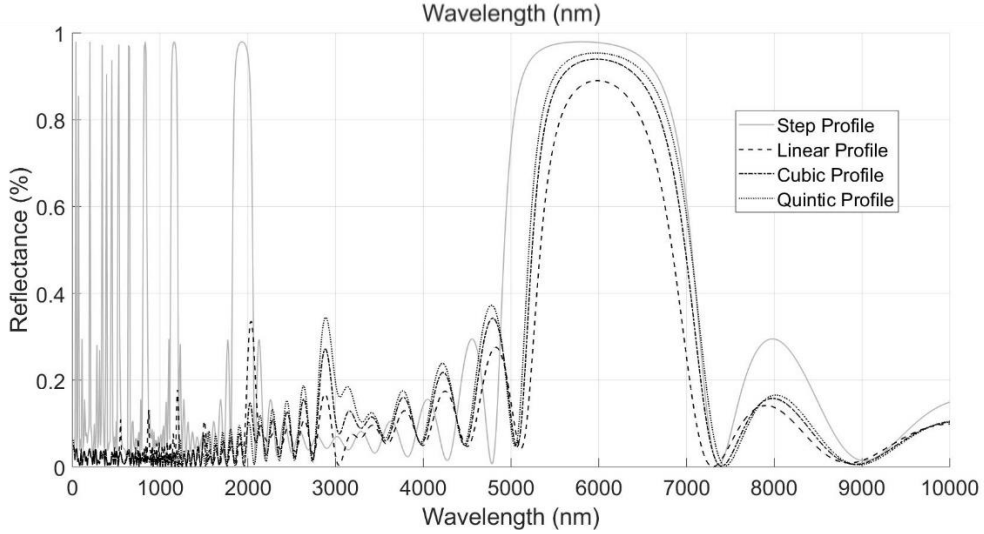

Figure 4-25. Reflectance spectra for $[HL]^5$, $[H_LL_L]^5$, $[H_CL_C]^5$ and $[H_QL_Q]^5$ with $W_{grin}=0.5\cdot(t_{L+H})$ and W* = 3 (Figure a.), W* = 10 (Figure b.) and W* = 100 (Figure c.)

a.

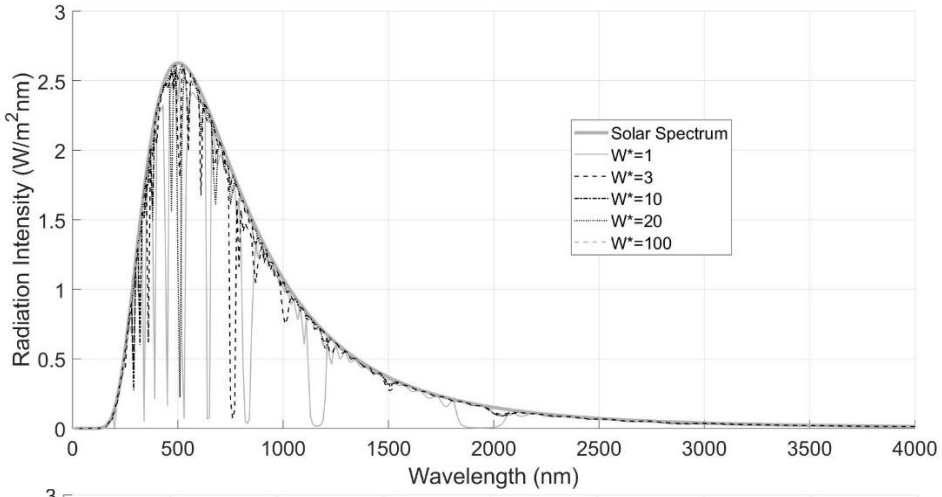

b.

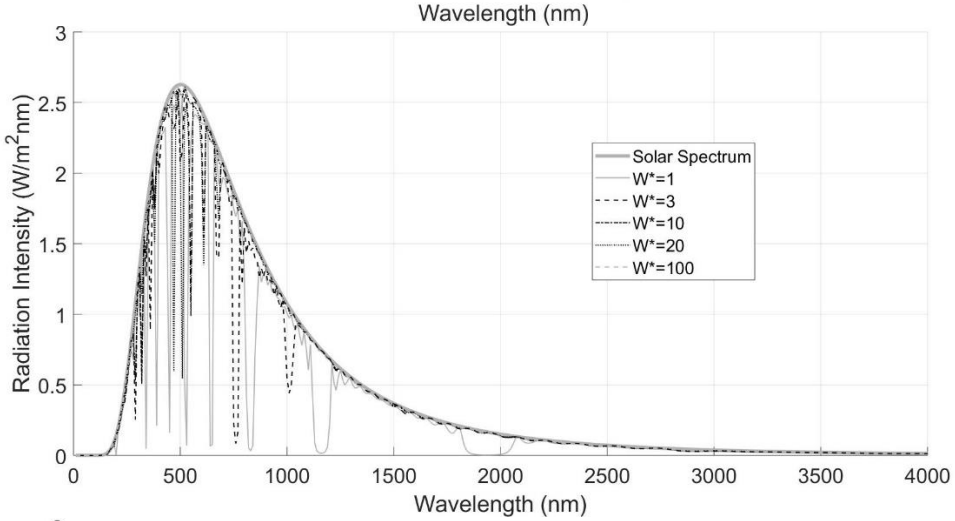

c.

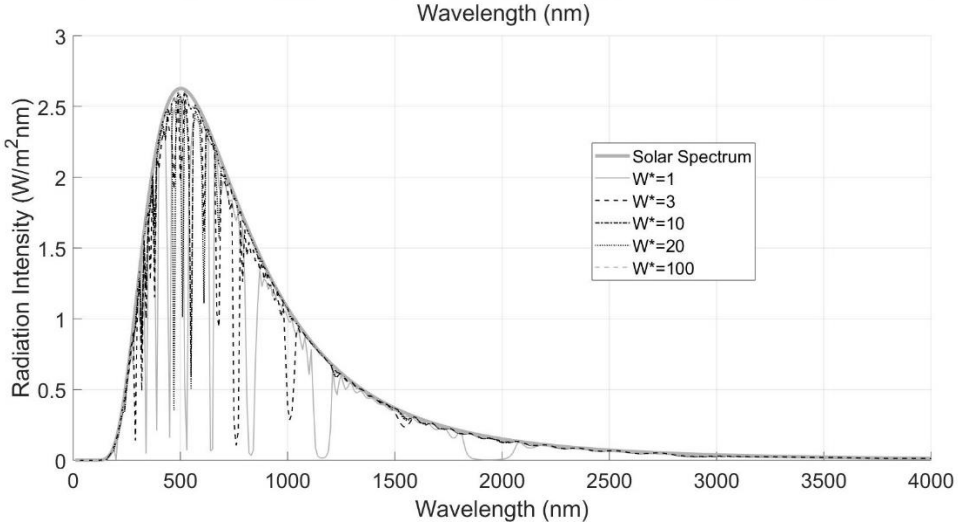

Figure 4-26. Solar irradiance spectra and the amount of spectral solar power transmitted through $[H_LL_L]^5$ (Figure a.), $[H_CL_C]^5$ (Figure b.) and $[H_QL_Q]^5$ (Figure c.) with $W_{grin}=0.5\cdot(t_{L+H})$ and W* = 1, 3, 10, 20 and 100. Here, W*=1 is representative of $[HL]^5$.

a.

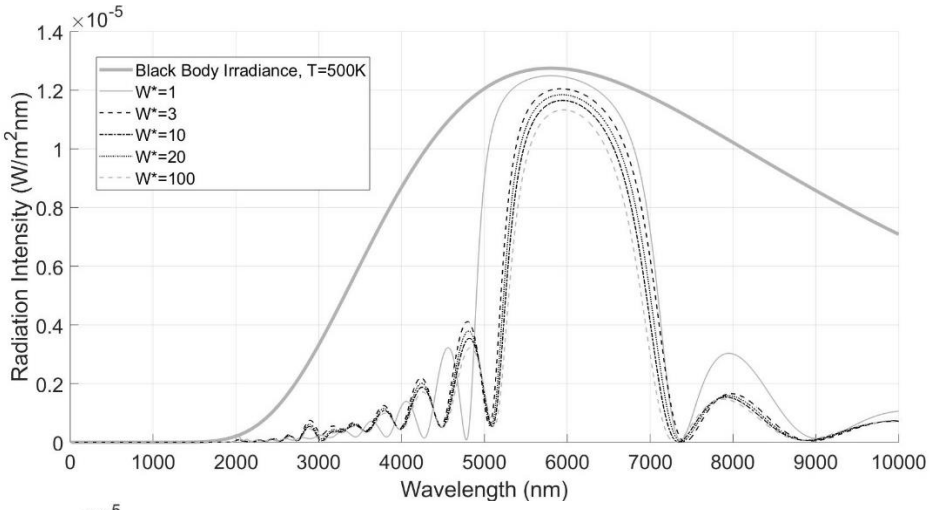

b.

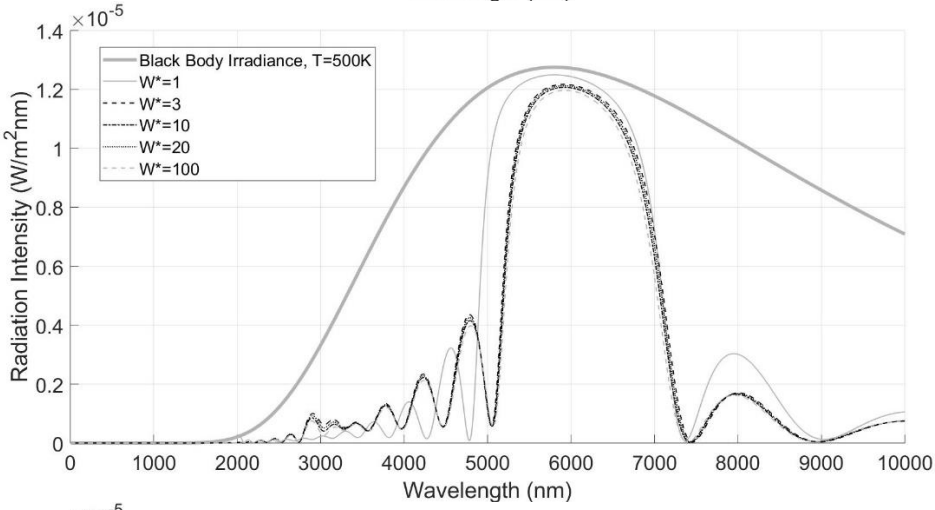

c.

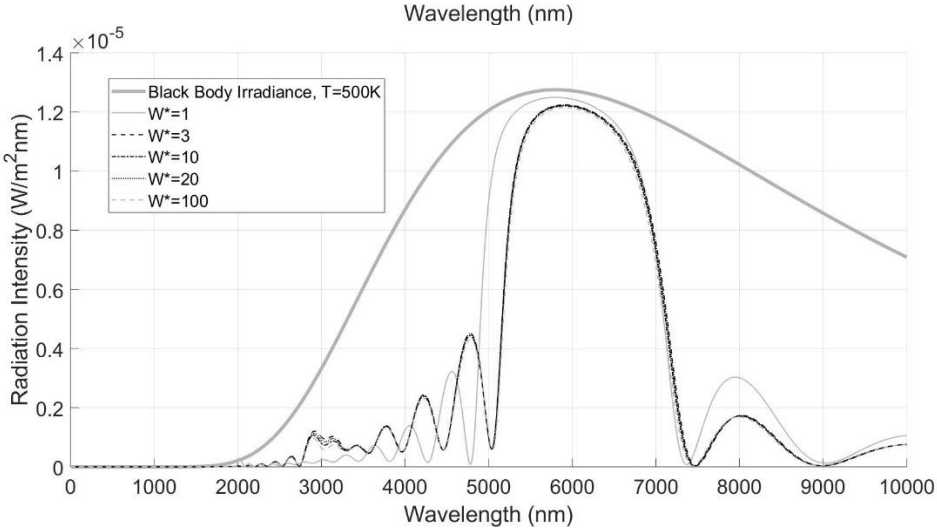

Figure 4-27. Radiation from a blackbody at T=500 K and the amount of spectral power reflected by $[H_L L_L]^5$ (Figure a.), $[H_C L_C]^5$ (Figure b.) and $[H_Q L_Q]^5$ (Figure c.) with $W_{grin}=0.5\cdot(d_{L+H})$ and W* = 1, 3, 10, 20 and 100. Here, W*=1 is representative of $[HL]^5$.

a.

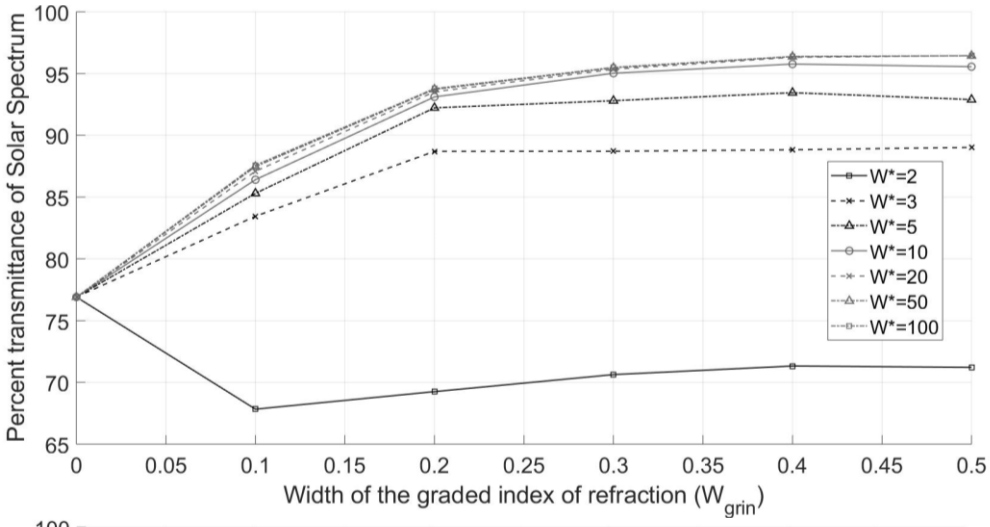

b.

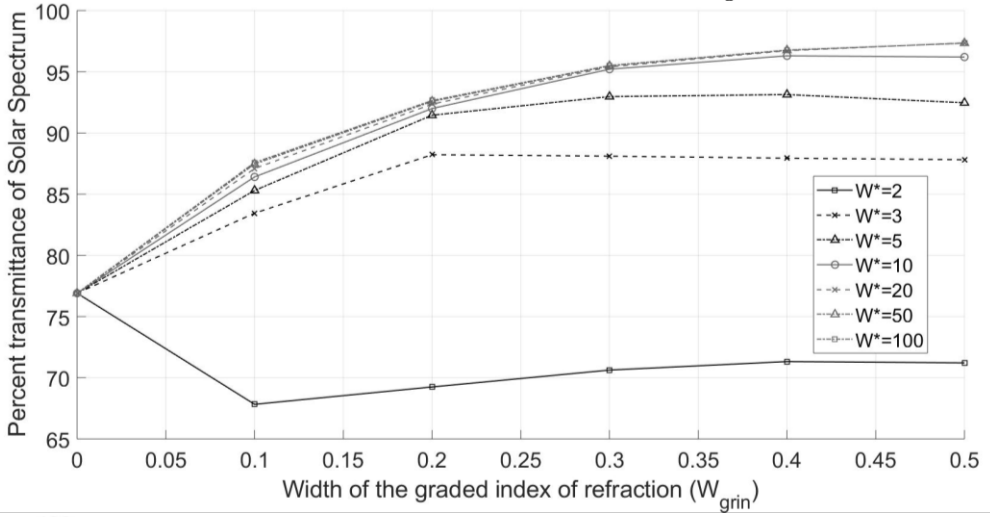

c.

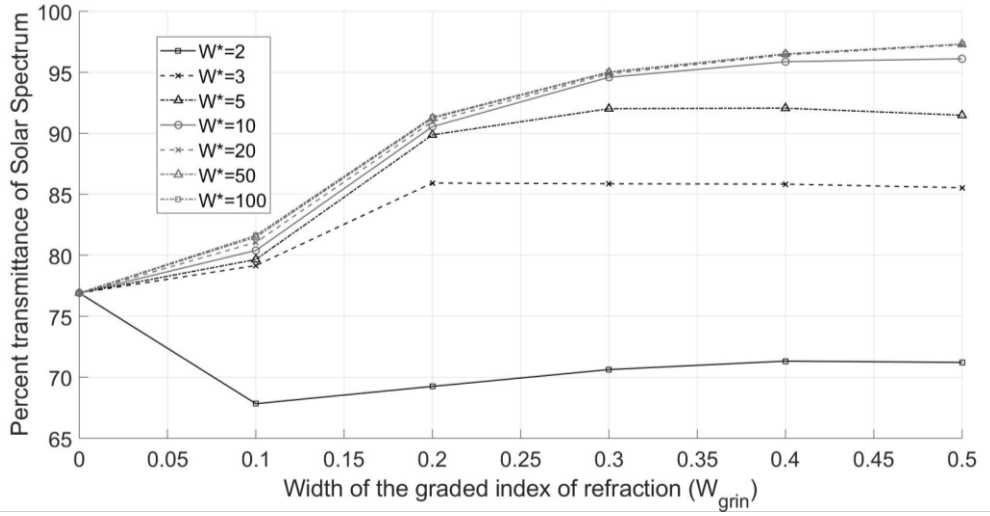

Figure 4-28. Percent transmittance of the solar irradiance for $[H_L L_L]^5$ (Figure a.), $[H_C L_C]^5$ (Figure b.) and $[H_Q L_Q]^5$ (Figure c.) plotted as a function of W_{grin} for W* = 2, 3, 5, 10, 20, 50, 100.

a.

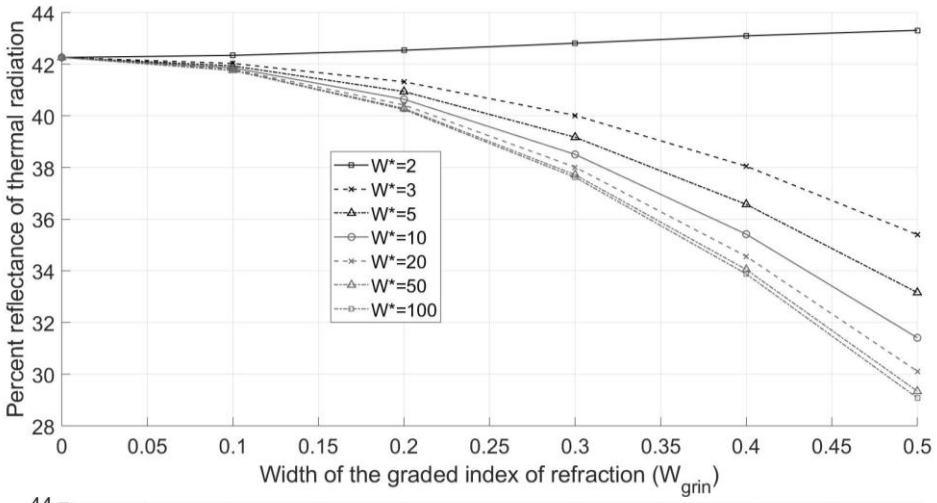

b.

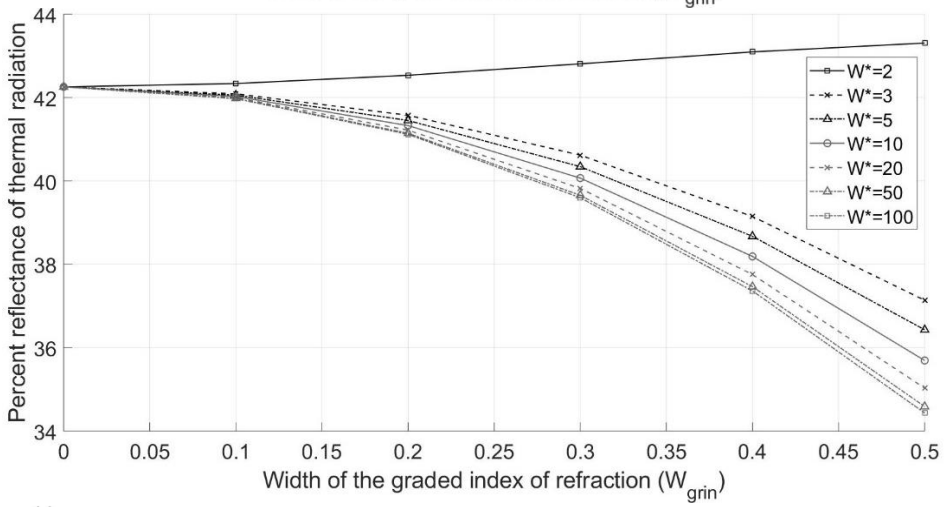

c.

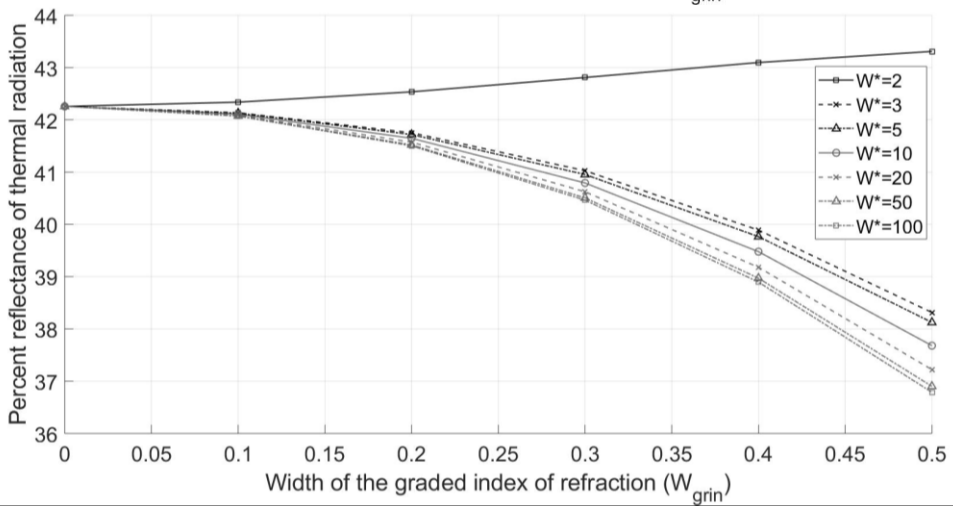

Figure 4-29. Percent reflectance of the radiation spectrum emitted from a blackbody at T= 500K for $[H_L L_L]^5$ (Figure a.), $[H_C L_C]^5$ (Figure b.) and $[H_Q L_Q]^5$ (Figure c.) and plotted as a function of W_{grin} for W* = 2, 3, 5, 10, 20, 50, 100.

4-4. Effects of changing the refractive index of the layers within a dielectric mirror on its performance

In this section, the sensitivity of the transmittance and reflectance spectra of dielectric mirrors towards changes in the refractive index of its films is analyzed for different dielectric mirror designs. As discussed earlier, throughout this thesis it has been assumed that the index of refraction of the alternating layers in the dielectric mirror are 1.3 and 2.0. In this section, the sensitivity analysis will be done with the lower index of refraction having a range of vales from the set n_L= [1.1, 1.2, 1.3, 1.4, 1.5] and the higher index of refraction having the set of values n_H= [1.5, 1.6, 1.7, 1.8, 1.9, 2, 2.1, 2.2, 2.3, 2.4, 2.5]. The corresponding results for the transmittance and reflectance spectra as well as the blackbody irradiance with the fraction of spectral power reflected by different dielectric mirrors and the solar radiation spectra with the fraction of spectral solar power transmitted through different dielectric mirrors are provided in Figure 4-30 through Figure 4-37. Finally, the maximum achievable temperature of a black body receiver subjected to solar irradiance that is transmitted through the dielectric mirrors considered in this section is provided in Figure 4-38, and the reflectance and transmittance spectra corresponding to the dielectric mirror that provided for the maximum blackbody temperature is plotted in Figure 4-39 and Figure 4-40, respectively.

Figure 4-30, Figure 4-32 and Figure 4-34 show the transmittance spectra for dielectric mirrors with n_H= [1.6, 2, 2.5], n_L= [1.1, 1.3, 1.5] and $W_{grin}=0.5\cdot(d_{L+H})$ for $[HL]^5$, $[H_LL_L]^5$, $[H_CL_C]^5$ and $[H_QL_Q]^5$ interfacial index of refraction profiles, respectively. Likewise, Figure 4-31, Figure 4-33 and Figure 4-35 show the reflectance spectra for the dielectric mirror design. As can be seen, by increasing the lower index of refraction from 1.1 to 1.5 for a constant n_H= 2.5, the FWHM of the reflection peak for $[HL]^5$, $[H_LL_L]^5$, $[H_CL_C]^5$ and $[H_QL_Q]^5$ decreases from 3,650 nm, 2,760 nm, 3,120 nm, and

3,260 nm to 2,440 nm, 1,830 nm, 2,080 nm, and 2,170 nm, respectively. Also, the corresponding maximum peak reflection values decrease from 99.97% to 99.41% for $[HL]^5$, from 99.24% to 95.17% for $[H_LL_L]^5$, from 99.68% to 97.49% for $[H_CL_C]^5$ and from 99.88% to 98.11% for $[H_QL_Q]^5$. This is while for a constant value of n_L= 1.1, by varying the higher index of refraction from 1.6 to 2.5, the FWHM increases from 930 nm to 3,650 nm for $[HL]^5$, form 1,310 nm to 2,760 nm for $[H_LL_L]^5$, from 1,530 nm to 3,120 nm for $[H_CL_C]^5$, and from 1,620 nm to 3,260 nm for $[H_QL_Q]^5$. Likewise, the corresponding maximum peak reflection values increase from 94.55%, 83.84%, 89.96% and 91.91% to a higher value of 99.97%, 99.24%, 99.68% and 99.88%, for $[HL]^5$, $[H_LL_L]^5$, $[H_CL_C]^5$ and $[H_QL_Q]^5$, respectively. Accordingly, an important note here is that the results improve with increasing contrast between the high and low values of the indices of refraction within the dielectric mirror. Consequently, the best dielectric mirror is the one with the highest n_H and lowest n_L, which is the one with n_H=2.5 and n_L=1.1.

Figure 4-36 shows the fraction of the solar irradiance transmitted through $[HL]^5$, $[H_LL_L]^5$, $[H_CL_C]^5$ and $[H_QL_Q]^5$ with n_L = 1.1 to 1.5 and n_H = 1.5 to 2.5 and with $W_{grin}=0.5\cdot(d_{L+H})$. As can be seen in Figure 4-36, the solar power transmitted through the dielectric mirror is maximized when n_H is between 1.5 and 1.7 while n_L is equal to 1.3 for the cases of the linear, cubic and quintic index of refraction profiles. However, for the dielectric stack with a $[HL]^5$ the amount of solar irradiance transmitted is maximized when n_H and n_L are equal to 1.5, which represents the case of a homogeneous film rather than a dielectric mirror since there is no contrast in the index of refraction between the alternating layers within the structure.

Figure 4-37 plots the fraction of radiant power emitted form a blackbody at 500 K that is reflected by $[HL]^5$, $[H_LL_L]^5$, $[H_CL_C]^5$ and $[H_QL_Q]^5$ with n_L = 1.2 to 1.5, n_H = 1.5 to 2.5, and with $W_{grin}=0.5\cdot(d_{L+H})$. Generally, more blackbody radiation will be reflected with increasing contrast

between the high and low values of the indices of refraction of the films comprising the dielectric heat mirrors. Consequently, the best reflector is the one with the highest n_H and lowest n_L, that is the one with n_H=2.5 and n_L=1.1.

As discussed in Chapter 2, to maximize the temperature of a blackbody, the transmittance for solar irradiation and the emissivity of a spectrally selective coating covering the black body should be maximized and minimized, respectively. Considering Equation 2-11 in Chapter 2, the temperature is proportional to $\left(\frac{t}{\varepsilon}\right)^{1/4}$, where t is the transmittance and ε is the emissivity of the dielectric mirror. Figure 4-38 illustrates the dependency of the temperature of a blackbody receiver when it is subjected to solar radiation and covered with a dielectric mirror on the index of refraction of the layers (n_H and n_L) within the dielectric mirror. This temperature dependency on n_H and n_L is plotted for $[HL]^5$, $[H_LL_L]^5$, $[H_CL_C]^5$ and $[H_QL_Q]^5$ with $W_{grin}=0.5\cdot(d_{L+H})$. The general trend apparent in Figure 4-38 is that by increasing the contrast between n_H and n_L, a higher temperature on the surface of the blackbody receiver is achieved. Consequently, the best design for all cases considered in this study is with n_H= 2.5 and n_L= 1.1. Figure 4-39 shows the transmittance and reflectance spectra for a dielectric mirror with n_H=2.5 and n_L=1.3 with $W_{grin}=0.5\cdot(d_{L+H})$ for $[HL]^5$, $[H_LL_L]^5$, $[H_CL_C]^5$ and $[H_QL_Q]^5$. Finally, Figure 4-40 depicts the radiation emitted from a blackbody at T=500 K and the fraction of this spectral power reflected by $[HL]^5$, $[H_LL_L]^5$, $[H_CL_C]^5$ and $[H_QL_Q]^5$ and the solar irradiance and fraction of solar irradiance transmitted through $[HL]^5$, $[H_LL_L]^5$, $[H_CL_C]^5$ and $[H_QL_Q]^5$ for the cases in which n_H=2.5 and n_L=1.1 and $W_{grin}=0.5\cdot(d_{L+H})$.

a.

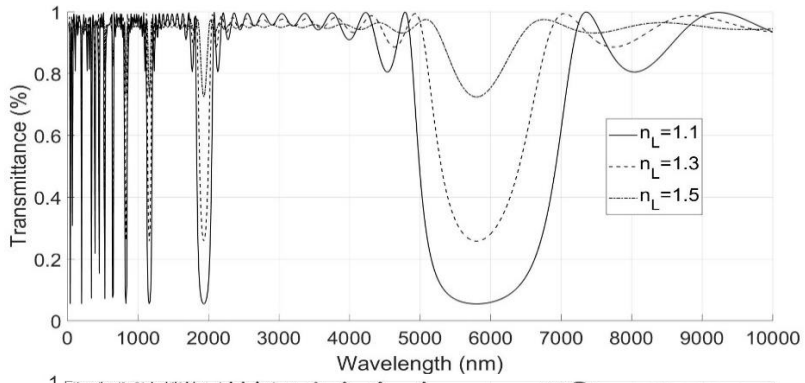

b.

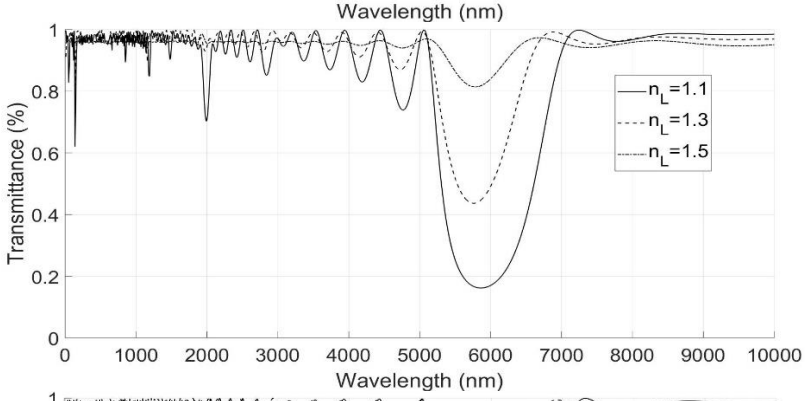

c.

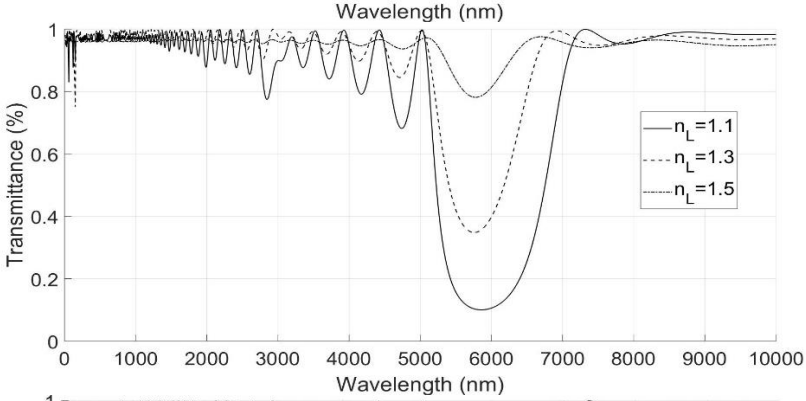

d.

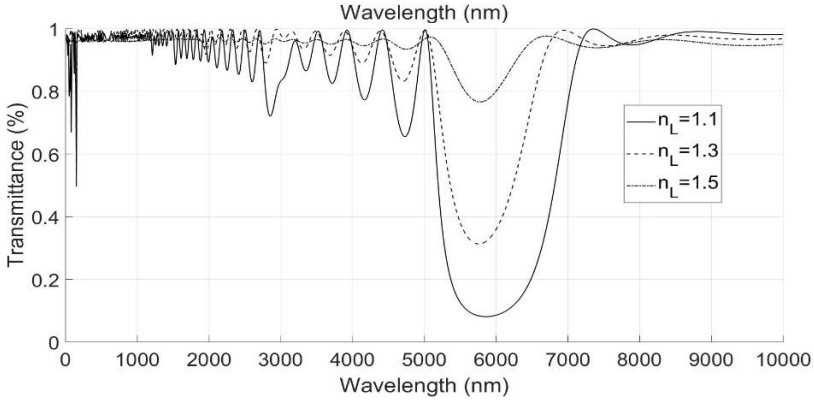

Figure 4-30. Transmittance spectra for $[HL]^5$ (Figure a.), $[H_LL_L]^5$ (Figure b.), $[H_CL_C]^5$ (Figure c.) and $[H_QL_Q]^5$ (Figure d.) with $W_{grin}=0.5\cdot(d_{L+H})$, $n_H=1.6$ and $n_L=1.1$, 1.3 and 1.5

a.

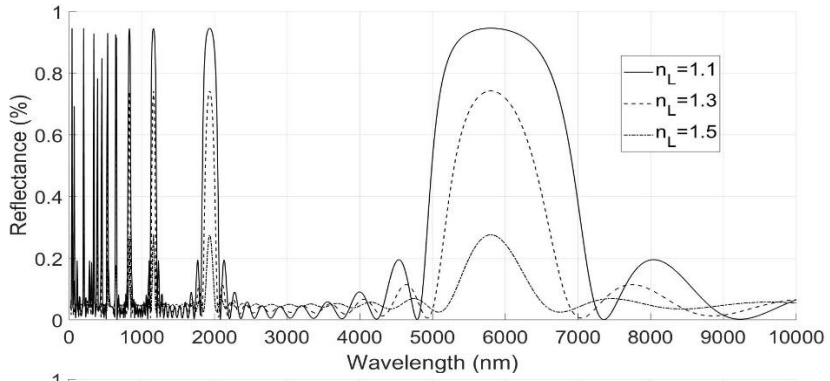

b.

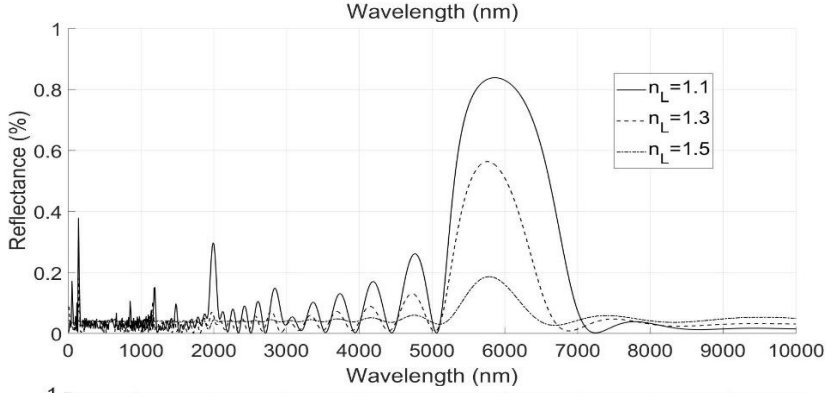

c.

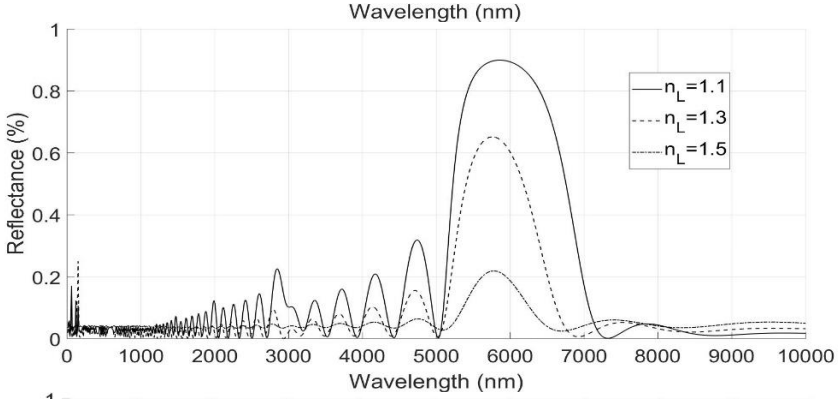

d.

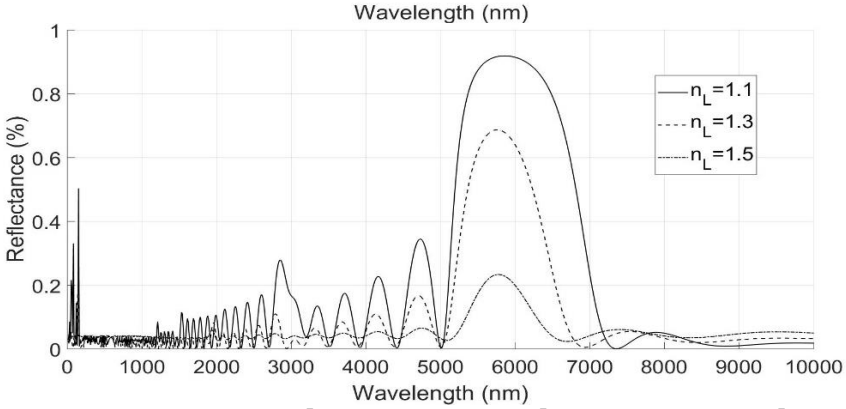

Figure 4-31. Reflectance spectra for $[HL]^5$ (Figure a.), $[H_LL_L]^5$ (Figure b.), $[H_CL_C]^5$ (Figure c.) and $[H_QL_Q]^5$ (Figure d.) with $W_{grin}=0.5\cdot(d_{L+H})$, $n_H=1.6$ and $n_L=1.1$, 1.3 and 1.5

a.

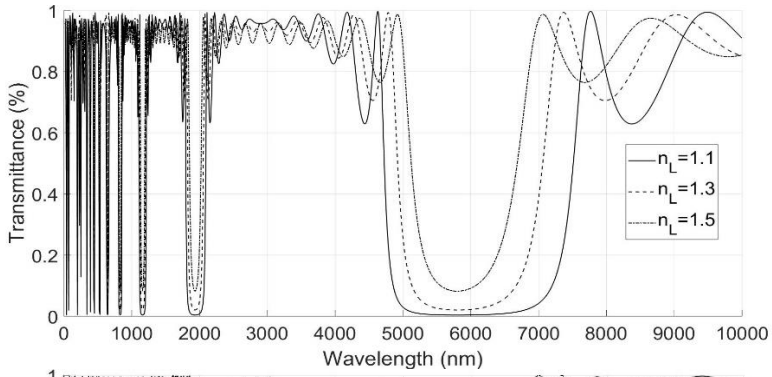

b.

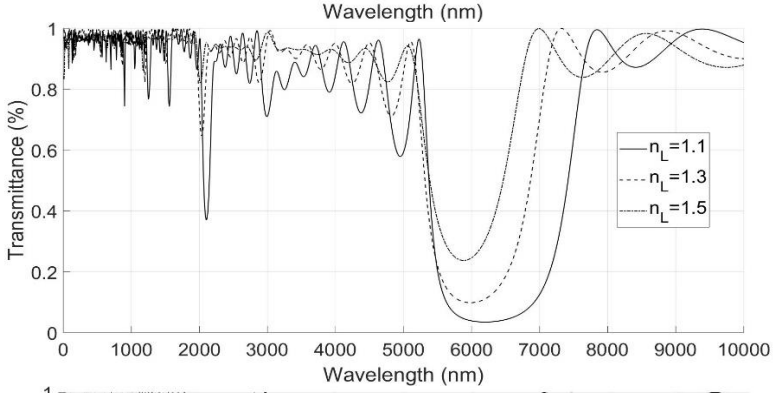

c.

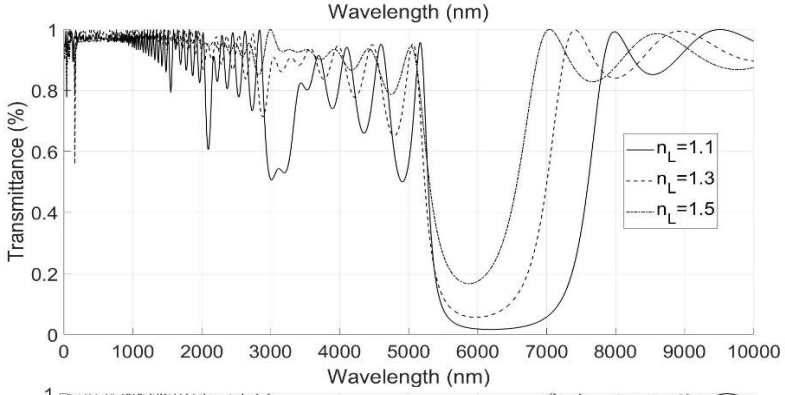

d.

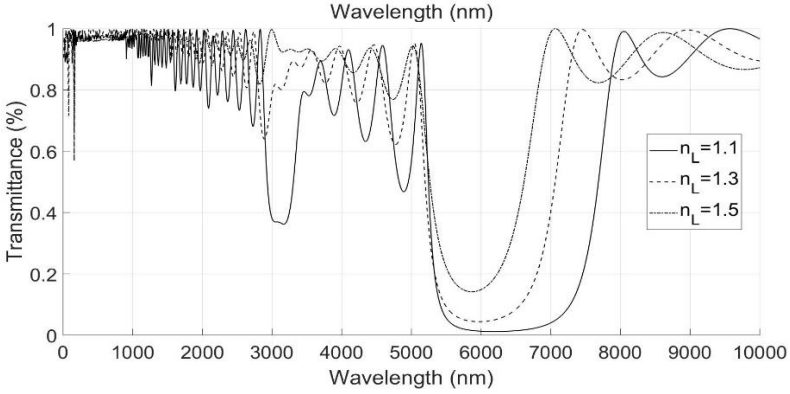

Figure 4-32. Transmittance spectra for $[HL]^5$ (Figure a.), $[H_LL_L]^5$ (Figure b.), $[H_CL_C]^5$ (Figure c.) and $[H_QL_Q]^5$ (Figure d.) with $W_{grin}=0.5\cdot(d_{L+H})$, $n_H=2$ and $n_L=1.1$, 1.3 and 1.5.

a.

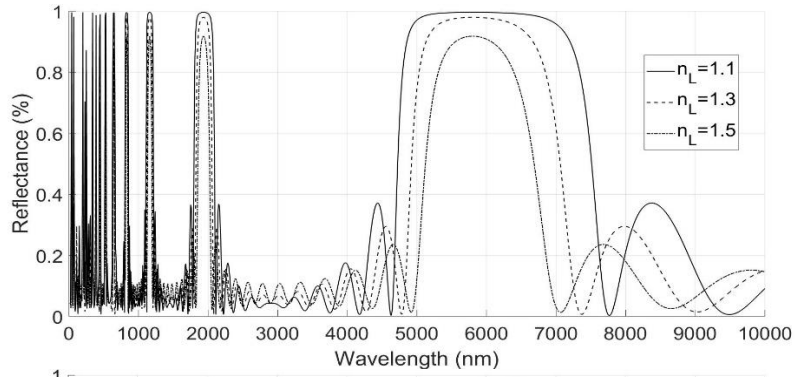

b.

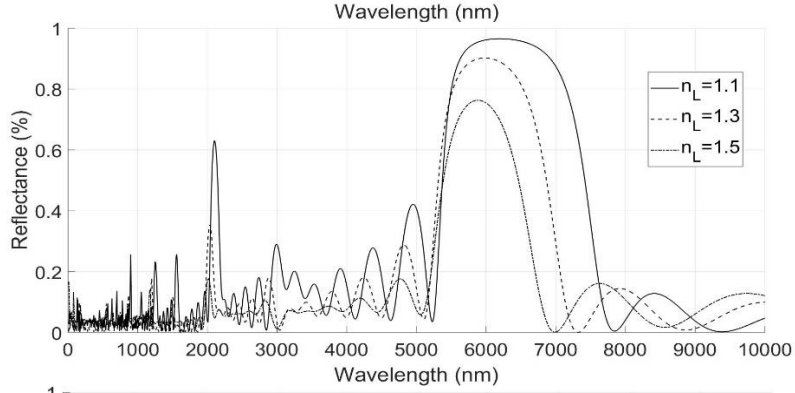

c.

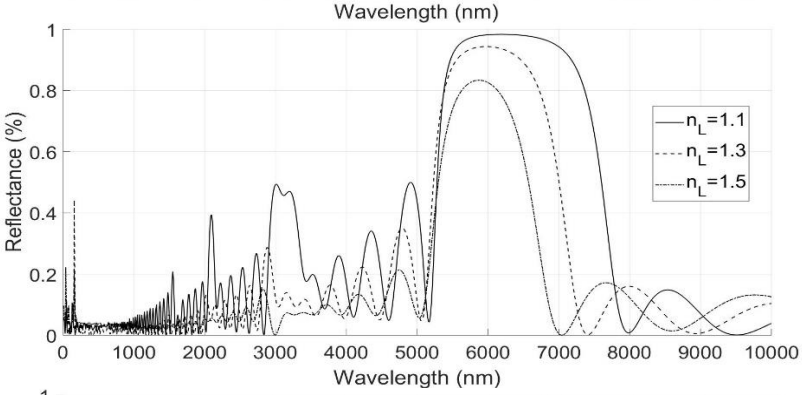

d.

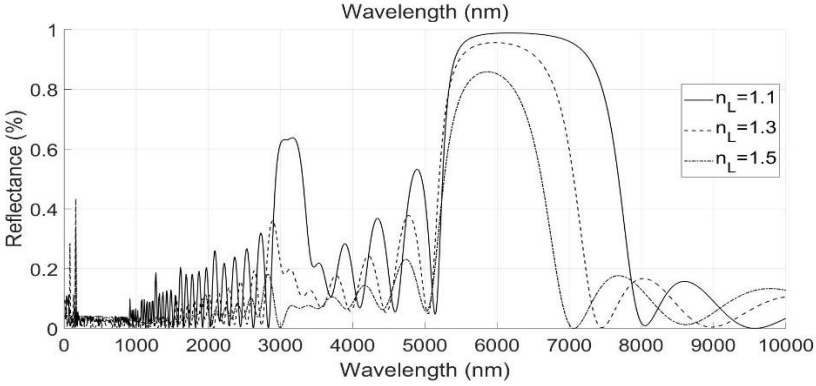

Figure 4-33. Reflectance spectra for $[HL]^5$ (Figure a.), $[H_LL_L]^5$ (Figure b.), $[H_CL_C]^5$ (Figure c.) and $[H_QL_Q]^5$ (Figure d.) with $W_{grin}=0.5\cdot(d_{L+H})$, $n_H=2$ and $n_L=1.1$, 1.3 and 1.5

a.

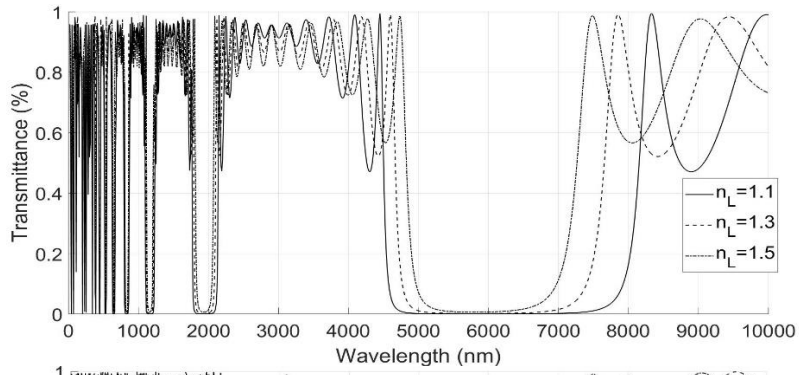

b.

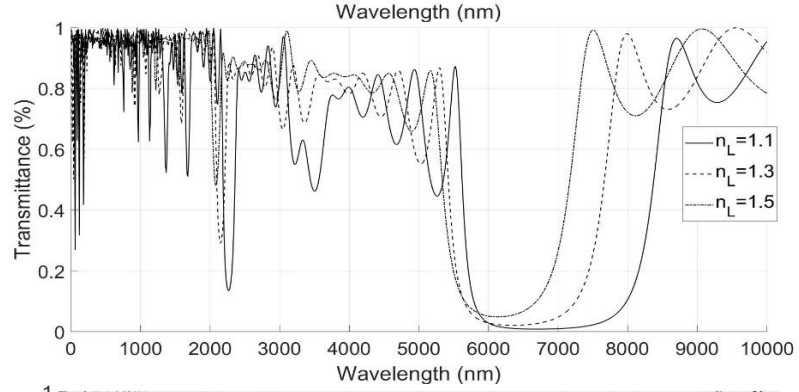

c.

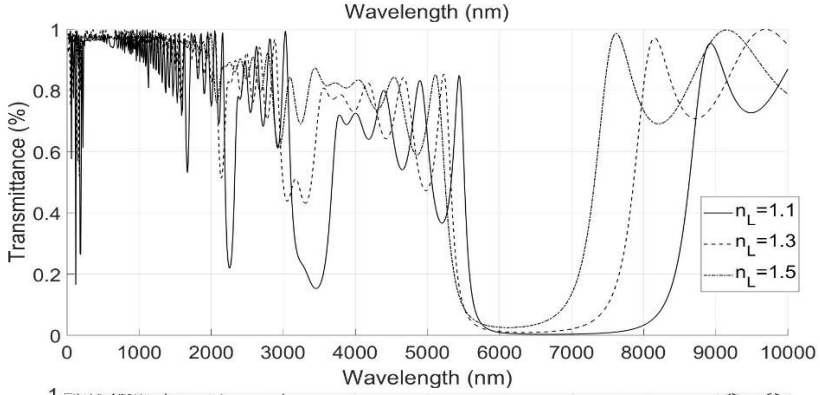

d.

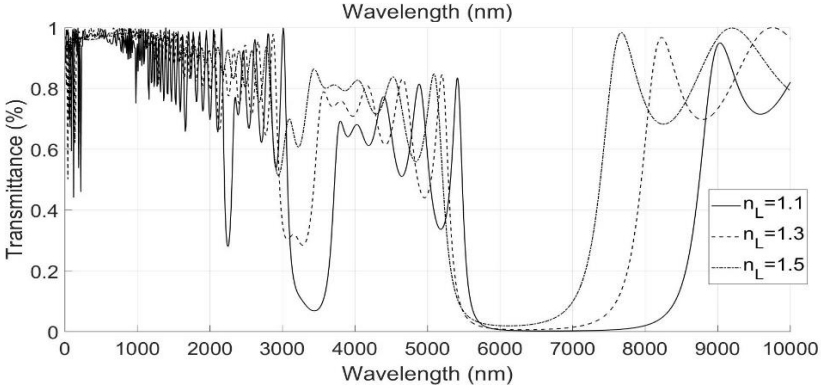

Figure 4-34. Transmittance spectra for $[HL]^5$ (Figure a.), $[H_LL_L]^5$ (Figure b.), $[H_CL_C]^5$ (Figure c.) and $[H_QL_Q]^5$ (Figure d.) with $W_{grin}=0.5\cdot(d_{L+H})$, $n_H=2.5$ and $n_L=1.1$, 1.3 and 1.5

a.

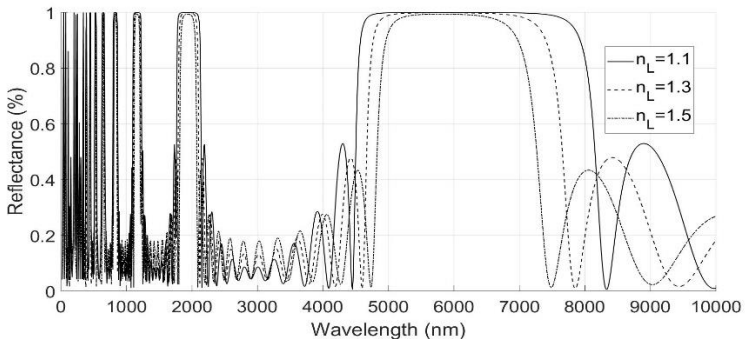

b.

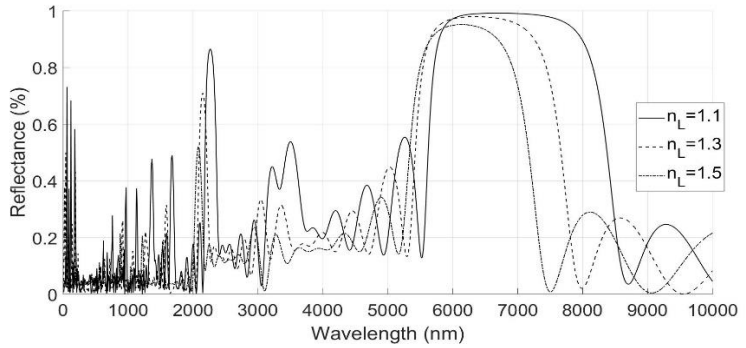

c.

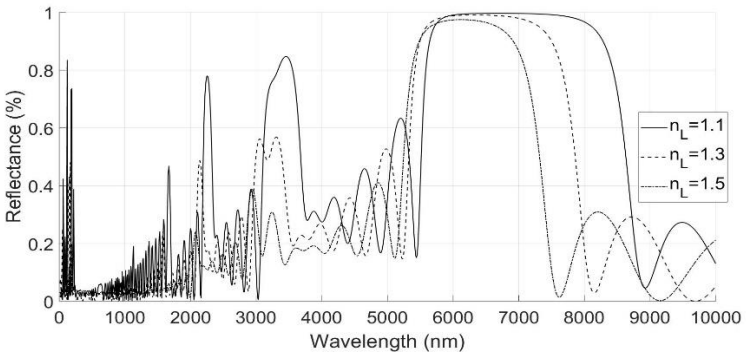

d.

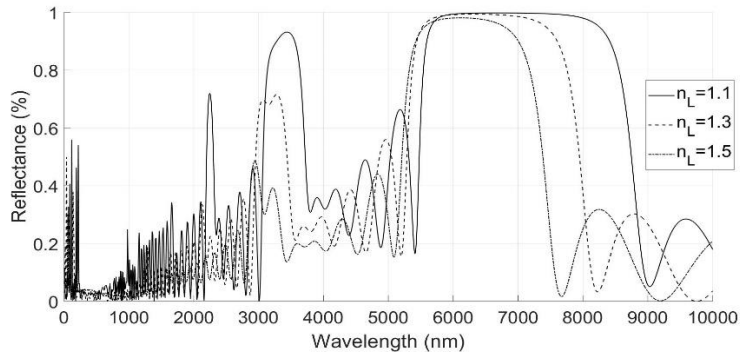

Figure 4-35. Reflectance spectra for $[HL]^5$ (Figure a.), $[H_LL_L]^5$ (Figure b.), $[H_CL_C]^5$ (Figure c.) and $[H_QL_Q]^5$ (Figure d.) with $W_{grin}=0.5\cdot(d_{L+H})$, $n_H=2.5$ and $n_L=1.1$, 1.3 and 1.5

a.

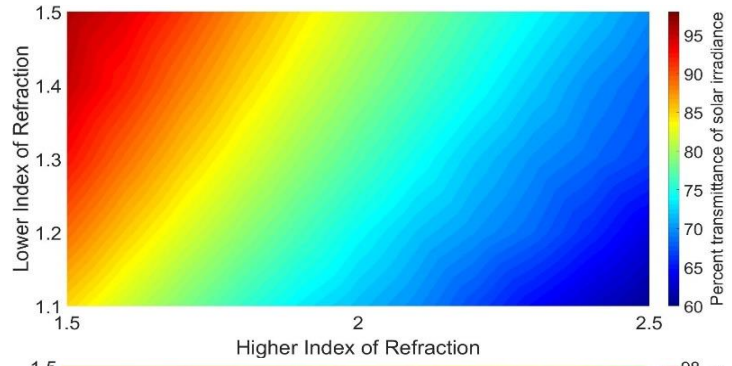

b.

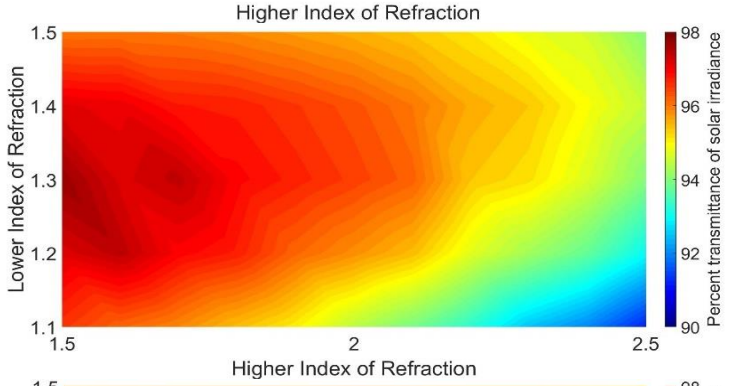

c.

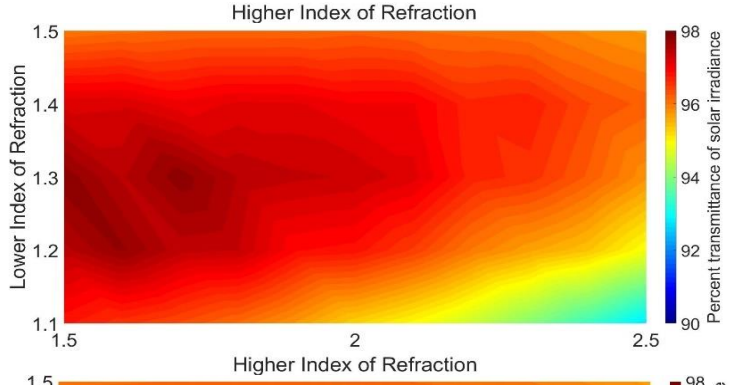

d.

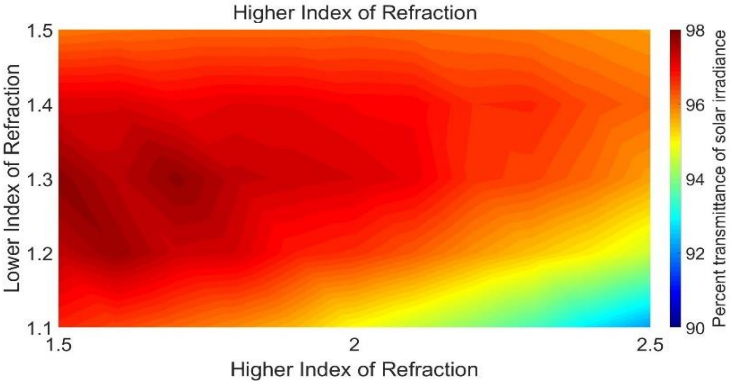

Figure 4-36. The fraction of the solar irradiance transmitted through $[HL]^5$ (Figure a.), $[H_LL_L]^5$ (Figure b.), $[H_CL_C]^5$ (Figure c.) and $[H_QL_Q]^5$ (Figure d.) with $W_{grin}=0.5\cdot(d_{L+H})$ plotted as a function of the index of refraction of its layers, n_H and n_L.

a.

b.

c.

d.

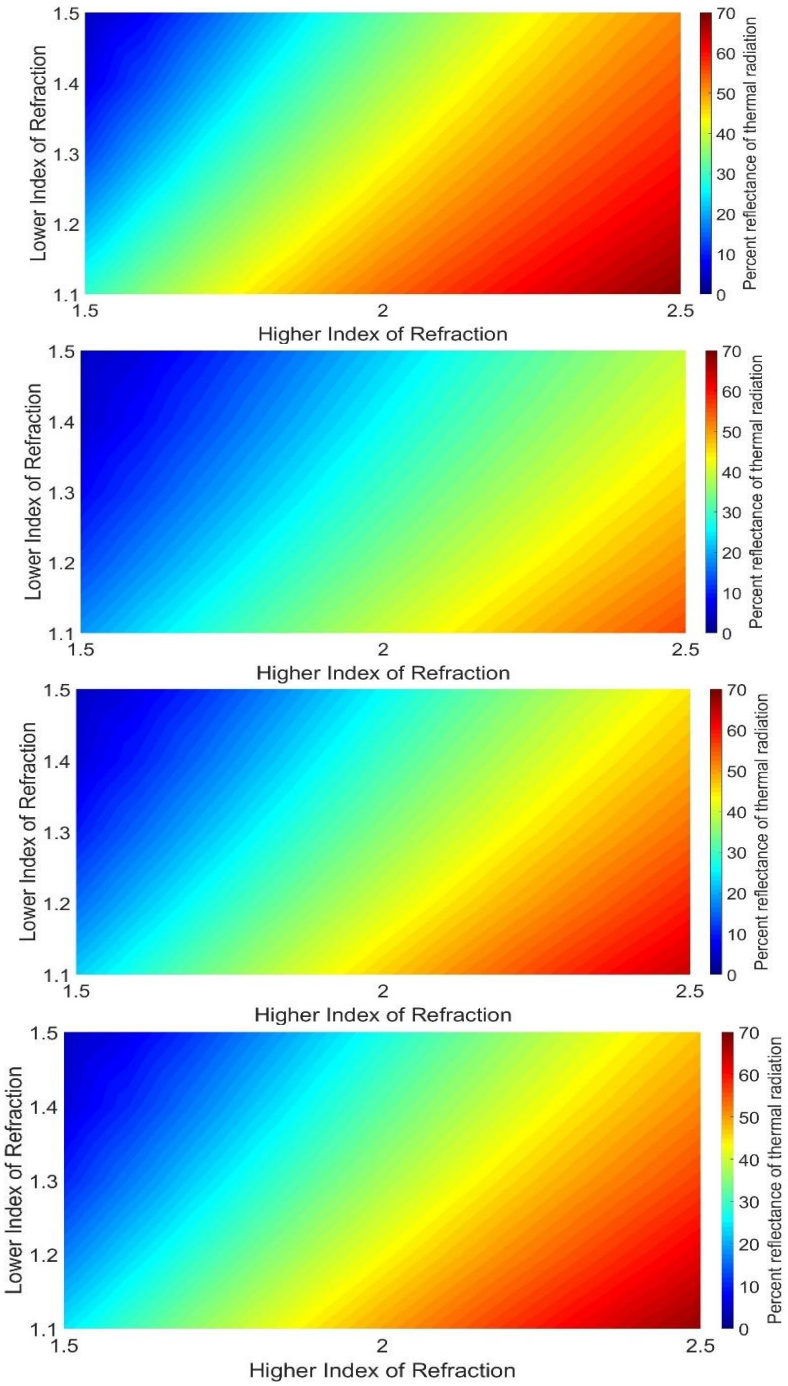

Figure 4-37. The fraction of power emitted from a blackbody at a temperature of 500 K that is reflected by $[HL]^5$ (Figure a.), $[H_LL_L]^5$ (Figure b.), $[H_CL_C]^5$ (Figure c.) and $[H_QL_Q]^5$ (Figure d.) with $W_{grin}=0.5\cdot(d_{L+H})$ plotted as a function of the index of refraction of its layers, n_H and n_L.

a.

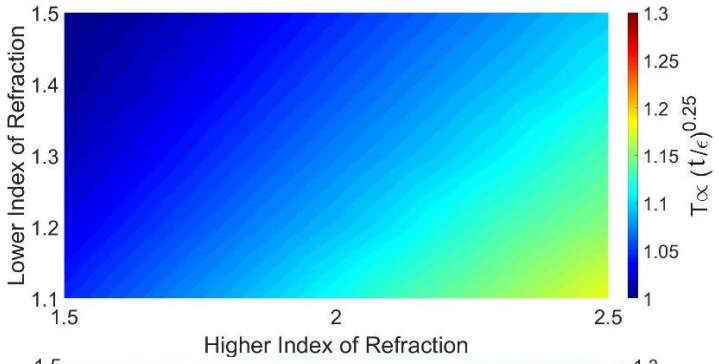

b.

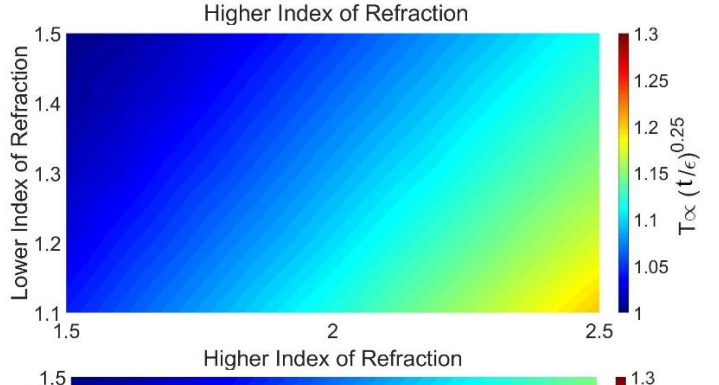

c.

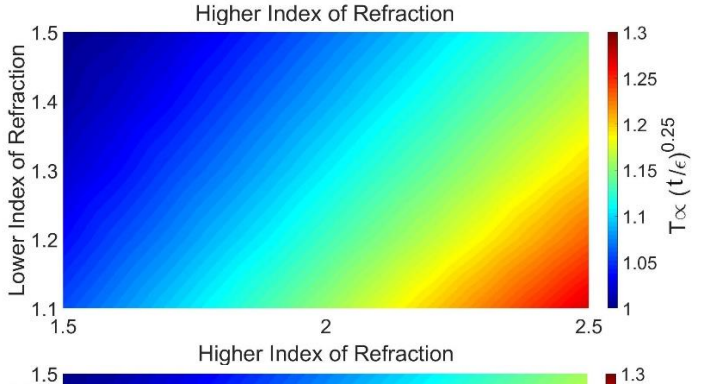

d.

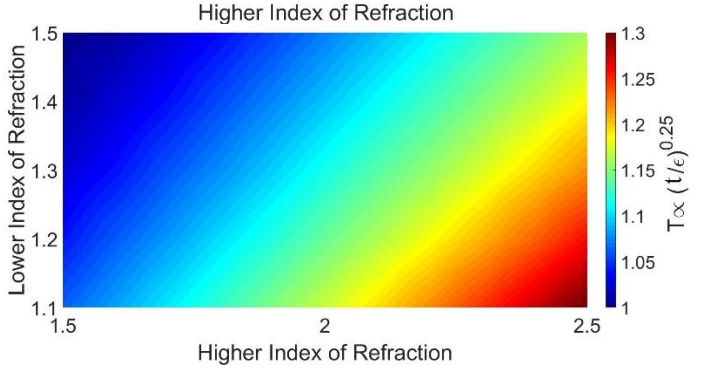

Figure 4-38. Temperature of a receiver covered with a transparent dielectric heat mirror designed with the form $[HL]^5$ (Figure a.), $[H_LL_L]^5$ (Figure b.), $[H_CL_C]^5$ (Figure c.) and $[H_QL_Q]^5$ (Figure d.) and $W_{grin}=0.5\cdot(d_{L+H})$ plotted as a function of the index of refraction, n_H and n_L, of the alternating layers within the heat mirror.

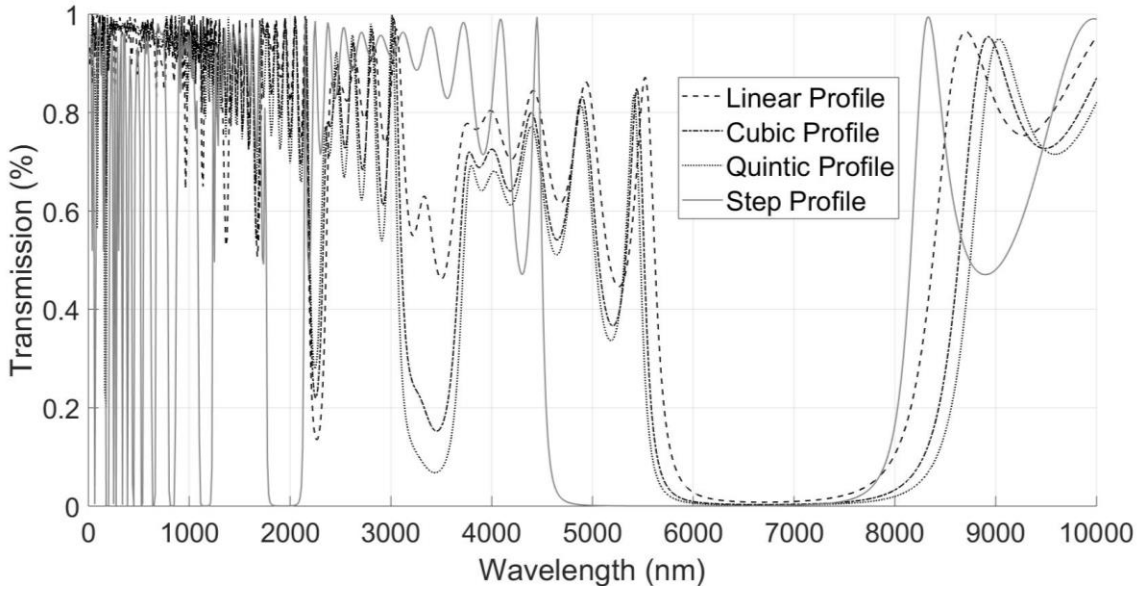

a.

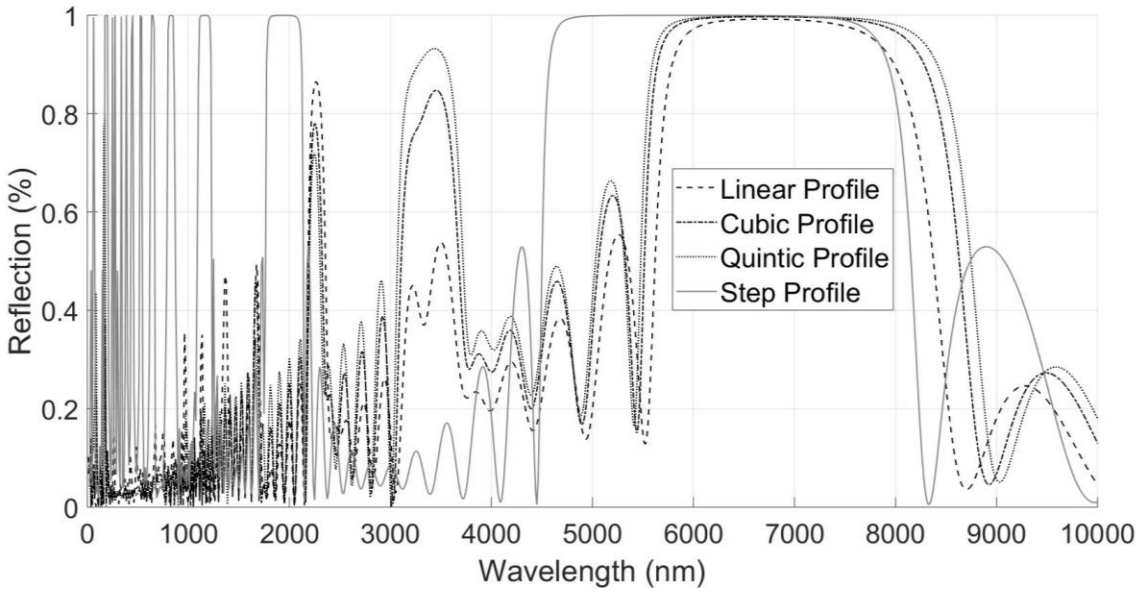

b.

Figure 4-39. Transmittance (Figure a.) and reflectance (Figure b.) spectra for n_H=2.5 and n_L=1.1 with $W_{grin}=0.5\cdot(d_{L+H})$ for $[HL]^5$, $[H_LL_L]^5$, $[H_CL_C]^5$ and $[H_QL_Q]^5$.

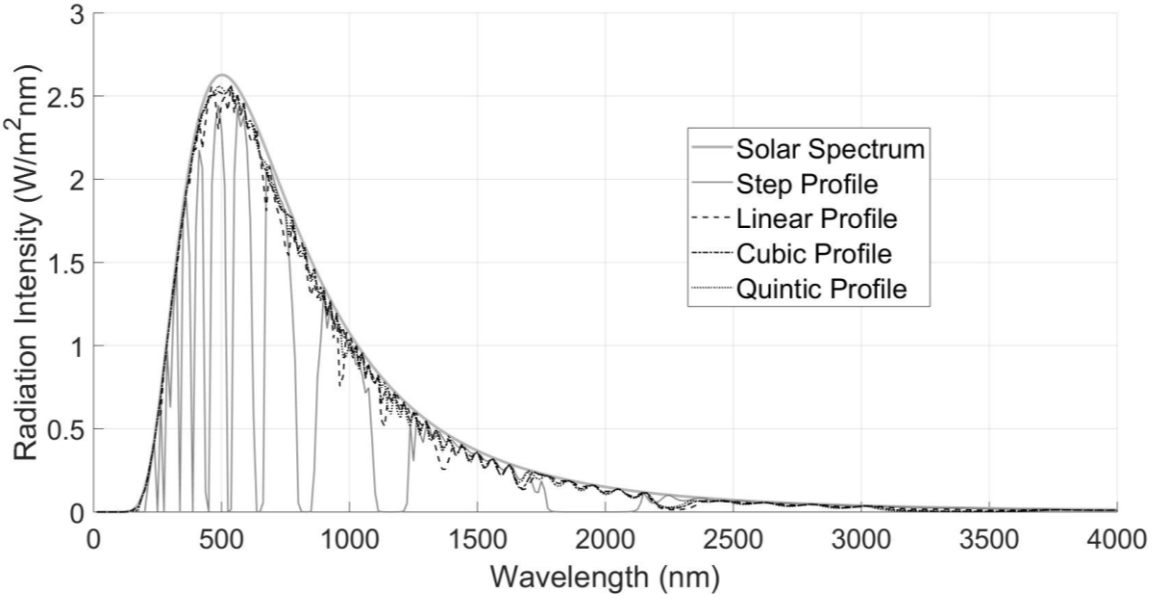

a.

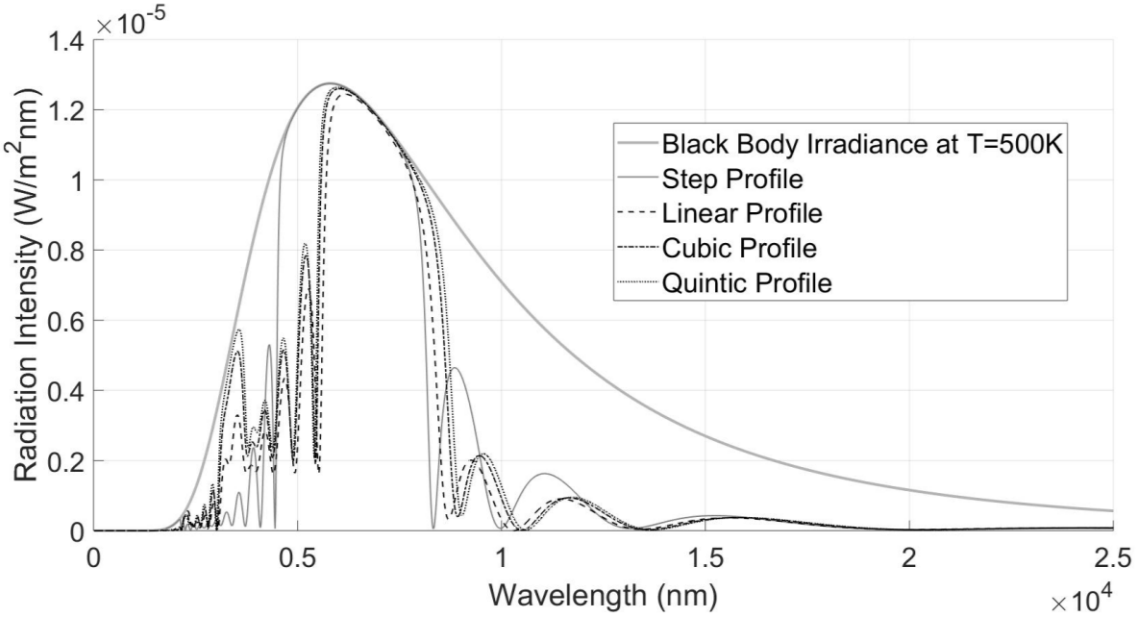

b.

Figure 4-40. The solar irradiance and amount of solar radiation that is transmitted through $[HL]^5$, $[H_LL_L]^5$, $[H_CL_C]^5$ and $[H_QL_Q]^5$ with n_H=2.5 and n_L=1.1 and $W_{grin}=0.5\cdot(d_{L+H})$ (Figure a) and the radiation spectra emitted from a blackbody at T=500 K and the amount of this radiation that is reflected from $[HL]^5$, $[H_LL_L]^5$, $[H_CL_C]^5$ and $[H_QL_Q]^5$ with n_H=2.5 and n_L=1.1 and $W_{grin}=0.5\cdot(d_{L+H})$ (Figure b)

4-5. Enhancing the performance of spectrally selective heat mirrors by stacking multiple dielectric mirrors in sequence

In this section, the transmittance and reflectance spectra of stacked dielectric mirrors are investigated. Accordingly, additional heat mirrors (quarter-wave dielectric mirrors) with different peak reflectance wavelengths can be stacked on top of each other. The reflectance and transmittance spectra for double-stack and triple-stack dielectric mirrors with $W_{grin}=0.5\cdot(d_{L+H})$ and different index of refraction profiles are investigated to determine their dependency on the reflectance peak position of the second and third dielectric mirrors within the stack. Herein, a double-stack dielectric mirror is comprised of two sets of five bi-layers of films with $n_L=2$ and $n_H=1.3$, denoted here as $[HL]^5_{f1}\cdot[HL]^5_{f2}$ for the case of the conventional quarter-wave stack, $[H_LL_L]^5_{f1}\cdot[H_LL_L]^5_{f2}$ when the interfaces between the films with the higher and lower refractive indices within the dielectric mirror is designed with a linear index of refraction profile, $[H_CL_C]^5_{f1}\cdot[H_CL_C]^5_{f2}$ when the dielectric mirror is designed with a cubic index of refraction profile and $[H_QL_Q]^5_{f1}\cdot[H_QL_Q]^5_{f2}$ when the dielectric mirror is designed with a quintic index of refraction profile, respectively. Here, f1 and f2 are the reflectance peak position of the first stack and second stack of the dielectric mirror, respectively.

A triple-stack dielectric mirror is comprised of three sets of five bi-layers of films with $n_L=2$ and $n_H=1.3$, denoted herein as $[HL]^5_{f1}\cdot[HL]^5_{f2}\cdot[HL]^5_{f3}$, $[H_LL_L]^5_{f1}\cdot[H_LL_L]^5_{f2}\cdot[H_LL_L]^5_{f3}$, $[H_CL_C]^5_{f1}\cdot[H_CL_C]^5_{f2}\cdot[H_CL_C]^5_{f3}$ and $[H_QL_Q]^5_{f1}\cdot[H_QL_Q]^5_{f2}\cdot[H_QL_Q]^5_{f3}$ when the interfaces between the films with the higher and lower refractive indices within the dielectric mirrors are designed with a step, linear, cubic and quintic index of refraction profile, respectively. Here, f1, f2 and f3 are the reflectance peak position of the first stack, second stack and third stack within the dielectric mirror, respectively.

The transmittance and reflectance spectra of stacked dielectric heat mirrors for the cases of the step, linear, cubic and quintic interfacial refractive index profiles are considered and the results are provided from Figure 4-41 through Figure 4-52.

Figure 4-41 shows the transmittance spectra dependency of the first stack and second stack reflectance peak positions for $[HL]^5_{f1}\cdot[HL]^5_{f2}$, $[H_LL_L]^5_{f1}\cdot[H_LL_L]^5_{f2}$, $[H_CL_C]^5_{f1}\cdot[H_CL_C]^5_{f2}$ and $H_QL_Q]^5_{f1}\cdot[H_QL_Q]^5_{f2}$. As can be seen, $[HL]^5_{f1}\cdot[HL]^5_{f2}$ shows a drastic drop in the amount of solar irradiance transmitted with a maximum transmittance of just ~75%. This is while, $[H_LL_L]^5_{f1}\cdot[H_LL_L]^5_{f2}$, $[H_CL_C]^5_{f1}\cdot[H_CL_C]^5_{f2}$ and $[H_QL_Q]^5_{f1}\cdot[H_QL_Q]^5_{f2}$ show much better transmittance, with values as high as 97 % in most cases. With respect to Figure 4-42, for the fraction of blackbody spectral power reflected by different double-stack dielectric mirrors with $[HL]^5_{f1}\cdot[HL]^5_{f2}$, $[H_LL_L]^5_{f1}\cdot[H_LL_L]^5_{f2}$, $[H_CL_C]^5_{f1}\cdot[H_CL_C]^5_{f2}$ and $[H_QL_Q]^5_{f1}\cdot[H_QL_Q]^5_{f2}$ and various reflectance peak positions for the first and second stacks, although $[HL]^5_{f1}\cdot[HL]^5_{f2}$ provides higher reflectance compared to the rest of the profiles, for the maximum peak positions the results are as high as ~54 % and 49 % for $[HL]^5_{f1}\cdot[HL]^5_{f2}$ and $[H_QL_Q]^5_{f1}\cdot[H_QL_Q]^5_{f2}$, respectively. This case is related to the dielectric mirror design with f1= 6,600 nm and f2= 9,200 nm.

As discussed earlier, the equilibrium temperature of a blackbody receiver under a dielectric heat mirror that is subjected to solar irradiation is proportional to $\left(\frac{t}{\varepsilon}\right)^{1/4}$. Figure 4-43 depicts the temperature dependency of a receiver, when subjected to solar radiation and covered with $[HL]^5_{f1}\cdot[HL]^5_{f2}$, $[H_LL_L]^5_{f1}\cdot[H_LL_L]^5_{f2}$, $[H_CL_C]^5_{f1}\cdot[H_CL_C]^5_{f2}$ and $[H_QL_Q]^5_{f1}\cdot[H_QL_Q]^5_{f2}$, on the values of f1 and f2. Accordingly, the best result for $[HL]^5_{f1}\cdot[HL]^5_{f2}$ is achieved with f1= 5,800 nm and f2= 9,800 nm and the corresponding $\left(\frac{t}{\varepsilon}\right)^{1/4}$ is equal to 1.129. For the case of the $[H_LL_L]^5_{f1}\cdot[H_LL_L]^5_{f2}$ structure, the best result is achieved with f1= 6,600 nm and f2= 9,200 nm and

the corresponding $\left(\frac{t}{\varepsilon}\right)^{1/4}$ is equal to 1.14. For the case of the $[H_CL_C]^5_{f1}\cdot[H_CL_C]^5_{f2}$ structure, the best result is achieved with f1= 6,600 nm and f2= 9,200 nm and the corresponding $\left(\frac{t}{\varepsilon}\right)^{1/4}$ is equal to 1.187. As can be seen in Figure 4-43.d, altogether $[H_QL_Q]^5_{f1}\cdot[H_QL_Q]^5_{f2}$ provided the best design followed by $[H_CL_C]^5_{f1}\cdot[H_CL_C]^5_{f2}$ and $[H_LL_L]^5_{f1}\cdot[H_LL_L]^5_{f2}$ where the best design is related to f1= 6,600 nm and f2= 9,200 nm and the corresponding $\left(\frac{t}{\varepsilon}\right)^{1/4}$ is equal to 1.21. Accordingly, the corresponding results including the transmittance and reflectance spectra as well as the fraction of spectral power transmitted from the solar spectrum and the fraction of spectral power reflected by the dielectric mirror are provided in Figure 4-44 to Figure 4-46. With respect to these results, $[H_QL_Q]^5_{f1}\cdot[H_QL_Q]^5_{f2}$ still provides the best design followed by $[H_CL_C]^5_{f1}\cdot[H_CL_C]^5_{f2}$ and $[H_LL_L]^5_{f1}\cdot[H_LL_L]^5_{f2}$.

Figure 4-47 shows the transmittance spectra dependency on the second stack and third stack reflectance peak positions (f1, f2 and f3) for the triple-stack transparent dielectric heat mirrors denoted as $[HL]^5_{f1}\cdot[HL]^5_{f2}\cdot[HL]^5_{f3}$, $[H_LL_L]^5_{f1}\cdot[H_LL_L]^5_{f2}\cdot[H_LL_L]^5_{f3}$, $[H_CL_C]^5_{f1}\cdot[H_CL_C]^5_{f2}\cdot[H_CL_C]^5_{f3}$ and $[H_QL_Q]^5_{f1}\cdot[H_QL_Q]^5_{f2}\cdot[H_QL_Q]^5_{f3}$. Here, the second stack has a reflectance peak position that coincides with the maximum of the thermal radiation spectra emitted from a black body at 500 K (f2= 5,800 nm) and the first stack and third stack reflectance peak positions are chosen according to the wavelength ranges from 0 nm to 15,000 nm with higher resolution in the ranges with higher blackbody intensity and less resolution in the ranges where the blackbody intensity decreases to find the best design for the triple-stack dielectric mirror.

As can be seen, $[HL]^5_{f1}\cdot[HL]^5_{f2}\cdot[HL]^5_{f3}$ exhibits a drastic drop in the fraction of spectral power transmitted from the solar spectrum with a maximum up to ~60%. This is while, $[H_LL_L]^5_{f1}\cdot[H_LL_L]^5_{f2}\cdot[H_LL_L]^5_{f3}$, $[H_CL_C]^5_{f1}\cdot[H_CL_C]^5_{f2}\cdot[H_CL_C]^5_{f3}$ and $[H_QL_Q]^5_{f1}\cdot[H_QL_Q]^5_{f2}\cdot[H_QL_Q]^5_{f3}$

show much better transmittance to as much as 98 % in most cases. With respect to Figure 4-48, the fraction of blackbody spectral power reflected by $[HL]^5_{f1}\cdot[HL]^5_{f2}\cdot[HL]^5_{f3}$, $[H_LL_L]^5_{f1}\cdot[H_LL_L]^5_{f2}\cdot[H_LL_L]^5_{f3}$, $[H_CL_C]^5_{f1}\cdot[H_CL_C]^5_{f2}\cdot[H_CL_C]^5_{f3}$ and $[H_QL_Q]^5_{f1}\cdot[H_QL_Q]^5_{f2}\cdot[H_QL_Q]^5_{f3}$ is plotted as a function of f1 and f3, and although $[HL]^5_{f1}\cdot[HL]^5_{f2}\cdot[HL]^5_{f3}$ provides higher reflectance compared to the rest of the profiles, when f1= 7,800 nm and f3= 10,500 nm the results are as high as ~80 % for both $[HL]^5_{f1}\cdot[HL]^5_{f2}\cdot[HL]^5_{f3}$ and $[H_QL_Q]^5_{f1}\cdot[H_QL_Q]^5_{f2}\cdot[H_QL_Q]^5_{f3}$. Considering the relation for temperature dependency, Figure 4-49 depicts the temperature dependency of a solar receiver on f1 and f3 when it is covered with $[HL]^5_{f1}\cdot[HL]^5_{f2}\cdot[HL]^5_{f3}$, $[H_LL_L]^5_{f1}\cdot[H_LL_L]^5_{f2}\cdot[H_LL_L]^5_{f3}$, $[H_CL_C]^5_{f1}\cdot[H_CL_C]^5_{f2}\cdot[H_CL_C]^5_{f3}$ and $[H_QL_Q]^5_{f1}\cdot[H_QL_Q]^5_{f2}\cdot[H_QL_Q]^5_{f3}$. Accordingly, the best result with the $[HL]^5_{f1}\cdot[HL]^5_{f2}\cdot[HL]^5_{f3}$ structure is achieved with f1= 8,200 nm and f3= 12,000 nm and the corresponding $\left(\frac{t}{\varepsilon}\right)^{1/4}$ is equal to 1.267. For the case of the $[H_LL_L]^5_{f1}\cdot[H_LL_L]^5_{f2}\cdot[H_LL_L]^5_{f3}$ structure, the best result is achieved with f1= 7,600 nm and f3= 10,000 nm and the corresponding $\left(\frac{t}{\varepsilon}\right)^{1/4}$ is equal to 1.223. For the case of the $[H_CL_C]^5_{f1}\cdot[H_CL_C]^5_{f2}\cdot[H_CL_C]^5_{f3}$ structure, the best result is achieved with f1= 7,800 nm and f3= 10,500 nm and the corresponding $\left(\frac{t}{\varepsilon}\right)^{1/4}$ is equal to 1.302. As can be seen in Figure 4-49.d, altogether $[H_QL_Q]^5_{f1}\cdot[H_QL_Q]^5_{f2}\cdot[H_QL_Q]^5_{f3}$ provided the best design where the best design is related to f1= 7,800 nm and f3= 10,500 nm and the corresponding $\left(\frac{t}{\varepsilon}\right)^{1/4}$ is equal to 1.341. Accordingly, the corresponding results including the transmittance and reflectance spectra as well as the fraction of spectral power transmitted from the solar spectrum and the fraction of spectral power reflected by $[HL]^5_{f1}\cdot[HL]^5_{f2}\cdot[HL]^5_{f3}$, $[H_LL_L]^5_{f1}\cdot[H_LL_L]^5_{f2}\cdot[H_LL_L]^5_{f3}$, $[H_CL_C]^5_{f1}\cdot[H_CL_C]^5_{f2}\cdot[H_CL_C]^5_{f3}$ and $[H_QL_Q]^5_{f1}\cdot[H_QL_Q]^5_{f2}\cdot[H_QL_Q]^5_{f3}$ with $W_{grin}=0.5\cdot(d_{L+H})$ and f1 = 7,800 nm and f3 = 10,500 nm are provided in Figure 4-50 through Figure 4-52. With respect to these results, the

$[H_QL_Q]^5_{f1}\cdot[H_QL_Q]^5_{f2}\cdot[H_QL_Q]^5_{f3}$ still provides the best design followed by $[H_CL_C]^5_{f1}\cdot[H_CL_C]^5_{f2}\cdot[H_CL_C]^5_{f3}$ and $[H_LL_L]^5_{f1}\cdot[H_LL_L]^5_{f2}\cdot[H_LL_L]^5_{f3}$.

In order to verify the results provided so far for a triples-stack dielectric mirror, instead of using a second stack with a reflectance peak position that coincides with the maximum of the thermal radiation spectra emitted from a black body at 500 K , the values for the first, second and third stack reflectance peak positions can be chosen according to the wavelength ranges from 0 nm to 15,000 nm with higher resolution in the ranges with higher blackbody intensity and less resolution in the ranges where the blackbody intensity decreases to find the best design for the triple-stack dielectric mirror. Hence, in the following the results for this case is presented and discussed.

Figure 4-53 shows the fraction of solar spectral power transmitted through $[H_QL_Q]^5_{f1}\cdot[H_QL_Q]^5_{f2}\cdot[H_QL_Q]^5_{f3}$, the fraction of blackbody spectral power reflected by $[H_QL_Q]^5_{f1}\cdot[H_QL_Q]^5_{f2}\cdot[H_QL_Q]^5_{f3}$ and the temperature of a blackbody solar receiver covered with $[H_QL_Q]^5_{f1}\cdot[H_QL_Q]^5_{f2}\cdot[H_QL_Q]^5_{f3}$ as a function of f1, f2, and f3. In order to find the best design, one can show the planar cross-sectional views for the optimal values of f1, f2 and f3. Accordingly, Figure 4-54 illustrates these cross-sectional views for the fraction of solar spectral power transmitted through $[H_QL_Q]^5_{f1}\cdot[H_QL_Q]^5_{f2}\cdot[H_QL_Q]^5_{f3}$ (Figure a.), the fraction of blackbody spectral power reflected by $[H_QL_Q]^5_{f1}\cdot[H_QL_Q]^5_{f2}\cdot[H_QL_Q]^5_{f3}$ (Figure b.), and the temperature dependency of a blackbody solar receiver for the case where $\left(\frac{t}{\varepsilon}\right)^{1/4}$ has the maximum value equal to 1.3409 when f1= 6,000 nm, f2= 8,000 nm and f3=10,750 nm (Figure c.).

Interestingly, even after optimizing all three reflectance peak positions (f1, f2, and f3) the best design for the triple-stack dielectric mirror is still the case where the second stack has a reflectance peak position that coincides with the maximum of the thermal radiation spectra emitted from a

black body at 500 K (f2= 5,800 nm) when f1= 7,800 nm and f3= 10,500 nm and the corresponding $\left(\frac{t}{\varepsilon}\right)^{1/4}$ has the maximum value equal to 1.341.

a.

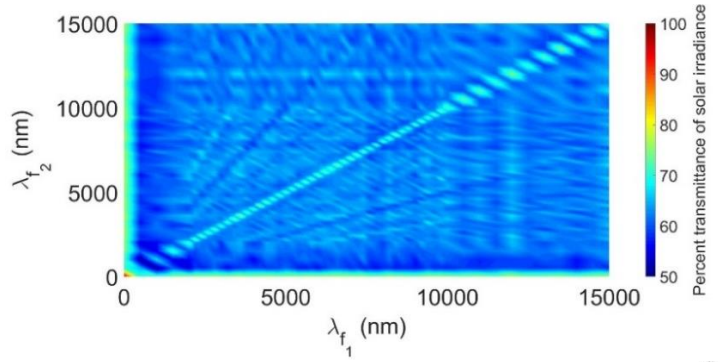

b.

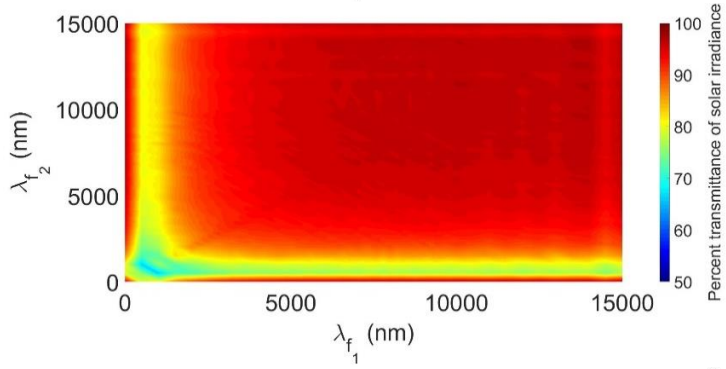

c.

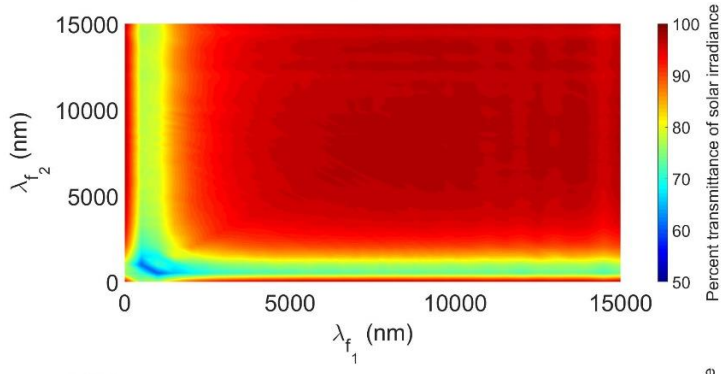

d.

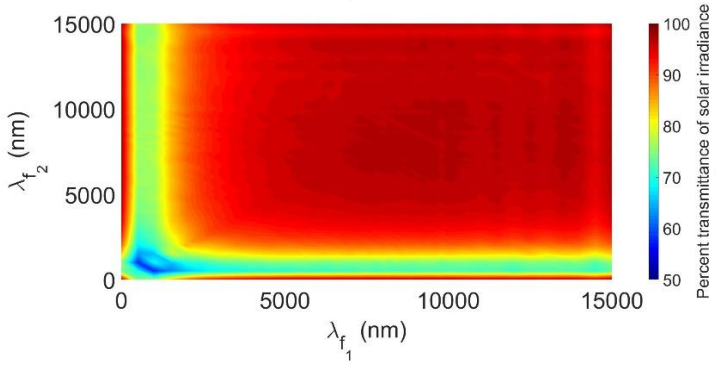

Figure 4-41. The fraction of solar spectral power transmitted through $[HL]^5_{f1}\cdot[HL]^5_{f2}$ (Figure a.), $[H_LL_L]^5_{f1}\cdot[H_LL_L]^5_{f2}$ (Figure b.), $[H_CL_C]^5_{f1}\cdot[H_CL_C]^5_{f2}$ (Figure c.) and $[H_QL_Q]^5_{f1}\cdot[H_QL_Q]^5_{f2}$ (Figure d.) plotted as a function of the reflectance peak positions for the first dielectric mirror (x axis) and the second dielectric mirror (y axis)

a.

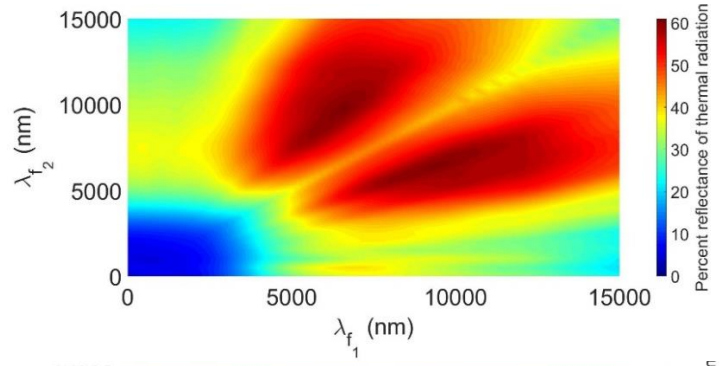

b.

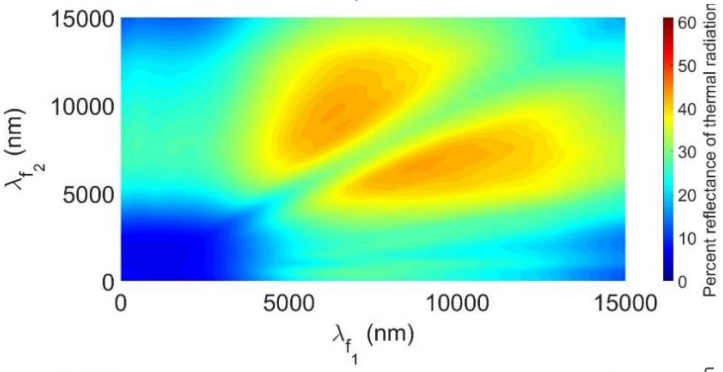

c.

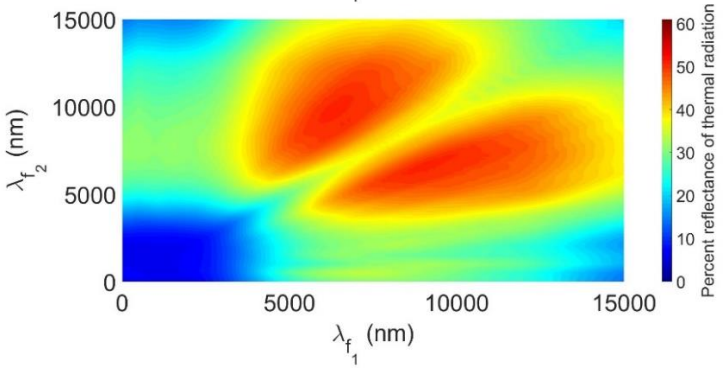

d.

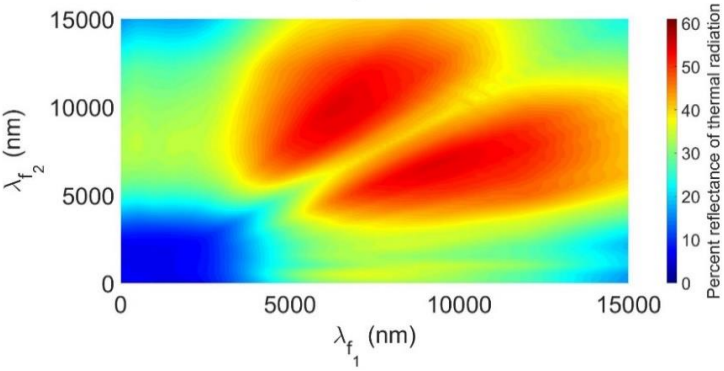

Figure 4-42. The fraction of blackbody spectral power reflected by $[HL]^5_{f1}\cdot[HL]^5_{f2}$ (Figure a.), $[H_LL_L]^5_{f1}\cdot[H_LL_L]^5_{f2}$ (Figure b.), $[H_CL_C]^5_{f1}\cdot[H_CL_C]^5_{f2}$ (Figure c.) and $[H_QL_Q]^5_{f1}\cdot[H_QL_Q]^5_{f2}$ (Figure d.) considering different reflectance peak positions for the first (x axis) and second stack (y axis)

a.

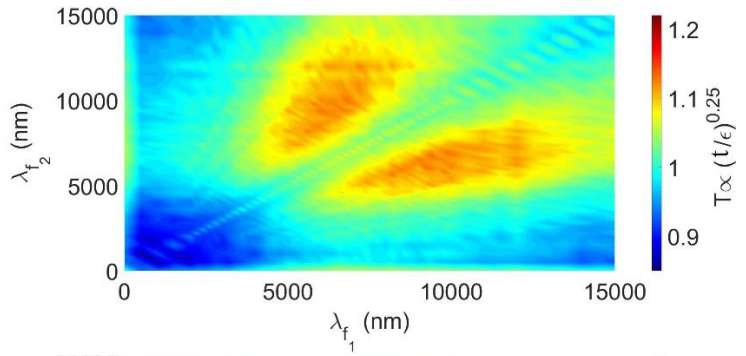

b.

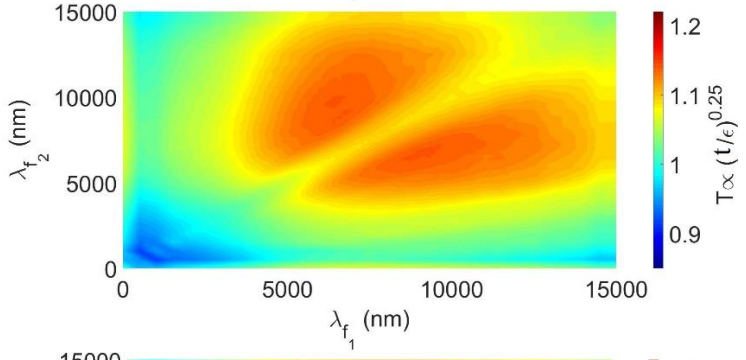

c.

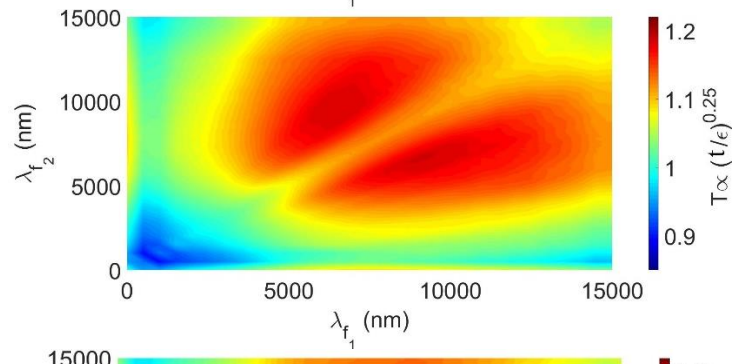

d.

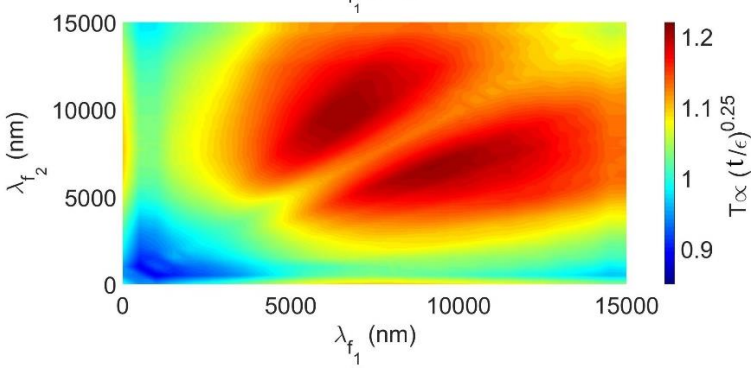

Figure 4-43. Temperature dependency of a blackbody solar receiver covered with $[HL]^5_{f1}\cdot[HL]^5_{f2}$ (Figure a.), $[H_LL_L]^5_{f1}\cdot[H_LL_L]^5_{f2}$ (Figure b.), $[H_CL_C]^5_{f1}\cdot[H_CL_C]^5_{f2}$ (Figure c.) and $[H_QL_Q]^5_{f1}\cdot[H_QL_Q]^5_{f2}$ (Figure d.) on the reflectance peak positions for the first (x axis) and second dielectric mirror (y axis) within the stacked structure.

a.

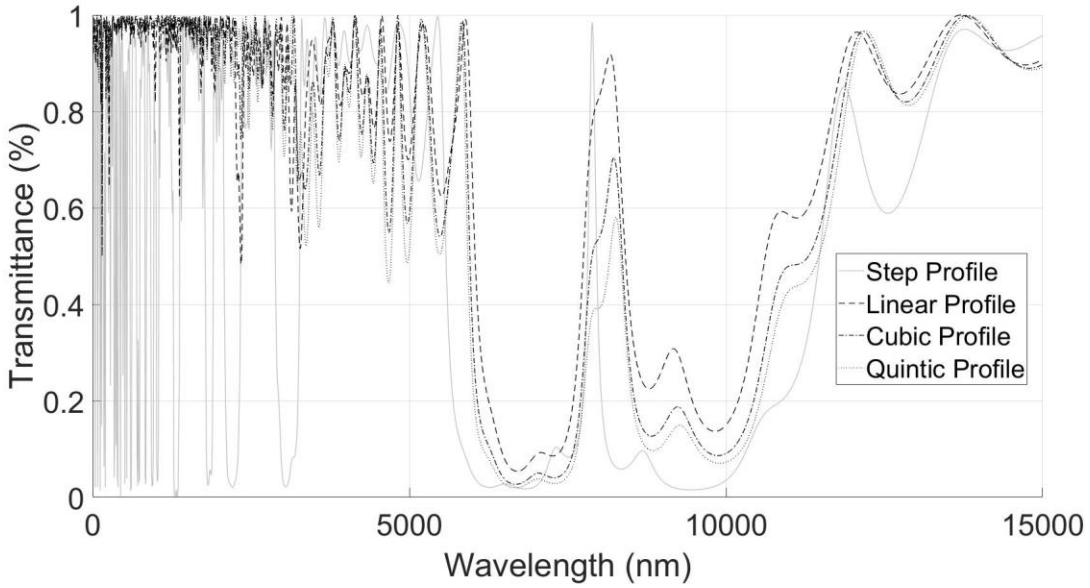

b.

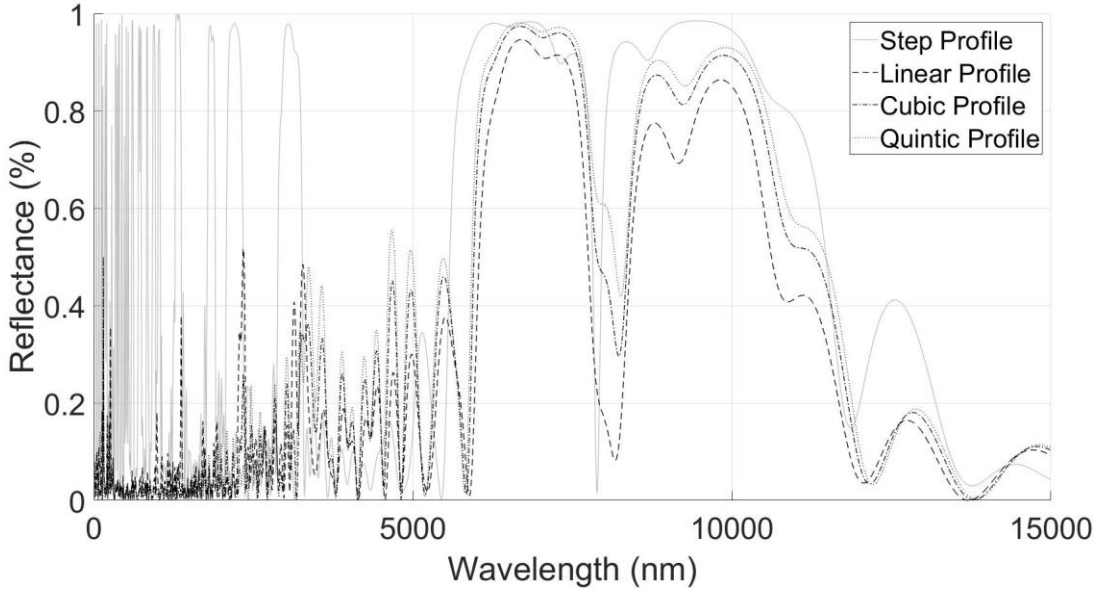

Figure 4-44. Transmittance (Figure a.) and reflectance (Figure b.) spectra for $[HL]^{5}_{f1}\cdot[HL]^{5}_{f2}$, $[H_LL_L]^{5}_{f1}\cdot[H_LL_L]^{5}_{f2}$, $[H_CL_C]^{5}_{f1}\cdot[H_CL_C]^{5}_{f2}$ and $[H_QL_Q]^{5}_{f1}\cdot[H_QL_Q]^{5}_{f2}$ with $W_{grin}=0.5\cdot(d_{L+H})$ considering the reflectance peak position of the first and second dielectric mirrors within the stack are at 6,600 nm and 9,200 nm, respectively.

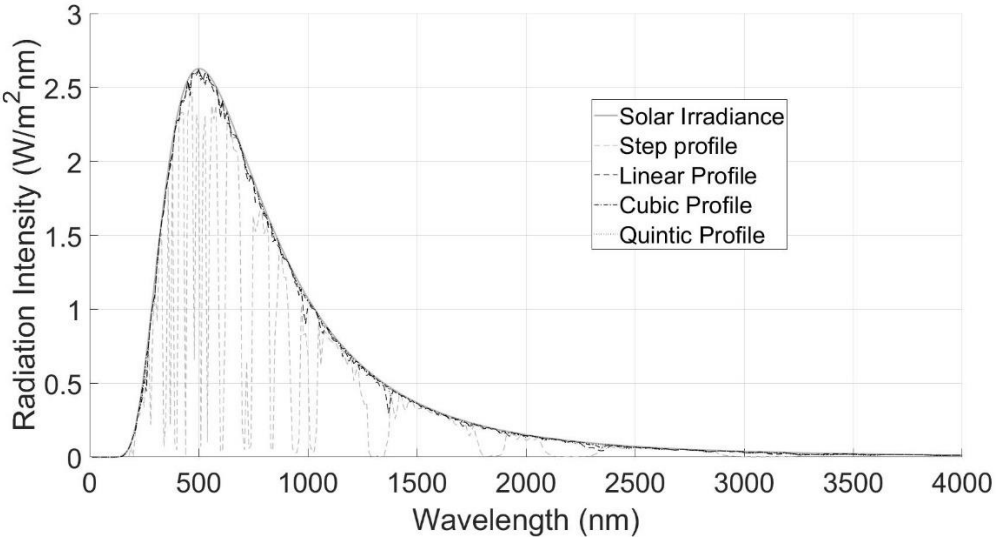

Figure 4-45. Solar irradiance and the amount of spectral power transmitted through $[HL]^{5}_{f1}\cdot[HL]^{5}_{f2}$, $[H_LL_L]^{5}_{f1}\cdot[H_LL_L]^{5}_{f2}$, $[H_CL_C]^{5}_{f1}\cdot[H_CL_C]^{5}_{f2}$ and $[H_QL_Q]^{5}_{f1}\cdot[H_QL_Q]^{5}_{f2}$ with $W_{grin}=0.5\cdot(d_{L+H})$ considering the reflectance peak position of the first and second dielectric mirrors within the stack are at 6,600 nm and 9,200 nm, respectively

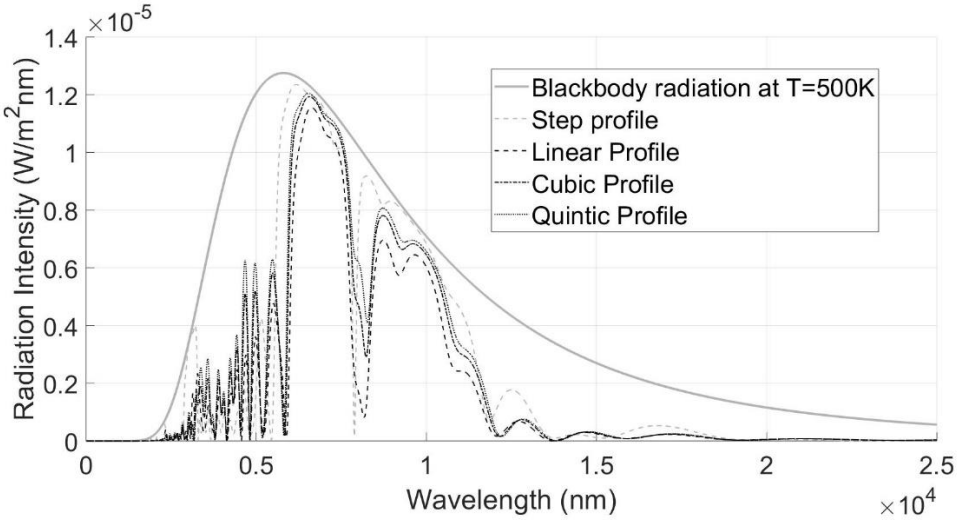

Figure 4-46. Blackbody radiation at T=500 K and the amount of spectral power reflected by $[HL]^{5}_{f1}\cdot[HL]^{5}_{f2}$, $[H_LL_L]^{5}_{f1}\cdot[H_LL_L]^{5}_{f2}$, $[H_CL_C]^{5}_{f1}\cdot[H_CL_C]^{5}_{f2}$ and $[H_QL_Q]^{5}_{f1}\cdot[H_QL_Q]^{5}_{f2}$ with $W_{grin}=0.5\cdot(d_{L+H})$ considering the reflectance peak position of the first and second dielectric mirrors within the stack are at 6,600 nm and 9,200 nm, respectively

a.

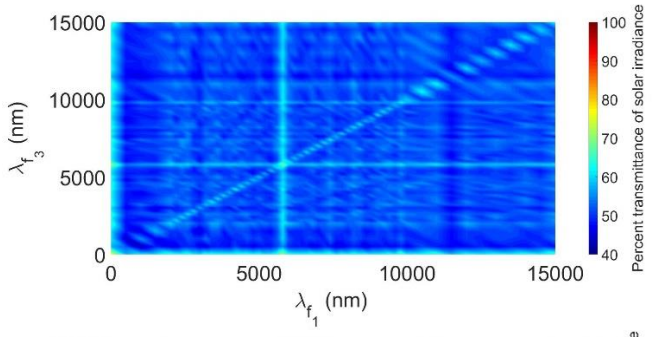

b.

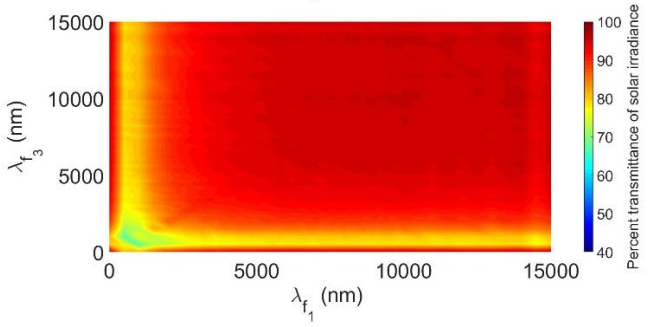

c.

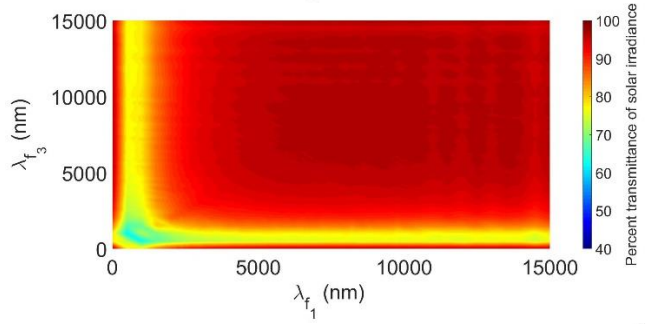

d.

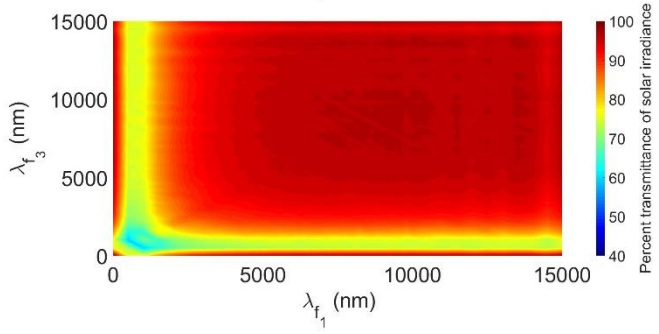

Figure 4-47. The fraction of solar spectral power transmitted through $[HL]^5_{f1}\cdot[HL]^5_{f2}\cdot[HL]^5_{f3}$ (Figure a.), $[H_LL_L]^5_{f1}\cdot[H_LL_L]^5_{f2}\cdot[H_LL_L]^5_{f3}$ (Figure b.), $[H_CL_C]^5_{f1}\cdot[H_CL_C]^5_{f2}\cdot[H_CL_C]^5_{f3}$ (Figure c.) and $[H_QL_Q]^5_{f1}\cdot[H_QL_Q]^5_{f2}\cdot[H_QL_Q]^5_{f3}$ (Figure d.) considering different peak positions for the second stack (x axis) and third stack (y axis)

a.

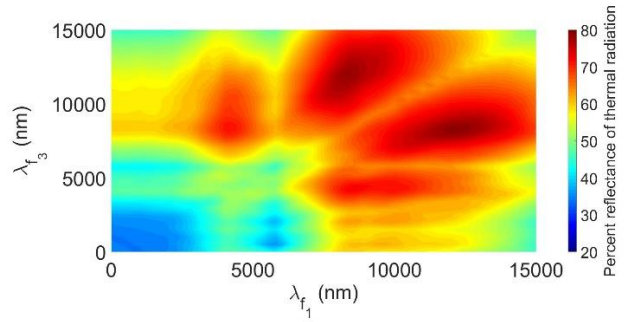

b.

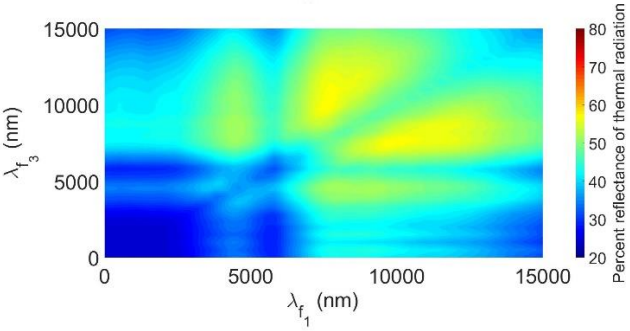

c.

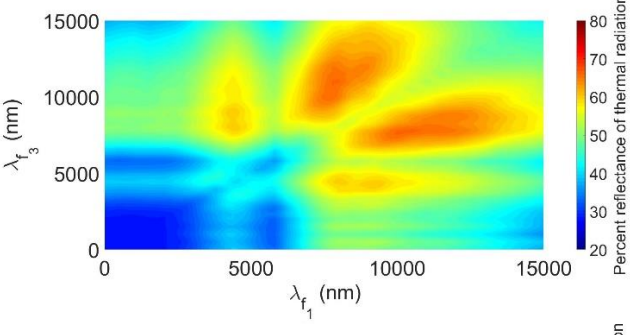

d.

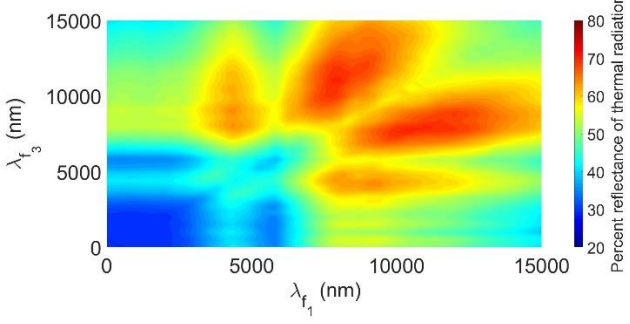

Figure 4-48. The fraction of blackbody spectral power reflected by $[HL]^5_{f1}\cdot[HL]^5_{f2}\cdot[HL]^5_{f3}$ (Figure a.), $[H_LL_L]^5_{f1}\cdot[H_LL_L]^5_{f2}\cdot[H_LL_L]^5_{f3}$ (Figure b.), $[H_CL_C]^5_{f1}\cdot[H_CL_C]^5_{f2}\cdot[H_CL_C]^5_{f3}$ (Figure c.) and $[H_QL_Q]^5_{f1}\cdot[H_QL_Q]^5_{f2}\cdot[H_QL_Q]^5_{f3}$ (Figure d.) considering different peak positions for the second (x axis) and third stack (y axis)

a.

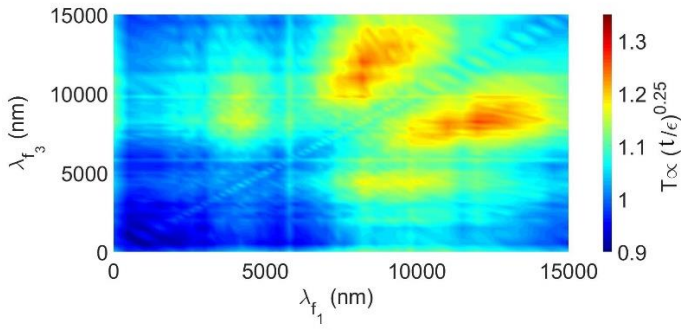

b.

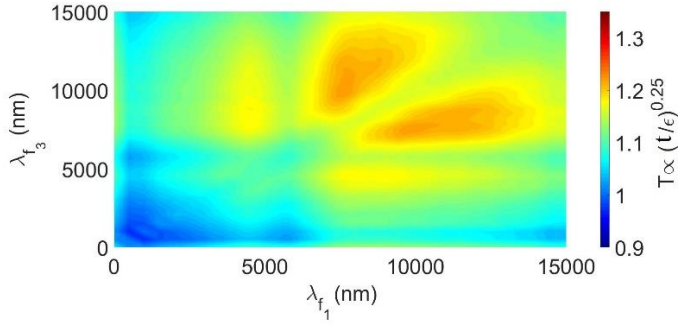

c.

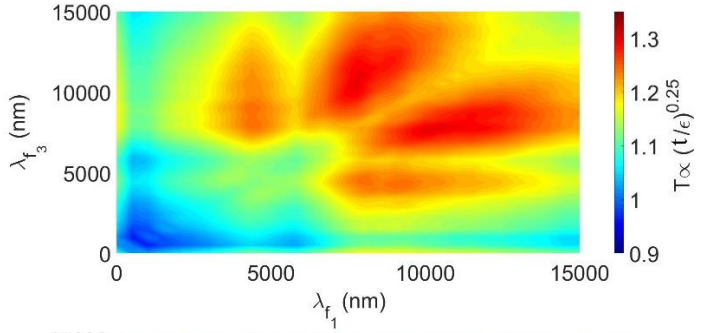

d.

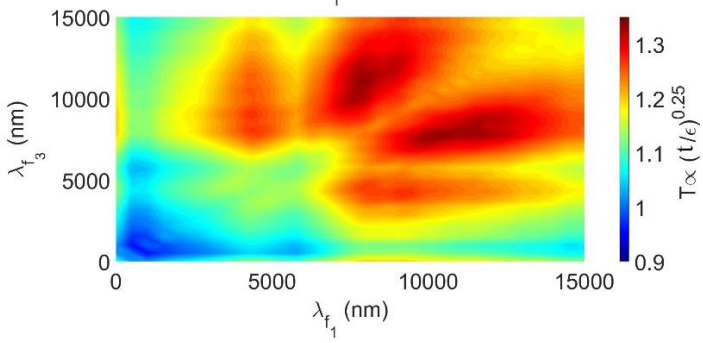

Figure 4-49. Temperature dependency of a solar blackbody receiver covered with $[HL]^5_{f1}\cdot[HL]^5_{f2}\cdot[HL]^5_{f3}$ (Figure a.), $[H_LL_L]^5_{f1}\cdot[H_LL_L]^5_{f2}\cdot[H_LL_L]^5_{f3}$ (Figure b.), $[H_CL_C]^5_{f1}\cdot[H_CL_C]^5_{f2}\cdot[H_CL_C]^5_{f3}$ (Figure c.) and $[H_QL_Q]^5_{f1}\cdot[H_QL_Q]^5_{f2}\cdot[H_QL_Q]^5_{f3}$ (Figure d.) on the reflectance peak positions for the first (x axis) and third dielectric mirrors (y axis) within the stacked structure

a.

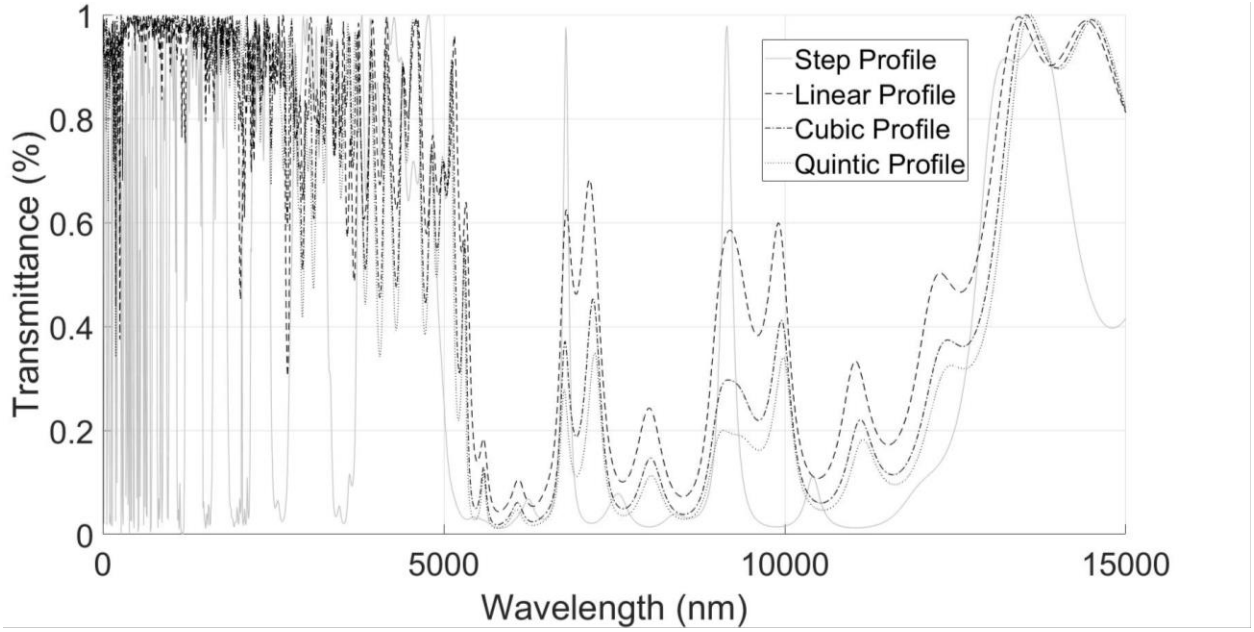

b.

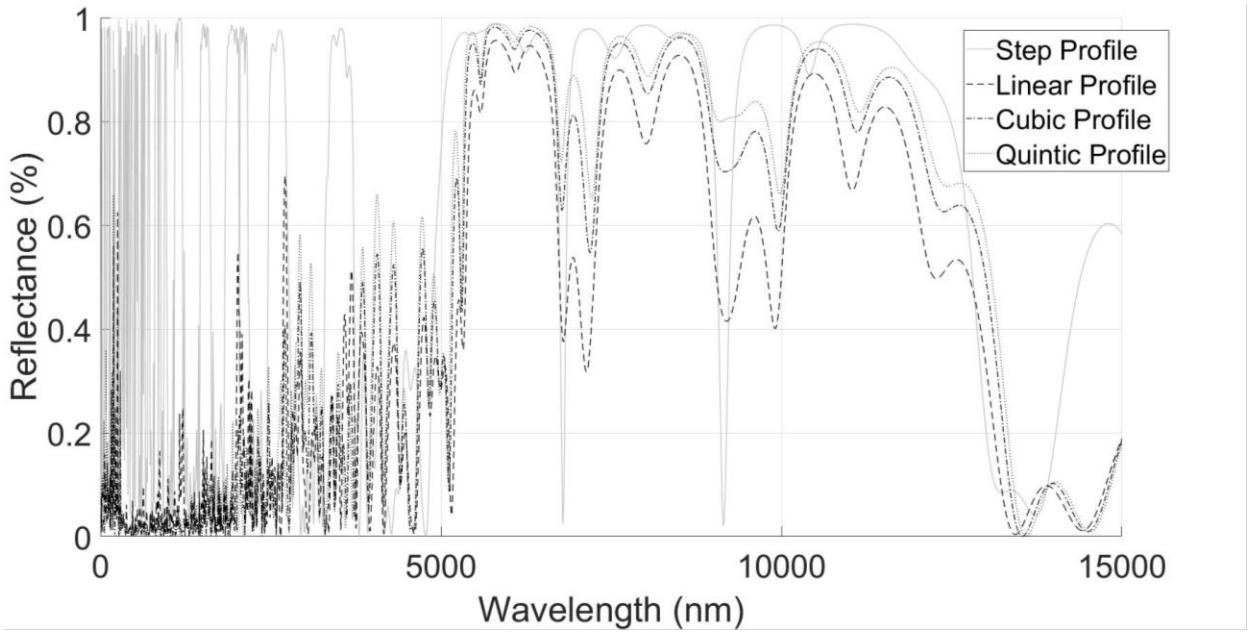

Figure 4-50. Transmittance (Figure a.) and reflectance (Figure b.) spectra for $[HL]^{5}_{f1}\cdot[HL]^{5}_{f2}\cdot[HL]^{5}_{f3}$, $[H_LL_L]^{5}_{f1}\cdot[H_LL_L]^{5}_{f2}\cdot[H_LL_L]^{5}_{f3}$, $[H_CL_C]^{5}_{f1}\cdot[H_CL_C]^{5}_{f2}\cdot[H_CL_C]^{5}_{f3}$ and $[H_QL_Q]^{5}_{f1}\cdot[H_QL_Q]^{5}_{f2}\cdot[H_QL_Q]^{5}_{f3}$ with $W_{grin}=0.5\cdot(d_{L+H})$ considering f1 = 7,800 nm and f3 = 10,500 nm.

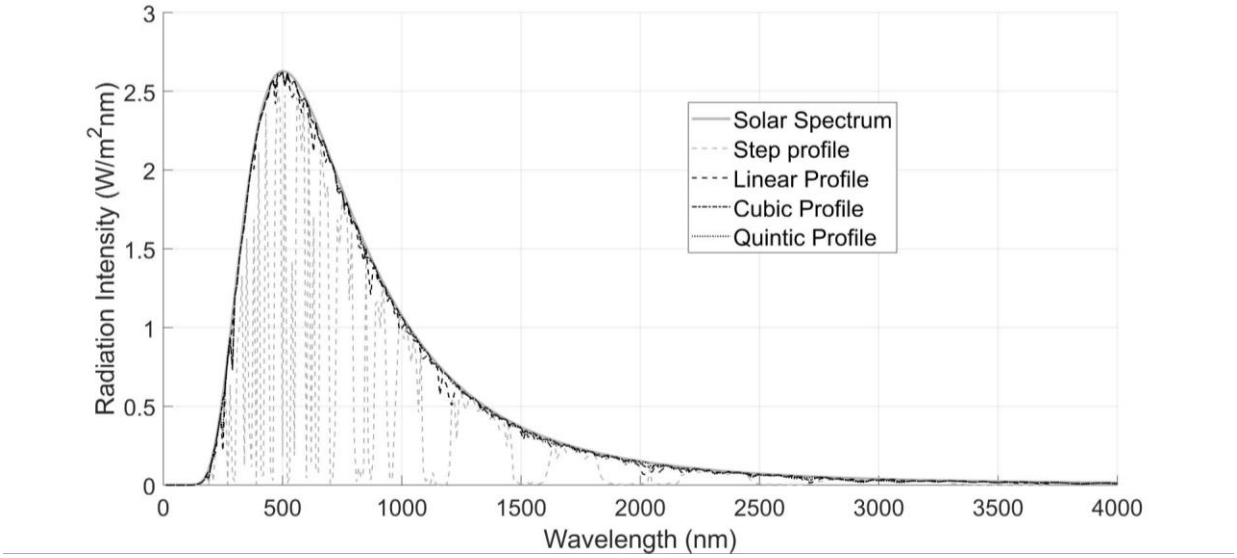

Figure 4-51. Solar irradiance and the amount of spectral power transmitted through $[HL]^5_{f1}\cdot[HL]^5_{f2}\cdot[HL]^5_{f3}$, $[H_LL_L]^5_{f1}\cdot[H_LL_L]^5_{f2}\cdot[H_LL_L]^5_{f3}$, $[H_CL_C]^5_{f1}\cdot[H_CL_C]^5_{f2}\cdot[H_CL_C]^5_{f3}$ and $[H_QL_Q]^5_{f1}\cdot[H_QL_Q]^5_{f2}\cdot[H_QL_Q]^5_{f3}$ with $W_{grin}=0.5\cdot(t_{L+H})$ considering f1 = 7,800 nm and f3 = 10,500 nm

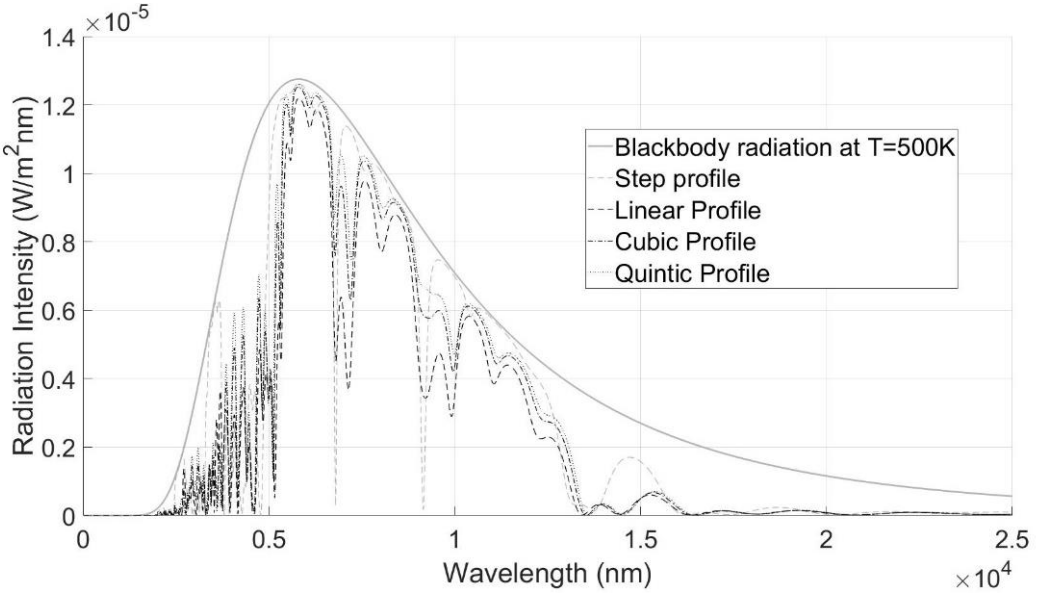

Figure 4-52. Blackbody radiation and the amount of spectral power reflected by $[HL]^5_{f1}\cdot[HL]^5_{f2}\cdot[HL]^5_{f3}$, $[H_LL_L]^5_{f1}\cdot[H_LL_L]^5_{f2}\cdot[H_LL_L]^5_{f3}$, $[H_CL_C]^5_{f1}\cdot[H_CL_C]^5_{f2}\cdot[H_CL_C]^5_{f3}$ and $[H_QL_Q]^5_{f1}\cdot[H_QL_Q]^5_{f2}\cdot[H_QL_Q]^5_{f3}$ with $W_{grin}=0.5\cdot(d_{L+H})$ considering f1 = 7,800 nm and f2 = 10,500 nm.

a.

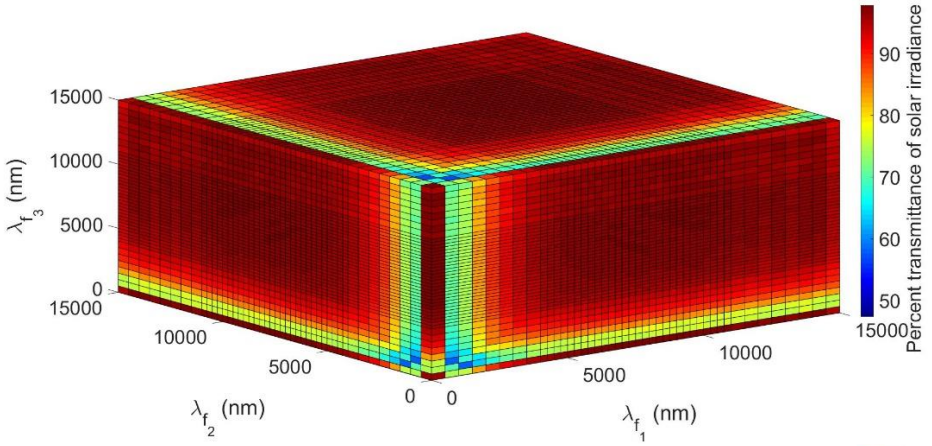

b.

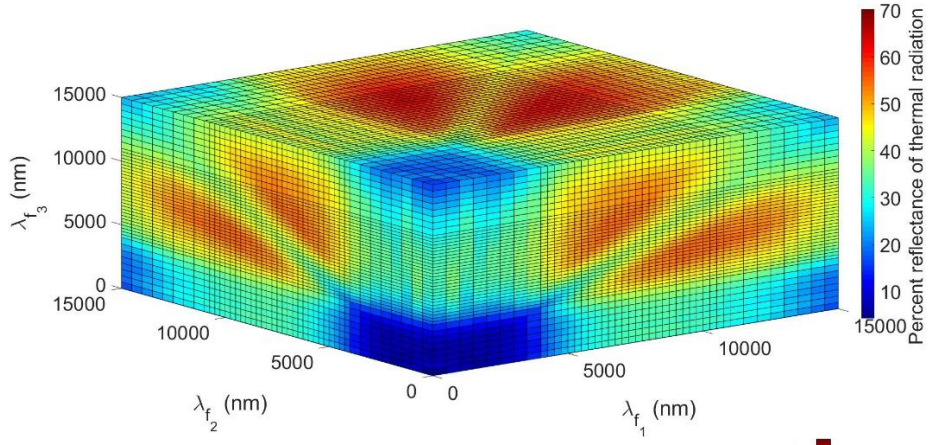

c.

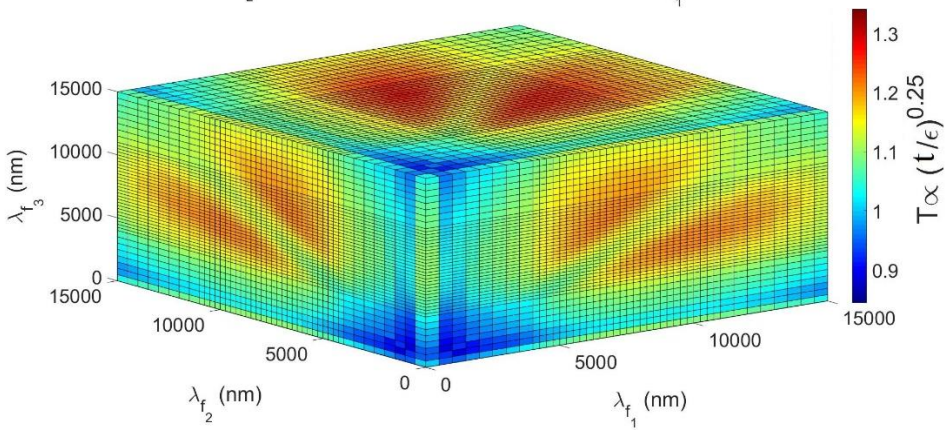

Figure 4-53. The fraction of solar spectral power transmitted through different triple-stack designs (Figure a.), the fraction of blackbody spectral power reflected by different triple-stack dielectric mirrors (Figure b.) and temperature dependency of the blackbody to different peak positions (Figure c.) with the $[H_QL_Q]^5{}_{f1}\cdot[H_QL_Q]^5{}_{f2}\cdot[H_QL_Q]^5{}_{f3}$ considering selected ranges of peak positions for the first stack (x axis), second stack (y axis) and third stack (z axis).

a.

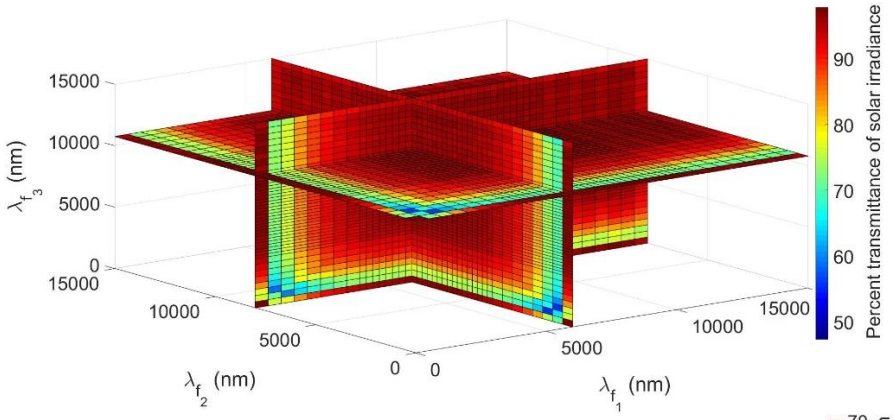

b.

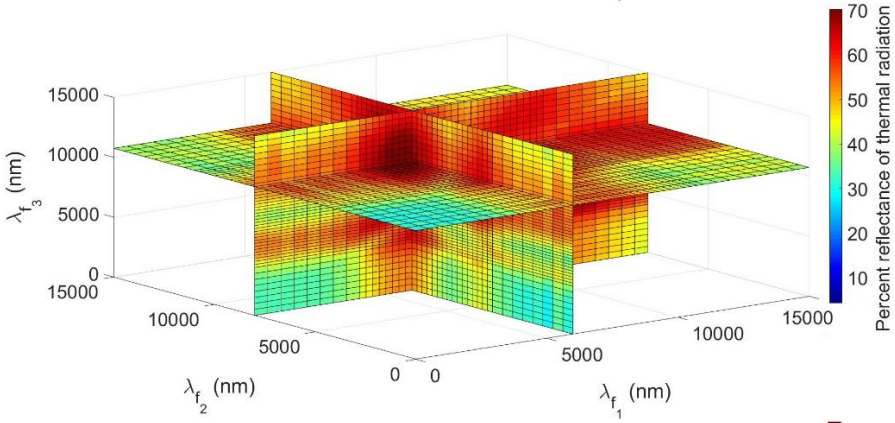

c.

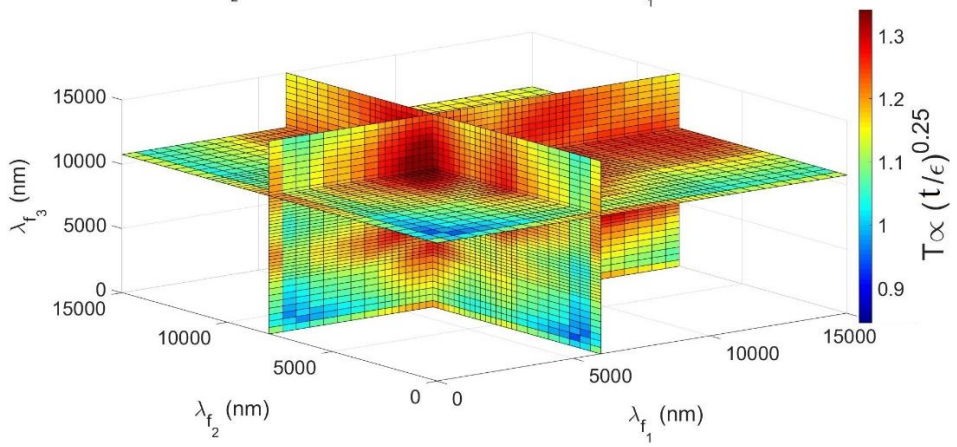

Figure 4-54. The fraction of solar spectral power transmitted through different triple-stack designs(Figure a.), the fraction of blackbody spectral power reflected by different triple-stack dielectric mirrors (Figure b.) and temperature dependency of the blackbody to different peak positions (Figure c.) with the $[H_QL_Q]^5{}_{f1}\cdot[H_QL_Q]^5{}_{f2}\cdot[H_QL_Q]^5{}_{f3}$ considering three different sets of the peak positions for the first stack (x axis), second stack (y axis) and third stack (z axis) in order to find the best design.

4-6. Effects of the absorptance of the films within the dielectric mirror on its performance

In this section the sensitivity of the absorptance, transmittance and reflectance spectra of dielectric heat mirrors towards changes in the wavelength dependant refractive index and extinction coefficient of its films is analyzed for different dielectric mirror designs. As discussed earlier, throughout this thesis it has been assumed that the index of refraction of the alternating layers in the dielectric mirror are 1.3 and 2.0, representative of a silica NP and TCO films, respectively. However, up to this point it has been assumed that the extinction coefficient, or light absorption in the thin films comprising the dielectric heat mirrors, is zero. In this section, the sensitivity analysis will be done with the lower index of refraction material considered to be silica NP and the higher index of refraction materials considered to be either TiO_2 or ZnSe thin films, taking into consideration the non-zero value of the extinction coefficient for these films. The results for the absorptance, transmittance and reflectance spectra for different index of refraction profiles are provided in Figure 4-55 through Figure 4-62.

In this work, the index of refraction and extinction coefficient of the SiO_2 NP film is approximated using the results from a solid thin film [162-163], and with respect to the method described in Chapter 2-6-2, considering the SiO_2 NP film is 30 % porous.

Figure 4-55 illustrates the wavelength dependence of the refractive index (n) and extinction coefficient (k) for a SiO_2 and SiO_2 NP thin film (Figure a.) as a low index material and a TiO_2 thin film (Figure b.) [163] as a high index TCO. As can be seen, for both materials, the graph shows an approximately zero value for the extinction coefficient up to 8,000 nm and a smooth trend for the refractive index values, which is always below 1.5 for the SiO_2 film and around 2 for the TiO_2 film. Figure 4-56 to Figure 4-58, show the absorptance (Figure a.), transmittance (Figure b.) and

reflectance (Figure c.) spectra of $[HL]^5$, $[H_LL_L]^5$, $[H_CL_C]^5$ and $[H_QL_Q]^5$ considering the wavelength dependant n and k values of the SiO_2 NP and TiO_2 thin films shown in Figure 4-55. With respect to these results, considering SiO_2 NP and TiO_2 thin films as low index and high index materials in the dielectric mirror design, but with a k value of zero, the fraction of spectral power transmitted through $[HL]^5$ is 67.29 %, through $[H_LL_L]^5$ is 94.84 %, through $[H_CL_C]^5$ is 96.73 % and through $[H_QL_Q]^5$ is 96.72 %. When considering the dielectric mirrors comprised of SiO_2 NP and TiO_2 thin films (with non-zero k values) the fraction of spectral power transmitted through $[HL]^5$, $[H_LL_L]^5$, $[H_CL_C]^5$ and $[H_QL_Q]^5$ reduces to 65.84 %, 84.72 %, 83.83 % and 84.73 %, respectively, for the case with wavelength dependant n and k. It would be interesting to note here that the corresponding values for the original calculations with constant refractive indices resulted in 76.91%, 96.45%, 97.36% and 97.25% for the fraction of spectral power transmitted through the $[HL]^5$, $[H_LL_L]^5$, $[H_CL_C]^5$ and $[H_QL_Q]^5$ stacking sequences, respectively. The absorptance spectra shows the contribution of extinction coefficient for longer wavelengths around 9,000 nm which results in a lower reflectance around this wavelength decreasing the fraction of spectral power reflected with 49.61 % for the $[HL]^5$, 42.47 % for the $[H_LL_L]^5$, 48.68 % for the $[H_CL_C]^5$, and 50.88 % for the $[H_QL_Q]^5$ for the dielectric mirrors with k = 0 to lower values of 47.33 %, 37.53 %, 41.12 % and 42.42 % for the case with wavelength dependant n and k. Also, the corresponding values for the original calculations with constant refractive indices resulted in 30.11%, 30.11%, 35.03% and 37.22% for the fraction of spectral power reflected by $[HL]^5$, $[H_LL_L]^5$, $[H_CL_C]^5$ and $[H_QL_Q]^5$, respectively.

illustrates the variation of the refractive index (n) and extinction coefficient (k) for a SiO_2 NP thin film (Figure a.) as a low index material and the ZnSe thin film [164-165] (Figure b.) as a high index TCO. As can be seen, the wavelength dependant graph for the ITO thin film shows a high

dependency on wavelength for both n and k values which results in more absorptance and accordingly higher variation in the reflectance spectra. Figure 4-60 to Figure 4-62, show the absorptance (Figure a.), transmittance (Figure b.) and reflectance (Figure c.) spectra of $[HL]^5$, $[H_LL_L]^5$, $[H_CL_C]^5$ and $[H_QL_Q]^5$ considering the wavelength dependant n and k for the SiO_2 NP and ZnSe thin films shown in Figure 4-59. With respect to these results, considering SiO_2 NP and ZnSe thin films as low index and high index materials in the dielectric mirror design, but with a k value of zero, the fraction of spectral power transmitted through $[HL]^5$ is 65.03 %, through $[H_LL_L]^5$ is 94.39 %, through $[H_CL_C]^5$ is 96.17 % and through $[H_QL_Q]^5$ is 96.13 %. When considering the dielectric mirrors comprised of SiO_2 NP and ITO thin films (with non-zero k values) the fraction of spectral power transmitted through $[HL]^5$, $[H_LL_L]^5$, $[H_CL_C]^5$ and $[H_QL_Q]^5$ reduces to 65.03 %, 84.22 %, 85.86 % and 85.82 %, respectively, for the case with wavelength dependant n and k. The absorptance spectra shows the contribution of extinction coefficient for longer wavelengths after 8,000 nm which results in a lower reflectance around this wavelength decreasing the fraction of spectral power reflected with 60.86 % for the $[HL]^5$, 53.94 % for the $[H_LL_L]^5$, 57.07 % for the $[H_CL_C]^5$, and 58.45 % for the $[H_QL_Q]^5$ for the dielectric mirrors with k=0 to all time lower values of 47.77 %, 43.09 %, 46.33 % and 47.8 % for the case with wavelength dependant n and k.

To recap this section, overall depending on the material selection for the TCO film, the transmittance and reflectance spectra will be affected. Although, the effect is towards reducing the efficiency of the dielectric mirror, by smart selection of the materials with near zero extinction coefficients better dielectric mirrors can be designed.

a.

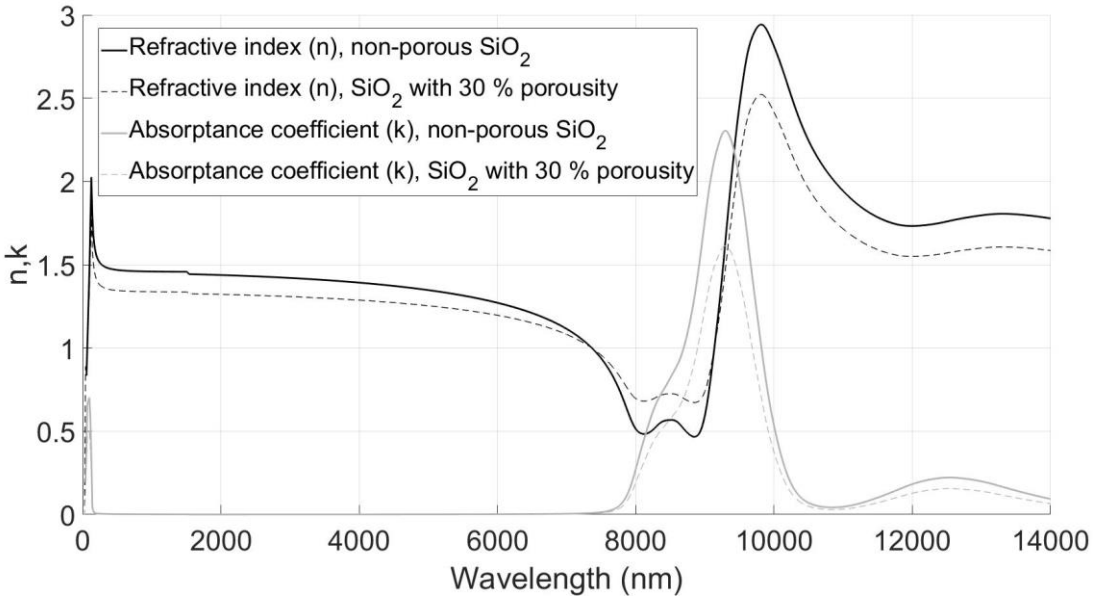

b.

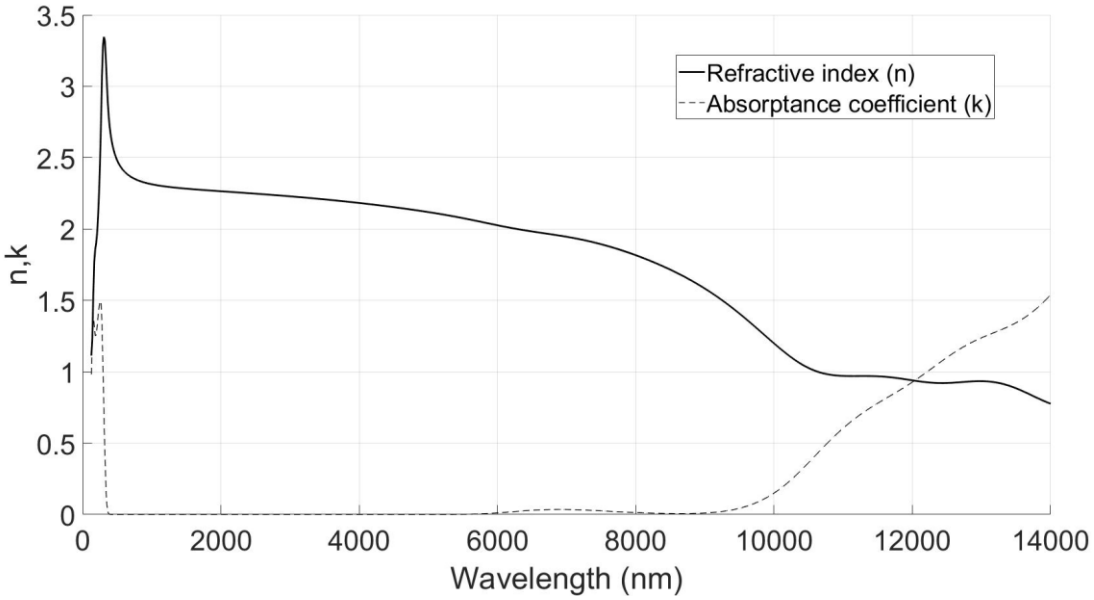

Figure 4-55. Variation of the refractive index (n) and extinction coefficient (k) for the SiO_2 NP film (Figure a.) as a low index material and the TiO_2 film (Figure b.) as a high index TCO [162-163]

a.

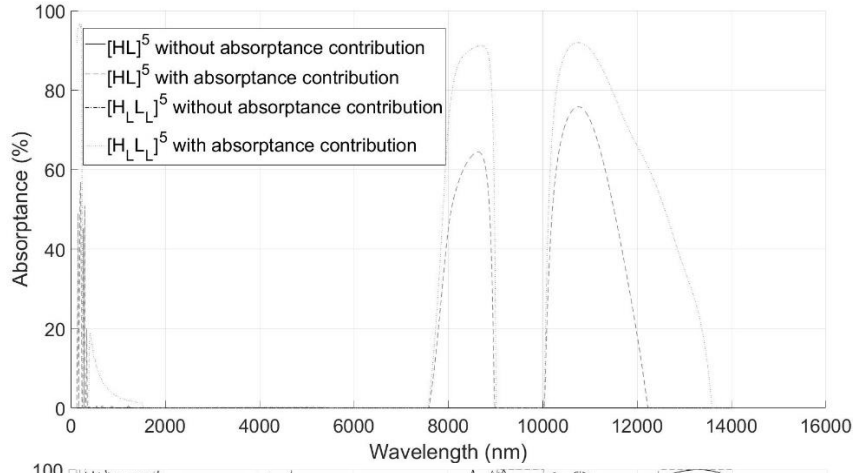

b.

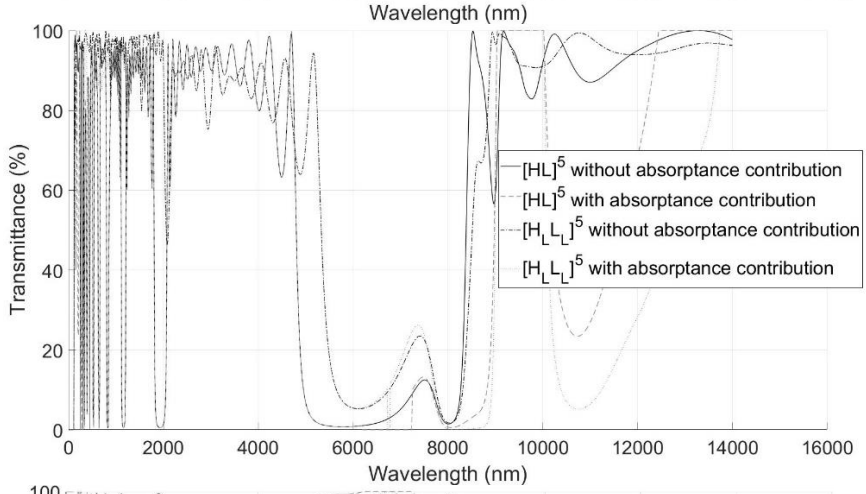

c.

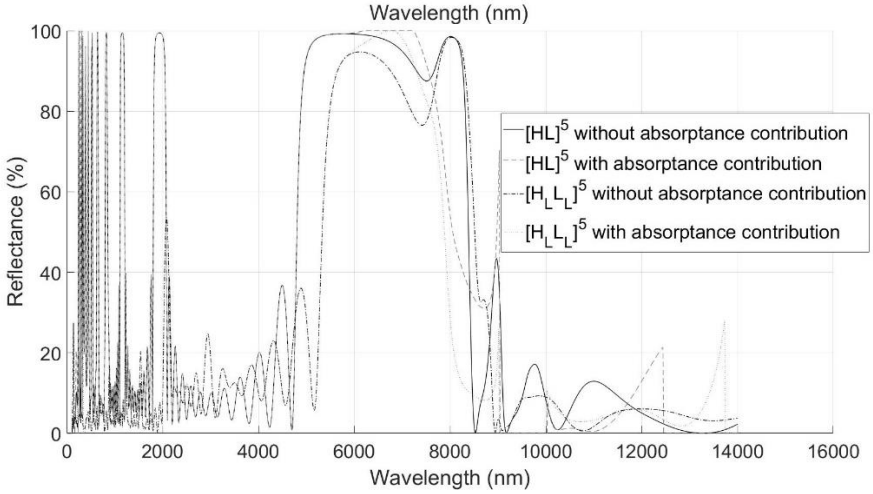

Figure 4-56. Absorptance (Figure a.), transmittance (Figure b.) and reflectance (Figure c.) spectra of $[HL]^5$, $[H_LL_L]^5$, $[H_LL_L]^5$ and $[H_QL_Q]^5$ comprised of alternating layers of SiO_2 NP and TiO_2 thin films with wavelength dependant n and k

a.

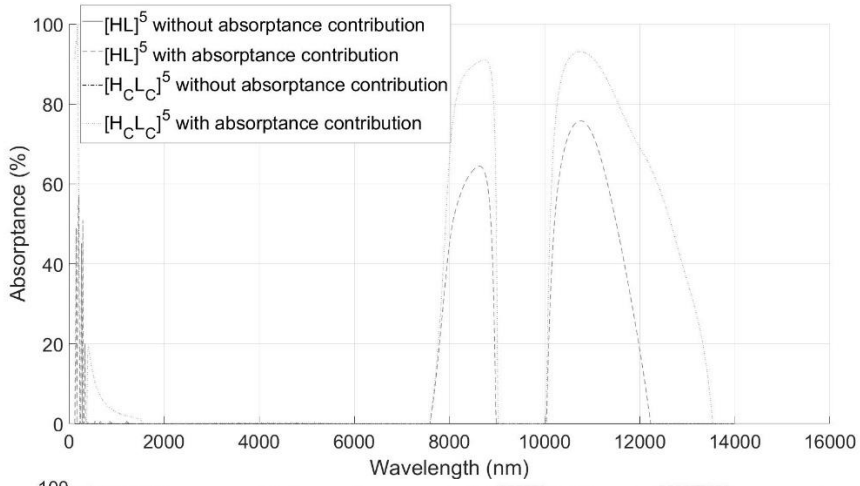

b.

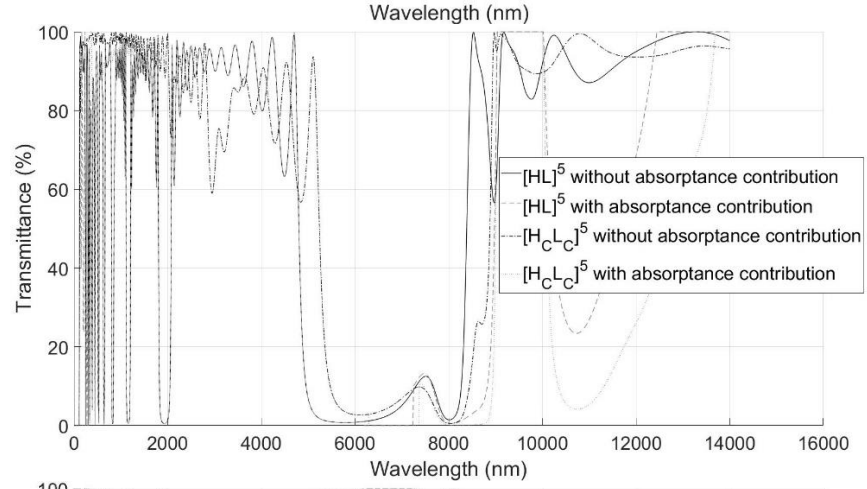

c.

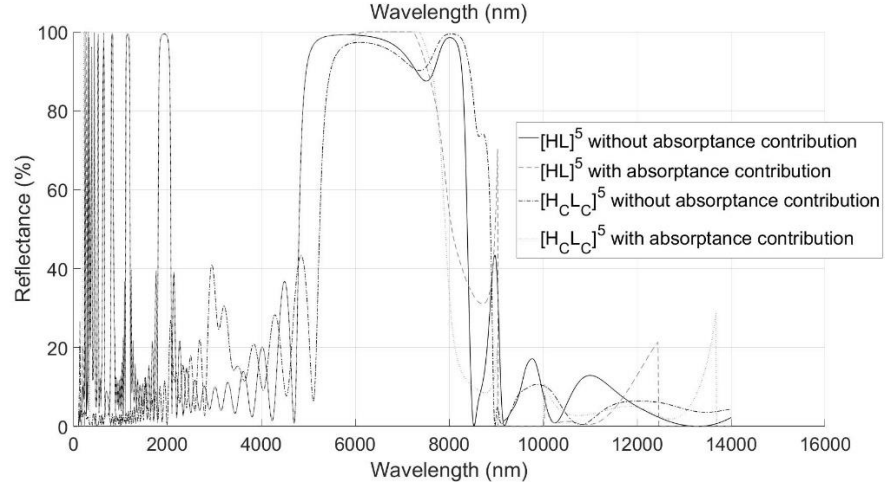

Figure 4-57. Absorptance (Figure a.), transmittance (Figure b.) and reflectance (Figure c.) spectra of $[HL]^5$, $[H_LL_L]^5$, $[H_CL_C]^5$ and $[H_CL_C]^5$ comprised of alternating layers of SiO_2 NP and TiO_2 thin films with wavelength dependant n and k

a.

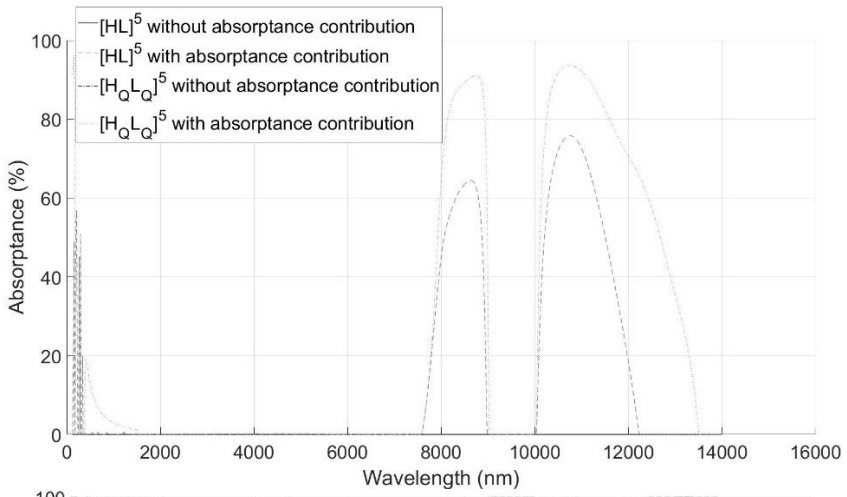

b.

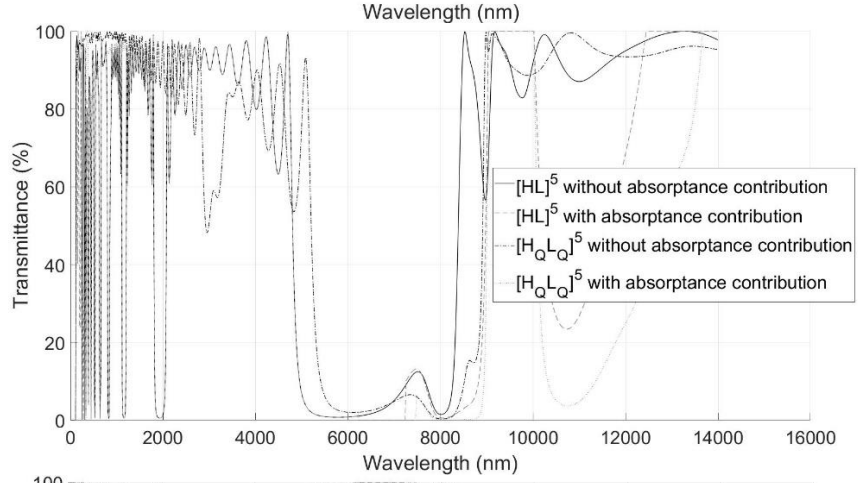

c.

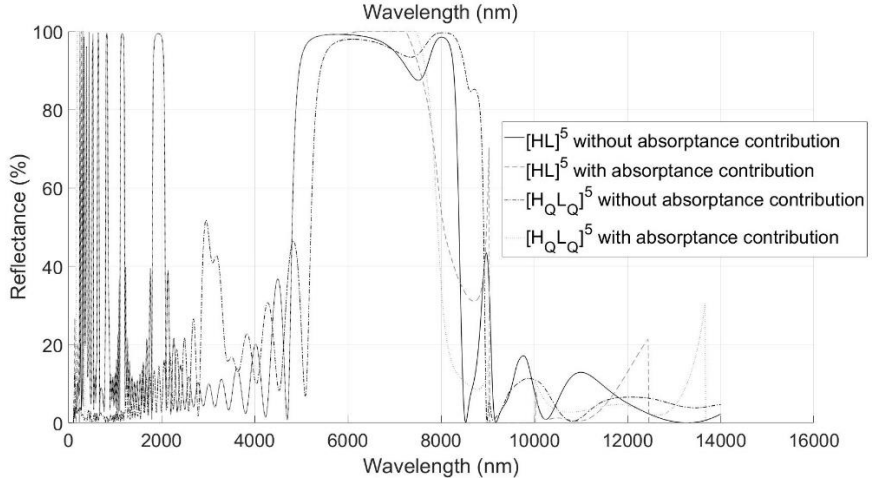

Figure 4-58. Absorptance (Figure a.), transmittance (Figure b.) and reflectance (Figure c.) spectra of $[HL]^5$, $[H_LL_L]^5$, $[H_QL_Q]^5$ and $[H_QL_Q]^5$ comprised of alternating layers of SiO_2 NP and TiO_2 thin films with wavelength dependant n and k

a.

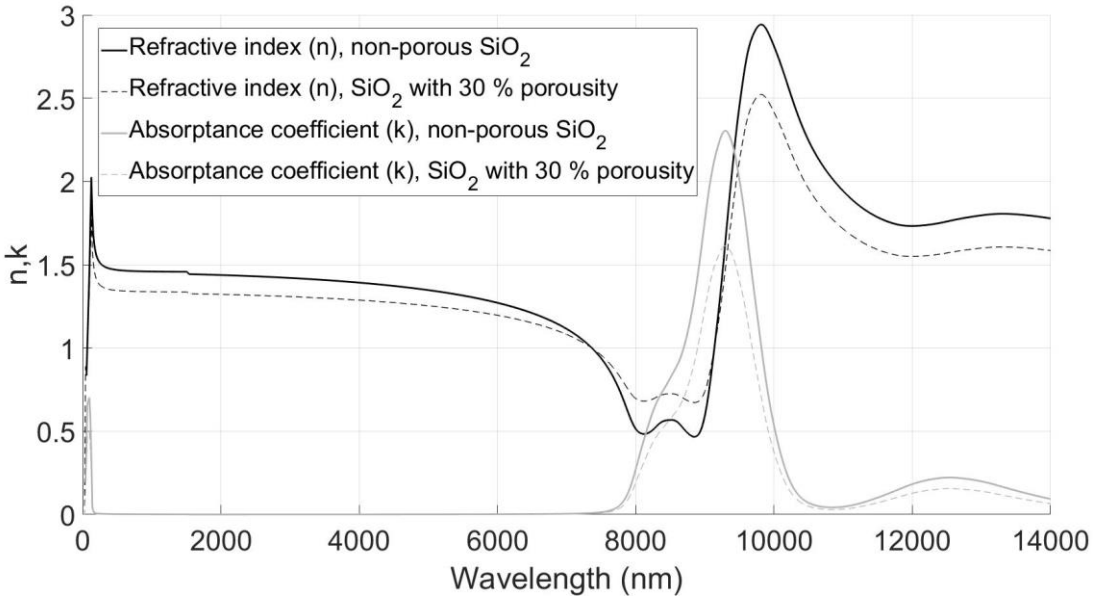

b.

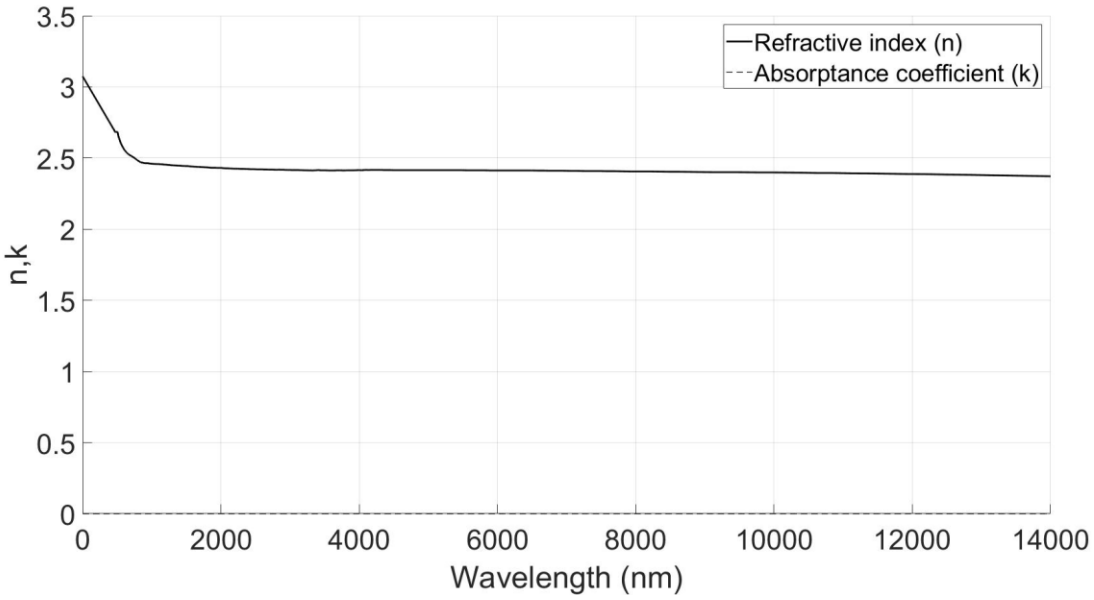

Figure 4-59. Variation of the refractive index (n) and extinction coefficient (k) for the SiO_2 NP film (Figure a.) as a low index material and the ZnSe film (Figure b.) as a high index TCO [162-165]

a.

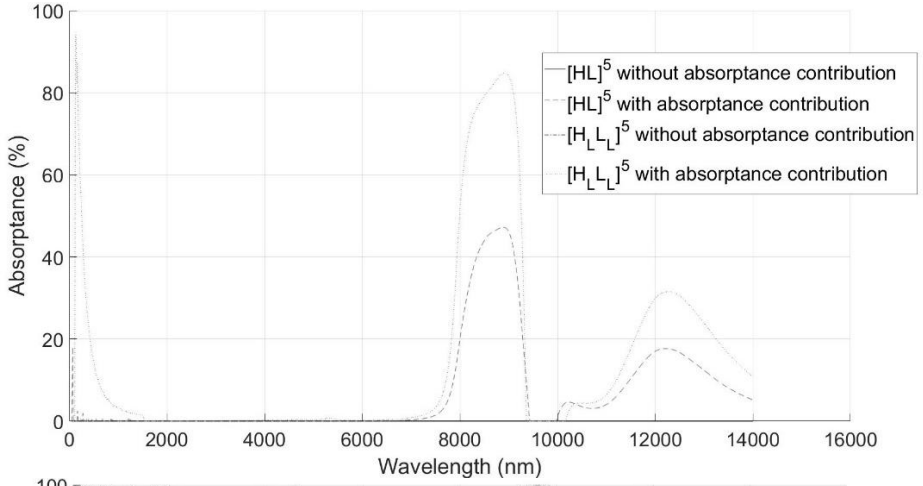

b.

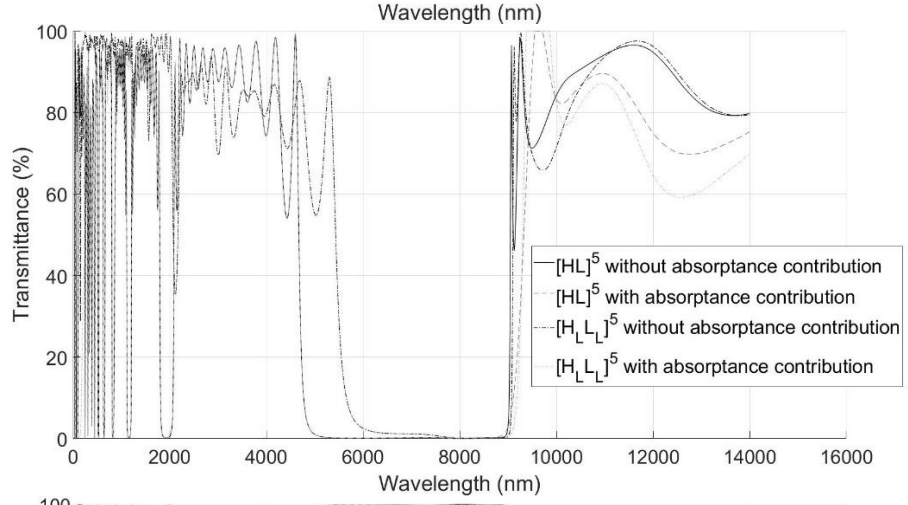

c.

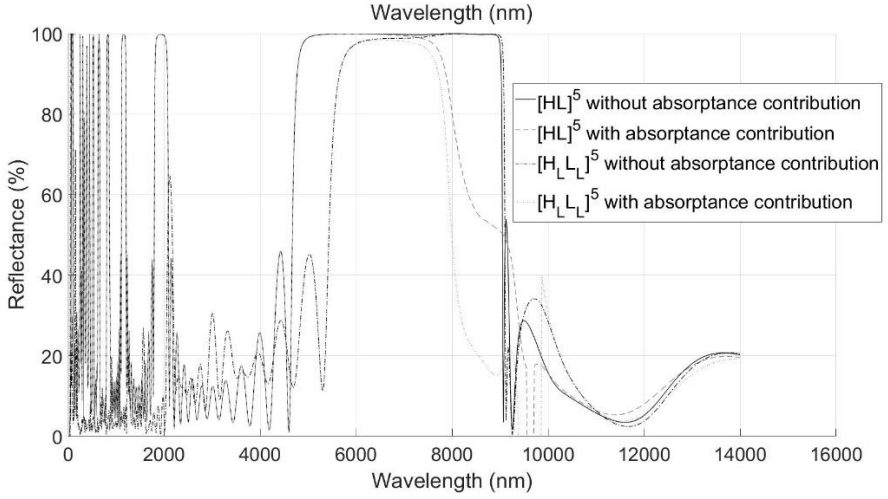

Figure 4-60. Absorptance (Figure a.), transmittance (Figure b.) and reflectance (Figure c.) spectra of $[HL]^5$, $[H_LL_L]^5$, $[H_LL_L]^5$ and $[H_LL_L]^5$ comprised of alternating layers of SiO_2 NP and ZnSe thin films with wavelength dependant n and k

a.

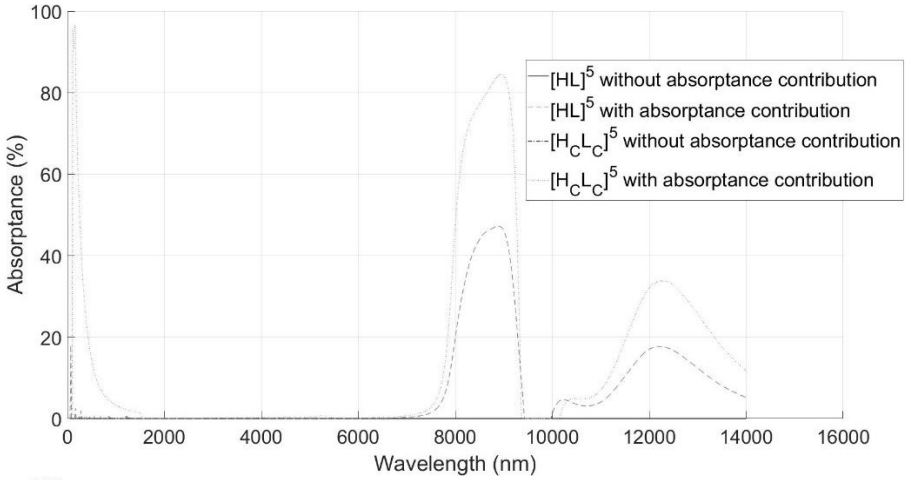

b.

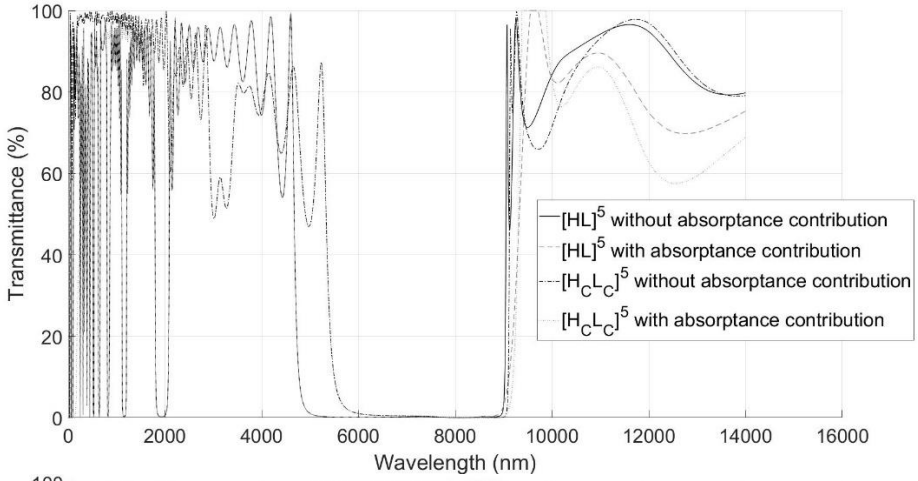

c.

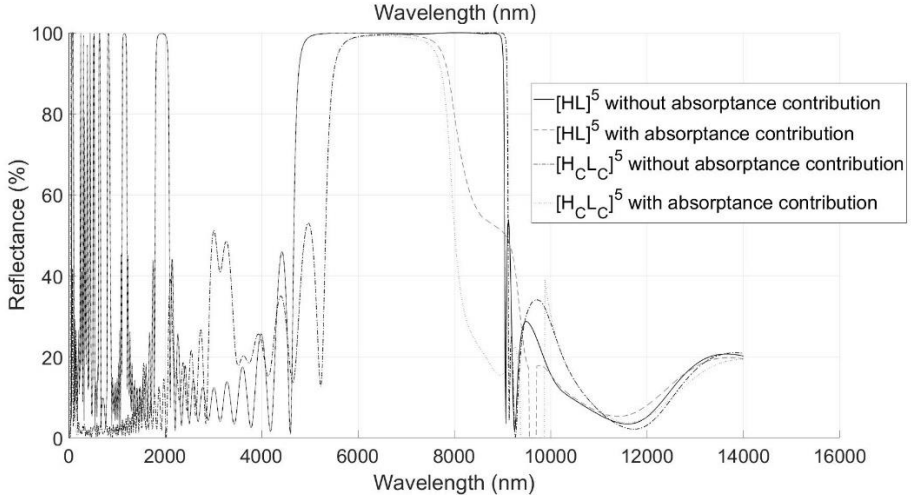

Figure 4-61. Absorptance (Figure a.), transmittance (Figure b.) and reflectance (Figure c.) spectra of $[HL]^5$, $[H_LL_L]^5$, $[H_CL_C]^5$ and $[H_CL_C]^5$ comprised of alternating layers of SiO_2 NP and ZnSe thin films with wavelength dependant n and k

a.

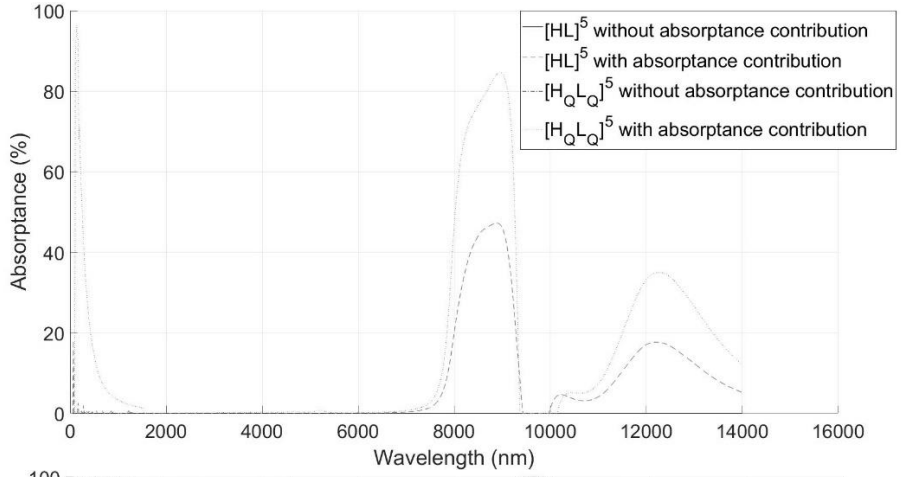

b.

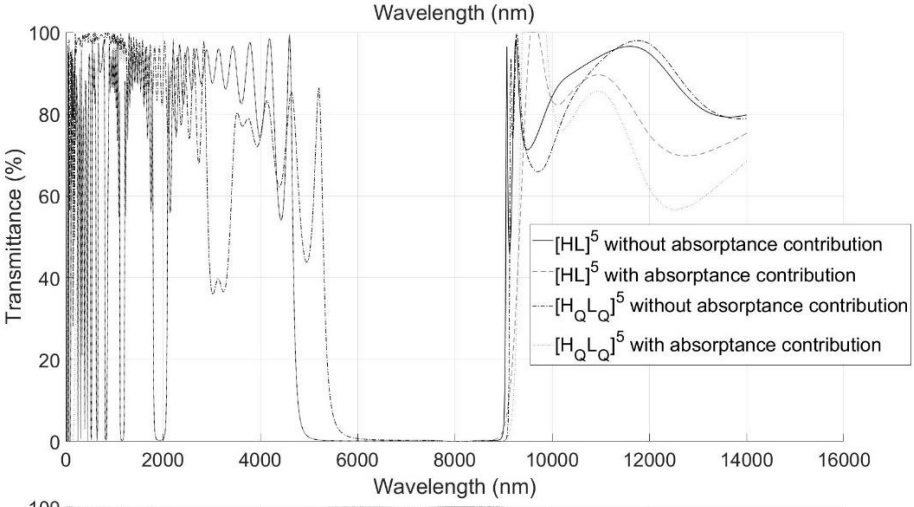

c.

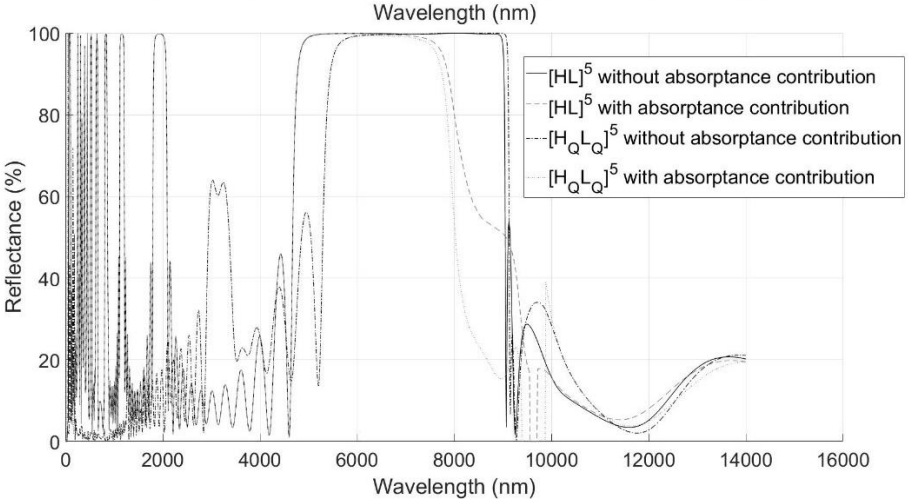

Figure 4-62. Absorptance (Figure a.), transmittance (Figure b.) and reflectance (Figure c.) spectra of $[HL]^5$, $[H_QL_Q]^5$, $[H_QL_Q]^5$ and $[H_QL_Q]^5$ comprised of alternating layers of SiO_2 NP and ZnSe thin films with wavelength dependant n and k

4-7. Conclusion

In this chapter, the sensitivity of the transmittance and reflectance spectra of the dielectric mirror towards its number of layers, resolution of its refractive index profiles, refractive index, number and reflectance peak position of dielectric mirrors in a stacked configuration, absorption of its constituent layers, and incident angle of the incoming light was analyzed. In the following a summary of the effects of altering each parameter on the performance of the dielectric mirror is provided.

Angle of incidence:

- For P-polarized light, increasing the angle of incidence causes the FWHM of the reflection peak and the corresponding maximum peak reflection to decrease.
- For S-Polarized light, increasing the angle of incidence results in an increase of the FWHM and peak reflectance value of the reflection peak.
- Although increasing the angle of incidence for the case of S-Polarized light results in a higher FWHM and peak reflectance maximum values, which causes a higher fraction of blackbody spectral power to be reflected, the reflectance values in the visible spectrum also increase which results in a significant reduction in the fraction of solar spectral power transmitted through the structure.
- For higher than 50° incident angles, the Bragg reflector behaviour is no longer seen and most of the energy from the sun is reflected by the dielectric mirror.

Number of layers:

- Increasing the number of layers decreases the FWHM and increases the maximum peak reflectance value.

- Increasing the number of layers results in a total reduction in the fraction of solar spectral power transmitted. However, beyond a certain number of layers, further increasing the number of layers decreases the total amount of thermal radiation reflected (this is because, although the reflectance peak for the heat mirror increases, the FWHM of the peak decreases resulting in a net decrease in the amount of thermal radiation reflected).
- When the number of layers in the dielectric mirror is 15 or greater, further increases in the number of layers does not result in a significant difference in the transmittance and reflectance spectra of the dielectric mirror.

Resolution of the refractive index profiles:

- Increasing the resolution of the graded index of refraction profiles results in a decrease of both the FWHM and maximum reflectance value of the reflectance peak.
- By increasing the value of W* more solar radiation is transmitted by the different dielectric mirrors considered. However, increasing W* also reduces the reflected fraction of blackbody spectral power.
- Increasing the value of W* from 20 to 50 and 100 does not cause a significant difference in the results.

Refractive index of the H and L layers within the heat mirror:

- Increasing n_H results in an increase of both the FWHM and intensity of the reflectance peak exhibited by the heat mirror.
- By increasing the value of n_H more blackbody radiation will be reflected by the different dielectric mirrors considered. However, the general trend for the solar power transmitted

through the dielectric mirror is that the transmitted solar power increases as the value of n_H is decreased and becomes closer to n_L, which is equal to 1.3.

- By increasing the contrast between the high and low refractive indices results improve and a higher temperature on the surface of a blackbody is achieved. Consequently, for all cases considered, the best design is with n_H= 2.5 and n_L= 1.1.

Additional heat mirrors

- Considering that additional heat mirrors (quarter-wave dielectric mirror) with different peak reflectance wavelengths can be stacked on top of each other, increasing the number of stacked mirrors generally results in a decrease and large increase of the amount of solar radiation transmitted and thermal radiation reflected, respectively. The benefits of increasing the amount of thermal radiation that is reflected outweighs the losses due to decreases in the transmittance of the incident solar radiation.

- The best result for a double-stack design (wherein each heat mirror in the stack is comprised of five bilayers) for a receiver operating at 500 K is for the case when both stacks have the $[H_QL_Q]^5$ structure and the first stack reflectance peak position is at 6,600 nm and the second stack reflectance peak position is at 9,200 nm. As a result, the total amount of thermal radiation reflected from a black body at 500 K increases from ~ 42 % for the $[HL]^5$ to ~ 55 % for $[H_QL_Q]^5 \cdot [H_QL_Q]^5$and the total amount of the solar radiation transmitted through the dielectric mirror increases from ~ 77 % for the $[HL]^5$ to more than 97 % for the $[H_QL_Q]^5 \cdot [H_QL_Q]^5$.

- The best result for a triple-stack design (wherein each heat mirror in the stack is comprised of five bilayers) for a receiver operating at 500 K and with one stack having a reflectance

peak position that coincides with the maximum of the thermal radiation spectra emitted from a black body at 500 K (5,800 nm) is for the case when all three stacks have the $[H_QL_Q]^5$ structure and the second stack reflectance peak position is at 7,800 nm and the third stack reflectance peak position is at 10,500 nm. As a result, the total amount of thermal radiation reflected from a black body at 500 K increases from ~42 % for the $[HL]^5$ to ~ 70 % for the $[H_QL_Q]^5 \cdot [H_QL_Q]^5 \cdot [H_QL_Q]^5$ and the total amount of the solar radiation transmitted through the dielectric mirror increases from ~ 77 % for the $[HL]^5$ to more than 96 % for the $[H_QL_Q]^5 \cdot [H_QL_Q]^5 \cdot [H_QL_Q]^5$.

Absorption Coefficient

- Depending on the absorption spectra of the material selected for the H and L films, the transmittance and reflectance spectra will be affected.
- Overall, increased absorption within the H and L films reduces the efficiency of the dielectric mirror.
- The best material is the one with near zero extinction coefficients.

5. Application of transparent dielectric mirrors

In this chapter, as an application of the transparent heat mirrors designed in this work, a parabolic dish collector (PDC) system, or a Dish-Stirling system, is analysed to determine the benefits of using the selective transparent heat mirror designed in this work on top of its receiver.

As discussed in Chapter 1, concentrated solar thermal power (CSP) technologies utilize four main types of solar concentrators: parabolic trough collectors (PTC), solar power towers (SPT), linear Fresnel reflectors (LFR), and PDC. In the following, a PDC system is being analysed with and without using the transparent heat mirrors on top of its receiver. Accordingly, Dish-Stirling systems operating at temperatures of 500 K, 1,000 K, and 1,500 K, are considered.

5-1. Dish-Stirling system design

Parabolic dish technology utilizes a concentrator in the form of a parabolic-shaped dish with a focal point. Using this dish, the system reflects the direct portion of the incident solar radiation onto a receiver located at the focal point. In a parabolic dish system, a two-axis tracking system is used, and a heat engine mounted on the receiver directly uses the collected heat. Currently, for power conversion processes, one can use Stirling or Brayton cycle engines.

CSP systems use the heat produced by concentrating and absorbing the energy from the sun to generate electricity. Among existing solar thermal systems, Dish-Stirling systems have been reported to be the most efficient one by converting approximately 30 percent of direct-normal solar radiation into electric power [36]. In the following, several black body receivers, surrounded by solar selective coatings in the form of a transparent dielectric mirror as presented in this thesis, are heated to different temperatures of 500 K, 1,000 K or 1,500 K such that they could potentially be

used in the operation of Dish-Stirling systems. Consider the schematic of the blackbody depicted in Figure 5-1. The entering energy is the solar radiation and the exiting energy comprises of radiative losses (denoted as L_R), usable power (denoted as P_{out}), and convective and conductive heat losses (denoted as L_H). The temperature of the Dish-Stirling system receiver and surrounding area are denoted by T_s and T_∞, respectively.

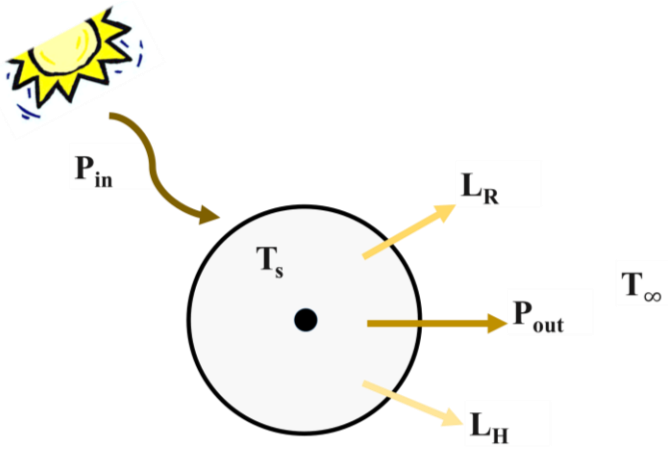

Figure 5-1. Schematic explanation of input and output energy for the receiver within a typical Dish-Stirling concentrator system.

The actual usable power generated by the Dish Stirling system at equilibrium, considering convective, conductive and radiative heat losses, given by [166-170] can be derived as follows:

$$P_{out} = P_{in} - (L_R + L_H)$$

$$P_{in} = IA_{ap}\eta_0$$

$$L_R + L_H = A_{rec}\left[h(T_s - T_\infty) + \varepsilon\sigma({T_s}^4 - {T_\infty}^4)\right]$$

$$P_{out} = IA_{ap}\eta_0 - A_{rec}\left[h(T_s - T_\infty) + \varepsilon\sigma({T_s}^4 - {T_\infty}^4)\right] \quad (5\text{-}1)$$

Where I is the direct solar flux intensity, which here is considered as the direct radiation from a blackbody at a temperature of ~ 5,700 K, A_{ap} is the collector aperture area, η_0 is the collector optical efficiency, A_{rec} is the area of the receiver which absorbs the incoming solar radiation, h is the local convective heat transfer coefficient between the receiver and the surrounding environment, T_s is the average receiver temperature, T_∞ is the ambient temperature, ε is emissivity of the receiver, and σ is Stefan's constant as provided by Equation 2.3. Herein, the average value for h is considered equal to 17.4 W/m^2K for air under clear sky conditions [171] and the ambient temperature is 300 K. A schematic diagram, shown as Figure 5-2.a and Figure 5-2.b, illustrates the collector and receiver, respectively, and shows the aperture diameter for the solar collector and receiver within the Dish-Stirling system.

a.

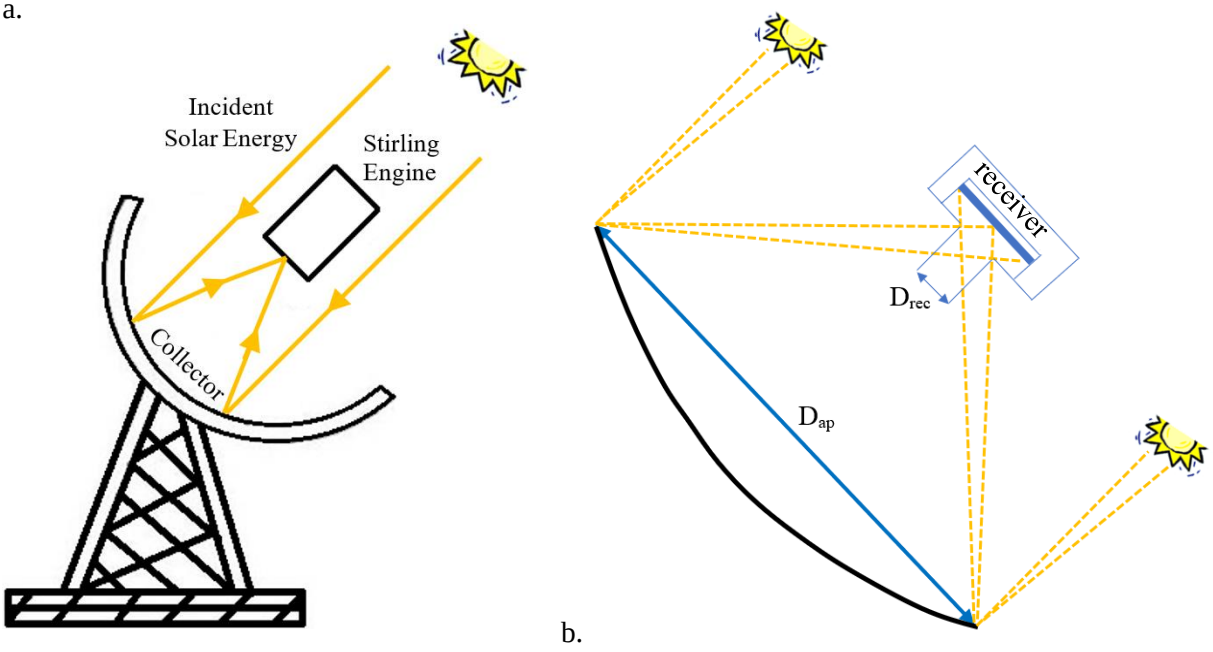

b.

Figure 5-2. Schematic diagram of a Dish Stirling System with

a. typical components

b. corresponding aperture areas of the collector and the receiver

5-2. Results and discussion

Considering different Dish-Stirling systems and applying the transparent heat mirrors on top of the receivers will result in a significant increase in the power conversion efficiency. In the following, results for different receiver temperatures of 500 K, 1,000 K and 1,500 K are provided in Figure 5-3 through Figure 5-8 for the cases when the receiver is covered with single-stack, double-stack and triple-stack dielectric heat mirrors. Moreover, the power generated in Dish-Stirling systems for the case when the receiver is covered with a single TCO (In_2O_3:Sn) layer and the case when the receiver is not covered is also shown for comparison. Furthermore, regarding the interfacial refractive index profiles within the dielectric heat mirrors, for this analysis only the conventional quarter-wave stack (e.g. step profile) and the quintic index of refraction profile, which yielded the top performance results presented in Chapter 4, are considered. Also, for all transparent dielectric heat mirrors considered in this work the indices of refraction of the alternating layers within the structure are n_L=2 and n_H =1.3.

For the single-stack transparent dielectric heat mirrors considered in this analysis, denoted as $[HL]^5_{f1}$ and $[H_QL_Q]^5_{f1}$, the subscript f1 is the reflectance peak position of the single-stack dielectric mirror and is equal to 5,800 nm, 3,240 nm and 2,160 nm for the cases when the receiver temperature within the Dish-Stirling system is 500 K, 1,000 K and 1,500 K, respectively. The values of f1 are set to 5,800 nm, 3,240 nm and 2,160 nm because these are the peak positions of the blackbody emission spectra from the receiver when it is at a temperature of 500 K, 1,000 K and 1,500 K, respectively. A double-stack dielectric mirror is comprised of two sets of five bi-layers of films with n_L=2 and n_H =1.3, denoted here as $[HL]^5_{f1}\cdot[HL]^5_{f2}$ and $[H_QL_Q]^5_{f1}\cdot[H_QL_Q]^5_{f2}$ for the case of the conventional quarter-wave stack and when the interfaces between the films with the higher and lower refractive indices within the dielectric mirror is designed with a quintic index

of refraction profile, respectively. Here, f1 is the reflectance peak position of the first stack of the dielectric mirror and is equal to 6,600 nm, 3,500 nm and 2,400 nm for the average receiver temperatures of 500 K, 1,000 K and 1,500 K, respectively, while f2 is the reflectance peak position of the second stack of the dielectric mirror and is equal to 9,200 nm, 4,800 nm and 3,700 nm for the average receiver temperatures of 500 K, 1,000 K and 1,500 K, respectively. The values for f1 and f2, as discussed earlier in Chapter 4, are chosen to maximize Equation 2-11, T = constant$\cdot\left(\frac{t}{\varepsilon}\right)^{1/4}$, where t is the transmittance and ε is the emissivity of the dielectric mirror. The triple-stack dielectric mirrors considered in this section are comprised of three sets of five bi-layers of films with n_L=2 and n_H =1.3, denoted here as $[HL]^5_{f1}\cdot[HL]^5_{f2}\cdot[HL]^5_{f3}$ and $[H_QL_Q]^5_{f1}\cdot[H_QL_Q]^5_{f2}\cdot[H_QL_Q]^5_{f3}$ for the case of the conventional quarter-wave stack and when the interfaces between the films with the higher and lower refractive indices within the dielectric mirror are designed with a quintic index of refraction profile, respectively. Here, f1 is the reflectance peak position of the first stack within the dielectric mirror and is equal to 5,800 nm, 2,900 nm and 1,930 nm for the cases when the receiver temperature is 500 K, 1,000 K and 1,500 K, respectively. The reflectance peak position of the second stack within the dielectric mirror, f2, is equal to 7,800 nm, 4,000 nm and 3,000 nm for the average receiver temperatures of 500 K, 1,000 K and 1,500 K, respectively, while f3 is the reflectance peak position of the third stack of the dielectric mirror and is equal to 10,500 nm, 5,600 nm and 4,800 nm for the receiver temperatures of 500 K, 1,000 K and 1,500 K, respectively. The values for f1, f2 and f3, as discussed earlier in Chapter 4, are chosen to maximize Equation 2-11, T = constant$\cdot\left(\frac{t}{\varepsilon}\right)^{1/4}$.

Figure 5-3 shows the generated power versus solar concentration ratio for different PDC systems with and without a single, double and triple -stack transparent heat mirror on top of the receiver operating at T = 500 K where alternating layers of films within the dielectric mirror with $[HL]^5_{f1}$, $[H_QL_Q]^5_{f1}$, $[H_QL_Q]^5_{f1}\cdot[H_QL_Q]^5_{f2}$, and $[H_QL_Q]^5_{f1}\cdot[H_QL_Q]^5_{f2}\cdot[HL]^5_{f3}$ have refractive indices of n_H =2 and n_L =1.3. In this work the solar concentration ratio is defined with reference to Fig 5-2b to be $(D_{ap}/D_{rec})^2$. In the literature, for a PDC system operating at T = 500 K, the concentration ratio can vary from 6 to more than 200 depending on the design and operation of the PDC system and the power generated at an operating temperature of 500 K typically ranges from 0.25 kW to 10 kW [171-172]. For example, Mary Nelima Ondiaka et. al. [174] reported a PDC system operating at T = 500 K with a solar concentration ratio of 30 and generated power of 2,200 W [171]. As can be seen in Figure 5-3, considering different solar concentration ratios, the generated power shows different behaviour. Accordingly, for a low concentration ratio, or low number of suns (e.g. less than 30), the generated power for the case when a dielectric mirror with $[H_QL_Q]^5_{f1}$ or $[H_QL_Q]^5_{f1}\cdot[H_QL_Q]^5_{f2}$ or $[H_QL_Q]^5_{f1}\cdot[H_QL_Q]^5_{f2}\cdot[HL]^5_{f3}$ is applied on top of the receiver is higher than the PDC system without any cover on top of the receiver or the case when a conventional TCO film (e.g. a In_2O_3:Sn film) coated on a glass substrate functions as the low-E coating on top of the receiver [171]. However, for the case of a PDC system operating at T=500 K with a high number of incident suns (e.g. higher than 30), the generated power for the PDC system without any cover on top of the receiver is always higher than the cases when a the receiver is covered with any transparent heat mirror or any form of low-E coating. The main reason for this behaviour is that, considering Equation 5-1, as the number of suns increases the solar power absorbed by the receiver plays a greater role compared to the radiative heat losses, which is almost a constant value considering the receiver is operating at a temperature of 500 K. Hence, the transmittance value for

different coatings significantly affects the amount of solar power absorbed by the receiver and for the case without any cover on top of the receiver the transmittance value is equal to 1, and this case provides more entering solar power compared to the other cases wherein the transmittance through the receiver cover is less than 1. It should be noted that usually a typical PDC system uses a conventional low-E coating on top of the receiver. Consequently, in Figure 5-4 the generated power using a PDC system operating at T= 500 K when a dielectric mirror with $[HL]^5_{f1}$, $[H_QL_Q]^5_{f1}$, $[H_QL_Q]^5_{f1}\cdot[H_QL_Q]^5_{f2}$, and $[H_QL_Q]^5_{f1}\cdot[H_QL_Q]^5_{f2}\cdot[HL]^5_{f3}$ is applied on top of the receiver is compared to the case wherein an In_2O_3:Sn film is on top of the receiver. With respect to Figure 5-4, compared to the case when an In_2O_3:Sn film is on top of the receiver, the generated power with low solar concentration ratio of 6 increases by ~ 60 % using $[H_QL_Q]^5_{f1}$ (equal to ~ 380 W), by ~ 85 % using $[H_QL_Q]^5_{f1}\cdot[H_QL_Q]^5_{f2}$ (equal to ~ 425 W) and by ~ 100 % using $[H_QL_Q]^5_{f1}\cdot[H_QL_Q]^5_{f2}\cdot[HL]^5_{f3}$ (equal to ~ 450 W) on top of the receiver. Considering higher solar concentration ratios (e.g. higher than 30), the improvement in generated power decreases to ~ 35 % for all three kinds of the dielectric mirrors with quintic profiles. To put it another way, for higher solar concentration ratios, a PDC system with a dielectric mirror with $[H_QL_Q]^5_{f1}$ is more efficient than those with $[H_QL_Q]^5_{f1}\cdot[H_QL_Q]^5_{f2}$ or $[H_QL_Q]^5_{f1}\cdot[H_QL_Q]^5_{f2}\cdot[HL]^5_{f3}$ on top of the receiver. However, the PDC system with $[HL]^5_{f1}$ on top of the receiver does not show higher generated power compared to the case with the conventional low-E coating at low solar concentration, although by increasing the number of suns to more than 15 the generated power with $[HL]^5$ increases and reaches to ~ 5 % more than the conventional case when an In_2O_3:Sn film coated on a glass substrate functions as the low-E coating on top of the receiver.

Figure 5-5 shows the generated power versus number of suns for different PDC systems with and without a single, double and triple -stack transparent heat mirror on top of the receiver operating

at T = 1,000 K where alternating layers of films within the dielectric mirror with $[HL]^{5}_{f1}$, $[H_QL_Q]^{5}_{f1}$, $[H_QL_Q]^{5}_{f1}\cdot[H_QL_Q]^{5}_{f2}$, and $[H_QL_Q]^{5}_{f1}\cdot[H_QL_Q]^{5}_{f2}\cdot[HL]^{5}_{f3}$ have refractive indices of n_H =2 and n_L =1.3. In practice, as an example, the solar concentration ratio for a PDC system operating at T = 1,000 K may be as high as 2,000 while the generated power may reach 25 kW [174-175]. For example, SolarTron Energy Systems Inc. [175] provides a commercial PDC system operating at T = 1,000 K with solar concentration ratio of 1,000 and generated power of 25 kW [171]. As can be seen in Figure 5-5, considering different solar concentration ratios, the generated power shows different behaviour. Accordingly, for a low number of incident suns (e.g. less than 200) the generated power for the case when a dielectric mirror with $[H_QL_Q]^{5}_{f1}$ or $[H_QL_Q]^{5}_{f1}\cdot[H_QL_Q]^{5}_{f2}$ or $[H_QL_Q]^{5}_{f1}\cdot[H_QL_Q]^{5}_{f2}\cdot[HL]^{5}_{f3}$ is applied on top of the receiver is higher than the PDC system without any cover on top of the receiver or the case when a conventional TCO film (e.g. an In_2O_3:Sn film) coated on a glass substrate functions as the low-E coating on top of the receiver [173]. However, for the case of a PDC system operating at T=1,000 K with a higher number of incident suns (e.g. higher than 200), the generated power for the PDC system without any cover on top of the receiver is always higher than the cases with cover on top of the receiver. The main reason for this behaviour is that, considering Equation 5-1, as number of suns increases the absorbed solar power plays a greater role compared to the heat losses which is almost a constant value considering the receiver operates at a temperature of 1,000 K. Hence, the transmittance value for different coatings significantly affects the entering solar power and because the transmittance value is 1 for the case when there is no cover on the receiver, more solar power is absorbed compared to the other cases wherein the transmittance is less than 1. It should be noted that usually a typical PDC system uses a conventional low-E coating on top of the receiver. Consequently, in Figure 5-6 the generated power using a PDC system operating at T= 1,000 K when a dielectric

mirror with $[HL]^5_{f1}$, $[H_QL_Q]^5_{f1}$, $[H_QL_Q]^5_{f1}\cdot[H_QL_Q]^5_{f2}$, and $[H_QL_Q]^5_{f1}\cdot[H_QL_Q]^5_{f2}\cdot[HL]^5_{f3}$ is applied on top of the receiver is compared to the case wherein an In_2O_3:Sn film is on top of the receiver. With respect to Figure 5-6, compared to the case when an In_2O_3:Sn film is on top of the receiver, the generated power when the solar concentration is 40 increases by ~ 129 % using $[H_QL_Q]^5_{f1}$ (equal to ~ 1,202 W), by ~ 283 % using $[H_QL_Q]^5_{f1}\cdot[H_QL_Q]^5_{f2}$ (equal to ~ 2,010 W) and by ~ 360 % using $[H_QL_Q]^5_{f1}\cdot[H_QL_Q]^5_{f2}\cdot[HL]^5_{f3}$ (equal to ~ 2,418 W) on top of the receiver. Considering higher solar concentration ratios, the improvement in generated power decreases to ~ 30 % for all three kinds of the dielectric mirrors with quintic profiles. To put it another way, for higher solar concentration ratios, a PDC system with a dielectric mirror with $[H_QL_Q]^5_{f1}$ is more efficient than those with $[H_QL_Q]^5_{f1}\cdot[H_QL_Q]^5_{f2}$ or $[H_QL_Q]^5_{f1}\cdot[H_QL_Q]^5_{f2}\cdot[HL]^5_{f3}$ on top of the receiver. However, the PDC system with $[HL]^5_{f1}$ on top of the receiver does not show higher generated power compared to the case with the conventional low-E coating at lower incident solar concentration ratios, although by increasing the number of incident suns to more than 100 the generated power with $[HL]^5$ increases and reaches to ~ 5 % more than the conventional case with an In_2O_3:Sn film coated on a glass substrate functions as the low-E coating on top of the receiver.

Figure 5-7 shows the generated power versus concentration ratio of the number of incident suns for different PDC systems with and without a single, double or triple -stack transparent heat mirror on top of its receiver for an operating temperature of T = 1,500 K, where the alternating layers of films within the dielectric mirror with $[HL]^5_{f1}$, $[H_QL_Q]^5_{f1}$, $[H_QL_Q]^5_{f1}\cdot[H_QL_Q]^5_{f2}$, and $[H_QL_Q]^5_{f1}\cdot[H_QL_Q]^5_{f2}\cdot[HL]^5_{f3}$ have refractive indices of n_H =2 and n_L =1.3. In practice, the maximum operating temperature of the receiver within a PDC system is typically less than 1,500 K. For example, Shuang-Ying Wu et all [176] reported a PDC system operating at T = 1,300 K with solar concentration ratio of more than 2,000. Nevertheless, here we model a PDC system operating at T

= 1,500 K at a solar concentration ratio of more than 3,000 with generated power up to 50 kW to investigate the performance of the transparent dielectric heat mirrors designed in this work at high operating temperatures [176-177]. As can be seen in Figure 5-7, considering different solar concentration ratios, the generated power shows different behaviour. Accordingly, for a low number of incident suns (e.g. less than 200) the generated power for the case when a dielectric mirror with $[H_QL_Q]^5_{f1}$ or $[H_QL_Q]^5_{f1}\cdot[H_QL_Q]^5_{f2}$ or $[H_QL_Q]^5_{f1}\cdot[H_QL_Q]^5_{f2}\cdot[HL]^5_{f3}$ is applied on top of the receiver is higher than the PDC system without any cover on top of its receiver or the case when a conventional TCO film (e.g. a In_2O_3:Sn film) coated on a glass substrate functions as the low-E coating on top of the receiver [173]. However, for the case of a PDC system operating at T=1,500 K with a higher number of incident suns (e.g. higher than 200), the generated power for the PDC system without any cover on top of the receiver is always higher than the cases when a cover is on top of the receiver. Similar to the cases when the PDC system is operating at 500 K or 1,000 K, the main reason for this behaviour is that, considering Equation 5-1, as the number of suns increases the absorbed solar power plays a more influential role compared to the heat losses, which are almost constant considering a consistent operating temperature of T = 1,500 K. Hence, the transmittance value for different coatings significantly affects the amount of solar power absorbed and because the transmittance value for the case when there is no cover on top of the receiver is equal to 1, the amount of solar power absorbed is greater compared to the other cases when the receiver is covered and the transmittance is less than 1. It should be noted that usually a typical PDC system uses a conventional low-E coating on top of the receiver. Consequently, in Figure 5-8 the generated power using a PDC system operating at T= 1,500 K when a dielectric mirror with $[HL]^5_{f1}$, $[H_QL_Q]^5_{f1}$, $[H_QL_Q]^5_{f1}\cdot[H_QL_Q]^5_{f2}$, and $[H_QL_Q]^5_{f1}\cdot[H_QL_Q]^5_{f2}\cdot[HL]^5_{f3}$ is applied on top of the receiver is compared to the case wherein an In_2O_3:Sn film is on top of the receiver. With

respect to Figure 5-8, the power generated when the solar concentration ratio is 200 increases by ~ 106 % using $[HL]^5_{f1}$ (equal to ~ 4,504 W), by ~ 245 % using $[H_QL_Q]^5_{f1}$ (equal to ~ 7,530 W), by ~ 426 % using $[H_QL_Q]^5_{f1}\cdot[H_QL_Q]^5_{f2}$ (equal to ~ 11,480 W) and by ~ 480 % using $[H_QL_Q]^5_{f1}\cdot[H_QL_Q]^5_{f2}\cdot[HL]^5_{f3}$ (equal to ~ 12,650 W) on top of the receiver. Considering higher solar concentration ratios, the improvement in generated power decreases to ~ 26 % for all three kinds of the dielectric mirrors with quintic profiles. To put it another way, for higher solar concentration ratios, a PDC system with a dielectric mirror with $[H_QL_Q]^5_{f1}$ is more efficient than those with $[H_QL_Q]^5_{f1}\cdot[H_QL_Q]^5_{f2}$ or $[H_QL_Q]^5_{f1}\cdot[H_QL_Q]^5_{f2}\cdot[HL]^5_{f3}$ on top of the receiver because the transmittance through $[H_QL_Q]^5_{f1}$ is higher. That is for the PDC system operating at higher temperatures of T = 1,500 K, the $[H_QL_Q]^5_{f1}\cdot[H_QL_Q]^5_{f2}\cdot[HL]^5_{f3}$ does not show higher generated power compared to the cases with $[H_QL_Q]^5_{f1}$ and $[H_QL_Q]^5_{f1}\cdot[H_QL_Q]^5_{f2}$ because the transmittance drops from 89.76 % for $[H_QL_Q]^5_{f1}$ and 89.36 % for $[H_QL_Q]^5_{f1}\cdot[H_QL_Q]^5_{f2}$ to ~ 84 % for $[H_QL_Q]^5_{f1}\cdot[H_QL_Q]^5_{f2}\cdot[HL]^5_{f3}$.

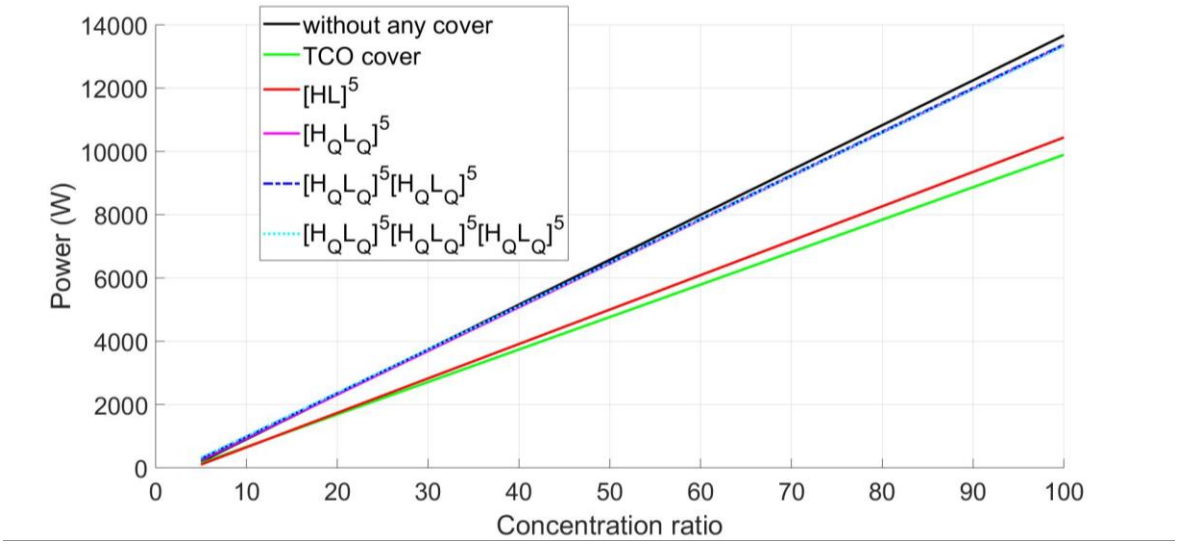

Figure 5-3. Generated power versus solar concentration ratio for different PDC systems operating at 500 K with transparent heat mirrors in the form of $[HL]^5_{f1}$, $[H_QL_Q]^5_{f1}$, $[H_QL_Q]^5_{f1}\cdot[H_QL_Q]^5_{f2}$ and $[H_QL_Q]^5_{f1}\cdot[H_QL_Q]^5_{f2}\cdot[HL]^5_{f3}$ on top of the receiver within a PDC system. The cases in which a TCO cover and no cover are over top of the receiver are also shown for comparison.

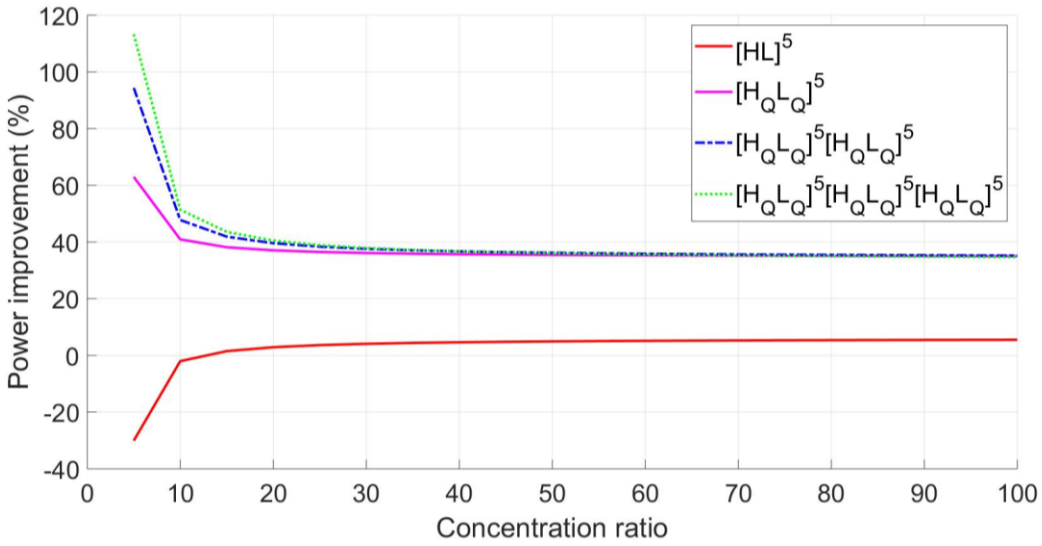

Figure 5-4. Power improvement for different PDC systems operating at 500 K with transparent heat mirrors in the form of $[HL]^5_{f1}$, $[H_QL_Q]^5_{f1}$, $[H_QL_Q]^5_{f1}\cdot[H_QL_Q]^5_{f2}$ and $[H_QL_Q]^5_{f1}\cdot[H_QL_Q]^5_{f2}\cdot[HL]^5_{f3}$ on top of the receiver within a PDC system in comparison to the case when a single TCO film (e.g. In2O3:Sn film) is used to cover the receiver within the PCD system.

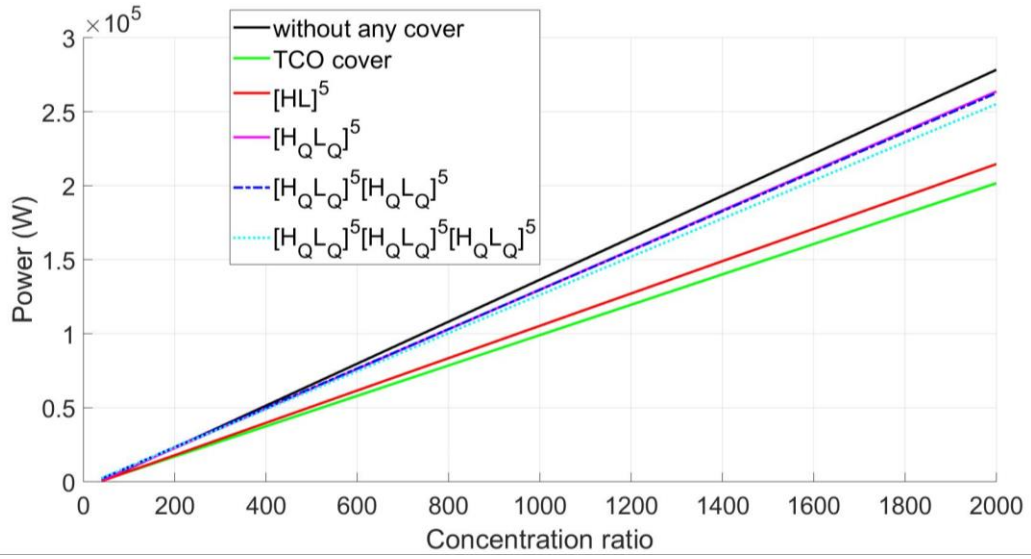

Figure 5-5. Generated power versus solar concentration ratio for different PDC systems operating at 1,000 K with transparent heats mirror in the form of $[HL]^5_{f1}$, $[H_QL_Q]^5_{f1}$, $[H_QL_Q]^5_{f1}\cdot[H_QL_Q]^5_{f2}$ and $[H_QL_Q]^5_{f1}\cdot[H_QL_Q]^5_{f2}\cdot[HL]^5_{f3}$ on top of the receiver within the PDC system. The cases in which a TCO cover and no cover over top of the receiver are also shown for comparison.

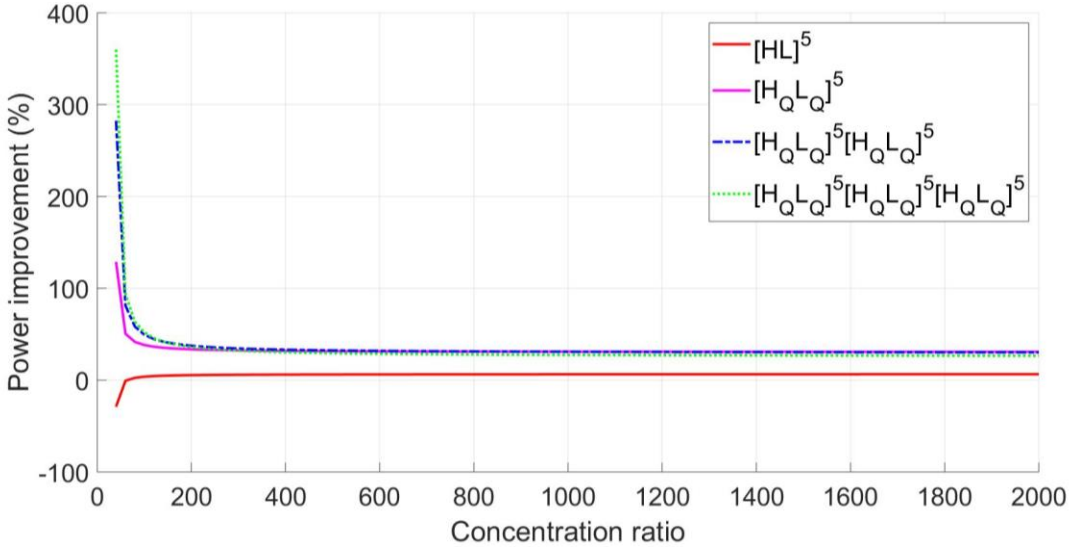

Figure 5-6. Power improvement for different PDC systems operating at 1,000 K with transparent heat mirrors in the form of $[HL]^5_{f1}$, $[H_QL_Q]^5_{f1}$, $[H_QL_Q]^5_{f1}\cdot[H_QL_Q]^5_{f2}$ and $[H_QL_Q]^5_{f1}\cdot[H_QL_Q]^5_{f2}\cdot[HL]^5_{f3}$ on top of the receiver within a PDC system in comparison to the case when a single TCO film (e.g. In2O3:Sn film) is used to cover the receiver within the PCD system.

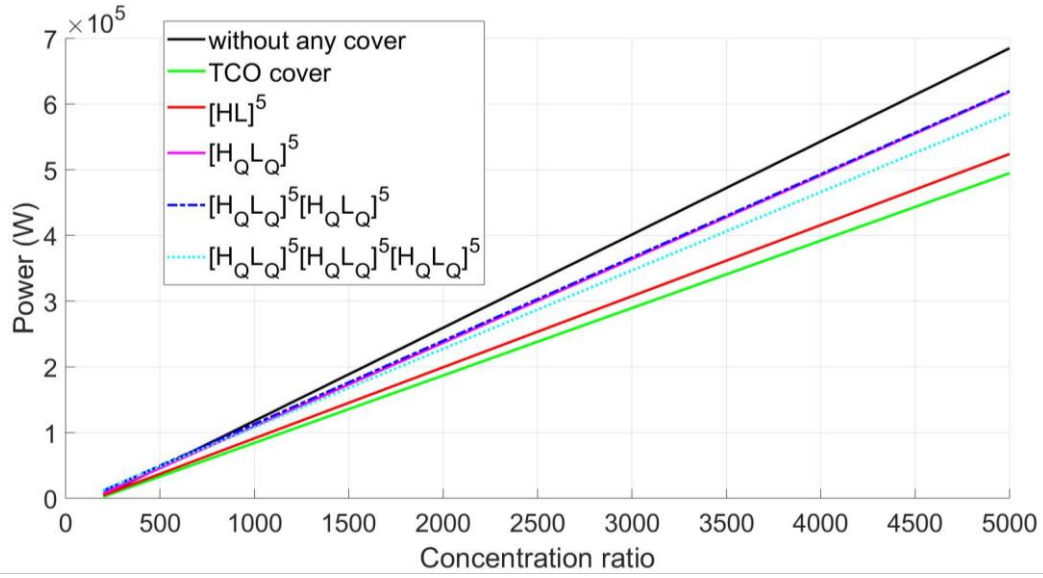

Figure 5-7. Generated power versus solar concentration ratio for different PDC systems operating at 1,500 K with transparent heat mirrors in the form of $[HL]^5_{f1}$, $[H_QL_Q]^5_{f1}$, $[H_QL_Q]^5_{f1}\cdot[H_QL_Q]^5_{f2}$ and $[H_QL_Q]^5_{f1}\cdot[H_QL_Q]^5_{f2}\cdot[HL]^5_{f3}$ on top of the receiver within a PDC system. The cases in which a TCO cover and no cover over top of the receiver are also shown for comparison.

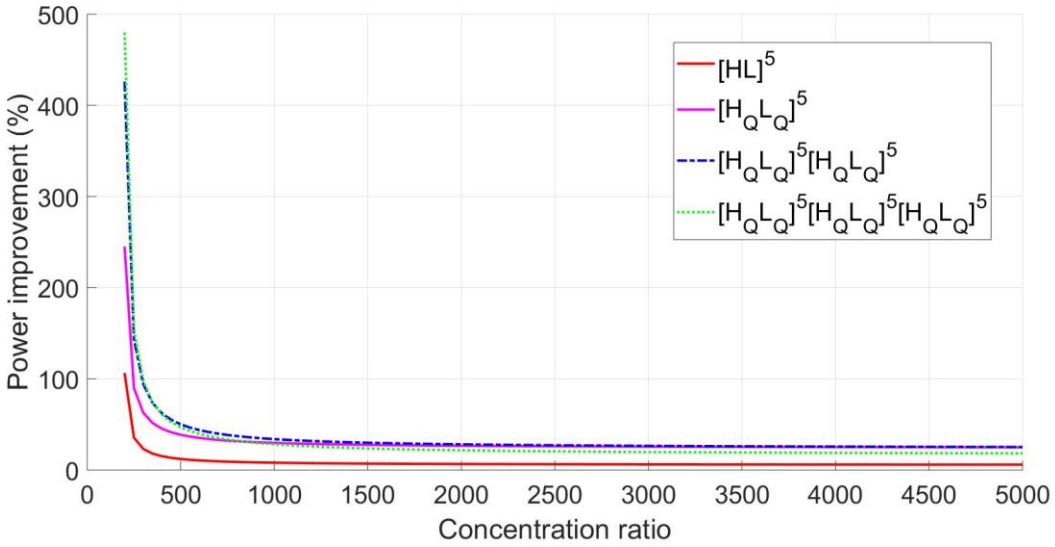

Figure 5-8. Power improvement for different PDC systems operating at 1,500 K with transparent heat mirrors in the form of $[HL]^5_{f1}$, $[H_QL_Q]^5_{f1}$, $[H_QL_Q]^5_{f1}\cdot[H_QL_Q]^5_{f2}$ and $[H_QL_Q]^5_{f1}\cdot[H_QL_Q]^5_{f2}\cdot[HL]^5_{f3}$ on top of the receiver within a PDC system in comparison to the case when a single TCO film (e.g. In2O3:Sn film) is used to cover the receiver within the PCD system.

5-3. Transmitted solar radiation and thermal radiation losses

Figure 5-9, Figure 5-10, and Figure 5-11 show the transmitted solar radiation and thermal radiation losses that pass from a receiver operating at 500 K through the single, double and triple stack heat mirrors, respectively. The cover of the PDC systems is either an In_2O_3:Sn film or a single-stack, a double-stack or a triple-stack transparent heat mirror located on top of the receiver and the alternating layers of the films within the dielectric mirror have refractive indices of $n_H = 2$ and $n_L = 1.3$. As discussed in Chapter 4, the temperature of a blackbody receiver under a dielectric heat mirror is proportional to $\left(\frac{t}{\varepsilon}\right)^{1/4}$. In order to design the double-stack dielectric mirror with maximum achievable temperature, the first stack reflectance peak position is at 6,600 nm and the second stack reflectance peak position is at 9,200 nm. Also, for the case of the triple-stack design with one stack having a reflectance peak position that coincides with the maximum of the thermal radiation spectra emitted from a black body at 500 K (5,800 nm), the second stack reflectance peak position is at 7,800 nm and the third stack reflectance peak position is at 10,500 nm. As can be seen, the radiative losses when $[H_QL_Q]^5$ is used as the receiver cover (in solid red color) are a lot less than for the cases when the emitter is covered with the In_2O_3:Sn cover, and without any cover, resulting in more power generated by the PDC system when its receiver is coated with $[H_QL_Q]^5$.

Figure 5-12, Figure 5-13 and Figure 5-14 show the transmitted solar radiation and thermal radiation losses that pass from a receiver operating at 1,000 K through the single, double and triple stack heat mirrors, respectively. The cover is either an In_2O_3:Sn film or a single-stack, a double-stack or a triple-stack transparent heat mirror located on top of the receiver where the alternating layers of the films within the dielectric mirror have refractive indices of $n_H = 2$ and $n_L = 1.3$. As discussed earlier, in order to design the double-stack dielectric mirror with maximum achievable

temperature, the first stack reflectance peak position is at 3,500 nm and the second stack reflectance peak position is at 4,800 nm. Also, for the case of the triple-stack design with one stack having a reflectance peak position that coincides with the maximum of the thermal radiation spectra emitted from a black body at 1,000 K (2,900 nm), the second stack reflectance peak position is at 4,000 nm and the third stack reflectance peak position is at 5,600 nm. As can be seen, the radiative losses for the $[H_QL_Q]^5$ (in solid red color) are still a lot less than that for the cases when the receiver is covered with a In_2O_3:Sn film or when the receiver is not covered, resulting in more power generated by the PDC system when $[H_QL_Q]^5$ is used on top the receiver.

Figure 5-15, Figure 5-16 and Figure 5-17 show the transmitted solar radiation and thermal radiation losses that pass from a receiver operating at 1,500 K through the single, double and triple-stack heat mirrors, respectively. The cover is either an In_2O_3:Sn film or a single-stack, a double-stack or a triple-stack transparent heat mirror located on top of the receiver where the alternating layers of the films within the dielectric mirror have refractive indices of $n_H = 2$ and $n_L = 1.3$. As discussed earlier, in order to design the double-stack dielectric mirror with maximum achievable temperature, the first stack reflectance peak position is at 2,400 nm and the second stack reflectance peak position is at 3,700 nm. Also, for the case of the triple-stack design with one stack having a reflectance peak position that coincides with the maximum of the thermal radiation spectra emitted from a black body at 1,500 K (1,930 nm), the second stack reflectance peak position is at 3,000 nm and the third stack reflectance peak position is at 4,800 nm. As can be seen, the radiative losses for $[H_QL_Q]^5$ (in solid red color) are still a lot less than that for the In_2O_3:Sn film and without any cover resulting in more power generated by the PDC system using this kind of dielectric mirror on top the receiver.

With respect to the results from Figure 5-9 to Figure 5-17, the overlap between the incoming solar irradiance and the thermal emission spectra from the emitter increases as the operating temperature of the receiver increases. Accordingly, this overlap, especially for the case with higher solar concentrations, results in a lower amount of incident solar radiation passing through the dielectric mirror coated on top of the receiver for a PDC system operating at higher temperatures and compared to the cases without any cover on top of the receiver, they provide lower average relative increases in power for high solar concentrations from ~ 35 % for a PDC system operating at 500 K to ~ 30 % for a PDC system operating at 1,000 K and to ~ 26 % for a PDC system operating at 1,500 K.

It can also be noted that the radiative power emitted from the receivers is spread out over a broader spectral range when the receiver is at a lower temperature, and it might be expected that the fraction of radiant energy reflected by [HL]5 or [HQLQ]5 decreases for lower emitter temperatures. However, the FWHM of the reflectance peaks from [HL]5 and [HQLQ]5 also increases when they are designed to reflect radiation from objects operating at lower temperatures. For example the FWHM of the reflectance peak for [HQLQ]5 is 6,870 nm, 3,450 nm, and 2,290 nm when it is designed to work with a receiver at temperatures of 500 K, 1,000 K, and 1,500 K, respectively.

The increase in the FWHM of the reflectance peak with decreasing receiver temperature tends to offset the increase, or broadening, of the radiation spectra that is emitted from the receiver as its temperature decreases. In fact, the amount of radiation from a receiver that is transmitted through [HQLQ]5 is calculated to be 61% whether it is operating at 500 K, 1000 K, or 1500 K.

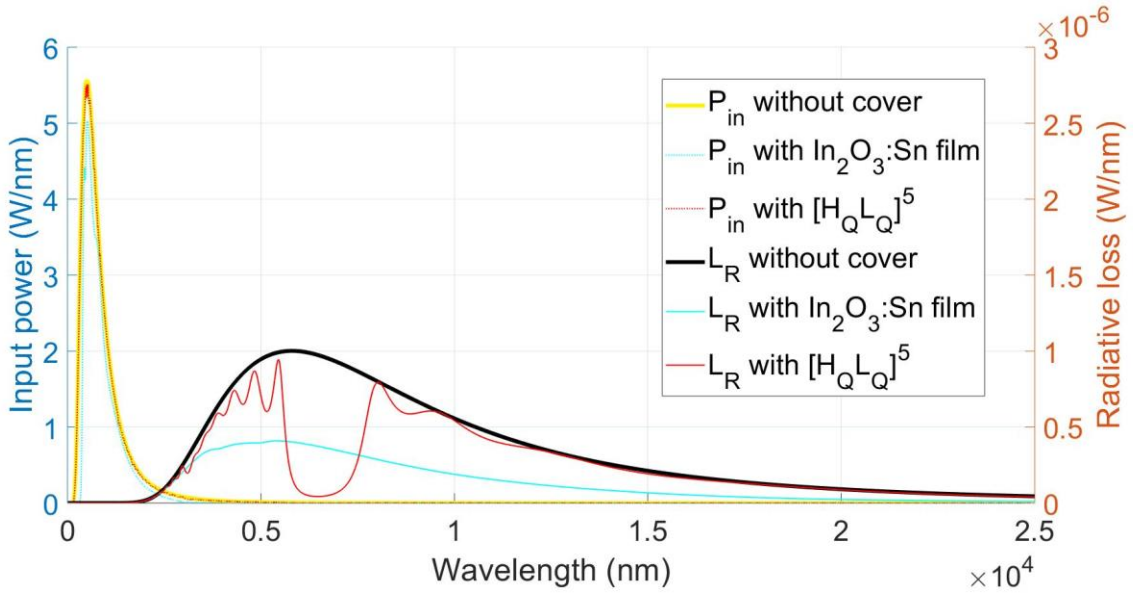

Figure 5-9. Solar power incident onto the receiver and radiative losses from the receiver for different PDC systems with and without a single-stack transparent heat mirror on top of the receiver operating at T = 500 K where alternating layers of films within the dielectric mirror with $[H_Q L_Q]^5{}_{f1}$ have refractive indices of $n_H = 2$ and $n_L = 1.3$.

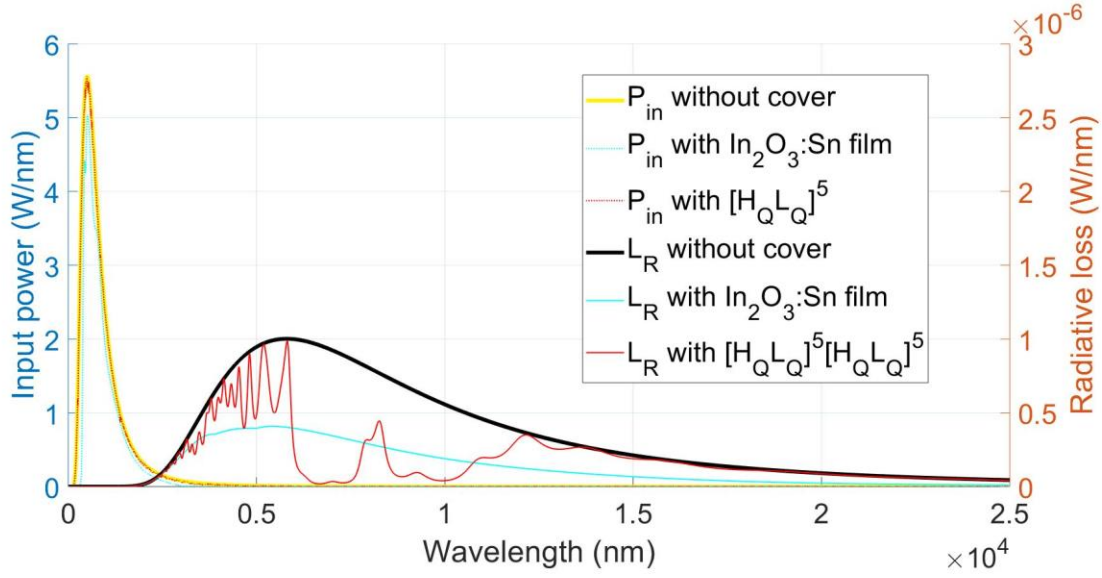

Figure 5-10. Solar power incident onto the receiver and radiative losses from the receiver for different PDC systems with and without a double-stack transparent heat mirror on top of the receiver operating at T = 500 K where alternating layers of films within the $[H_Q L_Q]^5{}_{f1} \cdot [H_Q L_Q]^5{}_{f2}$ dielectric mirrors have refractive indices of $n_H = 2$ and $n_L = 1.3$.

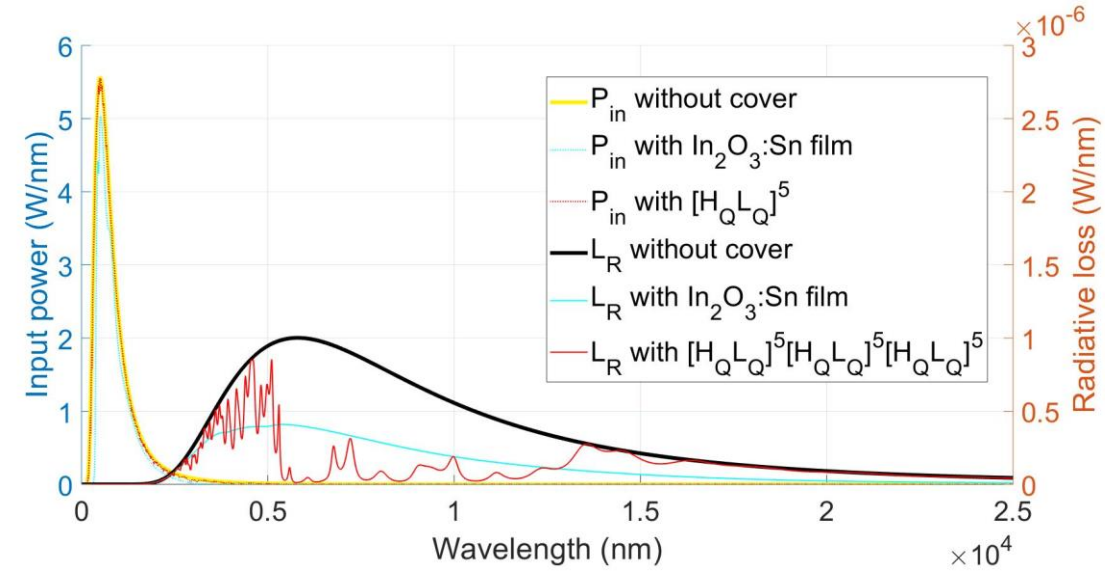

Figure 5-11. Solar power incident onto the receiver and radiative losses from the receiver for different PDC systems with and without a triple-stack transparent heat mirror on top of the receiver operating at T = 500 K where alternating layers of films within the $[H_QL_Q]^5{}_{f1}\cdot[H_QL_Q]^5{}_{f2}\cdot[HL]^5{}_{f3}$ dielectric mirrors have refractive indices of $n_H = 2$ and $n_L = 1.3$.

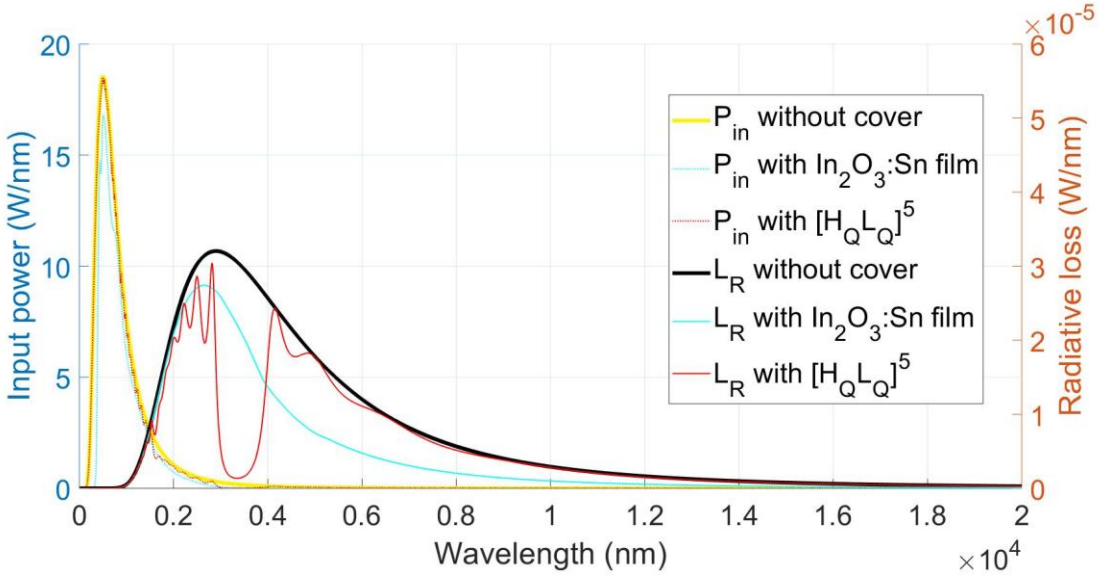

Figure 5-12. Solar power incident onto the receiver and radiative losses from the receiver for different PDC systems with and without a single-stack transparent heat mirror on top of the receiver operating at T = 1,000 K where alternating layers of films within the $[H_QL_Q]^5{}_{f1}$ dielectric mirrors have refractive indices of $n_H = 2$ and $n_L = 1.3$.

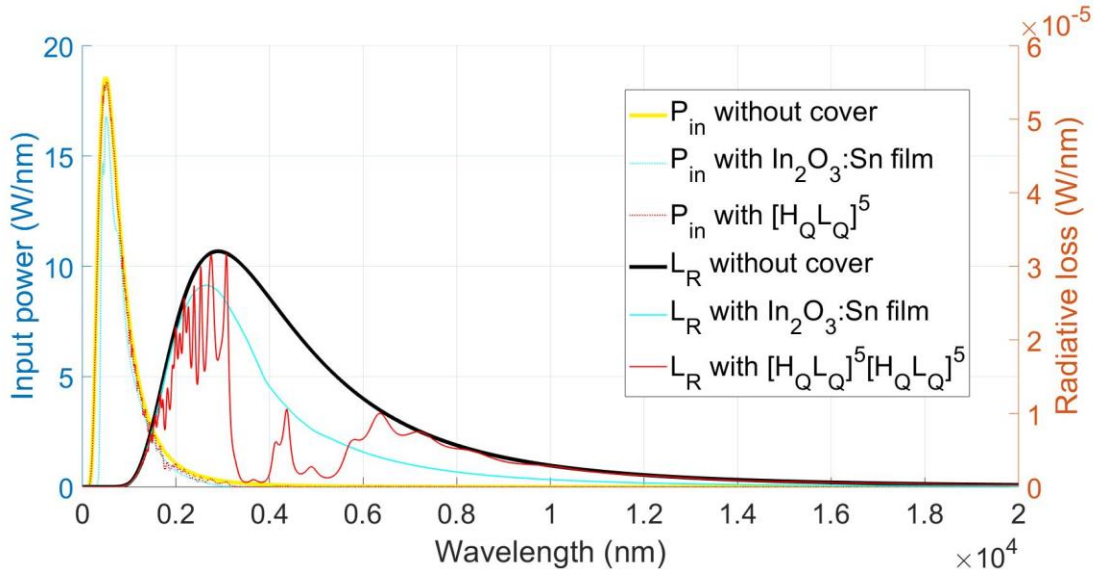

Figure 5-13. Solar power incident onto the receiver and radiative losses from the receiver for different PDC systems with and without a double-stack transparent heat mirror on top of the receiver operating at T= 1,000K where alternating layers of films within the $[H_QL_Q]^5{}_{f1}\cdot[H_QL_Q]^5{}_{f2}$ dielectric mirrors have refractive indices of $n_H = 2$ and $n_L = 1.3$.

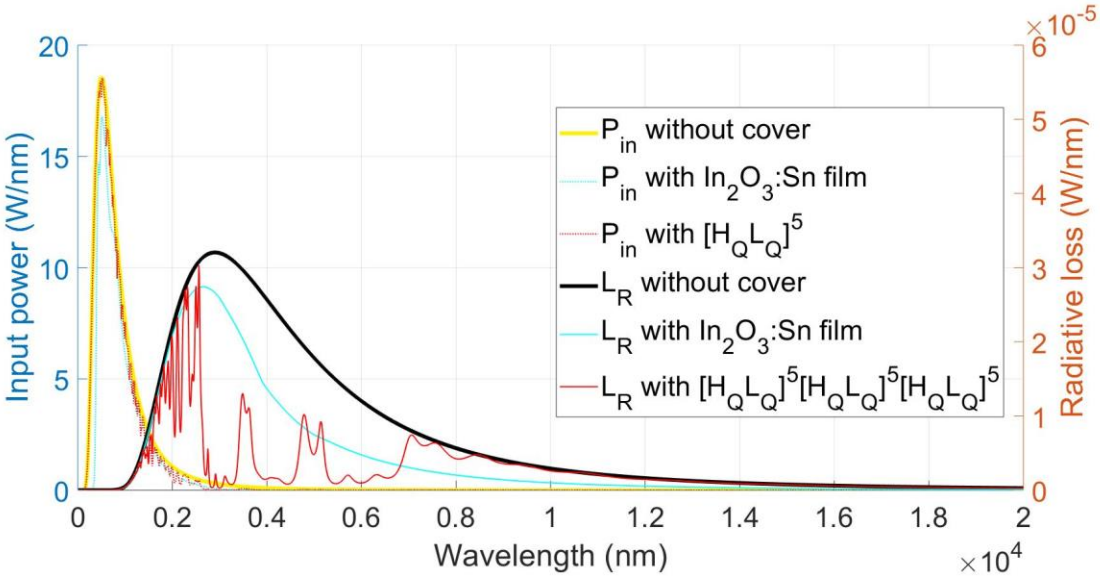

Figure 5-14. Solar power incident onto the receiver and radiative losses from the receiver for different PDC systems with and without a triple-stack transparent heat mirror on top of the receiver operating at T = 1,000K where alternating layers of films within the $[H_QL_Q]^5{}_{f1}\cdot[H_QL_Q]^5{}_{f2}\cdot[HL]^5{}_{f3}$ dielectric mirrors have refractive indices of $n_H = 2$ and $n_L = 1.3$.

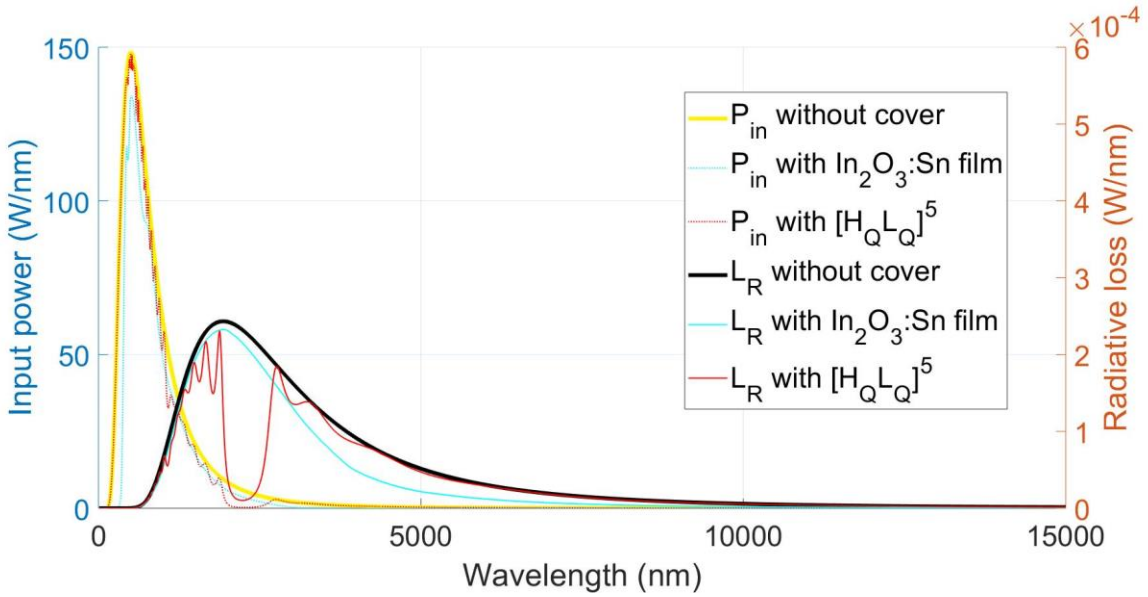

Figure 5-15. Solar power incident onto the receiver and radiative losses from the receiver for different PDC systems with and without a single-stack transparent heat mirror on top of the receiver operating at T = 1,500 K where alternating layers of films within the $[H_QL_Q]^5{}_{f1}$ dielectric mirrors have refractive indices of $n_H = 2$ and $n_L = 1.3$.

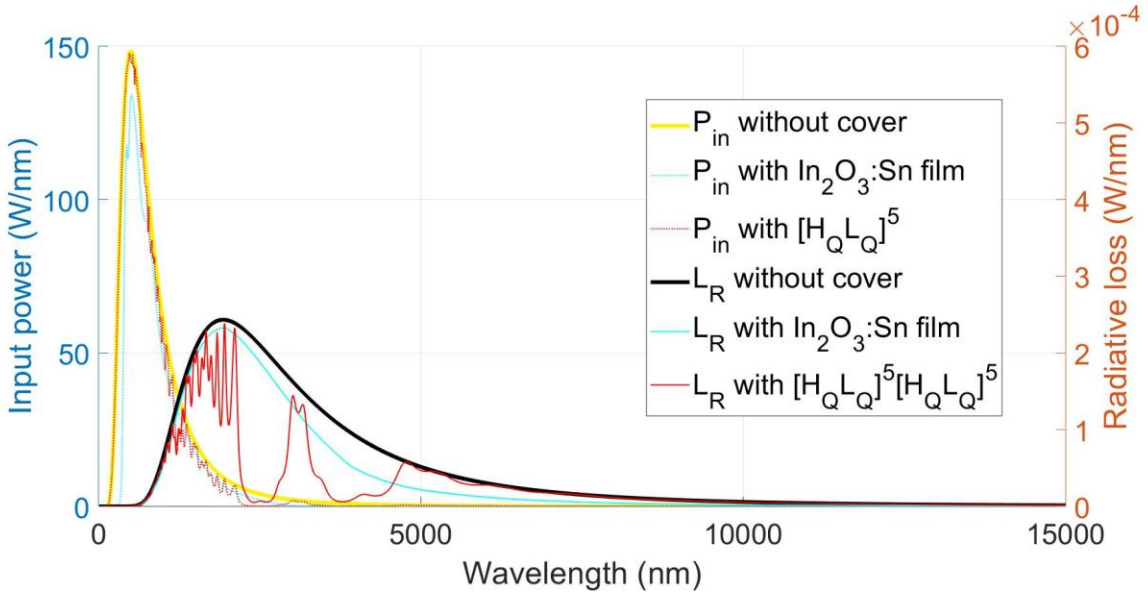

Figure 5-16. Solar power incident onto the receiver and radiative losses from the receiver for different PDC systems with and without a double-stack transparent heat mirror on top of the receiver operating at T= 1,500 K where alternating layers of films within the $[H_QL_Q]^5{}_{f1}\cdot[H_QL_Q]^5{}_{f2}$ dielectric mirror have refractive indices of $n_H = 2$ and $n_L = 1.3$.

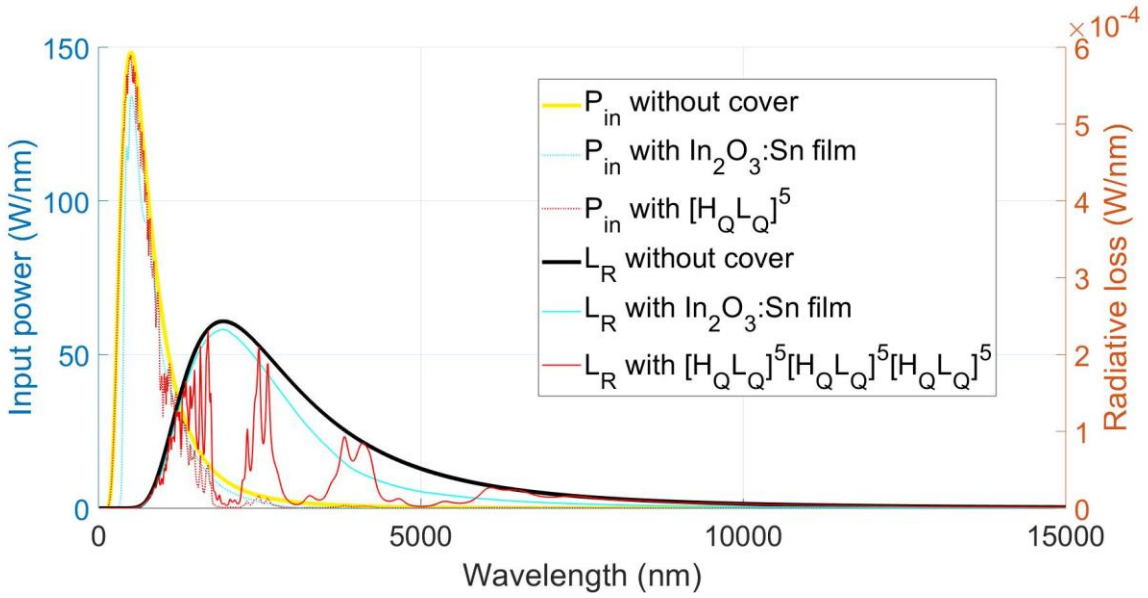

Figure 5-17. Solar power incident onto the receiver and radiative losses from the receiver for different PDC systems with and without a triple-stack transparent heat mirror on top of the receiver operating at T= 1,500K where alternating layers of films within the $[H_QL_Q]^5{}_{f1}\cdot[H_QL_Q]^5{}_{f2}\cdot[HL]^5{}_{f3}$ dielectric mirrors have refractive indices of $n_H = 2$ and $n_L = 1.3$.

6. Thesis summary

Accelerated global warming due to green house gas (GHG) emissions is an important modern-day challenge. Among all the renewable energy resources, solar energy is undoubtedly the largest useable resource, providing one of the cleanest energy resources. In general, solar energy technologies can be divided into two different groups: active and passive. Furthermore, active solar energy systems which are mainly used for energy harvesting can be categorized into two areas: 1. solar photovoltaic cells (PV) and 2. solar thermal technology or concentrated solar thermal power (CSP). CSP is unique among all renewable energy resources as it can simply be coupled with thermal energy storage and conventional fuels, making it extremely flexible. An efficient method to avoid radiative thermal losses and to achieve high temperatures on the receiver within CSP systems is to implement low-Emissivity (low-E) coatings on top of the surface of the receiver. Low-E materials can significantly reduce energy usage by reducing radiative heat losses. Furthermore, transparent solar selective coatings exhibit high transmittance for solar radiation and high reflectance in the near infrared and infrared spectral regions. Consequently, by applying a transparent solar selective surface, herein also referred to as a transparent heat mirror, on the surface of a receiver (which transmits solar radiation and functions as a low-E coating in the infrared region) subjected to concentrated solar radiation will result in a considerable reduction in thermal losses. For example, more electric power can be produced by Dish-Stirling systems when its receiver is coated with a highly efficient solar selective coating.

In order to maximize the temperature of a blackbody subjected to incident solar radiation, with respect to Equation 2-11, $T = \text{constant} \cdot \left(\frac{t}{\varepsilon}\right)^{1/4}$, where t is the transmittance and ε is the emissivity

of the dielectric mirror, the transmittance for solar irradiation and the emissivity of a spectral selective coating should be maximized and minimized, respectively.

6-1. Contributions

One-dimensional dielectric mirrors (otherwise referred to as a Bragg-reflector) have been designed to function as coatings for solar concentrators that reflect infrared radiation to reduce radiative heat losses. In this work, a dielectric mirror is considered wherein the index of refraction of the alternating layers within the mirror are 2.0 and 1.3. In practice, this structure can be fabricated using films such as titanium dioxide (TiO_2), colloidal yttrium oxide (Y_2O_3) and indium-doped tin oxide (ITO) films for the layers with the higher index of refraction (n_H=2) and using films such as SiO_2 nanoparticle films for the layers with the lower index of refraction (n_L=1.3). It is assumed that the spectral distribution of radiation emitted from the receiver approximates that of a blackbody at various temperatures from 500 K to 1500 K, and the thicknesses of the H and L films were chosen such that the spectral position of the reflectance peak of the dielectric mirror matched the peak of the radiation spectra emitted from the receiver, thereby minimizing the radiative heat losses from the receiver.

The design of the dielectric mirror is based on the quarter-wave stack (e.g. quarter-wave thickness equal to $\lambda_0/4n$, where λ_0 is the reference wavelength and n denotes the refractive index of either high or low index) which exhibits the largest reflectance peak for a dielectric mirror. For the quarter-wave stack condition the dielectric mirror is comprised of 725 nm thick TCO films and 1,115.4 nm thick SiO_2 NP films. These quarter-wave stacks reflect a large amount of radiation form the blackbody receiver, however, their reflectance peaks in the solar spectral region reduce

the amount of solar radiation incident onto the solar collector, and thus reduces its efficiency and performance.

To reduce reflection in the solar spectral region, the interfacial graded index technique has been used to increase transmittance in the visible wavelength range while keeping the large reflectance in infrared spectral regions. The technique includes producing continuously varying indices of refraction according to different thicknesses. Three different profiles as index variations (e.g. linear, cubic and quintic profiles) have been used to study antireflection in the interface of two dielectric media. The dielectric mirrors investigated in this thesis are comprised of five bilayers, and the cases of linear (e.g. $[H_L L_L]^5$) , cubic (e.g. $[H_C L_C]^5$), and quintic (e.g. $[H_Q L_Q]^5$) interfacial index of refraction profiles are considered along with the conventional quarter-wave stack wherein the index of refraction profile is a step-function (e.g. $[HL]^5$) at the interface between the H and L layers.

In order to define a design approach towards the best transparent heat mirror, the effects of altering the dielectric mirror parameters on its performance are investigated. That is, the sensitivity of the transmittance and reflectance spectra of the dielectric mirror towards its number of layers, resolution of the refractive index profiles, refractive index, number of stacked dielectric mirrors, absorption, and incident angle of the incoming light was analyzed. Results are shown in Table 1:

Table 6-1. Summary of the effects of altering the dielectric mirror parameters on its performance

Number of layers	• Increasing the number of layers results in a reduction in the fraction of solar spectral power transmitted. • Increasing the number of layers increases the reflectance peaks of the dielectric mirrors in the infrared spectral region. However, beyond a certain number of

	layers, further increasing the number of layers decreases the total amount of thermal radiation reflected (this is because, although the reflectance peak for the heat mirror increases, the FWHM of the peak decreases resulting in a net decrease in the amount of thermal radiation reflected)
Refractive index of the H and L layers within the heat mirror	• Increasing n_H results in an increase for both the FWHM and intensity of the reflectance peak exhibited by the heat mirror. • By increasing the value for n_H more blackbody radiation will be reflected by different dielectric mirrors. However, the general trend for the solar power transmitted through the dielectric mirror is that the transmitted solar power increases as the value of n_H is decreased and becomes closer to n_L, which is equal to 1.3. • By increasing the contrast between the high and low refractive indices results improve and higher temperature on the surface of a blackbody is achieved. Consequently, for all cases considered, the best design for all cases is with n_H= 2.5 and n_L= 1.1
Additional stacked heat mirrors	• Considering that additional heat mirrors (quarter-wave dielectric mirror) with different peak reflectance wavelengths can be stacked on top of each other, increasing the number of stacks generally results in a decrease and large increase of the amount of solar radiation transmitted and thermal radiation reflected, respectively. The benefits of increasing the amount of thermal radiation that is reflected outweighs the losses due to decreased transmittance of the incident solar radiation. • The best result for a double-stack design (wherein each heat mirror in the stack is comprised of five bilayers) for a receiver operating at 500 K is for the case

	when all two stacks have the $[H_QL_Q]^5$ structure and the first stack reflectance peak position is at 6,600 nm and the second stack reflectance peak position is at 9,200 nm. As a result, the total amount of thermal radiation reflected from a black body at 500 K increases from ~ 42 % for the $[HL]^5$ to ~ 55 % for $[H_QL_Q]^5 \cdot [H_QL_Q]^5$and the total amount of the solar radiation transmitted through the dielectric mirror increases from ~ 77 % for the $[HL]^5$ to more than 97 % for the $[H_QL_Q]^5 \cdot [H_QL_Q]^5$. • The best result for a triple-stack design (wherein each heat mirror in the stack is comprised of five bilayers) for a receiver operating at 500 K and with one stack having a reflectance peak position that coincides with the maximum of the thermal radiation spectra emitted from a black body at 500 K (5,800 nm) is for the case when all three stacks have the $[H_QL_Q]^5$ structure and the second stack reflectance peak position is at 7,800 nm and the third stack reflectance peak position is at 10,500 nm. As a result, the total amount of thermal radiation reflected from a black body at 500 K increases from ~42 % for the $[HL]^5$ to ~ 70 % for the $[H_QL_Q]^5 \cdot [H_QL_Q]^5 \cdot [H_QL_Q]^5$ and the total amount of the solar radiation transmitted through the dielectric mirror increases from ~ 77 % for the $[HL]^5$ to more than 96 % for the $[H_QL_Q]^5 \cdot [H_QL_Q]^5 \cdot [H_QL_Q]^5$.
Absorption coefficient	• Depending on the absorption spectra of the material selected for the H and L films, the transmittance and reflectance spectra will be affected. • Overall, increased absorption within the H and L films reduces the efficiency of the dielectric mirror.

As an application of the transparent heat mirrors designed in this work, a parabolic dish collector (PDC) system, or a Dish-Stirling system, was analysed to determine the benefits of using the

selective transparent heat mirror on top of its receiver. Considering different Dish-Stirling systems and applying the transparent heat mirrors on top of the receivers will result in a significant increase in the power conversion efficiency. Results for different receiver temperatures of 500 K, 1,000 K and 1,500 K were provided for the cases when the receiver is covered with single-stack, double-stack and triple-stack dielectric heat mirrors. Moreover, the power generated in Dish-Stirling systems for the case when the receiver is covered with a single TCO (In_2O_3:Sn) layer and the case when the receiver is not covered was also shown for comparison. Considering different solar concentration ratios, the generated power shows different behaviour.

In the following, Table 6-2 illustrates the generated power for different PDC systems with receiver temperatures of 500 K, 1,000 K and 1,500 K for the cases when the receiver is covered with single-stack, double-stack and triple-stack dielectric heat mirrors compared to the case when an In2O3:Sn film is on top of the receiver.

Table 6-2. Results for different receiver temperatures of 500 K, 1,000 K and 1,500 K for the cases when the receiver is covered with single-stack, double-stack and triple-stack dielectric heat mirrors compared to the case when an In_2O_3:Sn film is on top of the receiver.

	$[H_QL_Q]^5_{f1}$	$[H_QL_Q]^5_{f1}\cdot[H_QL_Q]^5_{f2}$	$[H_QL_Q]^5_{f1}\cdot[H_QL_Q]^5_{f2}\cdot[HL]^5_{f3}$	High SCR
	Low Solar Concentration Ratio (SCR)			
T= 500 K	~ 60 % (~ 380 W)	~ 85 % (~ 425 W)	~ 100 % (~ 450 W)	~ 35 %
	SCR = 6			SCR> 30
T= 1000 K	~ 129 % (~ 1,202 W)	~ 283 % (~ 2,010 W)	~ 360 % (~ 2,418 W)	~ 30 %
	SCR = 40			SCR> 200
T= 1500 K	~ 106 % (~ 4,504 W)	~ 245 % (~ 7,530 W)	~ 426 % (~ 11,480 W)	~ 26 %
	SCR = 200			SCR> 1000

Overall, for higher solar concentration ratios, a PDC system with a dielectric mirror with $[H_QL_Q]^5_{f1}$ is more efficient than those with $[H_QL_Q]^5_{f1}\cdot[H_QL_Q]^5_{f2}$ or $[H_QL_Q]^5_{f1}\cdot[H_QL_Q]^5_{f2}\cdot[HL]^5_{f3}$ on top of the receiver because the transmittance through $[H_QL_Q]^5_{f1}$ is higher.

6-2. Future works

Although graded index profiles exhibit excellent improvement in the design of transparent heat mirrors, it would be very difficult to precisely fabricate the linear, cubic, and quintic graded index profiles throughout the dielectric mirror. The main reason is that it is difficult to control the continuous change of the refractive index profile over the large number of periods in the dielectric mirror. Consequently, the dielectric mirrors presented in this work are not presently expected to the best option from an economic standpoint when compared to commercially available solar selective films. However, results recently reported in the literature show various emerging methods to fabricate graded-index films including lithography and wet etching, integrated nano-island coating arrays on nano-conical-frustum arrays, improved metal-induced chemical etching, oblique-angle deposition, electron beam coevaportion, ion beam assisted deposition, plasma-enhanced chemical vapor deposition and sol-gel process. Most of the reports demonstrate oblique-angle decomposition technique as a successful method to fabricate graded-index films. Future work will focus on using these fabrication techniques to demonstrate a decent method to simply fabricate graded index profiles and dielectric heat mirrors presented in this work such that they can be economically used in various solar thermal applications. Also, challenges due to the absorption within the material is of interest. A potential high index film, although a bit expensive, is zinc selenide (ZnSe) with refractive index as high as n = 2.5 and extinction coefficient as low as k = 5.62e-7 over a broad wavelength range extending from the visible spectral region to wavelengths

of 20 microns [178]. Furthermore, one material that may become very useful for the low index layer in this application is highly porous SiO_2 NP films or aerogels. Fabrication of SiO_2 NP films with refractive index of 1.23 for quarter-wave layers or even lower indices of 1.14 for thicker layers were demonstrated using sol-gel. Although, this method is good for very low index coatings, it is not presently suitable for depositing films with thicknesses on the order of ~100 nm. However, recently, electron-beam evaporation demonstrated fabrication of a highly porous thin SiO_2 NP films with a refractive index as low as 1.08 [179-181]. In general, the future development of thin-films with highly controlled optical properties in the infrared spectral region will benefit the advancement of the transparent dielectric heat mirrors designed in this work and will enable the enhancement of radiative energy control in a broad range of applications such as Dish-Stirling systems and other solar energy harvesting systems.

References

[1] Natural Resources Canada, “Energy and greenhouse gas emissions”, (url: https://www.nrcan.gc.ca/energy/facts/energy-ghgs/20063), 2018.

[2] S. Mekhilef, R. Saidur, and A. Safari, “A review on solar energy use in industries,” Renew. Sustain. Energy Rev., vol. 15, no. 4, pp. 1777–1790, 2011.

[3] US EIA, “International Energy Outlook 2018 (IEO 2018) Key takeaways,” U.S. Energy Inf. Adm. (url: https//www.eia.gov/pressroom/presentations/capuano_07242018.pdf), 2018.

[4] N. Y. Amponsah, M. Troldborg, B. Kington, I. Aalders, and R. L. Hough, “Greenhouse gas emissions from renewable energy sources: A review of lifecycle considerations,” Renew. Sustain. Energy Rev., vol. 39, pp. 461–475, 2014.

[5] R. P. Walker and A. Swift, “Greenhouse Gas Emissions,” Environment and climate change Canada, (url: https://www.canada.ca/content/dam/eccc/documents/pdf/cesindicators/greenhouse-gas-emissions/greenhouse-gas-emissions-en.pdf), 2018.

[6] A. DemirbaÅŸ, “Biomass resource facilities and biomass conversion processing for fuels and chemicals,” Energy Convers. Manag., vol. 42, pp. 1357–1378, 2001.

[7] R. A. Zakhidov, “Central Asian countries energy system and role of renewable energy sources,” Appl. Sol. Energy, vol. 44, no. 3, pp. 218–223, 2008.

[8] N. L. Panwar, S. C. Kaushik, and S. Kothari, “Role of renewable energy sources in environmental protection: A review,” Renew. Sustain. Energy Rev., vol. 15, no. 3, pp. 1513–1524, 2011.

[9] A. Bergmann, S. Colombo, and N. Hanley, “Rural versus urban preferences for renewable energy developments,” Ecol. Econ., vol. 65, no. 3, pp. 616–625, 2008.

[10] A. K. N. Reddy and D. K. Subramanian, “The design of rural energy centres,” Proc. Indian Acad. Sci., vol. 2, no. 3, pp. 395–416, 1979.

[11] D. G. Nocera and N. S. Lewis, “Powering the planet: Chemical challenges in solar energy utilization” vol. 103, no. 43, 2006.

[12] International Panel on Climate Change, Summary for Policymakers: Special Report on Renewable Energy Sources and Climate Change Mitigation. 2011.

[13] M. M. Aman et al., “A review of Safety, Health and Environmental (SHE) issues of solar energy system,” Renew. Sustain. Energy Rev., vol. 41, pp. 1190–1204, 2015.

[14] E. Kabir, P. Kumar, S. Kumar, A. A. Adelodun, and K. H. Kim, “Solar energy: Potential and future prospects,” Renew. Sustain. Energy Rev., vol. 82, no. August 2017, pp. 894–900, 2018.

[15] K. H. Solangi, M. R. Islam, R. Saidur, N. A. Rahim, and H. Fayaz, “A review on global solar energy policy,” Renew. Sustain. Energy Rev., vol. 15, no. 4, pp. 2149–2163, 2011.

[16] S. M. Hasnain, “Solar energy education a viable pathway for sustainable development” Renew. Energy, vol. 14, no. 98, pp. 387–392, 1998.

[17] K. Bilen et al., “Energy production, consumption, and environmental pollution for sustainable development: A case study in Turkey,” Renew. Sustain. Energy Rev., vol. 12, no. 6, pp. 1529–1561, 2008.

[18] Z. X. Zhang, “Asian energy and environmental policy: Promoting growth while preserving the environment,” Energy Policy, vol. 36, no. 10, pp. 3905–3924, 2008.

[19] M. Mussard, “Solar energy under cold climatic conditions: A review,” Renew. Sustain. Energy Rev., vol. 74, no. March, pp. 733–745, 2017.

[20] G. Rajgor, “Greater acceleration of renewables required to meet COP21 goal,” Renewable Energy Focus, vol. 17, no. 5, pp. 175–177, 2016.

[21] M. S. Arif, “Residential Solar Panels and Their Impact on the Reduction of Carbon Emissions Mashail S. Arif,” Spring, pp. 1–18, 2013.

[22] B. Xu, P. Li, and C. Chan, “Application of phase change materials for thermal energy storage in concentrated solar thermal power plants: A review to recent developments,” Appl. Energy, vol. 160, pp. 286–307, 2015.

[23] X. Py, Y. Azoumah, and R. Olives, “Concentrated solar power: Current technologies, major innovative issues and applicability to West African countries,” Renew. Sustain. Energy Rev., vol. 18, pp. 306–315, 2013.

[24] S. Dubey, J. N. Sarvaiya, and B. Seshadri, “Temperature dependent photovoltaic (PV) efficiency and its effect on PV production in the world - A review,” Energy Procedia, vol. 33, pp. 311–321, 2013.

[25] Y. Chu, “Review and Comparison of Different Solar Energy Technologies,” Geni, no. August, p. 56, 2011.

[26] J. Sun, Q. Liu, and H. Hong, “Numerical study of parabolic-trough direct steam generation loop in recirculation mode: Characteristics, performance and general operation strategy,” Energy Convers. Manag., vol. 96, pp. 287–302, 2015.

[27] A. Demirbas, “Progress and recent trends in biofuels,” Prog. Energy Combust. Sci., vol. 33, no. 1, pp. 1–18, 2007.

[28] M. Herrando and C. N. Markides, “Hybrid PV and solar-thermal systems for domestic heat and power provision in the UK: Techno-economic considerations,” Appl. Energy, vol. 161, pp. 512–532, 2016.

[29] B. Parida, S. Iniyan, and R. Goic, “A review of solar photovoltaic technologies,” Renew. Sustain. Energy Rev., vol. 15, no. 3, pp. 1625–1636, 2011.

[30] M. Hosenuzzaman, N. A. Rahim, J. Selvaraj, M. Hasanuzzaman, A. B. M. A. Malek, and A. Nahar, “Global prospects, progress, policies, and environmental impact of solar photovoltaic power generation,” Renew. Sustain. Energy Rev., vol. 41, pp. 284–297, 2015.

[31] V. V. Tyagi, N. A. A. Rahim, N. A. Rahim, and J. A. L. Selvaraj, “Progress in solar PV technology: Research and achievement,” Renew. Sustain. Energy Rev., vol. 20, pp. 443–461, 2013.

[32] F. Diner, “The analysis on photovoltaic electricity generation status, potential and policies of the leading countries in solar energy,” Renew. Sustain. Energy Rev., vol. 15, no. 1, pp. 713–720, 2011.

[33] P. G. V. Sampaio and M. O. A. González, “Photovoltaic solar energy: Conceptual framework,” Renew. Sustain. Energy Rev., vol. 74, no. February, pp. 590–601, 2017.

[34] Enviro-Energy Technologies Inc., “url: http://www.enviro-energytech.com/”

[35] B. Tamimi, C. Canizares, and K. Bhattacharya, “System stability impact of large-scale and distributed solar photovoltaic generation: The case of Ontario, Canada,” IEEE Trans. Sustain. Energy, vol. 4, no. 3, pp. 680–688, 2013.

[36] Independent Electricity System Operator, “url: http://www.ieso.ca/en/Sector-Participants/Feed-in-Tariff-Program/Overview”

[37] P. A. Basore and W. J. Cole, “Comparing supply and demand models for future photovoltaic power generation in the USA,” Prog. Photovoltaics Res. Appl., vol. 26, no. 6, pp. 414–418, 2018.

[38] M. Thirugnanasambandam, S. Iniyan, and R. Goic, “A review of solar thermal technologies,” Renew. Sustain. Energy Rev., vol. 14, no. 1, pp. 312–322, 2010.

[39] S. Kuravi, J. Trahan, D. Y. Goswami, M. M. Rahman, and E. K. Stefanakos, “Thermal energy storage technologies and systems for concentrating solar power plants,” Prog. Energy Combust. Sci., vol. 39, no. 4, pp. 285–319, 2013.

[40] E. González-Roubaud, D. Pérez-Osorio, and C. Prieto, “Review of commercial thermal energy storage in concentrated solar power plants: Steam vs. molten salts,” Renew. Sustain. Energy Rev., vol. 80, no. February, pp. 133–148, 2017.

[41] O. Behar, A. Khellaf, K. Mohammedi, and S. Ait-Kaci, “A review of integrated solar combined cycle system (ISCCS) with a parabolic trough technology,” Renew. Sustain. Energy Rev., vol. 39, pp. 223–250, 2014.

[42] U. Pelay, L. Luo, Y. Fan, D. Stitou, and M. Rood, “Thermal energy storage systems for concentrated solar power plants,” Renew. Sustain. Energy Rev., vol. 79, no. May, pp. 82–100, 2017.

[43] P. Pardo, A. Deydier, Z. Anxionnaz-Minvielle, S. Rougé, M. Cabassud, and P. Cognet, “A review on high temperature thermochemical heat energy storage,” Renew. Sustain. Energy Rev., vol. 32, pp. 591–610, 2014.

[44] R. Guédez, J. Spelling, and B. Laumert, “Reducing the Number of Turbine Starts in Concentrating Solar Power Plants Through the Integration of Thermal Energy Storage,” J. Sol. Energy Eng., vol. 137, no. 1, p. 011003, 2014.

[45] M. Liu et al., “Review on concentrating solar power plants and new developments in high temperature thermal energy storage technologies,” Renew. Sustain. Energy Rev., vol. 53, pp. 1411–1432, 2016.

[46] J. Stekli, L. Irwin, and R. Pitchumani, “Technical Challenges and Opportunities for Concentrating Solar Power with Thermal Energy Storage,” J. Therm. Sci. Eng. Appl., vol. 5, no. 2, p. 021011, 2013.

[47] G. Alva, L. Liu, X. Huang, and G. Fang, “Thermal energy storage materials and systems for solar energy applications,” Renew. Sustain. Energy Rev., vol. 68, no. October 2016, pp. 693–706, 2017.

[48] H. Chen, T. N. Cong, W. Yang, C. Tan, Y. Li, and Y. Ding, “Progress in electrical energy storage system: A critical review,” Prog. Nat. Sci., vol. 19, no. 3, pp. 291–312, 2009.

[49] E. González-Roubaud, D. Pérez-Osorio, and C. Prieto, “Review of commercial thermal energy storage in concentrated solar power plants: Steam vs. molten salts,” Renew. Sustain. Energy Rev., vol. 80, no. February, pp. 133–148, 2017.

[50] H. Ibrahim and A. Ilinc, “Techno-Economic Analysis of Different Energy Storage Technologies,” Energy Storage - Technol. Appl., pp. 1–40, 2013.

[51] H. Zhao, Q. Wu, S. Hu, H. Xu, and C. N. Rasmussen, “Review of energy storage system for wind power integration support,” Appl. Energy, vol. 137, pp. 545–553, 2015.

[52] D. O. Akinyele and R. K. Rayudu, “Review of energy storage technologies for sustainable power networks,” Sustain. Energy Technol. Assessments, vol. 8, pp. 74–91, 2014.

[53] X. Luo, J. Wang, M. Dooner, and J. Clarke, “Overview of current development in electrical energy storage technologies and the application potential in power system operation,” Appl. Energy, vol. 137, pp. 511–536, 2015.

[54] G. Alva, Y. Lin, and G. Fang, “An overview of thermal energy storage systems,” Energy, vol. 144, pp. 341–378, 2018.

[55] S. Lindner, “Space conditioning in the residential sector in Europe”, 2007.

[56] P. Pinel, C. A. Cruickshank, I. Beausoleil-Morrison, and A. Wills, “A review of available methods for seasonal storage of solar thermal energy in residential applications,” Renew. Sustain. Energy Rev., vol. 15, no. 7, pp. 3341–3359, 2011.

[57] H. Schnitzer, C. Brunner, and G. Gwehenberger, “Minimizing greenhouse gas emissions through the application of solar thermal energy in industrial processes,” J. Clean. Prod., vol. 15, no. 13–14, pp. 1271–1286, 2007.

[58] E. Biermann, M. Grupp, and R. Palmer, “Solar cooker acceptance in South Africa: Results of a comparative field-test,” Sol. Energy, vol. 66, no. 6, pp. 401–407, 1999.

[59] M. Tucker, “Can solar cooking save the forests?”, Ecol. Econ., vol. 31, no. 1, pp. 77–89, 1999.

[60] M. Wentzel and A. Pouris, “The development impact of solar cookers: A review of solar cooking impact research in South Africa,” Energy Policy, vol. 35, no. 3, pp. 1909–1919, 2007.

[61] N. L. Panwar, S. C. Kaushik, and S. Kothari, “Role of renewable energy sources in environmental protection: A review,” Renew. Sustain. Energy Rev., vol. 15, no. 3, pp. 1513–1524, 2011.

[62] A. Haines, R. Kovats, D. Campbell-Lendrum, and C. Corvalan, “Climate change and human health: impacts, vulnerability, and mitigation,” Lancet, vol. 367, no. 9528, pp. 2101–2109, 2006.

[63] I. Dincer, “Energy and environmental impacts: Present and future perspectives,” Energy Sources, vol. 20, no. 4–5, pp. 427–453, 1998.

[64] B. Xu, P. Li, and C. Chan, “Application of phase change materials for thermal energy storage in concentrated solar thermal power plants: A review to recent developments,” Appl. Energy, vol. 160, pp. 286–307, 2015.

[65] B. P. Jelle, S. E. Kalnæs, and T. Gao, “Low-emissivity materials for building applications: A state-of-the-art review and future research perspectives,” Energy Build., vol. 96, no. 7491, pp. 329–356, 2015.

[66] F. Giovannetti, S. Föste, N. Ehrmann, and G. Rockendorf, “High transmittance, low emissivity glass covers for flat plate collectors: Applications and performance,” Sol. Energy, vol. 104, pp. 52–59, 2014.

[67] L. Liu et al., “Achieving low-emissivity materials with high transmission for broadband radio-frequency signals,” Sci. Rep., vol. 7, no. 1, pp. 1–7, 2017.

[68] M. S. Al-Homoud, “Performance characteristics and practical applications of common building thermal insulation materials,” Build. Environ., vol. 40, no. 3, pp. 353–366, 2005.

[69] H. Price et al., “Advances in Parabolic Trough Solar Power Technology,” J. Sol. Energy Eng., vol. 124, no. 2, p. 109, 2002.

[70] S. A. Kalogirou, Solar thermal collectors and applications, vol. 30, no. 3. 2004.

[71] Y. Tian and C. Y. Zhao, “A review of solar collectors and thermal energy storage in solar thermal applications,” Appl. Energy, vol. 104, pp. 538–553, 2013.

[72] C. G. Granqvist, “Solar Energy Materials,” Adv. Mater., vol. 15, no. 21, pp. 1789–1803, 2003.

[73] J. Karlsson and A. Roos, “Annual energy window performance vs. glazing thermal emittance - The relevance of very low emittance values,” Thin Solid Films, vol. 392, no. 2, pp. 345–348, 2001.

[74] P. Würfel, “Physics of solar cells from principles to new concepts”,Wiley-VCH, 2009.

[75] C. Riordan and R. Hulstrom, “What is an air mass 1.5 spectrum”, IEEE, 1990.

[76] R. Hulstrom, R. Bird, and C. Riordan, “Spectral solar irradiance data sets for selected terrestrial conditions” Solar Cells, vol. 15, pp. 365–391, 1985.

[77] R. E. Bird, R. L. Hulstrom, and L. J. Lewis, “Terrestrial solar spectral data sets,” Sol. Energy, vol. 30, no. 6, pp. 563–573, 1983.

[78] M. Mahmoud, “Engineering Thermofluids”, Springer Berlin Heidelberg, pp. 431-600, 2005.

[79] J. R. Howell, R. Siegel, and M. P. Mengüç, book - Thermal Radiation Heat Transfer, 5th Edition. 2010.

[80] Goody, R. M.; Yung, Y. L. (1989). Atmospheric Radiation: Theoretical Basis (2nd ed.). Oxford University Press. ISBN 978-0-19-510291-8.

[81] T.M. Lillesand and R.W. Kieffer, Remote Sensing and Image Interpretation, 2nd Ed., © 1987.

[82] http://geoinfo.amu.edu.pl/wpk/rst/rst/Sect9/Sect9_2.html

[83] B. P. Jelle, S. E. Kalnæs, and T. Gao, “Low-emissivity materials for building applications: A state-of-the-art review and future research perspectives,” Energy Build., vol. 96, no. 7491, pp. 329–356, 2015.

[84] F. Giovannetti, S. Föste, N. Ehrmann, and G. Rockendorf, “High transmittance, low emissivity glass covers for flat plate collectors: Applications and performance,” Sol. Energy, vol. 104, pp. 52–59, 2014.

[85] L. Liu et al., “Achieving low-emissivity materials with high transmission for broadband radio-frequency signals,” Sci. Rep., vol. 7, no. 1, pp. 1–7, 2017.

[86] E. Hammarberg and A. Roos, “Antireflection treatment of low-emitting glazings for energy efficient windows with high visible transmittance,” Thin Solid Films, vol. 442, no. 1–2, pp. 222–226, 2003.

[87] M. Auslender and S. Hava, “Zero infrared reflectance anomaly in doped silicon lamellar gratings. I. From antireflection to total absorption,” Infrared Phys. Technol., vol. 36, no. 7, pp. 1077–1088, 1995.

[88] P. Pfrommer, K. J. Lomas, C. Seale, and C. Kupke, “The radiation transfer through coated and tinted glazing,” Sol. Energy, vol. 54, no. 5, pp. 287–299, 1995.

[89] J. Karlsson, Windows: optical performance and energy efficiency. 2001.

[90] Tco, “Review of TCO Thin Films,” TCO Singapore, pp. 1–17, 2008.

[91] G. Colangelo, E. Favale, P. Miglietta, and A. De Risi, “Innovation in flat solar thermal collectors: A review of the last ten years experimental results,” Renew. Sustain. Energy Rev., vol. 57, pp. 1141–1159, 2016.

[92] D. Alonso-Álvarez, L. Ferre Llin, N. J. Ekins-Daukes, and D. J. Paul, “ITO and AZO films for low emissivity coatings in hybrid photovoltaic-thermal applications,” Sol. Energy, vol. 155, pp. 82–92, 2017.

[93] J. Geissbühler et al., “22.5% Efficient Silicon Heterojunction Solar Cell with Molybdenum Oxide Hole Collector,” Appl. Phys. Lett., vol. 107, no. 8, 2015.

[94] R. Platz, D. Fischer, M. -a. Zufferey, J. a. a. Selvan, a. Haller, and a. Shah, “Hybrid collectors using thin-film technology,” Conf. Rec. Twenty Sixth IEEE Photovolt. Spec. Conf. - 1997, pp. 1293–1296, 1997.

[95] N. Ehrmann, R. Reineke-Koch, S. Föste, and F. Giovannetti, “The influence of process parameters and coating properties of double glazing coated with transparent conducting oxides on the efficiency of solar-thermal flat-plate collectors,” Thin Solid Films, vol. 532, pp. 132–140, 2013.

[96] N. Ehrmann and R. Reineke-Koch, “Selectively coated high efficiency glazing for solar-thermal flat-plate collectors,” Thin Solid Films, vol. 520, no. 12, pp. 4214–4218, 2012.

[97] F. Iskandar, “Nanoparticle processing for optical applications - A review,” Adv. Powder Technol., vol. 20, no. 4, pp. 283–292, 2009.

[98] D. DeJarnette, T. Otanicar, N. Brekke, P. Hari, and K. Roberts, “Selective spectral filtration with nanoparticles for concentrating solar collectors,” J. Photonics Energy, vol. 5, no. 1, p. 057008, 2015.

[99] X. Wang et al., “TiO2 nanotube arrays based flexible perovskite solar cells with transparent carbon nanotube electrode,” Nano Energy, vol. 11, pp. 728–735, 2015.

[100] M. F. L. De Volder, S. H. Tawfick, R. H. Baughman, and A. J. Hart, “Carbon nanotubes: present and future commercial applications - Supplemental Information,” Science, vol. 339, no. 6119, pp. 535–539, 2013.

[101] S. Ye, A. R. Rathmell, Z. Chen, I. E. Stewart, and B. J. Wiley, “Metal nanowire networks: The next generation of transparent conductors,” Adv. Mater., vol. 26, no. 39, pp. 6670–6687, 2014.

[102] H. Wu et al., “A transparent electrode based on a metal nanotrough network,” Nat. Nanotechnol., vol. 8, no. 6, pp. 421–425, 2013.

[103] J. L. Deschanvres et al., “Study of the growth and annealing conditions of SrCu 2O 2 (SCO) thin films deposited by injection MOCVD,” Phys. Status Solidi Appl. Mater. Sci., vol. 205, no. 8, pp. 2013–2017, 2008.

[104] R. A. Taylor, Y. Hewakuruppu, D. DeJarnette, and T. P. Otanicar, “Comparison of selective transmitters for solar thermal applications,” Appl. Opt., vol. 55, no. 14, p. 3829, 2016.

[105] D. V. Bellas and E. Lidorikis, “Design of high-temperature solar-selective coatings for application in solar collectors,” Sol. Energy Mater. Sol. Cells, vol. 170, no. February, pp. 102–113, 2017.

[106] T. Rosencrantz, H. Bülow-Hübe, B. Karlsson, and A. Roos, “Increased solar energy and daylight utilisation using anti-reflective coatings in energy-efficient windows,” Sol. Energy Mater. Sol. Cells, vol. 89, no. 2–3, pp. 249–260, 2005.

[107] F. Iskandar, “Nanoparticle processing for optical applications - A review,” Adv. Powder Technol., vol. 20, no. 4, pp. 283–292, 2009.

[108] B. E. Yoldas, “for Glass Surfaces,” Appl. Opt., vol. 19, no. May, pp. 1425–1429, 1980.

[109] I. M. Thomas, “Method for the preparation of porous silica antireflection coatings varying in refractive index from 122 to 144,” Appl. Opt., vol. 31, no. 28, p. 6145, 2009.

[110] M. S. Al-Homoud, “Performance characteristics and practical applications of common building thermal insulation materials,” Build. Environ., vol. 40, no. 3, pp. 353–366, 2005.

[111] H. Price et al., “Advances in Parabolic Trough Solar Power Technology,” J. Sol. Energy Eng., vol. 124, no. 2, p. 109, 2002.

[112] S. A. Kalogirou, Solar thermal collectors and applications, vol. 30, no. 3. 2004.

[113] Y. Tian and C. Y. Zhao, “A review of solar collectors and thermal energy storage in solar thermal applications,” Appl. Energy, vol. 104, pp. 538–553, 2013.

[114] C. G. Granqvist, “Solar Energy Materials,” Adv. Mater., vol. 15, no. 21, pp. 1789–1803, 2003.

[115] J. Karlsson, Windows: optical performance and energy efficiency. 2001.

[116] A. Anders, “Materials, Processes, and Issues in Low-Emissivity and Solar Control Coatings,” pp. 1–12, 2002.

[117] S. S. Kanu and R. Binions, “Thin films for solar control applications,” Proc. R. Soc. A Math. Phys. Eng. Sci., vol. 466, no. 2113, pp. 19–44, 2010.

[118] J. C. C. Fan and F. J. Bachner, “Transparent heat mirrors for solar-energy applications,” Appl. Opt., vol. 15, no. 4, p. 1012, 2008.

[119] P. T. Landsberg and A. De Vos, “Related content The Stefan-Boltzmann constant in n-dimensional space,” 1989.

[120] M. Modest, “Radiative Heat Transfer”, Academic Press, 2014

[121] R. Mccluney, “Fenestration Solar Gain Analysis,”, Florida Solar Energy Center/ University of Central Florida, 1996.

[122] G. Wu and D. Yu, “Preparation and characterization of a new low infrared-emissivity coating based on modified aluminum,” Prog. Org. Coatings, vol. 76, no. 1, pp. 107–112, 2013.

[123] B. P. Jelle, A. Hynd, A. Gustavsen, D. Arasteh, H. Goudey, and R. Hart, “Fenestration of today and tomorrow: A state-of-the-art review and future research opportunities,” Sol. Energy Mater. Sol. Cells, vol. 96, no. 1, pp. 1–28, 2012.

[124] P. Bermel, J. Lee, J. D. Joannopoulos, I. Celanovic, and M. Soljacie, “Selective Solar Absorbers,” Annu. Rev. Heat Transf., vol. 15, no. 15, pp. 231–254, 2012.

[125] P. Bermel, J. Lee, J. D. Joannopoulos, I. Celanovic, and M. Soljacie, “Selective Solar Absorbers,” Annu. Rev. Heat Transf., vol. 15, no. 15, pp. 231–254, 2012.

[126] C. E. Kennedy, “Review of Mid- to High-Temperature Solar Selective Absorber Materials,” no. July, 2002.

[127] C. G. Granqvist, “Solar Energy Materials,” Sol. Energy Mater., vol. 93, pp. 83–93, 1991.

[128] Å. Andersson, O. Hunderi, and C. G. Granqvist, “Nickel pigmented anodic aluminum oxide for selective absorption of solar energy,” J. Appl. Phys., vol. 51, no. 1, pp. 754–764, 1980.

[129] J. D. Joannopoulos, S. G. Johnson, J. N. Winn, R. D. Meade, “Photonic Crystals Molding the Flow of Light”, 2nd Edition, Princeton University Press, 2008.

[130] H. A. Macleod, “Thin-Film Optical Filters”, 4th Edition, Taylor and Francis Group, LLC, 2010.

[131] M. Moayedfar and M. K. Assadi, “Various types of anti-reflective coatings (ARCS) Based on the layer composition and surface topography: A review,” Rev. Adv. Mater. Sci., vol. 53, no. 2, pp. 187–205, 2018.

[132] H. K. Raut, V. A. Ganesh, A. S. Nair, and S. Ramakrishna, “Anti-reflective coatings: A critical, in-depth review,” Energy Environ. Sci., vol. 4, no. 10, pp. 3779–3804, 2011.

[133] A. Ramizy, W. J. Aziz, Z. Hassan, K. Omar, and K. Ibrahim, “The effect of porosity on the properties of silicon solar cell,” Microelectron. Int., vol. 27, no. 2, pp. 117–120, 2010.

[134] “Reduction of lens reflection by the "Moth Eye" principle”, NATURE VOL. 244 ,1973

[135] Lord Rayiieigh, “Lord Rayleigh on the Instability of Jets,” Proc. London Math. Soc., vol. s1-10, no. 1, pp. 4–13, 1878.

[136] J. A. Dobrowolski, “Optical properties of films and coatings optical properties of films and coatings”, Handbook of Optics: Fundamentals, Techniques, and Design, pp. 42.3-42.130, 1995.

[137] J. A. Dobrowolski, D. Poitras, P. Ma, H. Vakil, and M. Acree, “Toward perfect antireflection coatings: numerical investigation,” Appl. Opt., vol. 41, no. 16, p. 3075, 2007.

[138] M. Moayedfar and M. K. Assadi, “Various types of anti-reflective coatings (ARCS) Based on the layer composition and surface topography: A review,” Rev. Adv. Mater. Sci., vol. 53, no. 2, pp. 187–205, 2018.

[139] S. Callard, A. Gagnaire, and J. Joseph, “Fabrication and characterization of graded refractive index silicon oxynitride thin films,” J. Vac. Sci. Technol. A Vacuum, Surfaces, Film., vol. 15, no. 4, pp. 2088–2094, 2002.

[140] J. Q. Xi et al., “Optical thin-film materials with low refractive index for broadband elimination of Fresnel reflection,” Nat. Photonics, vol. 1, no. 3, pp. 176–179, 2007.

[141] W. H. Southwell, “Gradient-index antireflection coatings,” vol. 8, no. 11, pp. 584–586, 1983.

[142] X. Wang, H. Masumoto, Y. Someno, and T. Hirai, “Design and experimental approach of optical reflection filters with graded refractive index profiles,” J. Vac. Sci. Technol. A Vacuum, Surfaces, Film., vol. 17, no. 1, pp. 206–211, 2002.

[143] G. Wu et al., “Preparation and properties of scratch-resistant nanoporous broadband AR silica films derived by a two-step catalytic sol-gel process,” Fourth Int. Conf. Thin Film Phys. Appl., vol. 4086, no. November 2000, p. 807, 2003.

[144] J. C. Zhang, L. M. Xiong, M. Fang, and H. B. He, “Wide-angle and broadband graded-refractive-index antireflection coatings,” Chinese Phys. B, vol. 22, no. 4, pp. 1–5, 2013.

[145] D. P. Partlow and T. W. O’Keeffe, “Thirty-seven-layer optical filter from polymerized solgel solutions,” Appl. Opt., vol. 29, no. 10, p. 1526, 2009.

[146] J. Chen, B. Wang, Y. Yang, Y. Shi, G. Xu, and P. Cui, “Porous anodic alumina with low refractive index for broadband graded-index antireflection coatings,” Appl. Opt., vol. 51, no. 28, p. 6839, 2012.

[147] M.-L. Kuo et al., “Realization of a near-perfect antireflection coating for silicon solar energy utilization,” Opt. Lett., vol. 33, no. 21, p. 2527, 2008.

[148] P. G. Snyder, Y. Xiong, J. A. Woollam, G. A. Al-Jumaily, and F. J. Gagliardi, “Graded refractive index silicon oxynitride thin film characterized by spectroscopic ellipsometry,” J. Vac. Sci. Technol. A Vacuum, Surfaces, Film., vol. 10, no. 4, pp. 1462–1466, 2002.

[149] C. K. Carniglia, “Ellipsometric calculations for nonabsorbing thin films with linear refractive-index gradients,” J. Opt. Soc. Am. A, vol. 7, no. 5, p. 848, 2008.

[150] R. A. Taylor, Y. Hewakuruppu, D. DeJarnette, and T. P. Otanicar, “Comparison of selective transmitters for solar thermal applications,” Appl. Opt., vol. 55, no. 14, p. 3829, 2016.

[151] J. Zhang, Hyper-NA optical systems and applications in sample measurement, Appendix F, Thesis Report, University of Arizona, 2010.

[152] J. D. Joannopoulos, S. G. Johnson, J. N. Winn, and R. D. Meade, Photonic crystals: molding the flow of light, Princeton University Press, 2008.

[153] L. YOUNG, “Low-pass and high-pass filters consisting of multilayer dielectric stacks”, IEEE, VOL. MTT.14, NO. 2, 1966.

[154] E. K. Smith and S. Weintraub, “The Constants in the Equation for Atmospheric Refractive Index at Radio Frequencies,” Proc. IRE, vol. 41, no. 8, pp. 1035–1037, 1953.

[155] A. Macleod, “The Quarterwave Stack: 1. Early History,” Thin Film Center, Inc., Tucson, AZ, 2012.

[156] C. Tao et al., “Sol-gel based antireflective coatings with superhydrophobicity and exceptionally low refractive indices built from trimethylsilanized hollow silica nanoparticles,” Colloids Surfaces A Physicochem. Eng. Asp., vol. 509, pp. 307–313, 2016.

[157] N. Suzuki and Y. Tomita, “Silica-nanoparticle-dispersed methacrylate photopolymers with net diffraction efficiency near 100%,” Appl. Opt., vol. 43, no. 10, p. 2125, 2004.

[158] B. N. Khlebtsov, V. A. Khanadeev, and N. G. Khlebtsov, “Determination of the Size, Concentration, and Refractive Index of Silica Nanoparticles,” Orig. Russ. Text ©, vol. 105, no. 5, pp. 732–738, 2008.

[159] A. BEGANSKIENĖ, V. SIRUTKAITIS, M. KURTINAITIENĖ, R. JUŠKĖNAS, and A. KAREIVA, “FTIR, TEM and NMR Iinvestigations of Stöber Silica Nanoparticles,” Mater. Sicence, vol. 10, no. 4, pp. 287–290, 2004.

[160] J. Q. Xi, J. K. Kim, and E. F. Schubert, “Silica nanorod-array films with very low refractive indices,” Nano Lett., vol. 5, no. 7, pp. 1385–1387, 2005.

[161] Y. Fink et al., “A dielectric omnidirectional reflector” vol. 282, no. November, pp. 1679–1683, 1998.

[162] L. V. Rodríguez-de Marcos, J. I. Larruquert, J. A. Méndez, and J. A. Aznárez, “Self-consistent optical constants of SiO_2 and Ta_2O_5 films,” Opt. Mater. Express, vol. 6, no. 11, p. 3622, 2016.

[163] J. Kischkat et al., “Mid-infrared optical properties of thin films of aluminum oxide, titanium dioxide, silicon dioxide, aluminum nitride, and silicon nitride.,” Appl. Opt., vol. 51, no. 28, pp. 6789–98, 2012.

[164] M. Querry, “Optical Constants of Minerals and Other Materials from the Millimeter to the Ultraviolet,” p. 333, 1987.

[165] S. Adachi, T. Taguchi, “Optical properties of ZnSe” vol. 43, no. 12, 1991.

[166] M. H. Ahmadi, A. H. Mohammadi, S. Dehghani, and M. A. Barranco-Jiménez, “Multi-objective thermodynamic-based optimization of output power of Solar Dish-Stirling engine by implementing an evolutionary algorithm,” Energy Convers. Manag., vol. 75, pp. 438–445, 2013.

[167] M. H. Ahmadi, S. Sorouri Ghare Aghaj, and A. Nazeri, “Prediction of power in solar stirling heat engine by using neural network based on hybrid genetic algorithm and particle swarm optimization,” Neural Comput. Appl., vol. 22, no. 6, pp. 1141–1150, 2013.

[168] A. Sharma, Sh. K. Shukla, A. K. Rai, “Finite Time Thermodynamic Analysis and Optimization of Solar-Dish Stirling Heat Engine With,” Therm. Sci., vol. 15, no. 4, pp. 995–1009, 2011.

[169] L. Yaqi, H. Yaling, and W. Weiwei, “Optimization of solar-powered Stirling heat engine with finite-time thermodynamics,” Renew. Energy, vol. 36, no. 1, pp. 421–427, 2011.

[170] E. Chiavazzo, L. Ventola, F. Calignano, D. Manfredi, and P. Asinari, “A sensor for direct measurement of small convective heat fluxes: Validation and application to micro-structured surfaces,” Exp. Therm. Fluid Sci., vol. 55, pp. 42–53, 2014.

[171] M. N. Ondianka et all, “Evaluation of Solar Energy for Processing Aloe Secundiflora Sap into Paste Using Parabolic Solar Concentrating Technology,” Open Renew. Energy J., vol. 4, no. 1, pp. 93–103, 2011.

[172] A. Z. Hafez, A. Soliman, K. A. El-Metwally, and I. M. Ismail, “Solar parabolic dish Stirling engine system design, simulation, and thermal analysis,” Energy Convers. Manag., vol. 126, pp. 60–75, 2016.

[173] I. Hamberg and C. G. Granqvist, “Evaporated Sn-doped In2O3films: Basic optical properties and applications to energy-efficient windows,” J. Appl. Phys., vol. 60, no. 11, 1986.

[174] I. M. Saleh, K. Khalifa, M. Bughazem and N. Algharvbi, “Developments in Parabolic Solar Dish Concentrator for Enhanced System Developments in Parabolic Solar Dish Concentrator for Enhanced System Efficiency of Steam Generation”, 2016.

[175] SolarTron Energy Systems Inc., “Technology for OEM developers”,”url: http://www.solartronenergy.com/wp-content/uploads/2018/12/SolarBeam-7M-Datasheet-1NC.pdf”, 2018.

[176] S. Y. Wu, L. Xiao, Y. Cao, and Y. R. Li, “A parabolic dish/AMTEC solar thermal power system and its performance evaluation,” Appl. Energy, vol. 87, no. 2, pp. 452–462, 2010.

[177] T. Mancini et al., “Dish-Stirling Systems: An Overview of Development and Status,” J. Sol. Energy Eng., vol. 125, no. 2, p. 135, 2003.

[178] M. Querry, “Optical Constants of Minerals and Other Materials from the Millimeter to the Ultraviolet,” p. 333, 1987.

[179] M. Schmidt et al., “Ultralow refractive index substrates–a base for photonic crystal slab waveguides,” Appl. Phys. Lett., vol. 85, no. 1, pp. 16–18, 2004.

[180] B. A. Safe and T. Society, “As a,” Home Off., vol. 30, no. November, pp. 15–21, 2005.

[181] P. G. O. Brien et al., “Solar Energy Materials & Solar Cells Selectively transparent and conducting photonic crystal solar spectrum splitters made of alternating sputtered indium-tin oxide and spin-coated silica nanoparticle layers for enhanced photovoltaics,” Sol. Energy Mater. Sol. Cells, vol. 102, pp. 173–183, 2012.

Appendix

In this thesis, a MATLAB code was developed based on the methods described in Chapter 3, that calculates the reflectance and transmittance spectra of dielectric mirrors. In the following the code is presented through Sections I to V which is more of an example. Section I calculates the reflectance and transmittance of the multilayer film using different graded-index profiles (e.g. linear, cubic and quintic). Section II calculates the diagrams of the profiles, solar irradiance and the amount of spectral power transmitted through different designs and blackbody radiation and the amount of spectral power reflected by different dielectric mirror. Section III calculates the generated power and power distribution of a Dish-Stirling system considering different transparent heat mirrors on top of the receiver. In order to run each part of the code, one needs to call Section IV and V which are modified versions of the functions provided by J. Zhang et al [151].

I- Reflectance and transmittance code

```
clc
clear all;
close all;
um = 1e-6;
nm = 1e-9;
% define admittance for medium
Air = 1;
nH = 2;
% nL = 1.3;
yL=1.3;
Glass = 1.52;
tt=0.0:1/19:1;
number_of_steps_tt=length(tt);

 yH_1=yL+(nH-yL).*tt;
 yH_2=yL+(nH-yL).*(3.*(tt.^2)-2.*(tt.^3));
 yH_3=yL+(nH-yL).*(10.*(tt.^3)-15.*(tt.^4)+6.*(tt.^5));
 yH_1_rev=nH+(yL-nH).*tt;
 yH_2_rev=nH+(yL-nH).*(3.*(tt.^2)-2.*(tt.^3));
 yH_3_rev=nH+(yL-nH).*(10.*(tt.^3)-15.*(tt.^4)+6.*(tt.^5));

% define visible region of light
lambda_max=20000;
number_of_steps=2001;
step=lambda_max./number_of_steps;
lambda = linspace(0,lambda_max,number_of_steps)*nm;
% define thin film structure
y_inc = Air; % incident medium admittance
y_sub = Glass; % substrate medium admittance
theta = 0; % in degree

%--------------------------------------Black Body Radiation----------
----------------------------%
%-------------------------------------------------------------------
----------------------------%
c=3*10^8; % speed of light in vacuum
h=6.625*10.^-34; %  Planck constant
k=1.38*10.^-23; %   Boltzmann constant
T1=5340; % Temperatures in Kelvin
T2_contant=500;
T2_variable=500;
%--------------------------------------Planks Law--------------------
----------------------------%

I1=(2*h*c*c)./((lambda.^5).*(exp((h.*c)./(k.*T1.*lambda))-1)).*1e-13;
Sum_Sun=(sum(I1(2:number_of_steps))).*(step);
```

```
%-------------------------------------------------------------------------
----------------------------%

I2_constant=(2*h*c*c)./((lambda.^5).*(exp((h.*c)./(k.*T2_contant.*lamb
da))-1)).*1e-13;
I2=(2*h*c*c)./((lambda.^5).*(exp((h.*c)./(k.*T2_variable.*lambda))-
1)).*1e-13;
Sum_Black_body=(sum(I2(2:number_of_steps))).*(step);
%-------------------------------------------------------------------------
---%
[Peak_I2 Wavelengeth_Peak_I2]=max(I2);
lambda_f= lambda(1,Wavelengeth_Peak_I2);

portion=0.5;
thickness_11=(lambda_f./4./nH./nm);    % quarter stack
thickness_22=(lambda_f./4./yL./nm);    % quarter stack
thickness_11_variable=((thickness_11.*portion)./number_of_steps_tt).*o
nes(1,number_of_steps_tt);
thickness1_2_variable=(((thickness_11+thickness_22).*portion)./number_
of_steps_tt).*ones(1,number_of_steps_tt);
thickness_11_constant=thickness_11*(1-2*portion);
thickness_22_constant=thickness_22*(1-2*portion);

d                                                                       =
[thickness_11_variable*nm,thickness_11_constant*nm,thickness1_2_variab
le*nm,thickness_22_constant*nm,...

thickness1_2_variable*nm,thickness_11_constant*nm,thickness1_2_variabl
e*nm,thickness_22_constant*nm,...

thickness1_2_variable*nm,thickness_11_constant*nm,thickness1_2_variabl
e*nm,thickness_22_constant*nm,...

thickness1_2_variable*nm,thickness_11_constant*nm,thickness1_2_variabl
e*nm,thickness_22_constant*nm,...

thickness1_2_variable*nm,thickness_11_constant*nm,thickness1_2_variabl
e*nm,thickness_22_constant*nm,...

thickness1_2_variable*nm,thickness_11_constant*nm,thickness1_2_variabl
e*nm];

y1 = [yH_1,nH,yH_1_rev,yL,yH_1,nH,yH_1_rev,yL,...
      yH_1,nH,yH_1_rev,yL,yH_1,nH,yH_1_rev,yL,...
      yH_1,nH,yH_1_rev,yL,yH_1,nH,yH_1_rev];

y2 = [yH_2,nH,yH_2_rev,yL,yH_2,nH,yH_2_rev,yL,...
    yH_2,nH,yH_2_rev,yL,yH_2,nH,yH_2_rev,yL,...
    yH_2,nH,yH_2_rev,yL,yH_2,nH,yH_2_rev];

y3 = [yH_3,nH,yH_3_rev,yL,yH_3,nH,yH_3_rev,yL,...
    yH_3,nH,yH_3_rev,yL,yH_3,nH,yH_3_rev,yL,...
```

```
    yH_3,nH,yH_3_rev,yL,yH_3,nH,yH_3_rev];

    for ii=1:length(lambda)

            [rho_p_1(ii),tao_p_1(ii),R_p_1(ii),T_p_1(ii)]            =
calculation_p(d,y1,y_inc,y_sub,lambda(ii),theta);

    end

    for ii=1:length(lambda)

            [rho_s_1(ii),tao_s_1(ii),R_s_1(ii),T_s_1(ii)]            =
calculation_s(d,y1,y_inc,y_sub,lambda(ii),theta);

    end

    for ii=1:length(lambda)

            [rho_p_2(ii),tao_p_2(ii),R_p_2(ii),T_p_2(ii)]            =
calculation_p(d,y2,y_inc,y_sub,lambda(ii),theta);

    end

    for ii=1:length(lambda)

            [rho_s_2(ii),tao_s_2(ii),R_s_2(ii),T_s_2(ii)]            =
calculation_s(d,y2,y_inc,y_sub,lambda(ii),theta);

    end

    for ii=1:length(lambda)

            [rho_p_3(ii),tao_p_3(ii),R_p_3(ii),T_p_3(ii)]            =
calculation_p(d,y3,y_inc,y_sub,lambda(ii),theta);

    end

    for ii=1:length(lambda)

            [rho_s_3(ii),tao_s_3(ii),R_s_3(ii),T_s_3(ii)]            =
calculation_s(d,y3,y_inc,y_sub,lambda(ii),theta);

    end

R_p_1_sun=I2.*R_p_1;
R_p_2_sun=I2.*R_p_2;
R_p_3_sun=I2.*R_p_3;

T_p_1_sun=I1.*T_p_1;
T_p_2_sun=I1.*T_p_2;
T_p_3_sun=I1.*T_p_3;
```

```
thickness_11=(lambda_f./4./nH./nm);  % quarter stack
portion=0.0;
thickness_1_1=portion*(thickness_11./(number_of_steps_tt/2)).*ones(1,(
number_of_steps_tt/2));
thickness_1_2=thickness_11*(1-2.*portion);
thickness_1_3=thickness_1_1;
thickness_22=(lambda_f./4./yL/nm);   % quarter stack
thickness_2_1=portion*(thickness_22./(number_of_steps_tt/2)).*ones(1,(
number_of_steps_tt/2));
thickness_2_2=thickness_22*(1-2.*portion);
thickness_2_3=thickness_2_1;

d                                                                    =
[thickness_1_1*nm,thickness_2_1*nm,thickness_1_2*nm,thickness_1_3.*nm,
thickness_2_3*nm,thickness_2_2*nm,thickness_1_1*nm,...

thickness_2_1*nm,thickness_1_2*nm,thickness_1_3.*nm,thickness_2_3*nm,t
hickness_2_2*nm,thickness_1_1*nm,thickness_2_1*nm,...

thickness_1_2*nm,thickness_1_3.*nm,thickness_2_3*nm,thickness_2_2*nm,t
hickness_1_1*nm,thickness_2_1*nm,thickness_1_2*nm,...

thickness_1_3.*nm,thickness_2_3*nm,thickness_2_2*nm,thickness_1_1*nm,t
hickness_2_1*nm,thickness_1_2*nm,thickness_1_3.*nm,...

thickness_2_3*nm,thickness_2_2*nm,thickness_1_1*nm,thickness_2_1*nm,th
ickness_1_2*nm,thickness_1_3.*nm,thickness_2_3*nm];

y1                                                                   =
[yH_1,nH,yH_1_rev,yL,yH_1,nH,yH_1_rev,yL,yH_1,nH,yH_1_rev,yL,yH_1,nH,y
H_1_rev,yL,yH_1,nH,yH_1_rev,yL,yH_1,nH,yH_1_rev];

    for ii=1:length(lambda)


[rho_p_quarter(ii),tao_p_quarter(ii),R_p_quarter(ii),T_p_quarter(ii)] =
calculation_p(d,y1,y_inc,y_sub,lambda(ii),theta);

    end

    for ii=1:length(lambda)


[rho_s_quarter(ii),tao_s_quarter(ii),R_s_quarter(ii),T_s_quarter(ii)] =
calculation_s(d,y1,y_inc,y_sub,lambda(ii),theta);

    end

R_p_quarter_sun=I2.*R_p_quarter;
T_p_quarter_sun=I1.*T_p_quarter;
Sum_quarter=((sum(T_p_quarter_sun(2:number_of_steps))).*(step)./Sum_Su
n).*100;
```

```
% Power_Sun=(sum(I2(2:1001))).*(10000/1000);
%
Power_Quarter_Stack_Alone=(sum(T_p_quarter_sun(2:1001))).*(10000/1000)
;
% Power_Linear=(sum(T_p_1_sun(2:1001))).*(10000/1000);
% Power_Cubic=(sum(T_p_2_sun(2:1001))).*(10000/1000);
% Power_Quintic=(sum(T_p_3_sun(2:1001))).*(10000/1000);


 % plot the result
    figure
    axes1 = axes('Parent',figure);
    hold(axes1,'on');
    plot(lambda/nm,I1,'-','color',[0.7 0.7 0.7],'LineWidth',2)
    hold on
    plot(lambda/nm,T_p_quarter_sun,'-','color',[0.5                 0.5
0.5],'LineWidth',1)
    hold on
    plot(lambda/nm,T_p_1_sun,'--k','LineWidth',1);
    hold on
    plot(lambda/nm,T_p_2_sun,'-.k','LineWidth',1);
    hold on
    plot(lambda/nm,T_p_3_sun,':k','LineWidth',1);
    hold on
    legend({'Solar  Spectrum','Step  Profile','Linear  Profile','Cubic
Profile','Quintic Profile'},'fontsize',20)
    xlabel('Wavelength (nm)','fontsize',25);
    ylabel('Radiation Intensity (W/{m^2nm})','fontsize',25);
    set(axes1,'FontSize',25);
    xlim ([0 4000])
    % axis([350 850 0 105]);
    grid on;

    % plot the result
    figure
    axes1 = axes('Parent',figure);
    hold(axes1,'on');
    plot(lambda/nm,I2,'-','color',[0.7 0.7 0.7],'LineWidth',2)
    hold on
    plot(lambda/nm,R_p_quarter_sun,'-','color',[0.5                 0.5
0.5],'LineWidth',1)
    hold on
    plot(lambda/nm,R_p_1_sun,'--k','LineWidth',1);
    hold on
    plot(lambda/nm,R_p_2_sun,'-.k','LineWidth',1);
    hold on
    plot(lambda/nm,R_p_3_sun,':k','LineWidth',1);
    hold on
```

```
    legend({'Black Body Irradiance at T=500K','Step Profile','Linear
Profile','Cubic Profile','Quintic Profile'},'fontsize',20)
    xlabel('Wavelength (nm)','fontsize',25);
    ylabel('Radiation Intensity (W/{m^2nm})','fontsize',25);
    set(axes1,'FontSize',25);
%     ylim ([0 100])
    % axis([350 850 0 105]);
    grid on;

   % plot the result
    figure
    axes1 = axes('Parent',figure);
    hold(axes1,'on');
    plot(lambda/nm,T_p_1,'--k','LineWidth',1);
    hold on
    plot(lambda/nm,T_p_2,'-.k','LineWidth',1);
    hold on
    plot(lambda/nm,T_p_3,':k','LineWidth',1);
    hold on
    plot(lambda/nm,T_p_quarter,'-','color',[0.5 0.5 0.5],'LineWidth',1)
%     title('Transmission, 5 layers, T=100^oC','fontsize',16);
    legend({'Linear Profile','Cubic Profile','Quintic Profile','Step
Profile'},'fontsize',20)
    xlabel('Wavelength (nm)','fontsize',25);
    ylabel('Transmission (%)','fontsize',25);
    set(axes1,'FontSize',25)
    xlim ([0 10000])
    grid on;

    % plot the result
    figure
    axes1 = axes('Parent',figure);
    hold(axes1,'on');
    plot(lambda/nm,R_p_1,'--k','LineWidth',1);
    hold on
    plot(lambda/nm,R_p_2,'-.k','LineWidth',1);
    hold on
    plot(lambda/nm,R_p_3,':k','LineWidth',1);
    hold on
    plot(lambda/nm,R_p_quarter,'-','color',[0.5 0.5 0.5],'LineWidth',1)
%     title('Reflection, 5 layers, T=100^oC','fontsize',16);
    legend({'Linear Profile','Cubic Profile','Quintic Profile','Step
Profile'},'fontsize',20)
    xlabel('Wavelength (nm)','fontsize',25);
    ylabel('Reflection (%)','fontsize',25);
    set(axes1,'FontSize',25);
    xlim ([0 10000])
    grid on;
```

II- Profiles and blackbody fraction code

```
clc
clear all;
close all;
um = 1e-6;
nm = 1e-9;
% define admittance for medium
Air = 1;
nH = 2;
% nL = 1.3;
yL=1.3;
Glass = 1.52;
tt=0.0:1/19:1;
 yH_1=yL+(nH-yL).*tt;
 yH_2=yL+(nH-yL).*(3.*(tt.^2)-2.*(tt.^3));
 yH_3=yL+(nH-yL).*(10.*(tt.^3)-15.*(tt.^4)+6.*(tt.^5));
 yH_1_rev=nH+(yL-nH).*tt;
 yH_2_rev=nH+(yL-nH).*(3.*(tt.^2)-2.*(tt.^3));
 yH_3_rev=nH+(yL-nH).*(10.*(tt.^3)-15.*(tt.^4)+6.*(tt.^5));

% define visible region of light
lambda = linspace(0,10000,1001)*nm;
% define thin film structure
y_inc = Air; % incident medium admittance
y_sub = Glass; % substrate medium admittance
theta = 0; % in degree

%---------------------------------------Black Body Radiation-----------
----------------------------%
%-------------------------------------------------------------------------
----------------------------%
c=3*10^8; % speed of light in vaccum
h=6.625*10.^-34; %  Planck constant
k=1.38*10.^-23; %   Boltzmann constant
T1=5778; % Temperatures in Kelvin
T2_contant=500;
T2_variable=500;
%---------------------------------------Planks Law---------------------
----------------------------%

I1=(2*h*c*c)./((lambda.^5).*(exp((h.*c)./(k.*T1.*lambda))-1)).*1e-13;

Sum_Sun=(sum(I1(2:1001))).*(10000/1000);

%-------------------------------------------------------------------------
----------------------------%

I2_constant=(2*h*c*c)./((lambda.^5).*(exp((h.*c)./(k.*T2_contant.*lamb
da))-1)).*1e-13;
```

```
I2=(2*h*c*c)./((lambda.^5).*(exp((h.*c)./(k.*T2_variable.*lambda))-
1)).*1e-13;
Sum_Black_body=(sum(I2(2:1001))).*(10000/1000);
%-------------------------------------------------------------------
----------------------------%
[Peak_I2 Wavelengeth_Peak_I2]=max(I2_constant);

lambda_f= lambda(1,Wavelengeth_Peak_I2);


portion=0.0;
thickness_11=(lambda_f./4./nH./nm);  % quarter stack
thickness_22=(lambda_f./4./yL./nm);   % quarter stack
thickness_11_variable=((thickness_11.*portion)./20).*ones(1,20);
thickness1_2_variable=(((thickness_11+thickness_22).*portion)./20).*on
es(1,20);
thickness_11_constant=thickness_11*(1-2*portion);
thickness_22_constant=thickness_22*(1-2*portion);

d                                                                    =
[thickness_11_variable*nm,thickness_11_constant*nm,thickness1_2_variab
le*nm,thickness_22_constant*nm,...

thickness1_2_variable*nm,thickness_11_constant*nm,thickness1_2_variabl
e*nm,thickness_22_constant*nm,...

thickness1_2_variable*nm,thickness_11_constant*nm,thickness1_2_variabl
e*nm,thickness_22_constant*nm,...

thickness1_2_variable*nm,thickness_11_constant*nm,thickness1_2_variabl
e*nm,thickness_22_constant*nm,...

thickness1_2_variable*nm,thickness_11_constant*nm,thickness1_2_variabl
e*nm,thickness_22_constant*nm,...

thickness1_2_variable*nm,thickness_11_constant*nm,thickness1_2_variabl
e*nm];

y1 = [yH_1,nH,yH_1_rev,yL,yH_1,nH,yH_1_rev,yL,...
      yH_1,nH,yH_1_rev,yL,yH_1,nH,yH_1_rev,yL,...
      yH_1,nH,yH_1_rev,yL,yH_1,nH,yH_1_rev];

y2 = [yH_2,nH,yH_2_rev,yL,yH_2,nH,yH_2_rev,yL,...
    yH_2,nH,yH_2_rev,yL,yH_2,nH,yH_2_rev,yL,...
    yH_2,nH,yH_2_rev,yL,yH_2,nH,yH_2_rev];

y3 = [yH_3,nH,yH_3_rev,yL,yH_3,nH,yH_3_rev,yL,...
    yH_3,nH,yH_3_rev,yL,yH_3,nH,yH_3_rev,yL,...
    yH_3,nH,yH_3_rev,yL,yH_3,nH,yH_3_rev];


for iii=2:length(d)+1
```

```
    ww_00(1)=0./nm;
    ww_00(iii)=ww_00(iii-1)+d(iii-1)./nm;
end
ww_00=ww_00(2:252);


    for ii=1:length(lambda)

            [rho_p_1(ii),tao_p_1(ii),R_p_1(ii),T_p_1(ii)]              =
calculation_p(d,y1,y_inc,y_sub,lambda(ii),theta);

    end

    for ii=1:length(lambda)

            [rho_s_1(ii),tao_s_1(ii),R_s_1(ii),T_s_1(ii)]              =
calculation_s(d,y1,y_inc,y_sub,lambda(ii),theta);

    end

    for ii=1:length(lambda)

            [rho_p_2(ii),tao_p_2(ii),R_p_2(ii),T_p_2(ii)]              =
calculation_p(d,y2,y_inc,y_sub,lambda(ii),theta);

    end

    for ii=1:length(lambda)

            [rho_s_2(ii),tao_s_2(ii),R_s_2(ii),T_s_2(ii)]              =
calculation_s(d,y2,y_inc,y_sub,lambda(ii),theta);

    end

    for ii=1:length(lambda)

            [rho_p_3(ii),tao_p_3(ii),R_p_3(ii),T_p_3(ii)]              =
calculation_p(d,y3,y_inc,y_sub,lambda(ii),theta);

    end

    for ii=1:length(lambda)

            [rho_s_3(ii),tao_s_3(ii),R_s_3(ii),T_s_3(ii)]              =
calculation_s(d,y3,y_inc,y_sub,lambda(ii),theta);

    end

T_p_1_sun=I1.*T_p_1;
T_p_2_sun=I1.*T_p_2;
T_p_3_sun=I1.*T_p_3;
Sum_Linear_00=((sum(T_p_1_sun(2:1001))).*(10000/1000)./Sum_Sun).*100;
```

```
Sum_Cubic_00=((sum(T_p_2_sun(2:1001))).*(10000/1000)./Sum_Sun).*100;
Sum_Quintic_00=((sum(T_p_3_sun(2:1001))).*(10000/1000)./Sum_Sun).*100;

R_p_1_blackbody=I2.*R_p_1;
R_p_2_blackbody=I2.*R_p_2;
R_p_3_blackbody=I2.*R_p_3;

Sum_blackbody_Linear_00=((sum(R_p_1_blackbody(2:1001))).*(10000/1000).
/Sum_Black_body).*100;
Sum_blackbody_Cubic_00=((sum(R_p_2_blackbody(2:1001))).*(10000/1000)./
Sum_Black_body).*100;
Sum_blackbody_Quintic_00=((sum(R_p_3_blackbody(2:1001))).*(10000/1000)
./Sum_Black_body).*100;


[Peak_Reflection_001 Wavelengeth_Peak_Reflection_001]=max(R_p_1);
[Peak_Reflection_002 Wavelengeth_Peak_Reflection_002]=max(R_p_2);
[Peak_Reflection_003 Wavelengeth_Peak_Reflection_003]=max(R_p_3);

w1_low=629;
w1_high=876;
w2_low=699;
w2_high=997;

Half_Peak_Reflection_001=Peak_Reflection_001./2;
x_0011=interp1(R_p_1(w1_low:w1_high),lambda(w1_low:w1_high),Half_Peak_
Reflection_001)./nm;
x_0012=interp1(R_p_1(w2_low:w2_high),lambda(w2_low:w2_high),Half_Peak_
Reflection_001)./nm;
FWHM_001=x_0012-x_0011;

Half_Peak_Reflection_002=Peak_Reflection_002./2;
x_0021=interp1(R_p_2(w1_low:w1_high),lambda(w1_low:w1_high),Half_Peak_
Reflection_002)./nm;
x_0022=interp1(R_p_2(w2_low:w2_high),lambda(w2_low:w2_high),Half_Peak_
Reflection_002)./nm;
FWHM_002=x_0022-x_0021;

Half_Peak_Reflection_003=Peak_Reflection_003./2;
x_0031=interp1(R_p_3(w1_low:w1_high),lambda(w1_low:w1_high),Half_Peak_
Reflection_003)./nm;
x_0032=interp1(R_p_3(w2_low:w2_high),lambda(w2_low:w2_high),Half_Peak_
Reflection_003)./nm;
FWHM_003=x_0032-x_0031;

%=============================================


portion=0.1;
thickness_11=(lambda_f./4./nH./nm);  % quarter stack
thickness_22=(lambda_f./4./yL./nm);   % quarter stack
thickness_11_variable=((thickness_11.*portion)./20).*ones(1,20);
```

```
thickness1_2_variable=(((thickness_11+thickness_22).*portion)./20).*on
es(1,20);
thickness_11_constant=thickness_11*(1-2*portion);
thickness_22_constant=thickness_22*(1-2*portion);

d                                                                       =
[thickness_11_variable*nm,thickness_11_constant*nm,thickness1_2_variab
le*nm,thickness_22_constant*nm,...

thickness1_2_variable*nm,thickness_11_constant*nm,thickness1_2_variabl
e*nm,thickness_22_constant*nm,...

thickness1_2_variable*nm,thickness_11_constant*nm,thickness1_2_variabl
e*nm,thickness_22_constant*nm,...

thickness1_2_variable*nm,thickness_11_constant*nm,thickness1_2_variabl
e*nm,thickness_22_constant*nm,...

thickness1_2_variable*nm,thickness_11_constant*nm,thickness1_2_variabl
e*nm,thickness_22_constant*nm,...

thickness1_2_variable*nm,thickness_11_constant*nm,thickness1_2_variabl
e*nm];

for iii=2:length(d)+1
    ww_01(1)=0./nm;
    ww_01(iii)=ww_01(iii-1)+d(iii-1)./nm;
end
ww_01=ww_01(2:252);



    for ii=1:length(lambda)

            [rho_p_1(ii),tao_p_1(ii),R_p_1(ii),T_p_1(ii)]           =
calculation_p(d,y1,y_inc,y_sub,lambda(ii),theta);

    end

    for ii=1:length(lambda)

            [rho_s_1(ii),tao_s_1(ii),R_s_1(ii),T_s_1(ii)]           =
calculation_s(d,y1,y_inc,y_sub,lambda(ii),theta);

    end

    for ii=1:length(lambda)

            [rho_p_2(ii),tao_p_2(ii),R_p_2(ii),T_p_2(ii)]           =
calculation_p(d,y2,y_inc,y_sub,lambda(ii),theta);
```

```
    end

    for ii=1:length(lambda)

            [rho_s_2(ii),tao_s_2(ii),R_s_2(ii),T_s_2(ii)]             =
calculation_s(d,y2,y_inc,y_sub,lambda(ii),theta);

    end

    for ii=1:length(lambda)

            [rho_p_3(ii),tao_p_3(ii),R_p_3(ii),T_p_3(ii)]             =
calculation_p(d,y3,y_inc,y_sub,lambda(ii),theta);

    end

    for ii=1:length(lambda)

            [rho_s_3(ii),tao_s_3(ii),R_s_3(ii),T_s_3(ii)]             =
calculation_s(d,y3,y_inc,y_sub,lambda(ii),theta);

    end

T_p_1_sun=I1.*T_p_1;
T_p_2_sun=I1.*T_p_2;
T_p_3_sun=I1.*T_p_3;

Sum_Linear_01=((sum(T_p_1_sun(2:1001))).*(10000/1000)./Sum_Sun).*100;
Sum_Cubic_01=((sum(T_p_2_sun(2:1001))).*(10000/1000)./Sum_Sun).*100;
Sum_Quintic_01=((sum(T_p_3_sun(2:1001))).*(10000/1000)./Sum_Sun).*100;

R_p_1_blackbody=I2.*R_p_1;
R_p_2_blackbody=I2.*R_p_2;
R_p_3_blackbody=I2.*R_p_3;

Sum_blackbody_Linear_01=((sum(R_p_1_blackbody(2:1001))).*(10000/1000).
/Sum_Black_body).*100;
Sum_blackbody_Cubic_01=((sum(R_p_2_blackbody(2:1001))).*(10000/1000)./
Sum_Black_body).*100;
Sum_blackbody_Quintic_01=((sum(R_p_3_blackbody(2:1001))).*(10000/1000)
./Sum_Black_body).*100;


[Peak_Reflection_011 Wavelengeth_Peak_Reflection_011]=max(R_p_1);
[Peak_Reflection_012 Wavelengeth_Peak_Reflection_012]=max(R_p_2);
[Peak_Reflection_013 Wavelengeth_Peak_Reflection_013]=max(R_p_3);

w1_low=637;
w1_high=890;
w2_low=703;
w2_high=998;
```

```
Half_Peak_Reflection_011=Peak_Reflection_011./2;
x_0111=interp1(R_p_1(w1_low:w1_high),lambda(w1_low:w1_high),Half_Peak_
Reflection_011)./nm;
x_0112=interp1(R_p_1(w2_low:w2_high),lambda(w2_low:w2_high),Half_Peak_
Reflection_011)./nm;
FWHM_011=x_0112-x_0111;

Half_Peak_Reflection_012=Peak_Reflection_012./2;
x_0121=interp1(R_p_2(w1_low:w1_high),lambda(w1_low:w1_high),Half_Peak_
Reflection_012)./nm;
x_0122=interp1(R_p_2(w2_low:w2_high),lambda(w2_low:w2_high),Half_Peak_
Reflection_012)./nm;
FWHM_012=x_0122-x_0121;

Half_Peak_Reflection_013=Peak_Reflection_013./2;
x_0131=interp1(R_p_3(w1_low:w1_high),lambda(w1_low:w1_high),Half_Peak_
Reflection_013)./nm;
x_0132=interp1(R_p_3(w2_low:w2_high),lambda(w2_low:w2_high),Half_Peak_
Reflection_013)./nm;
FWHM_013=x_0132-x_0131;

%=============================================

portion=0.2;
thickness_11=(lambda_f./4./nH./nm);  % quarter stack
thickness_22=(lambda_f./4./yL./nm);   % quarter stack
thickness_11_variable=((thickness_11.*portion)./20).*ones(1,20);
thickness1_2_variable=(((thickness_11+thickness_22).*portion)./20).*on
es(1,20);
thickness_11_constant=thickness_11*(1-2*portion);
thickness_22_constant=thickness_22*(1-2*portion);

d                                                                    =
[thickness_11_variable*nm,thickness_11_constant*nm,thickness1_2_variab
le*nm,thickness_22_constant*nm,...

thickness1_2_variable*nm,thickness_11_constant*nm,thickness1_2_variabl
e*nm,thickness_22_constant*nm,...

thickness1_2_variable*nm,thickness_11_constant*nm,thickness1_2_variabl
e*nm,thickness_22_constant*nm,...

thickness1_2_variable*nm,thickness_11_constant*nm,thickness1_2_variabl
e*nm,thickness_22_constant*nm,...

thickness1_2_variable*nm,thickness_11_constant*nm,thickness1_2_variabl
e*nm,thickness_22_constant*nm,...

thickness1_2_variable*nm,thickness_11_constant*nm,thickness1_2_variabl
e*nm];

for iii=2:length(d)+1
```

```
    ww_02(1)=0./nm;
    ww_02(iii)=ww_02(iii-1)+d(iii-1)./nm;
end
ww_02=ww_02(2:252);



    for ii=1:length(lambda)

            [rho_p_1(ii),tao_p_1(ii),R_p_1(ii),T_p_1(ii)]            =
calculation_p(d,y1,y_inc,y_sub,lambda(ii),theta);

    end

    for ii=1:length(lambda)

            [rho_s_1(ii),tao_s_1(ii),R_s_1(ii),T_s_1(ii)]            =
calculation_s(d,y1,y_inc,y_sub,lambda(ii),theta);

    end

    for ii=1:length(lambda)

            [rho_p_2(ii),tao_p_2(ii),R_p_2(ii),T_p_2(ii)]            =
calculation_p(d,y2,y_inc,y_sub,lambda(ii),theta);

    end

    for ii=1:length(lambda)

            [rho_s_2(ii),tao_s_2(ii),R_s_2(ii),T_s_2(ii)]            =
calculation_s(d,y2,y_inc,y_sub,lambda(ii),theta);

    end

    for ii=1:length(lambda)

            [rho_p_3(ii),tao_p_3(ii),R_p_3(ii),T_p_3(ii)]            =
calculation_p(d,y3,y_inc,y_sub,lambda(ii),theta);

    end

    for ii=1:length(lambda)

            [rho_s_3(ii),tao_s_3(ii),R_s_3(ii),T_s_3(ii)]            =
calculation_s(d,y3,y_inc,y_sub,lambda(ii),theta);

    end

[Peak_Reflection_021 Wavelengeth_Peak_Reflection_021]=max(R_p_1);
[Peak_Reflection_022 Wavelengeth_Peak_Reflection_022]=max(R_p_2);
[Peak_Reflection_023 Wavelengeth_Peak_Reflection_023]=max(R_p_3);
```

```
w1_low=641;
w1_high=881;
w2_low=704;
w2_high=993;

T_p_1_sun=I1.*T_p_1;
T_p_2_sun=I1.*T_p_2;
T_p_3_sun=I1.*T_p_3;

Sum_Linear_02=((sum(T_p_1_sun(2:1001))).*(10000/1000)./Sum_Sun).*100;
Sum_Cubic_02=((sum(T_p_2_sun(2:1001))).*(10000/1000)./Sum_Sun).*100;
Sum_Quintic_02=((sum(T_p_3_sun(2:1001))).*(10000/1000)./Sum_Sun).*100;

R_p_1_blackbody=I2.*R_p_1;
R_p_2_blackbody=I2.*R_p_2;
R_p_3_blackbody=I2.*R_p_3;

Sum_blackbody_Linear_02=((sum(R_p_1_blackbody(2:1001))).*(10000/1000).
/Sum_Black_body).*100;
Sum_blackbody_Cubic_02=((sum(R_p_2_blackbody(2:1001))).*(10000/1000)./
Sum_Black_body).*100;
Sum_blackbody_Quintic_02=((sum(R_p_3_blackbody(2:1001))).*(10000/1000)
./Sum_Black_body).*100;

Half_Peak_Reflection_021=Peak_Reflection_021./2;
x_0121=interp1(R_p_1(w1_low:w1_high),lambda(w1_low:w1_high),Half_Peak_
Reflection_021)./nm;
x_0122=interp1(R_p_1(w2_low:w2_high),lambda(w2_low:w2_high),Half_Peak_
Reflection_021)./nm;
FWHM_021=x_0122-x_0121;

Half_Peak_Reflection_022=Peak_Reflection_022./2;
x_0221=interp1(R_p_2(w1_low:w1_high),lambda(w1_low:w1_high),Half_Peak_
Reflection_022)./nm;
x_0222=interp1(R_p_2(w2_low:w2_high),lambda(w2_low:w2_high),Half_Peak_
Reflection_022)./nm;
FWHM_022=x_0222-x_0221;

Half_Peak_Reflection_023=Peak_Reflection_023./2;
x_0321=interp1(R_p_3(w1_low:w1_high),lambda(w1_low:w1_high),Half_Peak_
Reflection_023)./nm;
x_0322=interp1(R_p_3(w2_low:w2_high),lambda(w2_low:w2_high),Half_Peak_
Reflection_023)./nm;
FWHM_023=x_0322-x_0321;
%==============================================

portion=0.3;
thickness_11=(lambda_f./4./nH./nm);  % quarter stack
thickness_22=(lambda_f./4./yL./nm);   % quarter stack
thickness_11_variable=((thickness_11.*portion)./20).*ones(1,20);
```

```
thickness1_2_variable=(((thickness_11+thickness_22).*portion)./20).*on
es(1,20);
thickness_11_constant=thickness_11*(1-2*portion);
thickness_22_constant=thickness_22*(1-2*portion);

d                                                                       =
[thickness_11_variable*nm,thickness_11_constant*nm,thickness1_2_variab
le*nm,thickness_22_constant*nm,...

thickness1_2_variable*nm,thickness_11_constant*nm,thickness1_2_variabl
e*nm,thickness_22_constant*nm,...

thickness1_2_variable*nm,thickness_11_constant*nm,thickness1_2_variabl
e*nm,thickness_22_constant*nm,...

thickness1_2_variable*nm,thickness_11_constant*nm,thickness1_2_variabl
e*nm,thickness_22_constant*nm,...

thickness1_2_variable*nm,thickness_11_constant*nm,thickness1_2_variabl
e*nm,thickness_22_constant*nm,...

thickness1_2_variable*nm,thickness_11_constant*nm,thickness1_2_variabl
e*nm];

for iii=2:length(d)+1
    ww_03(1)=0./nm;
    ww_03(iii)=ww_03(iii-1)+d(iii-1)./nm;
end
ww_03=ww_03(2:252);


    for ii=1:length(lambda)

            [rho_p_1(ii),tao_p_1(ii),R_p_1(ii),T_p_1(ii)]           =
calculation_p(d,y1,y_inc,y_sub,lambda(ii),theta);

    end

    for ii=1:length(lambda)

            [rho_s_1(ii),tao_s_1(ii),R_s_1(ii),T_s_1(ii)]           =
calculation_s(d,y1,y_inc,y_sub,lambda(ii),theta);

    end

    for ii=1:length(lambda)

            [rho_p_2(ii),tao_p_2(ii),R_p_2(ii),T_p_2(ii)]           =
calculation_p(d,y2,y_inc,y_sub,lambda(ii),theta);

    end
```

```
    for ii=1:length(lambda)

            [rho_s_2(ii),tao_s_2(ii),R_s_2(ii),T_s_2(ii)]             =
calculation_s(d,y2,y_inc,y_sub,lambda(ii),theta);

    end

    for ii=1:length(lambda)

            [rho_p_3(ii),tao_p_3(ii),R_p_3(ii),T_p_3(ii)]             =
calculation_p(d,y3,y_inc,y_sub,lambda(ii),theta);

    end

    for ii=1:length(lambda)

            [rho_s_3(ii),tao_s_3(ii),R_s_3(ii),T_s_3(ii)]             =
calculation_s(d,y3,y_inc,y_sub,lambda(ii),theta);

    end

T_p_1_sun=I1.*T_p_1;
T_p_2_sun=I1.*T_p_2;
T_p_3_sun=I1.*T_p_3;

w1_low=646;
w1_high=874;
w2_low=712;
w2_high=999;


Sum_Linear_03=((sum(T_p_1_sun(2:1001))).*(10000/1000)./Sum_Sun).*100;
Sum_Cubic_03=((sum(T_p_2_sun(2:1001))).*(10000/1000)./Sum_Sun).*100;
Sum_Quintic_03=((sum(T_p_3_sun(2:1001))).*(10000/1000)./Sum_Sun).*100;

R_p_1_blackbody=I2.*R_p_1;
R_p_2_blackbody=I2.*R_p_2;
R_p_3_blackbody=I2.*R_p_3;

Sum_blackbody_Linear_03=((sum(R_p_1_blackbody(2:1001))).*(10000/1000).
/Sum_Black_body).*100;
Sum_blackbody_Cubic_03=((sum(R_p_2_blackbody(2:1001))).*(10000/1000)./
Sum_Black_body).*100;
Sum_blackbody_Quintic_03=((sum(R_p_3_blackbody(2:1001))).*(10000/1000)
./Sum_Black_body).*100;


[Peak_Reflection_031 Wavelengeth_Peak_Reflection_031]=max(R_p_1);
[Peak_Reflection_032 Wavelengeth_Peak_Reflection_032]=max(R_p_2);
[Peak_Reflection_033 Wavelengeth_Peak_Reflection_033]=max(R_p_3);

Half_Peak_Reflection_031=Peak_Reflection_031./2;
```

```
x_0131=interp1(R_p_1(w1_low:w1_high),lambda(w1_low:w1_high),Half_Peak_
Reflection_031)./nm;
x_0132=interp1(R_p_1(w2_low:w2_high),lambda(w2_low:w2_high),Half_Peak_
Reflection_031)./nm;
FWHM_031=x_0132-x_0131;

Half_Peak_Reflection_032=Peak_Reflection_032./2;
x_0231=interp1(R_p_2(w1_low:w1_high),lambda(w1_low:w1_high),Half_Peak_
Reflection_032)./nm;
x_0232=interp1(R_p_2(w2_low:w2_high),lambda(w2_low:w2_high),Half_Peak_
Reflection_032)./nm;
FWHM_032=x_0232-x_0231;

Half_Peak_Reflection_033=Peak_Reflection_033./2;
x_0331=interp1(R_p_3(w1_low:w1_high),lambda(w1_low:w1_high),Half_Peak_
Reflection_033)./nm;
x_0332=interp1(R_p_3(w2_low:w2_high),lambda(w2_low:w2_high),Half_Peak_
Reflection_033)./nm;
FWHM_033=x_0332-x_0331;

%=============================================

portion=0.4;
thickness_11=(lambda_f./4./nH./nm);  % quarter stack
thickness_22=(lambda_f./4./yL./nm);   % quarter stack
thickness_11_variable=((thickness_11.*portion)./20).*ones(1,20);
thickness1_2_variable=(((thickness_11+thickness_22).*portion)./20).*on
es(1,20);
thickness_11_constant=thickness_11*(1-2*portion);
thickness_22_constant=thickness_22*(1-2*portion);

d                                                                    =
[thickness_11_variable*nm,thickness_11_constant*nm,thickness1_2_variab
le*nm,thickness_22_constant*nm,...

thickness1_2_variable*nm,thickness_11_constant*nm,thickness1_2_variabl
e*nm,thickness_22_constant*nm,...

thickness1_2_variable*nm,thickness_11_constant*nm,thickness1_2_variabl
e*nm,thickness_22_constant*nm,...

thickness1_2_variable*nm,thickness_11_constant*nm,thickness1_2_variabl
e*nm,thickness_22_constant*nm,...

thickness1_2_variable*nm,thickness_11_constant*nm,thickness1_2_variabl
e*nm,thickness_22_constant*nm,...

thickness1_2_variable*nm,thickness_11_constant*nm,thickness1_2_variabl
e*nm];

for iii=2:length(d)+1
    ww_04(1)=0./nm;
```

```
    ww_04(iii)=ww_04(iii-1)+d(iii-1)./nm;
end
ww_04=ww_04(2:252);


    for ii=1:length(lambda)

            [rho_p_1(ii),tao_p_1(ii),R_p_1(ii),T_p_1(ii)]              =
calculation_p(d,y1,y_inc,y_sub,lambda(ii),theta);

    end

    for ii=1:length(lambda)

            [rho_s_1(ii),tao_s_1(ii),R_s_1(ii),T_s_1(ii)]              =
calculation_s(d,y1,y_inc,y_sub,lambda(ii),theta);

    end

    for ii=1:length(lambda)

            [rho_p_2(ii),tao_p_2(ii),R_p_2(ii),T_p_2(ii)]              =
calculation_p(d,y2,y_inc,y_sub,lambda(ii),theta);

    end

    for ii=1:length(lambda)

            [rho_s_2(ii),tao_s_2(ii),R_s_2(ii),T_s_2(ii)]              =
calculation_s(d,y2,y_inc,y_sub,lambda(ii),theta);

    end

    for ii=1:length(lambda)

            [rho_p_3(ii),tao_p_3(ii),R_p_3(ii),T_p_3(ii)]              =
calculation_p(d,y3,y_inc,y_sub,lambda(ii),theta);

    end

    for ii=1:length(lambda)

            [rho_s_3(ii),tao_s_3(ii),R_s_3(ii),T_s_3(ii)]              =
calculation_s(d,y3,y_inc,y_sub,lambda(ii),theta);

    end

T_p_1_sun=I1.*T_p_1;
T_p_2_sun=I1.*T_p_2;
T_p_3_sun=I1.*T_p_3;

w1_low=656;
```

```
w1_high=884;
w2_low=722;
w2_high=991;


Sum_Linear_04=((sum(T_p_1_sun(2:1001))).*(10000/1000)./Sum_Sun).*100;
Sum_Cubic_04=((sum(T_p_2_sun(2:1001))).*(10000/1000)./Sum_Sun).*100;
Sum_Quintic_04=((sum(T_p_3_sun(2:1001))).*(10000/1000)./Sum_Sun).*100;

[Peak_Reflection_041 Wavelengeth_Peak_Reflection_041]=max(R_p_1);
[Peak_Reflection_042 Wavelengeth_Peak_Reflection_042]=max(R_p_2);
[Peak_Reflection_043 Wavelengeth_Peak_Reflection_043]=max(R_p_3);

R_p_1_blackbody=I2.*R_p_1;
R_p_2_blackbody=I2.*R_p_2;
R_p_3_blackbody=I2.*R_p_3;

Sum_blackbody_Linear_04=((sum(R_p_1_blackbody(2:1001))).*(10000/1000).
/Sum_Black_body).*100;
Sum_blackbody_Cubic_04=((sum(R_p_2_blackbody(2:1001))).*(10000/1000)./
Sum_Black_body).*100;
Sum_blackbody_Quintic_04=((sum(R_p_3_blackbody(2:1001))).*(10000/1000)
./Sum_Black_body).*100;

Half_Peak_Reflection_041=Peak_Reflection_041./2;
x_0141=interp1(R_p_1(w1_low:w1_high),lambda(w1_low:w1_high),Half_Peak_
Reflection_041)./nm;
x_0142=interp1(R_p_1(w2_low:w2_high),lambda(w2_low:w2_high),Half_Peak_
Reflection_041)./nm;
FWHM_041=x_0142-x_0141;

Half_Peak_Reflection_042=Peak_Reflection_042./2;
x_0241=interp1(R_p_2(w1_low:w1_high),lambda(w1_low:w1_high),Half_Peak_
Reflection_042)./nm;
x_0242=interp1(R_p_2(w2_low:w2_high),lambda(w2_low:w2_high),Half_Peak_
Reflection_042)./nm;
FWHM_042=x_0242-x_0241;

Half_Peak_Reflection_043=Peak_Reflection_043./2;
x_0341=interp1(R_p_3(w1_low:w1_high),lambda(w1_low:w1_high),Half_Peak_
Reflection_043)./nm;
x_0342=interp1(R_p_3(w2_low:w2_high),lambda(w2_low:w2_high),Half_Peak_
Reflection_043)./nm;
FWHM_043=x_0342-x_0341;


%=============================================

portion=0.5;
thickness_11=(lambda_f./4./nH./nm);  % quarter stack
thickness_22=(lambda_f./4./yL./nm);   % quarter stack
thickness_11_variable=((thickness_11.*portion)./20).*ones(1,20);
```

```
thickness1_2_variable=(((thickness_11+thickness_22).*portion)./20).*on
es(1,20);
thickness_11_constant=thickness_11*(1-2*portion);
thickness_22_constant=thickness_22*(1-2*portion);

d                                                                    =
[thickness_11_variable*nm,thickness_11_constant*nm,thickness1_2_variab
le*nm,thickness_22_constant*nm,...

thickness1_2_variable*nm,thickness_11_constant*nm,thickness1_2_variabl
e*nm,thickness_22_constant*nm,...

thickness1_2_variable*nm,thickness_11_constant*nm,thickness1_2_variabl
e*nm,thickness_22_constant*nm,...

thickness1_2_variable*nm,thickness_11_constant*nm,thickness1_2_variabl
e*nm,thickness_22_constant*nm,...

thickness1_2_variable*nm,thickness_11_constant*nm,thickness1_2_variabl
e*nm,thickness_22_constant*nm,...

thickness1_2_variable*nm,thickness_11_constant*nm,thickness1_2_variabl
e*nm];

for iii=2:length(d)+1
    ww_05(1)=0./nm;
    ww_05(iii)=ww_05(iii-1)+d(iii-1)./nm;
end
ww_05=ww_05(2:252);

    for ii=1:length(lambda)

            [rho_p_1(ii),tao_p_1(ii),R_p_1(ii),T_p_1(ii)]            =
calculation_p(d,y1,y_inc,y_sub,lambda(ii),theta);

    end

    for ii=1:length(lambda)

            [rho_s_1(ii),tao_s_1(ii),R_s_1(ii),T_s_1(ii)]            =
calculation_s(d,y1,y_inc,y_sub,lambda(ii),theta);

    end

    for ii=1:length(lambda)

            [rho_p_2(ii),tao_p_2(ii),R_p_2(ii),T_p_2(ii)]            =
calculation_p(d,y2,y_inc,y_sub,lambda(ii),theta);

    end

    for ii=1:length(lambda)
```

```
            [rho_s_2(ii),tao_s_2(ii),R_s_2(ii),T_s_2(ii)]              =
calculation_s(d,y2,y_inc,y_sub,lambda(ii),theta);

    end

    for ii=1:length(lambda)

            [rho_p_3(ii),tao_p_3(ii),R_p_3(ii),T_p_3(ii)]              =
calculation_p(d,y3,y_inc,y_sub,lambda(ii),theta);

    end

    for ii=1:length(lambda)

            [rho_s_3(ii),tao_s_3(ii),R_s_3(ii),T_s_3(ii)]              =
calculation_s(d,y3,y_inc,y_sub,lambda(ii),theta);

    end


T_p_1_sun=I1.*T_p_1;
T_p_2_sun=I1.*T_p_2;
T_p_3_sun=I1.*T_p_3;

w1_low=669;
w1_high=881;
w2_low=726;
w2_high=994;


Sum_Linear_05=((sum(T_p_1_sun(2:1001))).*(10000/1000)./Sum_Sun).*100;
Sum_Cubic_05=((sum(T_p_2_sun(2:1001))).*(10000/1000)./Sum_Sun).*100;
Sum_Quintic_05=((sum(T_p_3_sun(2:1001))).*(10000/1000)./Sum_Sun).*100;

R_p_1_blackbody=I2.*R_p_1;
R_p_2_blackbody=I2.*R_p_2;
R_p_3_blackbody=I2.*R_p_3;

Sum_blackbody_Linear_05=((sum(R_p_1_blackbody(2:1001))).*(10000/1000).
/Sum_Black_body).*100;
Sum_blackbody_Cubic_05=((sum(R_p_2_blackbody(2:1001))).*(10000/1000)./
Sum_Black_body).*100;
Sum_blackbody_Quintic_05=((sum(R_p_3_blackbody(2:1001))).*(10000/1000)
./Sum_Black_body).*100;


[Peak_Reflection_051 Wavelengeth_Peak_Reflection_051]=max(R_p_1);
[Peak_Reflection_052 Wavelengeth_Peak_Reflection_052]=max(R_p_2);
[Peak_Reflection_053 Wavelengeth_Peak_Reflection_053]=max(R_p_3);

Half_Peak_Reflection_051=Peak_Reflection_041./2;
```

```
x_0151=interp1(R_p_1(w1_low:w1_high),lambda(w1_low:w1_high),Half_Peak_
Reflection_051)./nm;
x_0152=interp1(R_p_1(w2_low:w2_high),lambda(w2_low:w2_high),Half_Peak_
Reflection_051)./nm;
FWHM_051=x_0152-x_0151;

Half_Peak_Reflection_052=Peak_Reflection_052./2;
x_0251=interp1(R_p_2(w1_low:w1_high),lambda(w1_low:w1_high),Half_Peak_
Reflection_052)./nm;
x_0252=interp1(R_p_2(w2_low:w2_high),lambda(w2_low:w2_high),Half_Peak_
Reflection_052)./nm;
FWHM_052=x_0252-x_0251;

Half_Peak_Reflection_053=Peak_Reflection_053./2;
x_0351=interp1(R_p_3(w1_low:w1_high),lambda(w1_low:w1_high),Half_Peak_
Reflection_053)./nm;
x_0352=interp1(R_p_3(w2_low:w2_high),lambda(w2_low:w2_high),Half_Peak_
Reflection_053)./nm;
FWHM_053=x_0352-x_0351;

      % plot the Profile diagram, Quintic
     figure
     axes1 = axes('Parent',figure);
     hold(axes1,'on');
     plot(ww_00,y1,'color',[0.75 0.75 0.75],'LineWidth',2)
     hold on
     plot(ww_01,y1,'-k',ww_02,y1,'--k',ww_03,y1,'-.k',ww_04,y1,':k')
     plot(ww_05,y1,'color',[0.5 0.5 0.5],'LineWidth',2)

legend({'W_{grin}=0','W_{grin}=0.1·t_{H+L}','W_{grin}=0.2·t_{H+L}','W_
{grin}=0.3·t_{H+L}','W_{grin}=0.4·t_{H+L}','W_{grin}=0.5·t_{H+L}'},'fo
ntsize',30)
     xlabel('Distance (nm)','fontsize',25);
     ylabel('Refractive Index','fontsize',25);
     set(axes1,'FontSize',25);
     grid on;


      % plot the Profile diagram, Quintic
     figure
     axes1 = axes('Parent',figure);
     hold(axes1,'on');
     plot(ww_00,y2,'color',[0.75 0.75 0.75],'LineWidth',2)
     hold on
     plot(ww_01,y2,'-k',ww_02,y2,'--k',ww_03,y2,'-.k',ww_04,y2,':k')
     plot(ww_05,y2,'color',[0.5 0.5 0.5],'LineWidth',2)

legend({'W_{grin}=0','W_{grin}=0.1·t_{H+L}','W_{grin}=0.2·t_{H+L}','W_
{grin}=0.3·t_{H+L}','W_{grin}=0.4·t_{H+L}','W_{grin}=0.5·t_{H+L}'},'fo
ntsize',30)
     xlabel('Distance (nm)','fontsize',25);
     ylabel('Refractive Index','fontsize',25);
```

```
      set(axes1,'FontSize',25);
      grid on;


       % plot the Profile diagram, Quintic
      figure
      axes1 = axes('Parent',figure);
      hold(axes1,'on');
      plot(ww_00,y3,'color',[0.75 0.75 0.75],'LineWidth',2)
      hold on
      plot(ww_01,y3,'-k',ww_02,y3,'--k',ww_03,y3,'-.k',ww_04,y3,':k')
      plot(ww_05,y3,'color',[0.5 0.5 0.5],'LineWidth',2)

legend({'W_{grin}=0','W_{grin}=0.1·t_{H+L}','W_{grin}=0.2·t_{H+L}','W_
{grin}=0.3·t_{H+L}','W_{grin}=0.4·t_{H+L}','W_{grin}=0.5·t_{H+L}'},'fo
ntsize',30)
      xlabel('Distance (nm)','fontsize',25);
      ylabel('Refractive Index','fontsize',25);
      set(axes1,'FontSize',25);
      grid on;


     % plot the results of Black body Reflection
      figure
      axes1 = axes('Parent',figure);
      hold(axes1,'on');

plot([0,0.1,0.2,0.3,0.4,0.5],[Sum_blackbody_Linear_00,Sum_blackbody_Li
near_01,Sum_blackbody_Linear_02,Sum_blackbody_Linear_03,Sum_blackbody_
Linear_04,Sum_blackbody_Linear_05],'o-k','LineWidth',1)
      hold on

plot([0,0.1,0.2,0.3,0.4,0.5],[Sum_blackbody_Cubic_00,Sum_blackbody_Cub
ic_01,Sum_blackbody_Cubic_02,Sum_blackbody_Cubic_03,Sum_blackbody_Cubi
c_04,Sum_blackbody_Cubic_05],'s--k','LineWidth',1)
      hold                                                          on
plot([0,0.1,0.2,0.3,0.4,0.5],[Sum_blackbody_Quintic_00,Sum_blackbody_Q
uintic_01,Sum_blackbody_Quintic_02,Sum_blackbody_Quintic_03,Sum_blackb
ody_Quintic_04,Sum_blackbody_Quintic_05],'^:k','LineWidth',1)
      legend({'Linear          Profile','Cubic          Profile','Quintic
Profile'},'fontsize',20)
      xlabel('Width    of    the    graded    index    of    refraction
(W_{grin})','fontsize',25);
      ylabel('Percent reflectance of thermal radiation','fontsize',25);
      set(axes1,'FontSize',16);
      grid on;
      % plot the results of Solar Transmission
      figure
      axes1 = axes('Parent',figure);
      hold(axes1,'on');
plot([0,0.1,0.2,0.3,0.4,0.5],[Sum_Linear_00,Sum_Linear_01,Sum_Linear_0
2,Sum_Linear_03,Sum_Linear_04,Sum_Linear_05],'o-k','LineWidth',1)
```

```
    hold                                                                on
plot([0,0.1,0.2,0.3,0.4,0.5],[Sum_Linear_00,Sum_Cubic_01,Sum_Cubic_02,
Sum_Cubic_03,Sum_Cubic_04,Sum_Cubic_05],'s--k','LineWidth',1)
    hold                                                                on
plot([0,0.1,0.2,0.3,0.4,0.5],[Sum_Linear_00,Sum_Quintic_01,Sum_Quintic
_02,Sum_Quintic_03,Sum_Quintic_04,Sum_Quintic_05],'^:k','LineWidth',1)
    legend({'Linear         Profile','Cubic         Profile','Quintic
Profile'},'fontsize',20)
    xlabel('Width    of    the    graded    index    of    refraction
(W_{grin})','fontsize',25);
    ylabel('Percent transmittance of solar irradiance','fontsize',25);
    set(axes1,'FontSize',25);
    grid on;

   % plot the results of Peak Reflection
    figure
    axes1                    =                    axes('Parent',figure);
plot([0,0.1,0.2,0.3,0.4,0.5],[Peak_Reflection_001,Peak_Reflection_011,
Peak_Reflection_021,Peak_Reflection_031,Peak_Reflection_041,Peak_Refle
ction_051],'o-k','LineWidth',1)
    hold                                                                on
plot([0,0.1,0.2,0.3,0.4,0.5],[Peak_Reflection_002,Peak_Reflection_012,
Peak_Reflection_022,Peak_Reflection_032,Peak_Reflection_042,Peak_Refle
ction_052],'s--k','LineWidth',1)
    hold                                                                on
plot([0,0.1,0.2,0.3,0.4,0.5],[Peak_Reflection_003,Peak_Reflection_013,
Peak_Reflection_023,Peak_Reflection_033,Peak_Reflection_043,Peak_Refle
ction_053],'^:k','LineWidth',1)
    legend({'Linear         Profile','Cubic         Profile','Quintic
Profile'},'fontsize',20)
    xlabel('Width    of    the    graded    index    of    refraction
(W_{grin})','fontsize',25);
    ylabel('Peak reflection (%)','fontsize',25);
    set(axes1,'FontSize',25);
    grid on;
 % plot the results of Full Width at Half Maximum
    figure

plot([0,0.1,0.2,0.3,0.4,0.5],[FWHM_001,FWHM_011,FWHM_021,FWHM_031,FWHM
_041,FWHM_051],'o-r','LineWidth',2)
    hold on

plot([0,0.1,0.2,0.3,0.4,0.5],[FWHM_002,FWHM_012,FWHM_022,FWHM_032,FWHM
_042,FWHM_052],'o-g','LineWidth',2)
    hold on

plot([0,0.1,0.2,0.3,0.4,0.5],[FWHM_003,FWHM_013,FWHM_023,FWHM_033,FWHM
_043,FWHM_053],'o-b','LineWidth',2)
    title('Full Width at Half Maximum for different profile width with
5 Layers , T=100^oC','fontsize',16);
    legend({'Linear         Profile','Cubic         Profile','Quintic
Profile'},'fontsize',16)
```

```
xlabel('Profile Width','fontsize',16);
ylabel('FWHM (nm)','fontsize',16);
grid on;
```

III- Generated power code

```
clc
clear all;
close all;
um = 1e-6;
nm = 1e-9;
% define admittance for medium
Air = 1;
nH = 2;
% nL = 1.3;
yL=1.3;
Glass =1.52;
tt=0.0:1/19:1;

    yH_1=yL+(nH-yL).*tt;
    yH_2=yL+(nH-yL).*(3.*(tt.^2)-2.*(tt.^3));
    yH_3=yL+(nH-yL).*(10.*(tt.^3)-15.*(tt.^4)+6.*(tt.^5));
    yH_1_rev=nH+(yL-nH).*tt;
    yH_2_rev=nH+(yL-nH).*(3.*(tt.^2)-2.*(tt.^3));
    yH_3_rev=nH+(yL-nH).*(10.*(tt.^3)-15.*(tt.^4)+6.*(tt.^5));

% define visible region of light
lambda_max=50000;
number_of_steps=5001;
step=10;
lambda = linspace(0,lambda_max,number_of_steps)*nm;

% define thin film structure
y_inc = Air; % incident medium admittance
y_sub = Glass; % substrate medium admittance
theta = 0;        % in degree
% theta = 0:5:89; % in degree

%---------------------------------------Black Body Radiation----------
---------------------------%

c=3*10^8; % speed of light in vaccum
h=6.625*10.^-34; %  Planck constant
k=1.38*10.^-23; %   Boltzmann constant
T1=5778; % Temperatures in Kelvin
T2_contant=500;
T2_variable=T2_contant;
% load data_second_layer_750K

%---------------------------------------Planks Law---------------------
---------------------------%

I1=(2*h*c*c)./((lambda.^5).*(exp((h.*c)./(k.*T1.*lambda))-1)).*1e-13;
Sum_Sun=(sum(I1(2:number_of_steps))).*(step);
```

```
%-------------------------------------------------------------------------
----------------------------%

I2_constant=(2*h*c*c)./((lambda.^5).*(exp((h.*c)./(k.*T2_contant.*lamb
da))-1)).*1e-13;
I2=(2*h*c*c)./((lambda.^5).*(exp((h.*c)./(k.*T2_variable.*lambda))-
1)).*1e-13;
Sum_black_body=(sum(I2(2:number_of_steps))).*(step);
%-------------------------------------------------------------------------
----------------------------%

[Peak_I2 Wavelengeth_Peak_I2]=max(I2_constant);
lambda_f= lambda(1,Wavelengeth_Peak_I2);


portion=0.0;
thickness_11=(lambda_f./4./nH./nm);    % quarter stack
thickness_22=(lambda_f./4./yL./nm);    % quarter stack
thickness_11_variable=((thickness_11.*portion)./20).*ones(1,20);
thickness1_2_variable=(((thickness_11+thickness_22).*portion)./20).*on
es(1,20);
thickness_11_constant=thickness_11*(1-2*portion);
thickness_22_constant=thickness_22*(1-2*portion);

d                                                                    =
[thickness_11_variable*nm,thickness_11_constant*nm,thickness1_2_variab
le*nm,thickness_22_constant*nm,...

thickness1_2_variable*nm,thickness_11_constant*nm,thickness1_2_variabl
e*nm,thickness_22_constant*nm,...

thickness1_2_variable*nm,thickness_11_constant*nm,thickness1_2_variabl
e*nm,thickness_22_constant*nm,...

thickness1_2_variable*nm,thickness_11_constant*nm,thickness1_2_variabl
e*nm,thickness_22_constant*nm,...

thickness1_2_variable*nm,thickness_11_constant*nm,thickness1_2_variabl
e*nm,thickness_22_constant*nm,...

thickness1_2_variable*nm,thickness_11_constant*nm,thickness1_2_variabl
e*nm];

y1 = [yH_1,nH,yH_1_rev,yL,yH_1,nH,yH_1_rev,yL,...
      yH_1,nH,yH_1_rev,yL,yH_1,nH,yH_1_rev,yL,...
      yH_1,nH,yH_1_rev,yL,yH_1,nH,yH_1_rev];

y2 = [yH_2,nH,yH_2_rev,yL,yH_2,nH,yH_2_rev,yL,...
    yH_2,nH,yH_2_rev,yL,yH_2,nH,yH_2_rev,yL,...
    yH_2,nH,yH_2_rev,yL,yH_2,nH,yH_2_rev];
```

```
y3 = [yH_3,nH,yH_3_rev,yL,yH_3,nH,yH_3_rev,yL,...
    yH_3,nH,yH_3_rev,yL,yH_3,nH,yH_3_rev,yL,...
    yH_3,nH,yH_3_rev,yL,yH_3,nH,yH_3_rev];


for iii=2:length(d)+1
    ww_00(1)=0./nm;
    ww_00(iii)=ww_00(iii-1)+d(iii-1)./nm;
end
ww_00=ww_00(2:252);


for jj=1:length(theta)
    for ii=1:length(lambda)


[rho_p_1_0(jj,ii),tao_p_1_0(jj,ii),R_p_1_0(jj,ii),T_p_1_0(jj,ii)]     =
calculation_p(d,y1,y_inc,y_sub,lambda(ii),theta(jj));

    end

    for ii=1:length(lambda)


[rho_s_1_0(jj,ii),tao_s_1_0(jj,ii),R_s_1_0(jj,ii),T_s_1_0(jj,ii)]     =
calculation_s(d,y1,y_inc,y_sub,lambda(ii),theta(jj));

    end

    for ii=1:length(lambda)


[rho_p_2_0(jj,ii),tao_p_2_0(jj,ii),R_p_2_0(jj,ii),T_p_2_0(jj,ii)]     =
calculation_p(d,y2,y_inc,y_sub,lambda(ii),theta(jj));

    end

    for ii=1:length(lambda)


[rho_s_2_0(jj,ii),tao_s_2_0(jj,ii),R_s_2_0(jj,ii),T_s_2_0(jj,ii)]     =
calculation_s(d,y2,y_inc,y_sub,lambda(ii),theta(jj));

    end

    for ii=1:length(lambda)


[rho_p_3_0(jj,ii),tao_p_3_0(jj,ii),R_p_3_0(jj,ii),T_p_3_0(jj,ii)]     =
calculation_p(d,y3,y_inc,y_sub,lambda(ii),theta(jj));

    end
```

```
    for ii=1:length(lambda)


[rho_s_3_0(jj,ii),tao_s_3_0(jj,ii),R_s_3_0(jj,ii),T_s_3_0(jj,ii)]     =
calculation_s(d,y3,y_inc,y_sub,lambda(ii),theta(jj));

    end
end

% Solar Transmittance

T_p_1_sun_0=I1.*T_p_1_0;
T_p_2_sun_0=I1.*T_p_2_0;
T_p_3_sun_0=I1.*T_p_3_0;

for iii=1:length(theta)

Sum_Linear_p_00(1,iii)=((sum(T_p_1_sun_0(iii,2:number_of_steps))).*(st
ep)./Sum_Sun).*100;
end
for iii=1:length(theta)

Sum_Cubic_p_00(1,iii)=((sum(T_p_2_sun_0(iii,2:number_of_steps))).*(ste
p)./Sum_Sun).*100;
end
for iii=1:length(theta)

Sum_Quintic_p_00(1,iii)=((sum(T_p_3_sun_0(iii,2:number_of_steps))).*(s
tep)./Sum_Sun).*100;
end

T_s_1_sun_0=I1.*T_s_1_0;
T_s_2_sun_0=I1.*T_s_2_0;
T_s_3_sun_0=I1.*T_s_3_0;

for iii=1:length(theta)

Sum_Linear_s_00(1,iii)=((sum(T_s_1_sun_0(iii,2:number_of_steps))).*(st
ep)./Sum_Sun).*100;
end
for iii=1:length(theta)

Sum_Cubic_s_00(1,iii)=((sum(T_s_2_sun_0(iii,2:number_of_steps))).*(ste
p)./Sum_Sun).*100;
end
for iii=1:length(theta)

Sum_Quintic_s_00(1,iii)=((sum(T_s_3_sun_0(iii,2:number_of_steps))).*(s
tep)./Sum_Sun).*100;
end
```

```
% Blackbody Reflectance
R_p_1_blackbody_0=I2.*R_p_1_0;
R_p_2_blackbody_0=I2.*R_p_2_0;
R_p_3_blackbody_0=I2.*R_p_3_0;
T_p_3_blackbody_0=I2.*(1-R_p_3_0);

for iii=1:length(theta)

Sum_blackbody_Linear_p_00(1,iii)=((sum(R_p_1_blackbody_0(iii,2:number_
of_steps))).*(step)./Sum_black_body).*100;
end

for iii=1:length(theta)

Sum_blackbody_Cubic_p_00(1,iii)=((sum(R_p_2_blackbody_0(iii,2:number_o
f_steps))).*(step)./Sum_black_body).*100;
end

for iii=1:length(theta)

Sum_blackbody_Quintic_p_00(1,iii)=((sum(R_p_3_blackbody_0(iii,2:number
_of_steps))).*(step)./Sum_black_body).*100;
end


R_s_1_blackbody_0=I2.*R_s_1_0;
R_s_2_blackbody_0=I2.*R_s_2_0;
R_s_3_blackbody_0=I2.*R_s_3_0;


for iii=1:length(theta)

Sum_blackbody_Linear_s_00(1,iii)=((sum(R_s_1_blackbody_0(iii,2:number_
of_steps))).*(step)./Sum_black_body).*100;
end

for iii=1:length(theta)

Sum_blackbody_Cubic_s_00(1,iii)=((sum(R_s_2_blackbody_0(iii,2:number_o
f_steps))).*(step)./Sum_black_body).*100;
end

for iii=1:length(theta)

Sum_blackbody_Quintic_s_00(1,iii)=((sum(R_s_3_blackbody_0(iii,2:number
_of_steps))).*(step)./Sum_black_body).*100;
end



% %
```

```
%=============================================

portion=0.5;
thickness_11=(lambda_f./4./nH./nm);  % quarter stack
thickness_22=(lambda_f./4./yL./nm);   % quarter stack
thickness_11_variable=((thickness_11.*portion)./20).*ones(1,20);
thickness1_2_variable=(((thickness_11+thickness_22).*portion)./20).*on
es(1,20);
thickness_11_constant=thickness_11*(1-2*portion);
thickness_22_constant=thickness_22*(1-2*portion);

d                                                                       =
[thickness_11_variable*nm,thickness_11_constant*nm,thickness1_2_variab
le*nm,thickness_22_constant*nm,...

thickness1_2_variable*nm,thickness_11_constant*nm,thickness1_2_variabl
e*nm,thickness_22_constant*nm,...

thickness1_2_variable*nm,thickness_11_constant*nm,thickness1_2_variabl
e*nm,thickness_22_constant*nm,...

thickness1_2_variable*nm,thickness_11_constant*nm,thickness1_2_variabl
e*nm,thickness_22_constant*nm,...

thickness1_2_variable*nm,thickness_11_constant*nm,thickness1_2_variabl
e*nm,thickness_22_constant*nm,...

thickness1_2_variable*nm,thickness_11_constant*nm,thickness1_2_variabl
e*nm];

% for iii=2:length(d)+1
%     ww_05(1)=0./nm;
%     ww_05(iii)=ww_05(iii-1)+d(iii-1)./nm;
% end
% ww_05=ww_05(2:252);

for jj=1:length(theta)
    for ii=1:length(lambda)


[rho_p_1_5(jj,ii),tao_p_1_5(jj,ii),R_p_1_5(jj,ii),T_p_1_5(jj,ii)]     =
calculation_p(d,y1,y_inc,y_sub,lambda(ii),theta(jj));

    end

    for ii=1:length(lambda)


[rho_s_1_5(jj,ii),tao_s_1_5(jj,ii),R_s_1_5(jj,ii),T_s_1_5(jj,ii)]     =
calculation_s(d,y1,y_inc,y_sub,lambda(ii),theta(jj));

    end
```

```
    for ii=1:length(lambda)


[rho_p_2_5(jj,ii),tao_p_2_5(jj,ii),R_p_2_5(jj,ii),T_p_2_5(jj,ii)]     =
calculation_p(d,y2,y_inc,y_sub,lambda(ii),theta(jj));

    end

    for ii=1:length(lambda)


[rho_s_2_5(jj,ii),tao_s_2_5(jj,ii),R_s_2_5(jj,ii),T_s_2_5(jj,ii)]     =
calculation_s(d,y2,y_inc,y_sub,lambda(ii),theta(jj));

    end

    for ii=1:length(lambda)


[rho_p_3_5(jj,ii),tao_p_3_5(jj,ii),R_p_3_5(jj,ii),T_p_3_5(jj,ii)]     =
calculation_p(d,y3,y_inc,y_sub,lambda(ii),theta(jj));

    end

    for ii=1:length(lambda)


[rho_s_3_5(jj,ii),tao_s_3_5(jj,ii),R_s_3_5(jj,ii),T_s_3_5(jj,ii)]     =
calculation_s(d,y3,y_inc,y_sub,lambda(ii),theta(jj));

    end
end


% Solar Transmittance

T_p_1_sun_5=I1.*T_p_1_5;
T_p_2_sun_5=I1.*T_p_2_5;
T_p_3_sun_5=I1.*T_p_3_5;

for iii=1:length(theta)

Sum_Linear_p_05(1,iii)=((sum(T_p_1_sun_5(iii,2:number_of_steps))).*(st
ep)./Sum_Sun).*100;
end
for iii=1:length(theta)

Sum_Cubic_p_05(1,iii)=((sum(T_p_2_sun_5(iii,2:number_of_steps))).*(ste
p)./Sum_Sun).*100;
end
for iii=1:length(theta)
```

```
Sum_Quintic_p_05(1,iii)=((sum(T_p_3_sun_5(iii,2:number_of_steps))).*(s
tep)./Sum_Sun).*100;
end

T_s_1_sun_5=I1.*T_s_1_5;
T_s_2_sun_5=I1.*T_s_2_5;
T_s_3_sun_5=I1.*T_s_3_5;

for iii=1:length(theta)

Sum_Linear_s_05(1,iii)=((sum(T_s_1_sun_5(iii,2:number_of_steps))).*(st
ep)./Sum_Sun).*100;
end
for iii=1:length(theta)

Sum_Cubic_s_05(1,iii)=((sum(T_s_2_sun_5(iii,2:number_of_steps))).*(ste
p)./Sum_Sun).*100;
end
for iii=1:length(theta)

Sum_Quintic_s_05(1,iii)=((sum(T_s_3_sun_5(iii,2:number_of_steps))).*(s
tep)./Sum_Sun).*100;
end


% Blackbody Reflectance
R_p_1_blackbody_5=I2.*R_p_1_5;
R_p_2_blackbody_5=I2.*R_p_2_5;
R_p_3_blackbody_5=I2.*R_p_3_5;
T_p_3_blackbody_5=I2.*(1-R_p_3_5);

for iii=1:length(theta)

Sum_blackbody_Linear_p_05(1,iii)=((sum(R_p_1_blackbody_5(iii,2:number_
of_steps))).*(step)./Sum_black_body).*100;
end

for iii=1:length(theta)

Sum_blackbody_Cubic_p_05(1,iii)=((sum(R_p_2_blackbody_5(iii,2:number_o
f_steps))).*(step)./Sum_black_body).*100;
end

for iii=1:length(theta)

Sum_blackbody_Quintic_p_05(1,iii)=((sum(R_p_3_blackbody_5(iii,2:number
_of_steps))).*(step)./Sum_black_body).*100;
end


R_s_1_blackbody_5=I2.*R_s_1_5;
```

```
R_s_2_blackbody_5=I2.*R_s_2_5;
R_s_3_blackbody_5=I2.*R_s_3_5;

for iii=1:length(theta)

Sum_blackbody_Linear_s_05(1,iii)=((sum(R_s_1_blackbody_5(iii,2:number_
of_steps))).*(step)./Sum_black_body).*100;
end

for iii=1:length(theta)

Sum_blackbody_Cubic_s_05(1,iii)=((sum(R_s_2_blackbody_5(iii,2:number_o
f_steps))).*(step)./Sum_black_body).*100;
end

for iii=1:length(theta)

Sum_blackbody_Quintic_s_05(1,iii)=((sum(R_s_3_blackbody_5(iii,2:number
_of_steps))).*(step)./Sum_black_body).*100;
end

%==================================== Input data for power contribution
================================================%
Solar_concentration_ratio=5:5:100;                                    %
Solar_concentration_ratio=Area_aperture/Area_receiver
Area_receiver=0.1.*(pi/4);              % receiver area
Area_aperture=Solar_concentration_ratio.*Area_receiver;               %
collector area
etta=0.9;                          % efficiency of the collector
T_inf=300;                         % environment temperature
h=17.4;                              % the local convective heat transfer
coefficient between the receiver and the surrounding environmentthe
local convective heat transfer coefficient between the receiver and the
surrounding environment


%==================================== Determining input power from Sun
================================================%

P_in_sollar_without_area=I1.*etta;
P_in_sollar_sum_without_area=sum(P_in_sollar_without_area(2:number_of_
steps)).*step;
Sum_black_body=(sum(I2(2:number_of_steps))).*(step);

%==================================== Determining output power for the
case                 without                 any                 cover
================================================%

% Input power after passing the dielectric mirror
P_in_nothing=P_in_sollar_without_area.*1;
P_in_nothing_sum=(sum(P_in_nothing(2:number_of_steps)).*step).*Area_ap
erture;
```

```
% Radiative loss and Conductive&Convective losses after passing the
dielectric mirror

L_R_nothing=Area_receiver.*(1).*5.67.*(10^(-8)).*((T2_contant^4)-
(T_inf^4));        % Radiative loss
L_H_nothing=Area_receiver.*h.*(T2_contant-T_inf);
% Conductive&Convective losses


P_out_nothing_sum= P_in_nothing_sum-(L_R_nothing+L_H_nothing);


%================================== Determining output power for a
quintic profile ================================================%

% Input power after passing the dielectric mirror
P_in_quintic=P_in_sollar_without_area.*T_p_3_5;
P_in_quintic_sum=(sum(P_in_quintic(2:number_of_steps)).*step).*Area_ap
erture;

% Radiative loss and Conductive&Convective losses after passing the
dielectric mirror
R_p_quintic_blackbody=I2.*R_p_3_5;
R_p_quintic=((sum(R_p_quintic_blackbody(2:number_of_steps))).*(step)./
Sum_black_body);

L_R_quintic=Area_receiver.*(1-R_p_quintic).*5.67.*(10^(-
8)).*((T2_contant^4)-(T_inf^4));   % Radiative loss
L_H_quintic=Area_receiver.*h.*(T2_contant-T_inf);
% Conductive&Convective losses

P_out_quintic_sum= P_in_quintic_sum-(L_R_quintic+L_H_quintic);


eff_quintic=((P_out_quintic_sum-
P_out_nothing_sum)./P_out_nothing_sum).*100;

%============================== Determining output power based on the
reference TCO ==============================================%

load Adjusted_data_TCO_ref

% Input power after passing the dielectric mirror
P_in_TCO=P_in_sollar_without_area.*T_Bare_Glass_new_1;
P_in_TCO_sum=(sum(P_in_TCO(24:number_of_steps)).*step).*Area_aperture;

% Radiative loss and Conductive&Convective losses after passing the
dielectric mirror
R_p_TCO_blackbody=I2.*(1-T_R_Bare_Glass_new_1);
R_p_TCO=((sum(R_p_TCO_blackbody(24:number_of_steps))).*(step)./Sum_bla
ck_body);
```

```
L_R_TCO=Area_receiver.*(1-R_p_TCO).*5.67.*(10^(-8)).*((T2_contant^4)-
(T_inf^4));   % Radiative loss
L_H_TCO=Area_receiver.*h.*(T2_contant-T_inf);
% Conductive&Convective losses

P_out_TCO_sum= P_in_TCO_sum-(L_R_TCO+L_H_TCO);



eff_TCO=((P_out_TCO_sum-P_out_nothing_sum)./P_out_nothing_sum).*100;


%=================================== Determining output power for a
quarter profile ================================================%

% Input power after passing the dielectric mirror
P_in_quarter=P_in_sollar_without_area.*T_p_3_0;
P_in_quarter_sum=(sum(P_in_quarter(2:number_of_steps)).*step).*Area_ap
erture;

% Radiative loss and Conductive&Convective losses after passing the
dielectric mirror
R_p_quarter_blackbody=I2.*R_p_3_0;
R_p_quarter=((sum(R_p_quarter_blackbody(2:number_of_steps))).*(step)./
Sum_black_body);

L_R_quarter=Area_receiver.*(1-R_p_quarter).*5.67.*(10^(-
8)).*((T2_contant^4)-(T_inf^4));   % Radiative loss
L_H_quarter=Area_receiver.*h.*(T2_contant-T_inf);
% Conductive&Convective losses

P_out_quarter_sum= P_in_quarter_sum-(L_R_quarter+L_H_quarter);


eff_quarter=((P_out_quarter_sum-
P_out_nothing_sum)./P_out_nothing_sum).*100;
```

IV- P-polarized calculation code

```
function [ro,to,R,T] = calculation_p(d,y,y_i,y_s,l,ia)

for m = 1:length(ia)
for i = 1:length(y)
y_s(m,i)     =     sqrt(real(y(i))^2-imag(-y(i))^2-y_i^2*sind(ia(m))^2-
2*1i*real(y(i))*imag(-y(i)));
if imag(y_s(m,i))>0
y_s(m,i) = -(y_s(m,i));
end
delta_s(m,i) = 2*pi*d(i)/l*y_s(m,i);
y_i_s(m) = y_i*cosd(ia(m));
y_s_s(m)      =      sqrt(real(y_s)^2-imag(-y_s)^2-y_i^2*sind(ia(m))^2-
2*1i*real(y_s)*imag(-y_s));
if imag(y_s_s(m))>0
y_s_s(m) = -(y_s_s(m));
end
y_p(m,i) = y(i)^2/y_s(m,i);
delta_p(m,i) = delta_s(m,i);
y_i_p(m) = y_i^2/y_i_s(m);
y_s_p(m) = y_s^2/y_s_s(m);
tp = [cos(delta_p(m,i)), 1i*sin(delta_p(m,i))/y_p(m,i);
1i*y_p(m,i)*sin(delta_p(m,i)), cos(delta_p(m,i))];
if i == 1
M = tp;
else
M = M*tp;
end
end
BC = M*[1; y_s_p(m)];
B(m) = BC(1);
C(m) = BC(2);

ro(m) = (y_i_p(m)*B(m)-C(m))/(y_i_p(m)*B(m)+C(m));
phi_r(m) = angle(ro(m))/pi*180; % phase
to(m) = 2*y_i_s(m)/(y_i_s(m)*B(m)+C(m));
phi_t(m) = angle(to(m))/pi*180; % phase

R(m) = abs(ro(m))^2;
T(m) =4*y_i_p(m)*real(y_s_p(m))/abs((y_i_p(m)*B(m)+C(m)))^2;
end
```

V- S-polarized calculation code

```
function [ro,to,R,T] = calculation_s(d,y,y_i,y_s,l,ia)

for m = 1:length(ia)
for i = 1:length(y)
y_s(m,i) = sqrt(real(y(i))^2-imag(-y(i))^2-...
y_i^2*sind(ia(m))^2-2*1i*real(y(i))*imag(-y(i)));
if imag(y_s(m,i))>0
y_s(m,i) = -(y_s(m,i));
end
delta_s(m,i) = 2*pi*d(i)/l*y_s(m,i);
y_i_s(m) = y_i*cosd(ia(m));
y_s_s(m) = sqrt(real(y_s)^2-imag(-y_s)^2-...
y_i^2*sind(ia(m))^2-2*1i*real(y_s)*imag(-y_s));
if imag(y_s_s(m))>0
y_s_s(m) = -(y_s_s(m));
end
tp = [cos(delta_s(m,i)), 1i*sin(delta_s(m,i))/y_s(m,i);
1i*y_s(m,i)*sin(delta_s(m,i)), cos(delta_s(m,i))];
if i == 1
M = tp;
else
M = M*tp;
end
end
BC = M*[1; y_s_s(m)];
B(m) = BC(1);
C(m) = BC(2);

ro(m) = (y_i_s(m)*B(m)-C(m))/(y_i_s(m)*B(m)+C(m));
phi_r(m) = angle(ro(m))/pi*180; % phase
to(m) = 2*y_i_s(m)/(y_i_s(m)*B(m)+C(m));
phi_t(m) = angle(to(m))/pi*180; % phase

R(m) = abs(ro(m))^2;
T(m) = 4*y_i_s(m)*real(y_s_s(m))/abs((y_i_s(m)*B(m)+C(m)))^2;
end
```